Contributions instrumentales et théoriques à l'héliosismologie

par

Thierry Appourchaux

Un mémoire soumis en vue de l'obtention d'une
habilitation à diriger des recherches

délivrée par

Le département d'Astrophysique
de
l'Université de Nice

Jury d'habilitation:

Eric Fossat, Université de Nice, Président
Julien Borgnino, Université de Nice
Bo Andersen, Norwegian Space Center, Oslo, Norvège
Claus Fröhlich, World Radiation Center, Davos, Suisse
Douglas Gough, Cambridge University, Royaume Uni
Sylvaine Turck-Chièze, Commissariat à l'énergie atomique, Saclay

2000

Le mémoire de Thierry Appourchaux est accepté par:

Président Date

Date

Date

Date

Date

Date

Université de Nice

2000

Contributions instrumentales et théoriques à l'héliosismologie

par
Thierry Appourchaux

Résumé

Contributions instrumentales et théoriques à l'héliosismologie

par

Thierry Appourchaux
habilitation à diriger des recherches

Université de Nice

Eric Fossat, Université de Nice, Président

Après une introduction à l'histoire du domaine, on aborde la description des méthodes théoriques, intrumentales et d'analyse de données pertinente à l'héliosismologie. Les apports scientifiques de l'auteur sont ensuite décrits dans ces sous-domaines correspondants, nommément:

- Intrumentation: Fabry-Pérot à lame d'hydrocarbure et de niobate de lithium, filtre magnéto-optique et photomètre imageur,
- Analyse théorique de la mesure héliosismique: optimisation de la mesure en vitesses radiales et en intensité, maximum de vraisemblance pour imageurs et non-imageurs, évaluation des erreurs statistiques et biais associées à la mesure des paramètres des modes p.
- Structure et dynamique interne solaire: 'splittings' et modes de gravité,
- Astéroseismologie

Les articles les plus importants associés à ce travail sont inclus dans le mémoire.

Eric Fossat, Université de Nice
Président du jury

A ma femme et mes enfants

Table des Matières

Liste des Figures

Remerciements

Je voudrais tout d'abord remercier Eric Fossat d'avoir bien voulu accepter de diriger cette hdr, rien ne l'y obligeait si ce n'est son honnêteté scientifique. Merci aussi à Julien Borgnino pour sa participation.

Je voudrais aussi remercier les membres du jury pour leur coopération dans cette aventure, notamment d'avoir accepter pour certain de lire ce mémoire en Français. Tout d'abord un grand merci à Claus qui a la qualité rare de toujours vous pousser dans vos derniers retranchements; il a la capacité de vous faire penser ce à quoi on n'aurait imaginé. J'ai particulièrement apprécié son soutien dans les moments les plus difficiles de la construction et de l'opération du LOI (damné clapet...). Je n'oublie pas et n'oublierai pas que je lui dois ma carrière scientifique. Merci Claus.

Je ne sais pas si je saurai traduire tout le respect que j'ai pour Bo. Il fut aussi un des rares à me soutenir dans les moments difficiles, je ne l'oublie pas. Bo a une intelligence rare et de rares qualités. Il a une créativité scientifique et une habileté politique qui sont des atouts majeurs, j'en suis toujours admiratif. De plus, il a eu l'audace de ne pas me juger hâtivement... il pense sans doute que je suis comme un Bonnes-Mares qui doit se bonifier avec le temps. Merci Bo.

Je remercie vivement Douglas d'avoir accepté de participer à mon jury. Je sais que son temps est précieux, tout comme il peut l'être pour notre domaine. Il serait vain d'écrire en quelques phrases à quel point il est une source d'aspiration et de connaissances pour moi. Je me rappelerai toujours l'une de nos premières rencontres à Versailles où je lui demanda un rendez-vous comme on demande une audience au Roi Soleil...j'ai toujours cet immense respect qui confine à une admiration illimitée. Merci Douglas.

Je remercie aussi Sylvaine de sa participation. Elle est une rare personne dans le domaine qui ne mâche pas ses mots. C'est sans aucun doute ce qui me rapproche d'elle. Il devient de plus en plus rare de dire ce que l'on pense. Au moins avec Sylvaine on sait où l'on va. Merci Sylvaine.

Il y a bien sûr les collègues du domaine que je voudrais remercier. Tout d'abord Thierry Toutain, qui est en quelque sorte mon jumeau scientifique. Nos vues sont souvent si proches (trop?) que l'on ne sait parfois plus qui a dit quoi. Il a la qualité d'être plus tempéré et plus calme, et aussi de moins s'emporter que moi. Nos longues conversations téléphoniques sur de divers sujets ont laissé des stigmates visibles sur mon oreille gauche!

Merci Thierry.

Ensuite vient Takashi Sekii avec lequel j'ai eu lorqu'il était à Cambridge de nombreux échanges par e-mail (ce fut parfois à la limite de saturer nos disques durs...). Ces échanges ne furent pas seulement scientifiques mais aussi culturels; je suis toujours impressionné par la connaissance littéraire de Takashi. Il m'a permit de découvrir notamment 'Zen and the art of...', Mishima, pour ne citer que quelques exemples. Merci Takashi.

Je remercie aussi mes collaborateurs pour leur travail fructueux et utile qui m'a notamment permit d'essayer d'améliorer mon contact humain. Il y a encore beaucoup de chemin à faire. Merci à Laurent Gizon pour sa considération et son amitié; je suis sûr que l'on fera un bon bout de chemin ensemble. Merci donc à Cristina Rabello-Soares (j'espère qu'elle s'est remise de la défaite du Brésil...), merci à Mohamed Lazrek (ton couscous du 12 Juillet restera dans les mémoires), merci à William Chaplin (l'homme qui écrit plus vite que son ombre), merci d'avance à David Fierry-Fraillon (ta tartiflette du 2 Juillet restera aussi dans les mémoires...). Par la même occasion, merci aux Bleus pour les moments de bonheur qu'ils nous ont donnés et ceux à venir.

Une grande partie de ce mémoire doit au dévouement de l'équipe du LOI que j'ai encadrée de 1988 à 1996. Je remercie de tout mon coeur Thierry Beaufort, Jos Fleur, Samuel Lévêque, Didier Martin, Udo Telljohann sans lesquels cet instrument ('simple et élégant') n'aurait pas vu le jour. Merci à tous.

Un grand merci à Jocelyne et Isabelle pour la logistique de l'hôtel et du pot. Merci à Alex pour sa mémorable tourte de blettes; puisse ainsi l'authenticité niçoise être conservée. Merci à Fix pour son aide dans la mise au point des derniers détails techniques d'avant soutenance. Merci à Christine et Bernard pour le prêt de la voiture de course. Merci à Mohamed et sa soeur pour leurs keftas, et merci à Eric pour la vue. Enfin merci à la personne de l'assistance qui m'a permit de me rappeler que je savais toujours parler Français.

Last but not least, je ne sais comment exprimer par écrit mes remerciements à ma famille proche. Ma mie, Maryse, toujours là pour supporter mon caractère infernal (Belzébuth et sa clique sont en stage chez moi...). Il n'est pas exagéré de dire que moi-même, je ne peux dire si la soupe au lait va déborder dans la minute qui vient. Merci à mes deux enfants, Kévin et Thibault, qui ont également partagé cette lourde charge.

Partie I

Aperçu scientifique

Préambule

Pourquoi étudier le Soleil?

Le Soleil est source de vie. De tous temps, l'astre qui nous fournit la vie nous a intrigué. On le retrouve dans nos aliments, et l'on ne peut imaginer que des soleils artificiels soient capables de subvenir à nos besoins, où d'aider à produire du bon vin!

Depuis des milliers d'années, la nourriture dont nous dépendons a été liée à l'apparition régulière du Soleil; il en devint une divinité. Les Egyptiens l'appelait Râ, les Mayas Ah-Kin, les celtes Lug, les grecs Phobos. La disparition du Soleil au cours des éclipses apportait le spectre de la nuit éternelle synonyme de châtiment divin. Les incantations des shamans évoluèrent lentement vers des réactions plus prévisibles. Le sorcier-astronome des Mayas établissait le calendrier des saisons, et donnait les dates de production du maïs. Les prédictions des éclipses pouvaient alors être utilisées pour des fins plus politiques.

Avec l'avènement du Christianisme, le Soleil disparut de nos panthéons modernes, tout au moins dans le Vieux Monde. Au XVIème siècle, l'astre solaire perdit de sa superbe lorsque l'on trouva les premières imperfections à sa surface: les taches. Cela n'empêcha pas Louis XIV au siècle suivant d'utiliser la symbolique solaire pour se faire appeler le Roy Soleyl. Ce n'est pas par hasard non plus que ce siècle s'appela le siècle des Lumières.

Avec la découverte des premières taches solaires commencèrent les études systématiques de la surface de l'astre solaire. Ces observations permirent de mettre à jour le cycle de 11 ans de l'activité solaire qui est encore inexpliqué à l'aube du troisième millénaire. Au cours du XXième siècle, le Soleil fut de nouveau placé au rang de divinité incontournable surtout pour ses capacités colorantes et moralement bienfaisantes. Au cours de ce siècle, le Soleil fut de plus en plus étudié et permit à de nombreux astrophysiciens de l'utiliser pour vérifier leurs théories.

De nombreux développements techniques sont à mettre à l'actif de la physique

solaire. Par exemple, la première fusée lançée en 1945 par les Américains pour faire de l'astronomie, le fut pour étudier le spectre solaire. Jusqu'en 1962, il n'était pas possible d'imaginer que l'on puisse connaitre indirectement la structure de l'intérieur du Soleil. C'est ce que permet ce nouvel outil qu'est l'héliosismologie et que je me propose de vous faire connître dans le chapitre suivant. En espèrant que ce nouvel outil, dans un siècle prochain, nous ouvrira le coeur des étoiles.

Figure 0.1: Collage huichol de Makueyika (www.huicholartphil.org.mx). Le soleil ou Tao Jreeku symbolise la source de la vie. Les huichols sont des indiens mexicains qui se servent d'un champignon hallucinogène, le peyotl, pour avoir des *visions*. Cette tribu de quelques 10000 âmes essayent de préserver son authenticité depuis quelques millénaires, tout comme les Mayas essayent de le faire dans les Chiapas.

Chapitre 1

Qu'est ce que l'héliosismologie?

1.1 Historique

La découverte by Leighton et al. (1962) des 'oscillations solaires' marque le début d'une science qui ne s'appelait pas encore héliosismologie. Leighton et al. (1962) observèrent les vitesses radiales de l'atmosphère solaire dans une raie de Fraunhofer. Ils découvrirent que ces vitesses radiales présentaient une période d'environ 5 minutes. Ulrich (1970) donna l'interprétation théorique correcte de ces oscillations solaires. Elles sont causées par des ondes acoustiques qui sont emprisonnées à l'intérieur du Soleil donnant naissance à des modes propres. De part l'existence de cette cavité résonante, des modes à fréquences discrètes sont suceptibles d'être observés. Ulrich (1970) donna la relation de dispersion associée à ces modes. Cette prédiction fut confirmée par Deubner (1975) qui observa pour la première fois un diagramme (k, ω), où k est le nombre d'onde horizontal ($k = 2\pi/\lambda$) et ω est la fréquence circulaire ($\omega = 2\pi\nu$). Les vitesses observées à l'époque étaient de quelques centaines de m/s, et des longueurs d'ondes de quelques milliers de kms. Figure 1.1 montre un diagramme (l, ν) analogue au diagramme (k, ω) obtenu vers la fin des années 1990. On y voit clairement la discrétisation des modes prévue par Ulrich (1970) où elle apparait sous forme de crêtes.

La confirmation observationnelle de Deubner (1975), bien qu'intéressante, fit croire que les modes n'étaient que locaux. Les équipes de l'Université de Birmingham et Nice avaient développées des cellules à résonance magnétique pour détecter les modes globaux. Claverie et al. (1979) de Birmingham mettèrent en évidence l'existence de périodicités en observant le Soleil comme une étoile. Le spectre de ces périodicités ressemblait à un peigne, l'écart moyen entre les pics de puissance était de l'ordre de 67 μHz. Cette observation

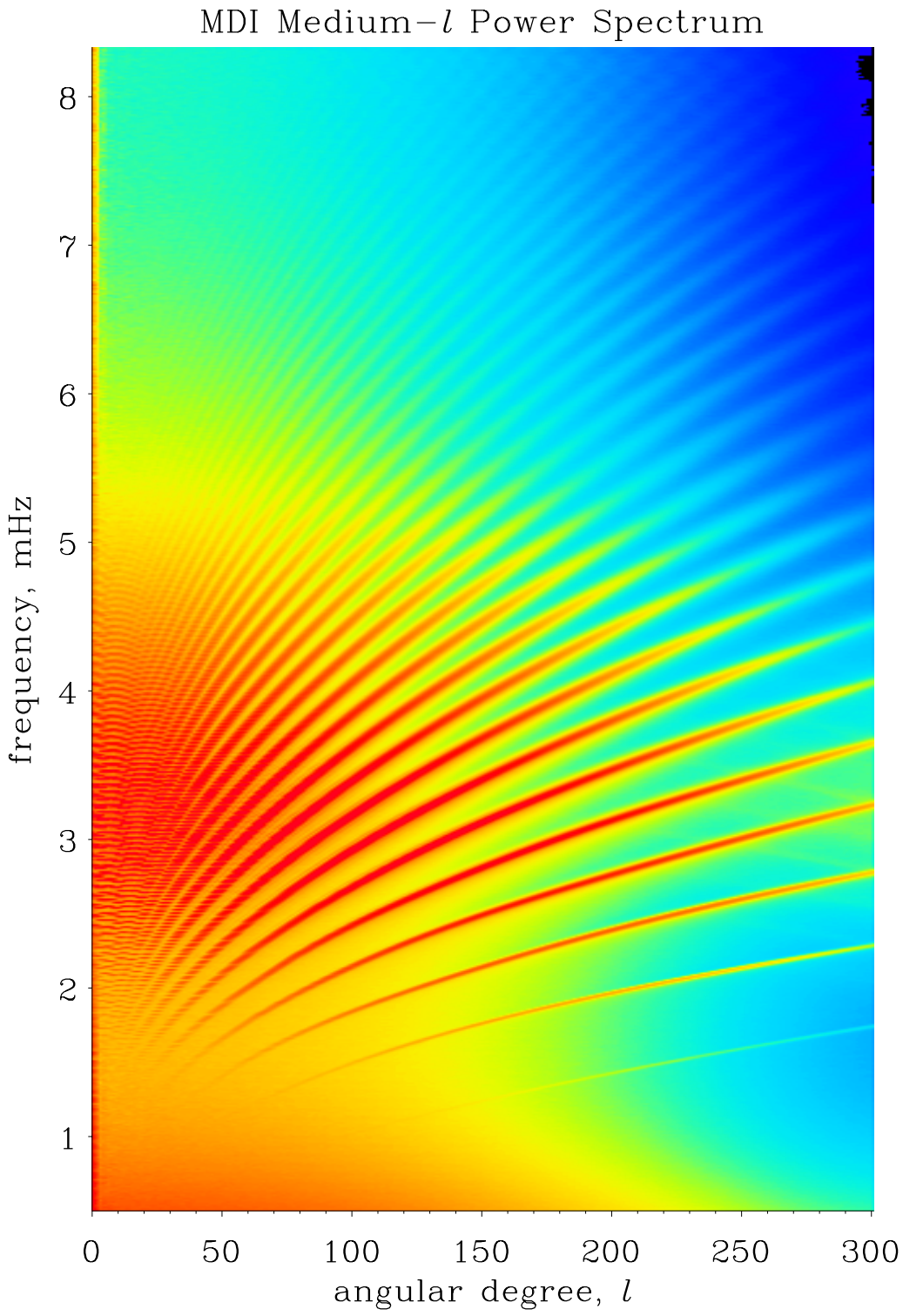

Figure 1.1: Diagramme (l, ν) obtenu par l'instrument MDI/SOI à bord de la sonde spatiale SOHO. Une trentaine de crêtes sont visibles. La plus faible en bas à droite est le fundamental ou mode f (n=0).

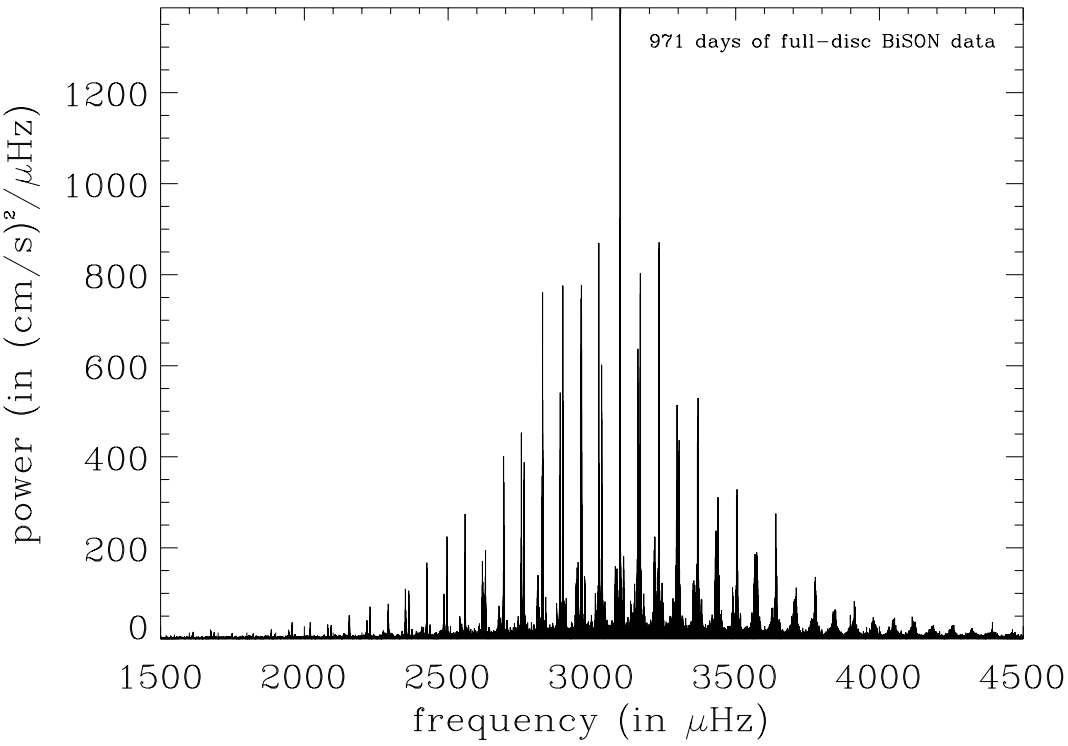

Figure 1.2: Spectre de puissance de BiSON. On peut facilement voir un spectre cannelé causé par les modes propres solaires. Lorsque le Soleil est observé comme une étoile, seuls les modes de degrés bas ($l < 5$) sont détectables. Ils correspondent aux modes se trouvant près de l'axe des ordonnées dans la Fig. 1.1.

confirma que les modes étaient globaux car les degrés observés ne pouvaient être que petits ($l \leq 4$). L'observation de l'Université de Birmingham fut confirmée par celle de Nice (Grec et al. 1980). Figure 1.2 illustre un spectre typique obtenu en observant le Soleil comme une étoile; le peigne est facilement visible.

Ce n'est que quelques années plus tard que l'héliosismologie put enfin commencer. Duvall (1982) put réduire les diagrammes (l, ν) à une simple relation de dispersion (loi de Duvall). Duvall & Harvey (1984) mesurèrent les variations des fréquences des modes induites par la rotation solaire. Ces deux résultats furent utilisés par Duvall et al. (1984) pour faire les premières inversions des données héliosismiques d'après une méthode développée par Gough (1984). La mesure des fréquences des modes pouvait enfin nous renseigner sur les conditions à l'intérieur du Soleil. L'héliosismologie pouvait mériter son nom. La puissance

de l'héliosismologie tient à sa capacité à trouver les inconsistences de notre description de la physique solaire. Un exemple en est la correction qu'il fut nécessaire d'apporter à l'équation d'état suite aux problèmes rencontrés par **??**.

Le développement de l'héliosismologie s'accéléra considérablement dans les années qui suivirent. Les principaux modes détectés étaient des modes dits de pression (la force de rappel est la pression) ou modes p. Ces modes, comme nous le verrons plus loin, se propagent principalement dans les zones convective et radiative. La détection d'un grand nombre de modes de degrés l différents permet ainsi de remonter par inversion à la structure de ces zones. Il restait néanmoins une zone aveugle où seuls les modes dits de gravité (modes g) s'y propagent: le coeur du Soleil. Une meilleure connaissance de cette partie du Soleil fut la principale motivation pour allonger la durée de mesure et pour se placer en dehors de l'atmosphère. Des réseaux tels que GONG[1], IRIS[2] et BiSON[3], sur lesquels le Soleil ne se couche jamais, virent le jour au milieu des années 1980. Différents projets spatiaux, dont DISCO[4], furent étudiés dont seul SOHO[5] survécut, il fut approuvé à la même époque que les réseaux.

Du milieu des années 1980 jusqu'au lancement de SOHO et le démarrage de GONG fin 1995, l'héliosismologie évolua lentement vers l'utilisation de durée d'observation plus longue. Cette période de latence permit de développer des instruments pouvant s'affranchir d'une grande partie du bruit atmosphérique tel que LOWL[6] et le LOI[7].

1.2 Théorie de l'héliosismologie

Les oscillations solaires perturbent faiblement la structure du Soleil. Une linéarisation au 1er ordre des équations décrivant le modèle solaire à l'équilibre est suffisante pour calculer les fréquences des modes propres et leur fonction propre (Unno et al. 1989). La résolution de ce problème a beaucoup de points communs avec la description des orbites de l'électron de l'atome d'hydrogène. De nombreuses méthodes utilisées en mécanique

[1]Global Oscillation Network Group (Volume dédié de *Science*, 1996, **272**)
[2]Investigation on the Rotation and Interior of the Sun (Egamberdiev & Fossat 1991)
[3]Birmingham Solar-Oscillations Network (Elsworth et al. 1991)
[4]Dual Spectral Irradiance and Solar Constant Orbiter (Rapport de Phase A, ESA-SCI(82)2)
[5]Solar and Heliospheric Observatory, une mission ESA/NASA (Volumes dédiés de *Solar Physics*, 1995, **162**;1997, **170**; et 1997,**175**)
[6]The low-l instrument (Tomczyk et al. 1995a)
[7]Luminosity Oscillations Imager

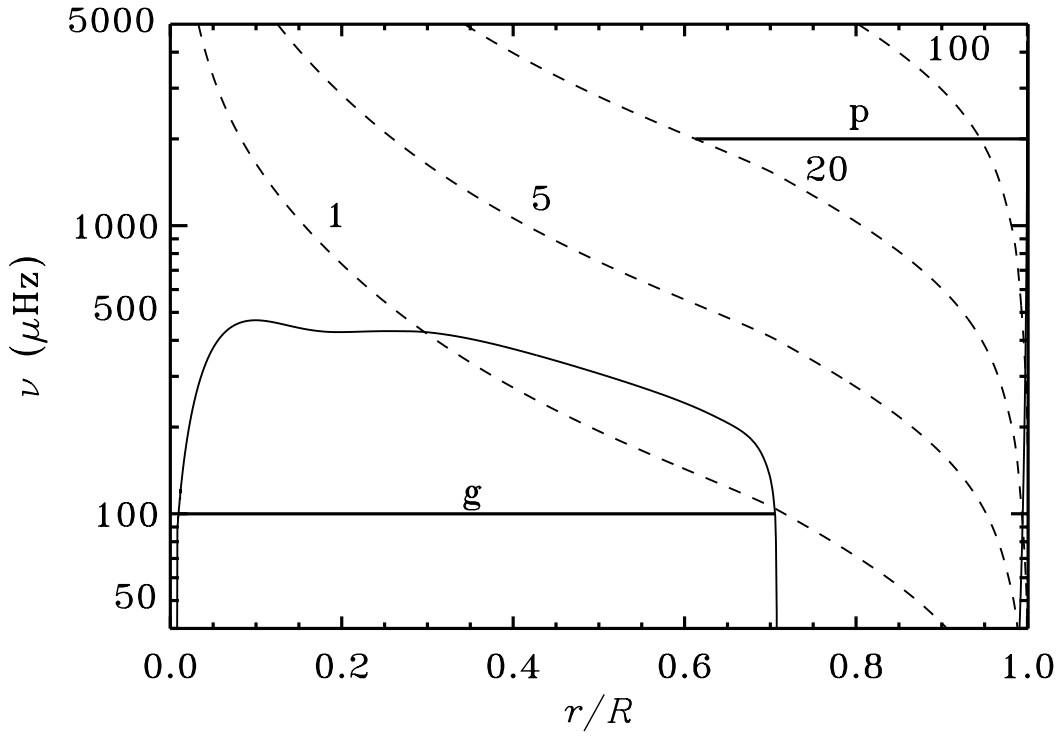

Figure 1.3: Fréquence de gravité N (ligne continue) and fréquence acoustique charactéristique S_l (lignes tiretées, identifiées par l) en function du rayon réduit $r/R_\odot$, pour un modèle actuel du Soleil. Les lignes horizontales en gras indiquent les cavités où un mode g ($\nu = 100\mu$Hz) et un mode p ($\nu = 2000\mu$Hz, l=20) sont emprissonnés. (Figure tirée de Christensen-Dalsgaard, 1998).

quantique le sont aussi en héliosimologie tel que par exemple la méthode Wentzel-Kramers-Brillouin (WKB).

1.2.1 Modes propres du Soleil

Après linéarisation des équations du modèle solaire, on doit résoudre un système d'équations différentielles. De par les conditions aux limites, le problème se réduit à trouver les valeurs propres et fonctions propres du système (voir Unno et al. 1989). De par la symétrie sphérique, il est possible de séparer les variables. On peut donc écrire génériquement l'expression suivante pour les vecteurs propres:

$$\delta r(\theta, \phi, r, t) = \xi_r Y_l^m(\theta, \phi) e^{i\omega t} \tag{1.1}$$

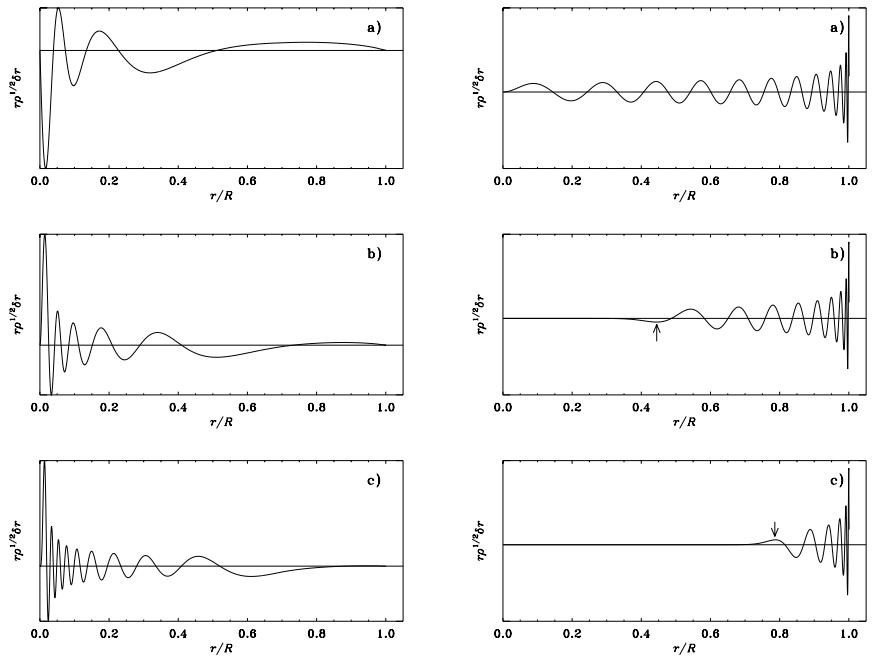

Figure 1.4: $\xi_r(r)$ pour quelque modes g (à gauche), et modes p (à droite)(Figure tirée de Christensen-Dalsgaard, 1998).

où (r, θ, ϕ) sont les coordonnées sphériques, $\xi_r(r)$ est la fonction propre en r, $Y_l^m(\theta, \phi)$ est l'harmonique sphérique (fonction propre en (θ, ϕ)), où l est le degré, m l'ordre azimuthal et ω la fréquence du mode propre. Il est possible de trouver une équation différentielle pour $\xi_r(r)$ en utilisant l'approximation de Cowling[8] et en supposant que les oscillations sont adiabatiques.

Cette équation est la suivante:

$$\frac{d^2\xi_r}{dr^2} = \frac{\omega^2}{c^2}\left(1 - \frac{N^2}{\omega^2}\right)\left(\frac{S_l^2}{\omega^2} - 1\right)\xi_r \tag{1.2}$$

où N est la fréquence de Brünt-Vaïsala, S_l la fréquence de Lamb et c est la vitesse du son. Cette équation simplifiée rend compte des propriétés des oscillations. En effet les solutions de l'Eq. (1.2) sont des fonctions du type $e^{ik(r)r}$ où $k(r)$ est donné par:

$$k^2(r) = \frac{\omega^2}{c^2}\left(1 - \frac{N^2}{\omega^2}\right)\left(1 - \frac{S_l^2}{\omega^2}\right) \tag{1.3}$$

Lorsque les solutions de l'Eq. (1.3) sont réelles les fonctions propres sont alors des combinaisons de fonctions circulaires. Il y a deux régions qui satisfont cette condition: la région

[8] Dans l'approximation de Cowling, on suppose que les modes perturbent peu le potentiel gravitationnel.

où se propagent les modes p, et celle où se propagent les modes g.

$$\text{mode p} : |\omega| > \ |N| \ et \ |\omega| \ > S_l \tag{1.4}$$

$$\text{mode g} : |\omega| < \ |N| \ et \ |\omega| \ < S_l \tag{1.5}$$

En dehors de ces régions les solutions sont exponentielles et les modes ne s'y propagent plus mais se transmettent par 'effet tunnel'. La figure 1.3 montre les régions où les modes se propagent. Les modes p sont principalement emprisonnés entre l'atmosphère solaire et un point dont la position dépend de la fréquence du mode et de son degré. Les modes g sont principalement emprisonnés dans la zone radiative, sous la zone convective; ils ne s'y propagent que par effet tunnel. Pour les modes p la force de rappel est la pression, pour les modes g c'est la gravité. La période typique des modes p est le l'ordre de 3 à 15 min, celle des modes g est de quelques heures. La figure 1.4 montre quelques solutions de $\xi_r(r)$ montrant clairement les zones de propagation des modes.

Chaque mode est donc décrit dans la symétrie sphérique par 3 nombres quantiques: n, l, m. L'ordre n représente le nombre de noeuds le long d'un rayon. Le degré l est associé au nombre de noeuds à la surface du Soleil, et l'ordre azimuthal m au nombre de noeuds passant par l'axe de rotation du Soleil. Notre étoile est en quelque sorte une corde de guitare tri-dimensionnelle. Le couple (l, m) représente l'image du mode observé en surface par l'intermédiaire de l'harmonique sphérique associée $Y_m^l(\theta, \phi)$. Chaque mode (n, l, m) est associé à une fréquence particulière ν_{nlm} correspondant à un volume particulier du Soleil. Chaque mode échantillonne donc le Soleil de manière différente (Figure 1.5). C'est la connaissance de ces fréquences qui permet de remonter à la structure interne du Soleil.

1.2.2 Propagation des modes

Une méthode asymptotique de tracé de rayon est souvent utilisée pour voir comment les modes se propagent. L'utilisation de cette méthode permet aussi de remonter à la structure interne du Soleil, ainsi qu'à sa dynamique. Un exemple de propagation de modes p de différents degrés est montré sur la Fig. 1.6. On y voit notamment que les modes de degrés les plus bas se propagent plus profondément. La trajectoire des rayons est incurvée dans l'intérieur solaire car la vitesse du son augmente vers l'intérieur réfractant donc plus les rayons. Dans l'atmosphère solaire, les modes p sont réfléchis par la chute brutale de la densité au-dessus de la photospère.

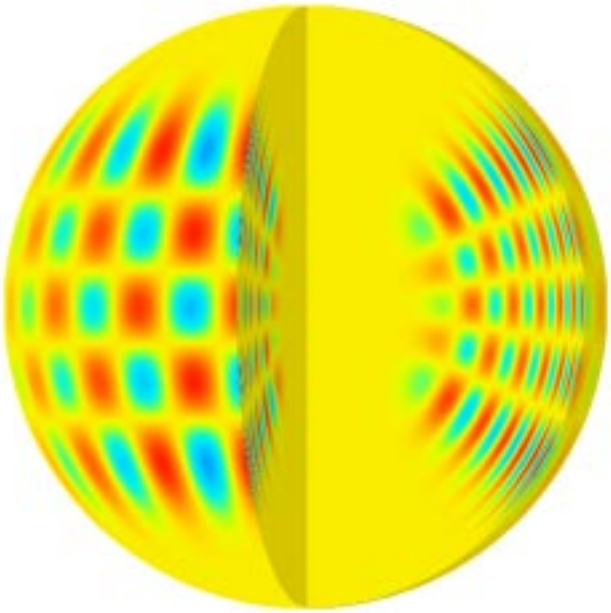

Figure 1.5: Un mode propre en 3 dimensions pour une fréquence de 2935.88 μHz, $n = 14$, l=20, $m = 16$. Le rouge et le bleu rendent compte de déplacements de signes opposés. On voit bien quel volume ce mode échantillonne en profondeur tout aussi bien qu'en latitude. L'information des fréquences de million de modes permet de remonter à une connaissance volumétrique du Soleil (Figure faite par A.Kosovichev, 1996).

1.2.3 Fréquences et modèle solaire

On a vu que les fréquences dépendent fortement de la structure interne du Soleil. Pour comprendre quel modèle répond aux fréquences mesurées, on peut comparer des fréquences mesurées avec des fréquences issues d'un modèle solaire. Une manière plus simple de comprendre l'influence de la structure interne du Soleil est de rechercher des expressions asymptotiques de ces fréquences en fonction de caractéristiques de la structure interne.

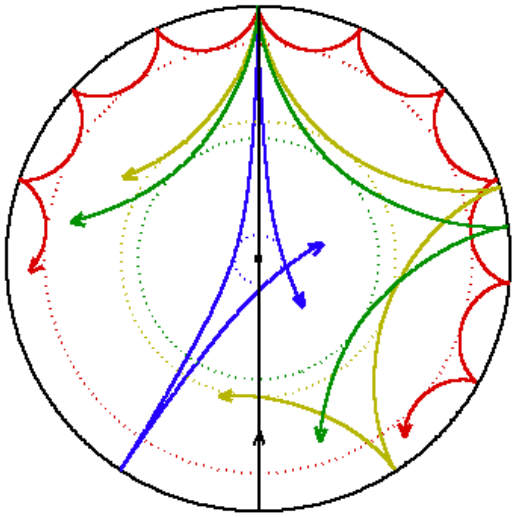

Figure 1.6: Propagation des modes pour $l = 0$ (noir), $l = 2$ (bleu), $l = 20$ (vert), $l = 25$ (jaune) et $l = 75$ (rouge) pour un mode à 3000 μHz. Dans la théorie de propagation asymptotique des modes, on peut représenter la direction de propagation du front d'onde par un tracé de rayon (analogie optique ou acoustique). Les cercles en tireté correspondent au point de reflection interne du mode ()

modes p

Tassoul (1980) donna, pour les modes p d'ordre n élevés et de degrés bas, une telle expression:

$$\nu_{nl} \approx (n + \frac{l}{2} + \frac{1}{4} + \alpha)\Delta\nu - (AL^2 - \delta)\frac{\Delta\nu^2}{\nu_n l} \tag{1.6}$$

où ν_{nl} est la fréquence du mode, α dépend de la réflection à la surface du Soleil, $L^2 = l(l+1)$, $\Delta\nu$ est l'inverse de la durée de propagation des ondes sonores dans un diamètre solaire donné par:

$$\Delta\nu = \left(2\int_0^{R_\odot} \frac{\mathrm{d}r}{c}\right)^{-1}, \tag{1.7}$$

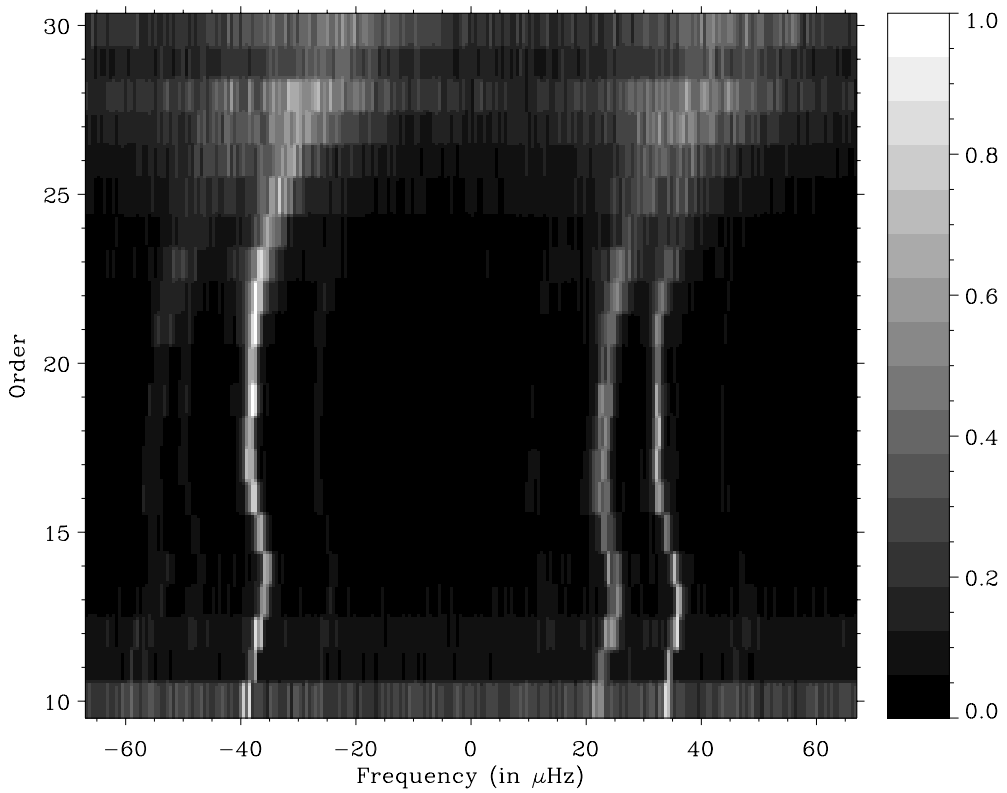

Figure 1.7: Diagramme échelle du spectre de la Fig. 1.2. Ce diagramme consiste à découper en tranches le spectre, et à superposer ces tranches, d'où le nom d'*échelle*. La longueur des tranches est d'environ 136 μHz correspondant à l'écart entre les modes d'adjacent n et de même degré l. Cette équidistance varie avec le degré et permet d'identifier le degré. La lente variation de cette équidistance avec n reflète les conditions sur la structure interne. La crête des modes $l = 0$ sont à l'extrême droite, celle des modes $l = 2$ sont 10 μHz à gauche des modes $l = 0$. La crête des modes $l = 1$ sont à l'extrême droite. On peut aussi voir des crêtes fantômes autour de la crête principale. Ces fantômes sont créés par les interruptions jour-nuit; ils sont à 11.57 μHz de par et d'autre de la crête originale.

où c est la vitesse du son. Dans l'Eq. (1.6), A est fonction de la dérivée de la vitesse du son:

$$A = \frac{1}{4\pi^2 \Delta\nu} \left(\frac{c(R_\odot)}{R_\odot} - \int_0^{R_\odot} \frac{\mathrm{d}c}{\mathrm{d}r} \frac{\mathrm{d}r}{r} \right) \tag{1.8}$$

D'après l'Eq. (1.6), on a donc que les modes d'un même degré sont espacés d'une quantité qui est fonction de la taille du Soleil ($\Delta\nu \approx 136$ μHz pour $l < 4$ et $n \approx 22$). C'est cette propriété qui est utilisée pour obtenir des diagrammes échelles telle que celui de la Fig. 1.7

(Grec 1981). En première approximation on a aussi:

$$\nu_{nl} - \nu_{n-1,l+2} \approx -(4l+6)\frac{\Delta\nu}{4\pi^2\nu_{nl}}\int_0^{R_\odot}\frac{\mathrm{d}c}{\mathrm{d}r}\frac{\mathrm{d}r}{r} \tag{1.9}$$

Cette différence est effectivement petite mais intéressante car elle montre que la fréquence des modes est sensible à la structure du Soleil près du coeur, notamment au gradient de la vitesse du son. Pour le Soleil, cette différence est de l'ordre de 10 à 13 μHz, comme le montre le diagramme échelle de la Fig. 1.7.

modes g

Tassoul (1980) donna l'expression asymptotique suivante de la fréquence des modes g d'ordre n élevés et de degrés bas:

$$\nu_{nl} = \frac{L\int_{r_1}^{r_2} N\frac{\mathrm{d}r}{r}}{2\pi^2(n+l/2+\alpha_g)} \tag{1.10}$$

où α_g est une phase, r_1 and r_2 sont les points de réflection du mode dans la zone radiative, N est la fréquence de Brunt-Vaïsala. D'après cette équation, ce sont les périodes des modes g qui sont espacées régulièrement en fonction de n. Malheureusement un tel comportement n'a pas pu encore être observé. En effet, les modes g sont fortement atténués dans la zone convective, et donc ne perturbent que faiblement l'atmosphère solaire. Leur détection reste une des dernières découvertes majeures à faire en héliosismologie.

1.2.4 Inversion du modèle solaire

De nombreuses techniques ont été développées pour remonter à la structure interne du Soleil depuis la mesure des fréquences. Il n'est pas possible de rendre compte de toutes les techniques possibles. Beaucoup de développements sont en cours et sont eux-mêmes dérivés des techniques utilisées depuis plus de 40 ans en géophysique, pour notre Terre. La première méthode nécessite de comparer des fréquences mesurées avec des fréquences issues d'un modèle solaire: c'est la méthode directe décrite plus haut. Un inconvénient majeur de cette technique est qu'il faut avoir recourt à un grand nombre de modèles pour imiter les mesures obtenues. Les résultats obtenus ne sont donc limités que par notre imagination.

Une autre méthode plus utile nécessite d'inverser les fréquences des modes pour connaitre la structure solaire. La loi de Duvall est une bonne illustration de la méthodologie employée. Dans la loi simplifiée et asymptotique de l'Eq. (1.2), on a une expression pour le

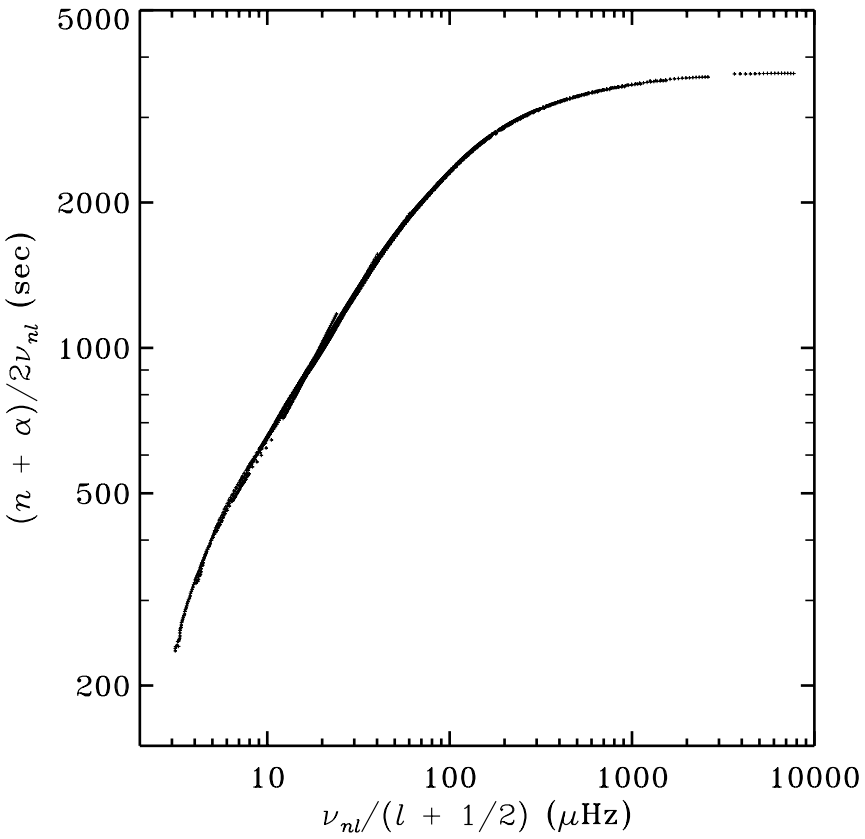

Figure 1.8: Loi de Duvall (Figure tirée de Christensen-Dalsgaard, 1998).

nombre k que l'on peut utiliser pour écrire une condition de quantification. D'après Gough (1986), on peut écrire la condition[9] suivante:

$$\int_{r_t}^{R_\odot} k \mathrm{d}r = (n - \frac{1}{2})\pi \tag{1.11}$$

où r_t est le point de réflection interne. En utilisant l'Eq. (1.2), sachant que $S_l = L^2c^2/r^2$ et en supposant que l'on peut négliger N ($N << \omega$), on obtient finalement pour les modes p d'ordre élevée:

$$F(w) \equiv \int_{r_t}^{R_\odot} \left(1 - \frac{L^2c^2}{\omega^2 r^2}\right)^{\frac{1}{2}} \frac{\mathrm{d}r}{c} \approx \left(n - \frac{1}{2}\right)\frac{\pi}{\omega} \tag{1.12}$$

Cette équation est en essence la loi de Duvall qui montre que $(n - 1/2)/\omega$ est une fonction de ω/L comme le montre la Fig. 1.8. L'Eq. (1.12) montre qu'en première approximation

[9]Condition de Einstein-Brillouin-Keller (EBK) analogue à celle de Bohr-Sommerfeld

que le rapport $(n - 1/2)/\omega$ dépend principalement du rapport $w = \omega/L$. Gough (1984) montra que l'Eq. (1.12) est une équation d'Abel qui peut être inversée facilement pour obtenir implicitement la vitesse du son c:

$$r = R_\odot \exp\left(-\frac{2}{\pi}\int_{a_s}^{a}(w^{-2} - a^{-2})^{-\frac{1}{2}}\frac{\mathrm{d}F}{\mathrm{d}w}\mathrm{d}w\right) \tag{1.13}$$

où $a = c/r$ et a_s est la valeur a à la surface du Soleil. On peut donc tirer des fréquences la vitesse du son, et ce de manière absolue. Il est quand même plus intéressant de comparer la vitesse du son inversée à celle obtenue par des modèles solaires. En supposant que les écarts de vitesse du son (δc) au modèle soient petits, et que les variations de fréquence ($\delta\omega$) le soient aussi, on obtient en différenciant l'Eq. (1.12) au premier ordre en δc et en $\delta\omega$ la relation suivante:

$$\frac{\delta\omega}{\omega} \approx \int_{r_t}^{R_\odot} K_{nl}(r)\frac{\delta c}{c}\mathrm{d}r \tag{1.14}$$

où $K_{nl}(r)$ est une fonction noyau dont l'expression a été donnée par Christensen-Dalsgaard et al. (1988); on peut aussi la déduire de l'Eq. (1.12). Une approximation de la fonction noyau permet de mieux comprendre la source des écarts de fréquences induite par la vitesse du son. Christensen-Dalsgaard et al. (1988) ont montré que loin du point de réflection la fonction noyau peut s'écrire comme:

$$K_{nl}(r) \approx \left(c\int_{r_t}^{R_\odot}\frac{\mathrm{d}r}{c}\right)^{-1} \tag{1.15}$$

Cette expression montre que la contribution des écarts de vitesse du son à la variation des fréquences est plus forte là où la vitesse du son est plus faible. Donc les effets sont plus grands dans les régions où l'onde passe plus de temps. En l'occurence, comme la vitesse du son augmente vers l'intérieur du Soleil, l'onde passe plus de temps dans les couches les plus externes. C'est une des raisons pour laquelle il est plus difficile de bien connaître le coeur solaire car celui-ci est presque opaque, acoustiquement parlant, aux modes p. Tel n'est pas le cas des modes g. Il est possible de trouver pour ces modes une équation similaire à l'Eq (1.14) donnée par:

$$\frac{\delta\omega}{\omega} = \frac{\int_{r_1}^{r_2}\delta N\,\frac{\mathrm{d}r}{r}}{\int_{r_1}^{r_2}N\,\frac{\mathrm{d}r}{r}} \tag{1.16}$$

où r_1 et r_2 sont les points de réflection du mode dans la zone radiative. On constate que les modes g sont plus particulièrement sensibles aux conditions dans le coeur solaire de par le factor $1/r$.

Des expressions asymptotiques telles que celles de l'Eq. (1.14) sont maintenant moins d'actualité. Elles ont été remplacées par des expressions moins approximatives qui furent données par Dziembowski et al. (1990). Ces expressions font intervenir deux fonctions noyaux qui dépendent de la quantité que l'on veut étudier (vitesse du son, pression). Christensen-Dalsgaard (1998) donne par exemple l'expression suivante:

$$\frac{\delta\omega}{\omega} = \int_0^{R_\odot} \left(K^{nl}_{c^2,\rho}(r)\frac{\delta c^2}{c^2} + K^{nl}_{\rho,c^2}(r)\frac{\delta\rho}{\rho} \right) \mathrm{d}r \tag{1.17}$$

où $K^{nl}_{c^2,\rho}(r)$ et $K^{nl}_{\rho,c^2}(r)$ sont les noyaux dérivés des fonctions propres. Tout l'art de l'inversion est d'appliquer des fonctions de poids tel que l'on puisse extraire $\delta c^2/c^2$ et $\delta\rho/\rho$ depuis les fréquences des modes. Ce sujet est trop vaste pour être traité ici. On pourra trouver une bonne introduction dans Basu et al. (1996). Néanmoins, l'Eq. (1.17) montre le lien implicite entre le modèle solaire et les fréquences observées. Les techniques d'inversions reposent sur des fréquences mesurées, fréquences qui peuvent être entachées d'erreurs statistiques et/ou systématiques. Le processus de mesure des fréquences revêt donc une importance particulière quant à la connaissance de l'intérieur du Soleil. Ces deux aspects ne peuvent et ne doivent pas être dissociés.

1.2.5 Dynamique interne

L'importance de l'Eq. (1.11) ne doit pas être négligée. Toutes les petites perturbations de la vitesse du son peuvent être étudiées par cette méthode. C'est par analogie à la mécanique quantique, la 'petite' perturbation de l'Hamiltonien occasionnant des modifications des valeurs propres et vecteurs propres. Avant de passer à cette étape, Gough (1984) montra que l'Eq. (1.11) pouvait aussi rendre compte des effets de la rotation sur les fréquences. Par exemple, lorsque la rotation est une fonction que du rayon r, la perturbation des fréquences s'écrit:

$$\delta\omega \approx m \int_{r_t}^{R_\odot} K_{nl}(r)\Omega(r)\mathrm{d}r \tag{1.18}$$

où $\Omega(r)$ décrit la rotation du Soleil et $K_{nl}(r)$ est le noyau précédemment défini. Chaque mode l, m, n voit donc sa fréquence modifiée de par la rotation. C'est analogue à l'effet Zeeman qui lève la dégénérescence des niveaux. Par analogie, cet effet est appelé le 'splitting' rotationnel. La perturbation des fréquences des modes p occasionée par la rotation est plus grande là où les modes passent plus de temps. L'intérieur profond du Soleil ne peut donc être sondé que par des degrés bas. Le modes l=1 sont ceux qui pénètrent le plus profondément,

mais malheureusement pas assez pour permettre de mesurer la rotation du coeur; celle-ci attend encore la détection des modes g.

L'expression asymptotique de l'Eq. (1.18) fut rapidement remplacée par une expression très similaire mais avec un noyau plus compliqué:

$$\delta\omega = \int_0^{R_\odot} \int_0^{\pi} K_{nlm}(r,\theta)\Omega(r,\theta) r \mathrm{d}r\theta \tag{1.19}$$

L'expression de $K_{nlm}(r,\theta)$ est dérivée des fonctions propres. L'influence de la rotation différentielle (apparente à la surface du Soleil) est de modifier la relation simple linéaire de l'Eq. (1.18) en une expression dépendant de polynômes impairs en m (Brown et al. 1989). Ces effets sont bien visibles dans la figure 1.9 qui rendent bien compte des effets de 'splittings' rotationnels sur la fréquence des modes. L'intérêt de la mesure de ces 'splittings' est tel que l'on puisse étudier comment la rotation différentielle varie avec la profondeur. Ce sujet est aussi très vaste. De nombreux travaux traitent de l'inversion des 'splitting' pour connaitre la rotation solaire (Schou et al. 1994).

1.2.6 Excitation et durée de vie des modes

La détection des modes ne peut bien sûr s'effectuer que si les modes sont excités. Par analogie, la sismologie terrestre n'est possible que parce que les modes terrestres sont excités par des tremblements de Terre. Pour le Soleil, les modes sont excités stochastiquement par la convection turbulente (Goldreich & Keeley 1977). Par analogie, les modes se comportent comme des oscillateurs harmoniques excités aléatoirement (Goldreich & Keeley 1977, Kumar et al. 1988). Les amplitudes des modes solaires est de l'ordre de quelques dizaines de cm/s en vitesse radiale, et de quelques parties par million (ppm) en intensité. Les modes sont amortis de diverses manières: viscosité turbulente, intéraction avec la turbulence, dissipation radiative (voir Houdek 1996 pour une revue complète sur ce sujet). La durée de vie typique des modes est de l'ordre d'une dizaine de jours; les plus cohérents ont une durée de vie de plusieurs mois, les moins cohérents de quelques jours. La convection turbulente se manifeste par les granules se trouvant à la surface du Soleil. Les modes sont excités de manière indépendante pourvu que la taille des granules soit petite devant l'échelle spatiale des modes. L'équation d'un oscillateur harmonique sécrit comme suit:

$$\frac{d^2x}{dt^2} + 2\pi\gamma\frac{dx}{dt} + (2\pi)^2\nu_0^2 x = F(t) \tag{1.20}$$

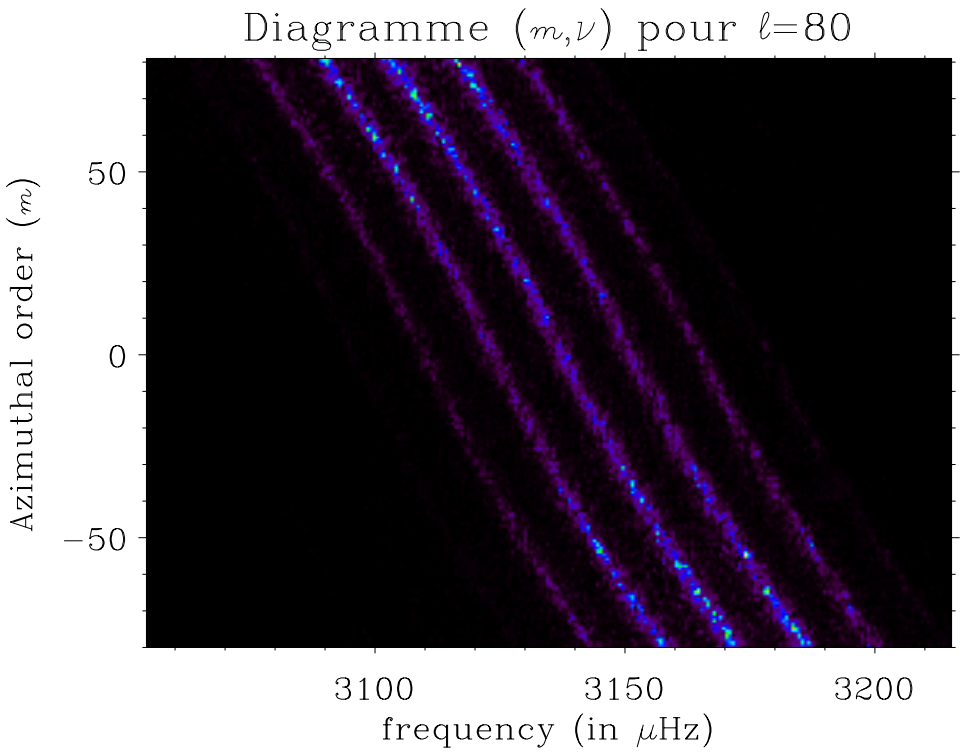

Figure 1.9: Diagramme (m, ν) pour GONG pour $l = 80$. La crête centrale la plus intense est celle de $l = 80$. Les crêtes fantômes de part et d'autres correspndent à $l = 78, 79$ (à gauche) et à $l = 81, 82$ (à droite). Ces denières sont causées par le fait que l'on observe seulement une moitié du Soleil. Les crêtes sont inclinées de par l'effet de la rotation solaire qui affecte la fréquence des modes comme $m\Omega$; l'écart de fréquence entre $m = 80$ et $m = -80$ est donc d'environ 70 μHz. On observe aussi que les crêtes ne sont pas strictement rectiligne mais légèrement déformées comme un S. Cette déformation est causée par la rotation différentielle dans la zone convective.

où t est le temps, x est le déplacement, γ est le terme d'amortissement, ν_0 est la fréquence du mode et $F(t)$ est la fonction de forçage. Cette dernière de par l'excitation stochastique est une variable aléatoire. De l'Eq. (1.20) on en déduit une relation entre la transformée de Fourier de $x(t)$ et de $F(t)$:

$$\tilde{x}(\nu) = \frac{\tilde{F}(\nu)}{(2\pi)^2(\nu_0^2 - \nu^2 + i\gamma\nu)} \tag{1.21}$$

où $\tilde{x}(\nu)$ et $\tilde{F}(\nu)$ sont les transformées de Fourier de $x(t)$ and $F(t)$. De par le grand nombre de granules, on peut déduire que la fonction de forçage est une variable aléatoire distribuée normalement. Par conséquent, il en découle que les parties réelle et imaginaire de $\tilde{F}(\nu)$ sont aussi des variables aléatoires distribuées normalement. L'Eq. (1.21) est très importante

puisqu'elle permet de comprendre le comportement statistique des modes (Kumar et al. 1988), mais aussi d'appliquer des méthodes particulières d'analyse de données: le Maximum de Vraisemblance. Ce domaine particulier sera traité plus loin dans la section 'Analyse de données'. De plus, il est à noter que le profil lorentzien qui découle de l'Eq. (1.21) est très simplifié. Gabriel (1992) fut le premier à reconnaitre que les profils des modes pourraient ne pas être symétriques; ce n'est que plus tard que cette prédiction put être mesurée.

1.3 Observations héliosismiques

L'information que l'on cherche doit pouvoir s'observer sur la seule surface visible du disque solaire: la photosphère. Les oscillations solaires produisent des perturbations occasionant des déplacements de la surface de l'astre, et aussi des perturbations de température et d'opacité.

1.3.1 Mesures de vitesse radiale

Les déplacements de l'atmosphère sont mesurées avec la vitesse radiale occasionée par ces déplacements. On observe donc une raie de Fraunhofer qui retranscrit les déplacements de l'atmosphère. Ceci est une simplification car on ne mesure qu'une vitesse radiale équivalente. En effet le principe de mesure repose sur la mesure de deux intensités de par et d'autres de la raie de Fraunhofer (I_r et I_b), le rapport $\frac{I_r - I_b}{I_r + I_b}$. Ce rapport est supposé être proportionnel à la vitesse radiale du déplacement. D'autres effets indésirables causé par le transfert radiatif viennent perturber cette image idyllique. C'est néanmoins la technique employée.

Disque intégré

Les mesures de vitesses radiales ont commencé dans les années 60 pour déterminer le décalage Doppler dû à l'effet de la gravitation sur la lumière solaire (Blamont & Roddier 1961, Roddier 1967, Brookes et al. 1976). Ces instruments utilisaient des cellules à résonance soit à Sodium soit à Potassium. Suite aux découvertes de Leighton et al. (1962) de nombreux observateurs ont détecté les oscillations solaires en regardant le Soleil globalement avec de telles cellules (Claverie et al. 1979, Grec et al. 1980). C'est l'instrument GOLF[10], utilisant

[10]Global Oscillations at Low Frequency

une cellule à Sodium, qui fut choisi pour être spatialisé et plcé à bord de SOHO (Gabriel et al. 1995).

D'autres techniques furent développées d'après des magnétographes de Babcock modifiés pour observer des vitesses radiales (Dittmer et al. 1978, Severnyi et al. 1976). L'intérêt de cette dernière technique réside dans le fait que c'est la différence de vitesse radiale entre deux régions du disque solaire qui est mesurée. Ces deux régions, contigües, sont un disque central et un anneau extérieur. Cette particularité géométrique modifie la sensibilité de l'instrument au degré des modes; des degrés plus élevés sont observés comparés aux cellules à résonance. Les observations effectuées avec cet instrument confirmèrent ces sensibilités (Scherrer et al. 1982, Scherrer et al. 1983). D'autres résultats plus controversés portèrent sur la détection d'une périodicité à 160 minutes très proche de la neuvième harmonique du jour. La controverse s'éteignit lorsqu'il fut démontré que cette périodicité était un artefact produit par les séquences d'observation journalière amplifiant justement cette harmonique du jour (Elsworth et al. 1989).

Imagerie

La détection des modes de degré bas ($l < 4$) n'est pas suffisante pour comprendre en détail la structure interne du Soleil. L'inversion nécessite d'avoir accès à des degrés plus élevés que seule une instrumentation faisant des images peut fournir. Deubner (1975) utilisa un spectromètre pour mesurer les vitesses radiales sur une région restreinte par la fente. L'observation dans le temps fournit une carte bidimensionnelle des vitesses radiales à laquelle on peut associer une carte (l, ν) ou (k, ω) (Voir Fig. 1.1). L'utilisation de spectromètres atteignit rapidement ses limites malgré l'observation des modes p de bas degrés par Duvall & Harvey (1983).

L'ère des imageurs bidimensionnels démarra avec le tachomètre de Tim Brown (Brown 1985). Cet instrument est basé sur l'utilisation d'un interféromètre de Michelson qui permet de mesurer les vitesses radiales en tous points du disque solaire. L'intérêt en est considérable puisque que l'on peut mesurer des phénomènes dépendant de la latitude (e.g. la rotation différentielle; Brown 1985). D'autres instruments de conception similaire obtinrent aussi de très bons résultats avec un filtre biréfringent combiné à un crystal électro-optique (KDP) (Libbrecht & Zirin 1986) où avec un filtre magnéto-optique (Rhodes et al. 1984, Rhodes et al. 1990). C'est d'ailleurs ce dernier concept qui s'avéra le plus efficace en

ce qui concerne la détection des modes de degrés bas par un imageur. Grâce à cette stabilité inhérente, l'instrument LOWL permit la première observation avec un imageur des modes de degrés bas en vitesse radiale (Tomczyk et al. 1995a, Tomczyk et al. 1995b). C'est néanmoins le tachomètre de Tim Brown qui fut choisi pour des projets de plus grande envergure tel que GONG (Harvey & the GONG instrument development team (1988)) constitué d'un réseau de 6 tachomètres, mis en place en 1995. C'est aussi ce concept adapté et amélioré pour l'environnement spatial qui fut choisi pour MDI[11] (Scherrer et al. 1995).

1.3.2 Mesure d'intensité

Les déplacements de l'atmosphère sont aussi mesurés avec les fluctuations d'intensité lumineuse occasionnées par les variations de température et d'opacité. La technique de mesure est assez simple: on mesure l'intensité lumineuse du Soleil avec une instrumentation suffisamment stable, et on déduit les variations relatives de cette intensité. La simplicité de l'instrumentation est telle qu'un instrument très simple est capable de donner de bonnes mesures.

Disque integré

Les premières mesures datent de Woodard & Hudson (1983) en utilisant le radiomètre ACRIM[12] (Willson 1979) à bord de SMM[13]. Les modes détectés étaient similaires à ceux détectés par les instruments intégrés mesurant des vitesses radiales; seule la distribution en l était légèrement différente en raison d'un effet d'intégration (Woodard 1984). La longueur impressionnante de la série temporelle préfigurera les durées d'observations actuelles.

Par la suite, des mesures de radiance spectrale à bord de vol ballon furent introduites par Fröhlich & Van der Raay (1984) en utilisant des photomètres. Du sol la détection des modes est rendue très difficile de part le bruit occasioné par l'atmosphère solaire; une détection n'est possible qu'en supposant *a priori* que les modes sont présents (Jiménez et al. 1987). Le concept évolua donc naturellement vers un instrument spatialisé (IPHIR[14]) qui fut placé sur PHOBOS[15]. Ce dernier instrument obtint d'excellents résultats notamment

[11] Michelson Doppler Imager
[12] Active Cavity Radiometer Irradiance Monitor
[13] Solar Maximum Mission
[14] InterPlanetary Helioseismology by IRradiance measurements
[15] Mission soviétique d'exploration de Mars

concernant le 'splitting' rotationnel des modes p (Toutain & Fröhlich 1992).

Des radiomètres (DIARAD et PMO6) et des photomètres (SPMs) font partie de l'instrument VIRGO[16] placé à bord de SOHO (Fröhlich et al. 1995).

Imagerie

La détection en intensité des modes de degré intermédiaire (l >20) datent de Duvall et al. (1986) et Nishikawa et al. (1986). Les premiers observèrent, du Pôle Sud, le Soleil dans la raie du Calcium; c'est d'ailleurs un instrument similaire qui est utilisé dans le TON[17] développé par Chou et al. (1995). Nishikawa et al. (1986) observèrent en ville le Soleil en lumière blanche. Malgré toutes les perturbations atmopshériques, il est possible de détecter les modes grâce notamment à la cohérence de ces pertubations sur le disque solaire; occasionnant donc des perturbations négligeables à petite échelle (l élevés). Nous verrons par la suite quelle a été ma contribution spécifique dans ce domaine.

1.3.3 Mesure du bord solaire

L'objectif premier des mesures de bord solaire est la définition de la forme du Soleil. En effet, la forme du Soleil influence l'orbite de Mercure (Dicke 1965), et pourrait donc discréditer la théorie relativiste de la gravitation due à Einstein (1916). Un instrument pour mesurer l'aplatissement du Soleil fut donc développé à Princeton, New Jersey (Dicke & Goldenberg 1967). Cet instrument[18] ne fut que peu utilisé pour des mesures de détection des modes p ou g. Pourtant, Kuhn et al. (1986) mentionna que l'instrument de Dicke ne pouvait pas détecter de modes g comme il avait été fait mention par Delache & Scherrer (1983). Cet instrument fut surtout utile pour déterminer le contraste des facules sur le bord solaire (Libbrecht & Kuhn 1984, Kuhn et al. 1985).

Néanmoins un autre instrument, le SCLERA[19] conçu par Henry Hill (Hill & Stebbins (1975)), fut plus employé pour la détection des oscillations solaires. La détection des modes p et de leurs caractéristiques fut publiée par Hill (1985) confirmée ensuite par Hill & Caudell (1985). Les modes g furent aussi détectés avec le même instrument (Hill 1992). Malheureusement des 'splittings' de modes p aussi haut que 1.5 μHz, ou des fluctuations

[16] Variability of IRradiance and Gravity Oscillations
[17] Taiwanese Oscillation Network
[18] Princeton Solar Distortion Telescope
[19] Santa Catalina Laboratory for Experimental Relativity by Astrometry

d'intensité de ∼100 ppm ne furent pas mesurées à l'époque des observations 78-79 par Woodard & Hudson (1983). De plus ces mêmes données analysées par Brown et al. (1978) et Brown (1979) ne montraient pas clairement les modes p. Les détections de SCLERA étaient déjà à l'époque très controversées. Les mesures devenant de plus en plus longue, il s'est avéré que le 'splitting' des modes p n'était pas aussi élevé (Toutain & Fröhlich 1992). Les fluctuations au bord solaire ont été aussi récemment faite grâce a MDI et ne confirment pas non plus de telles fluctuations (Toner et al. 1999). J'ai effectué sur ce sujet une contribution spécifique que l'on trouvera dans la partie concernée.

1.4 Analyse des données

On a vu précedemment quelle était l'expression pour le déplacement de la surface du Soleil occasioné par les oscillations. Les observations les plus communes (vitesse radiale ou intensité) supposent en première approximation que la perturbation observée peut s'écrire de la manière suivante:

$$p_{\rm obs}(\theta,\phi,t) = \mathcal{R}(A_{nlm}Y_l^m(\theta,\phi)e^{i\omega_{nlm}t}) \tag{1.22}$$

où $\mathcal{R}$ désigne la partie réelle d'un nombre complexe, A_{nlm} est l'amplitude du mode observé. Comme nous l'avons vu dans la section précédente, cette perturbation est observée soit en regardant le Soleil comme une étoile, ou en faisant des images du Soleil. Les techniques d'analyses dans les deux cas sont très similaires. Elles se ramènent toujours à produire une série temporelle qui dépend du filtre spatial. Lorsque cette série est obtenue, il est naturel de par la périodicité du signal d'utiliser la transformée de Fourier. Les deux types d'analyses (spatiale et temporelle) sont détaillés ci-après.

1.4.1 Filtres spatiaux

Disque intégré

Il est bien évident que dans ce cas un seul pixel est utilisé: le Soleil lui-même. C'est cette intégration sur le disque solaire qui fournit le filtrage naturel des modes. Seuls les modes de degrés bas sont visibles. Les filtres furent calculés par Dziembowski (1977), et puis ensuite par Christensen-Dalsgaard & Gough (1982). Le filtre est d'ailleurs différent suivant que l'on observe des vitesses ou des intensités. Dans ce dernier cas, les modes $l = 3$ sont plus atténués.

Imagerie

Dans ce cas, il faut prendre en compte la structure spatiale du mode, pour l'analyse de données. De par la présence de l'harmonique sphérique, il est naturel d'utiliser le conjugué de celle-ci pour le filtrage spatial. Malheureusement, les harmoniques sphériques ne forment pas une base orthogonale sur la demi-sphère solaire. Il en résulte que pour un mode cible de l et m donnés, d'autres l' et m' sont transmis (Tomczyk 1988, Korzennik 1990, Schou 1992, Schou & Brown 1994, voir Fig. 1.9). Il n'est malheureusement pas possible de s'affranchir de ce problème de manière globale, mais il est possible de minimiser l'effet de ces modes fantômes pour certains degrés. Une de mes contributions porte sur ce sujet.

1.4.2 Analyse spectrale

La présence d'une périodicité dans l'expression temporelle de l'amplitude des modes rend naturelle l'utilisation de la transformée de Fourier. On a vu dans la section sur l'excitation des modes que malgré l'excitation stochastique des modes, il était possible d'exprimer le profil d'un mode en fonction de sa fréquence centrale. L'Eq. (1.21) est essentielle pour la compréhension statistique de l'observation: elle permet d'appliquer des méthodes d'ajustement des données qui ne soit pas basées sur les moindres carrés. Néanmoins, il est important de noter que les interruptions jour-nuit sont une source de création de pics fantômes ou alias temporels. De par la périodicité de ces interruptions (24 heures), ces fantômes se trouvent à environ 11.57 μHz du pic principal. C'est pour cela que de nombreux réseaux (GONG, IRIS, BiSON) ont vu le jour pour réduire l'amplitude des ces pics fantômes. Une technique récemment mise au point par Fossat et al. (1999) apporte une solution intéressante à ce problème. Fossat et al. (1999) utilisent les propriétés de cohérence des modes p pour remplir les trous de données, et ainsi diminuer l'amplitude des pics fantômes.

1.4.3 Ajustement des données

La nature particulière de la statistique du spectre de puissance observé en héliosismologie fait que les techniques classiques d'analyses (moindres carrés par exemple) ne peuvent pas s'appliquer.

Ce fait fut reconnu pour la première fois par Duvall & Harvey (1986) qui suggérèrent d'utiliser la méthode du Maximum de Vraisemblance pour l'ajustement des données hélio-

sismiques. La méthode fut démontrée sur des données synthétiques par Anderson et al. (1990), et est maintenant universellement employée dans le domaine pour ajuster les spectres issus d'instruments observant le Soleil comme une étoile (Toutain & Fröhlich 1992). Dans ce cas simple de mesure en disque intégré, les spectres obtenus ont une statistique donnée par un χ^2 à deux degrés de liberté. Cette approximation n'est d'ailleurs valable que lorsque le manque de données (ou trous dans les séries temporelles) introduit un déterminisme négligeable (Gabriel 1994).

En ce qui concerne les instruments imageurs, la présence dans les données de modes fantômes (ou *leaks*) introduit une corrélation entre les séries temporelles de l, m différents, mais proches. Le fait de négliger ces corrélations introduit des biais dans les mesures, notamment, de 'splitting'. Cet aspect de la statistique des modes observés par les instruments imageurs fut noté par Schou (1992). La statistique possède alors une distribution multi-normale, tout au moins en première approximation. Il est à noter que cet aspect du traitement de données est suffisamment compliqué et qu'il n'a pas encore été largement diffusé dans le domaine. Une de mes contributions fut de généraliser l'approche de Schou (1992) et de spécialement initier certains collaborateurs dans ce domaine.

Chapitre 2

Contributions à l'héliosismologie

2.1 Introduction

J'ai soutenu ma thèse de 3ème cycle en Juillet 1984. Le sujet de ma thèse était 'Observations des oscillations solaires à l'aide d'un Fabry-Pérot à bord d'un véhicule spatial'. Ce titre pourrait résumer à lui seul mon engagement dans l'héliosismologie depuis près de 16 ans. Pendant cette période je me suis attaché à m'impliquer complètement dans la conception technique et scientifique d'un instrument novateur, puis ensuite d'en tirer la moisson scientifique en analysant les données obtenues. Cette approche est refletée dans la structure de ce chapitre: la 1ère section s'attache à décrire mes contributions à l'instrumentation héliosismique, la 2ème section résume mes contributions à l'analyse théorique de la mesure héliosismique et à l'analyse des données, la 3ème section rend compte des contributions et des résultats scientifiques qui en découlent.

2.2 Instrumentation

En 1985, le Solar and Heliospheric Observatory de l'Agence Spatiale Européenne (ESA) devenait une véritable mission spatiale. Cette date marqua l'accélération du développement de l'instrumentation destinée à mesurer les oscillations solaires. J'ai activement participé à cette 'course' qui m'a permis de développer 3 instruments de mesure des vitesses radiales solaires et un instrument de mesure des fluctuations d'intensité. Ces 4 instruments sont décris çi-après.

2.2.1 Mesures de vitesses radiales

Un des moyens de détecter les pertubations de l'atmosphère solaire générées par les oscillations solaires est de mesurer les déplacements de la photosphère en utilisant des raies de Fraunhofer. Parmi tous les concepts possibles, j'ai étudié principalement le Fabry-Pérot et le filtre magnéto-optique.

Fabry-Pérot à lame d'hydrocarbure

Le premier Fabry-Pérot (FP) développé après ma thèse était basé sur le même principe que celui de la thèse. Ce filtre, développé au Service d'Aéronomie de Verrières-le-Buisson, était un FP à lame d'hydrocarbure en phase gazeuse dont la pression de vapeur saturante était controlée par l'intermédiaire d'un effet Peltier. Bien que l'instrument fonctionnait parfaitement, il n'a jamais été utilisé pour obtenir des mesures dans un observatoire solaire. Il n'existe qu'un rapport interne du Service d'Aéronomie, non publié à ce jour, sur les performances de cet instrument. Cet instrument fonctionna seulement quelque mois avant mon départ sous les drapeaux, départ qui arrêta le projet.

Filtre magnéto-optique

En marge de mon service militaire, j'ai développé un filtre magnéto-optique utilisant une vapeur de Sodium (filtre type Cacciani, Cacciani et al. 1981). Ce filtre est basé sur une cellule à Sodium plongée dans un champ magnétique, placée entre deux polariseurs croisés. Lorsque la cellule est froide ou en absence de champ magnétique aucune lumière n'est transmise. Dès que la cellule est chauffée, la vapeur de Sodium plongée dans un champ magnétique absorbe les composantes polarisées circulairement gauche et droite. Ce changement de polarisation de la lumière avant le dernier polariseur va permettre à la lumière d'être transmise. L'effet d'absorption combiné à l'effet Faraday contribue à augmenter la transmission du filtre et à modifier le profil spectral de la lumière transmise. C'est l'effet Faraday dans ce filtre que j'ai particulièrement étudié. Pour cette étude, il fut nécessaire de calculer l'effet Zeeman des raies D1 et D2 du sodium, non pas en utilisant les facteurs de Landé mais le calcul exact fourni par la mécanique quantique. Une thermodynamique simplifiée de la cellule fut utilisée. Le champ magnétique était supposé homogène. Ce modèle théorique d'un filtre magnéto-optique fut testé expérimentalement et les résultats publiés (Appourchaux 1987). Ce travail a aussi contribué à une meilleure modélisation des filtres

magnéto-optiques en général. Une collaboration avec le créateur du filtre magnéto-optique, Allessandro Cacciani, permit la publication d'un rapport technique du Jet Propulsion Laboratory (Cacciani et al. 1991).

Fabry-Pérot en niobate de lithium

Après mon service militaire, j'ai collaboré avec David M. Rust de l'Applied Physics Laboratory, Maryland, pour développer un FP à lame solide de niobate de lithium. L'indice de réfraction était modifié en utilisant les propriétés ferro-électriques de ce matériau. Un champ électrique était appliqué le long de l'axe optique en utilisant les électrodes naturelles que constituaient les 2 lames d'argent du FP. Cette collaboration permit l'observation des oscillations solaires (Rust et al. 1988; Hill et al. 1988), puis ensuite de participer à l'élaboration d'une proposition pour le Solar Oscillations Investigation (SOI) de SOHO (Rust et al. 1987). La modélisation théorique de la mesure effectuée pour le FP put être vérifiée par des mesures sur le Soleil. L'instrument, appelé le Stable Solar Analyzer (Anlyseur solaire stabilisé), avait 2 autres particularités: le FP était incliné pour compenser au 1er ordre l'effet de rotation solaire dans le champ, en plus le FP était stabilisé par une diode laser. Les performances de cet instrument sont décrites dans la proposition SOHO (Rust et al. 1987; Rust & Appourchaux 1988). Ce projet ne fut pas accepté par L'ESA. Il fut envisagé de construire un réseau de 2 instruments auquel il ne fut pas donné suite pour des raisons budgétaires.

2.2.2 Mesures en intensité

L'autre moyen de détecter les oscillation solaires est de mesurer les fluctuations de lumière générées par les perturbations de température et d'opacité de la photosphère. En 1988, je démarrais un autre projet instrumental: le Luminosity Oscillations Imager (LOI) destiné à détecter ces fluctuations d'intensité depuis SOHO, en dehors de l'atmosphère. Ce projet a été développé au sein du Space Science Department de l'ESA situé à Noordwijk, Pays-Bas. L'idée originale du concept du LOI en revient à Andersen et al. (1988).

Le LOI est un sous-ensemble de VIRGO (Variabilities of IRradiance and Gravity Oscillations) instrument spatial faisant partie de la charge utile de SOHO. J'avais la responsabilité de scientifique de l'instrument LOI (Instrument Co-Investigator) et en était le chef de projet. J'ai donc effectué la conception scientifique et technique de l'instrument d'après l'idée initiale de Andersen et al. (1988). Le LOI est un instrument qui fait une image du

Soleil sur un détecteur muni de 16 photodiodes. Le télescope est un Ritchey-Chrétien dont le miroir secondaire est asservi pour fournir le pointage (Figure 2.1). Le miroir secondaire est déplacé au moyen d'actuateurs piézoélectriques permettant à la fois le pointage gros et fin (Figure 2.2). Au cours de ce développement, j'ai conçu le masque du détecteur, étudié l'optique du télescope et filtre, conçu le concept du système de pointage, et intégré l'optique et le détecteur.

Le masque du détecteur répondait à une optimisation pour observer les modes de bas degrés (Appourchaux & Andersen 1990). La stabilité thermique du rendement quantique du détecteur fut analysée en détail et mesurée (Appourchaux et al. 1992). L'effet des radiations sur le filtre et sur les verres le composant fut particulièrement étudié (Appourchaux 1993, Appourchaux et al. 1994). Une modélisation thermique du filtre d'entrée fut aussi effectuée (Appourchaux & Cislaghi 1992). L'instrument complet fut qualifié fin 1993. Le concept de l'instrument est détaillé dans Appourchaux et al. (1995a) et ses objectifs scientifiques dans Fröhlich et al. (1995).

En Mai 1994, un modèle d'ingénieur du LOI fut installé aux îles Canaries (Ténérife). Ce test grandeur nature avant le lancement de l'instrument en Décembre 1995 permit de vérifier l'excellent fonctionnement opérationnel du LOI, et permit même d'obtenir des résultats scientifiques nouveaux (Appourchaux et al. 1995b; Voir Section 4). Les performances en vol du LOI sont excellentes et permettent à ce jour de réaliser presque tous nos objectifs scientifiques (Appourchaux et al. 1997).

2.3 Analyse théorique de la mesure héliosismique

Mon soucis permanent a toujours été de modéliser mathématiquement la mesure héliosismique, que ce soit pour l'observation des vitesses radiales ou des fluctuations d'intensité. Le prolongement naturel de cette approche a été aussi appliqué à l'analyse de données. Ces 3 sujets sont développés ci-après.

2.3.1 Mesures de vitesses radiales

Le principe de mesure de vitesse radiale solaire repose sur l'utilisation d'un filtre à bande étroite qui mesure la position d'une raie de Fraunhofer par rapport à la position moyenne du filtre. En général, le filtre accordable est placé de part et d'autre de la raie et mesure l'intensité en 2 points (I_a et I_b). La différence de ces 2 intensités divisée par leur

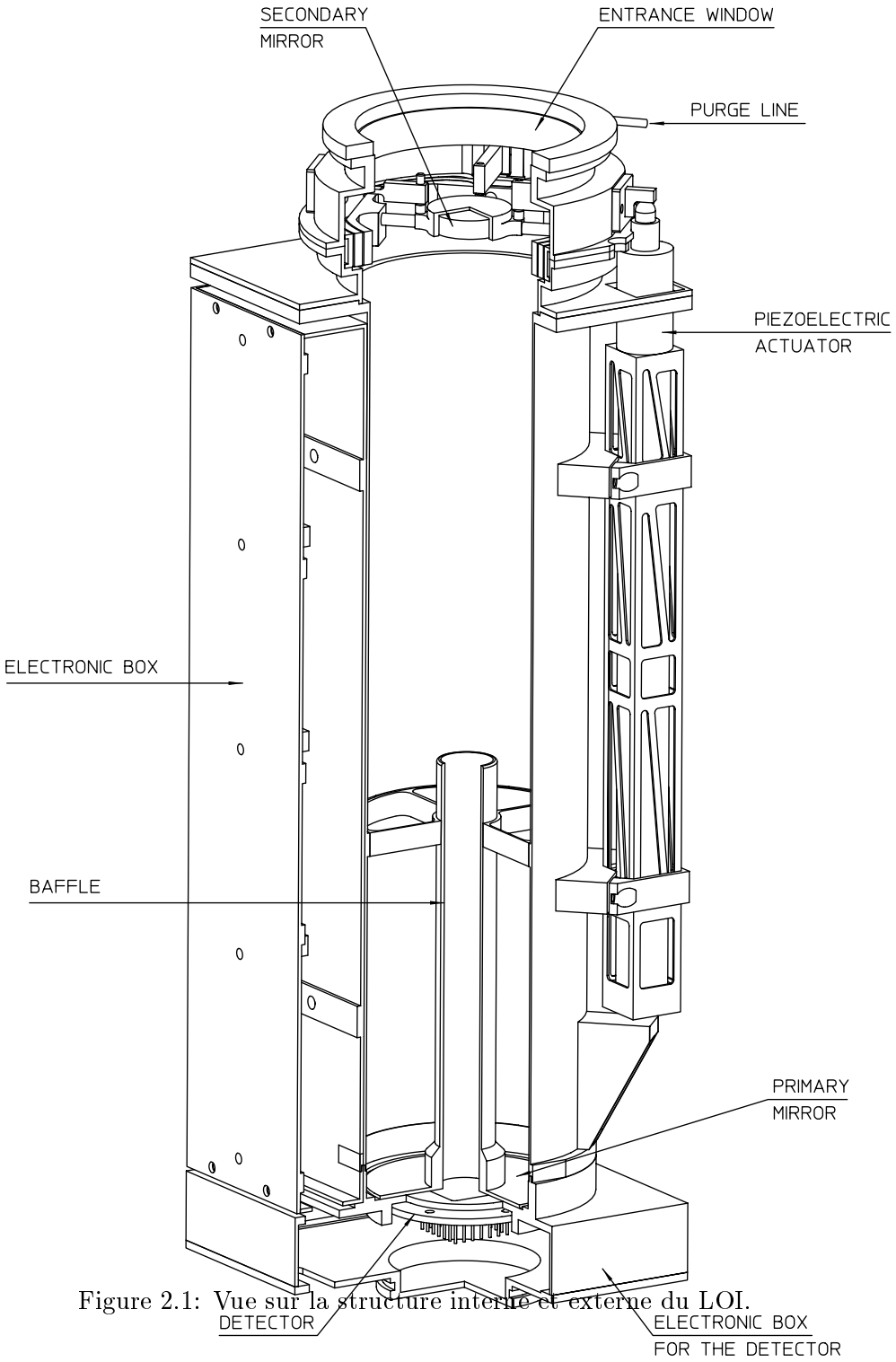

Figure 2.1: Vue sur la structure interne et externe du LOI.

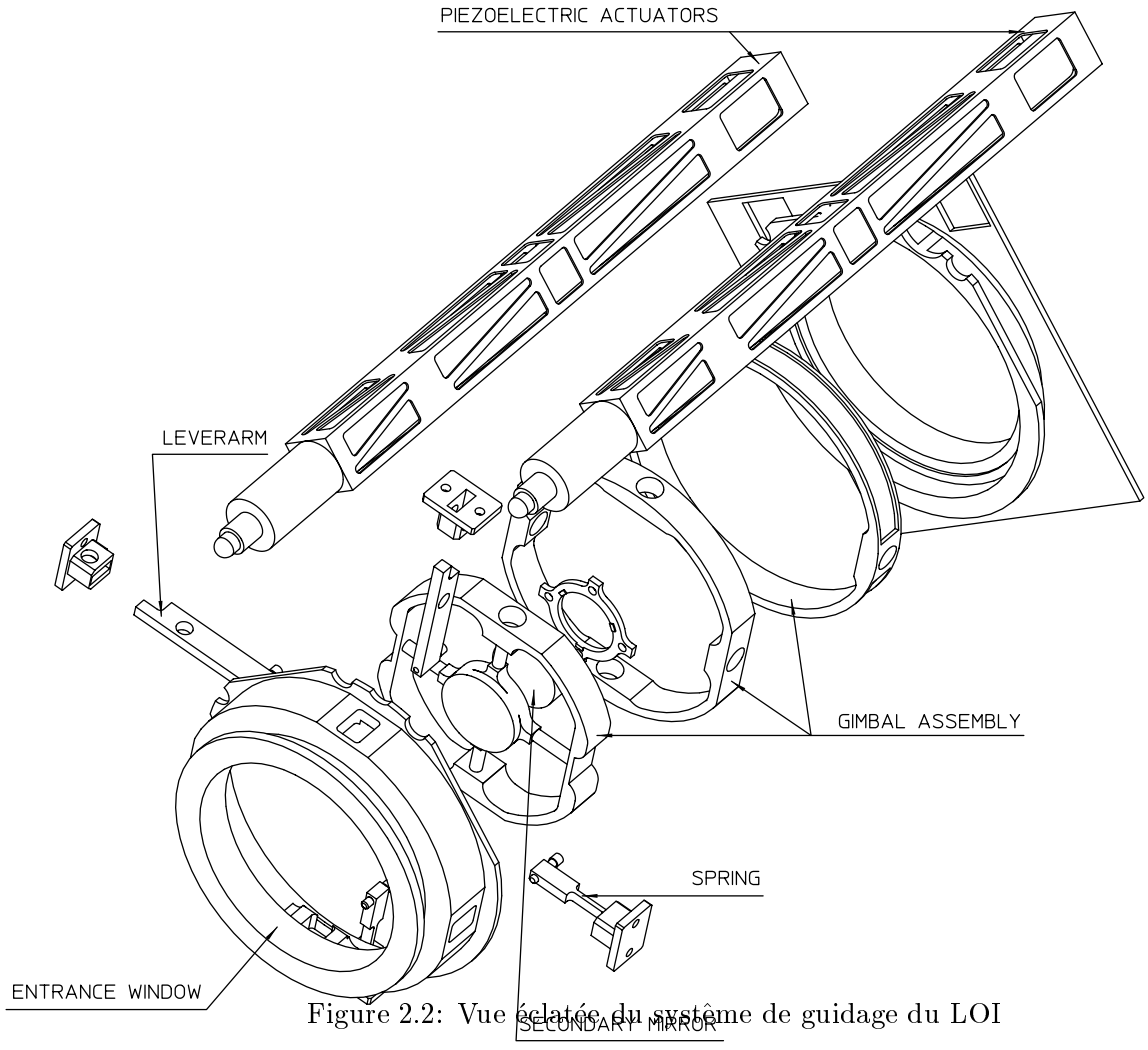

Figure 2.2: Vue éclatée du système de guidage du LOI

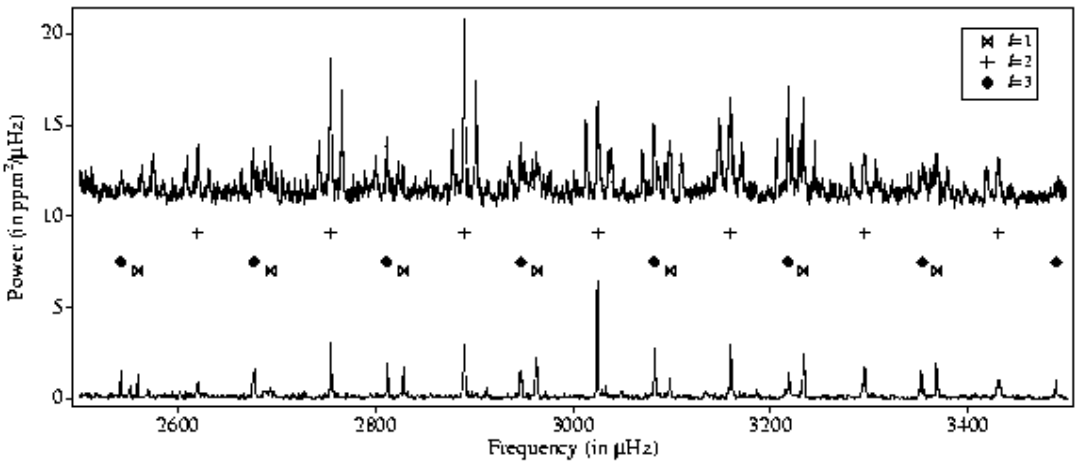

Figure 2.3: Spectres du LOI basé au sol (haut, décalé de 10 ppm$^2/\mu$Hz), et dans l'espace (bas) pour un $l = 1, m = 0$. On voit bien les pics fantômes temporels de part et d'autres des pics principaux. Le bruit atmosphérique contribue de manière non négligeable. La détection des modes $l = 1, m = 0$ fut un résulat observationnel nouveau (Appourchaux et al., 1995). Le gain en rapport signal sur bruit est d'environ 10.

somme est proportionnelle à la vitesse radiale lorsque celle-ci est petite devant la largeur de raie. L'écart de longueur d'onde entre les 2 positions spectrales du filtre et la largeur de sa bande passante sont fonction de la largeur de la raie solaire, de la profondeur de la raie et de son profil spectral. Ces 2 caractéristiques principales du filtre peuvent être optimisées en minimisant le bruit sur la vitesse radiale dû au bruit de photons (Appourchaux 1989). Une optimisation des mesures de vitesses radiales n'avait jamais été faite auparavant. D'autres paramètres de la mesure ont aussi été optimisés tels que le choix de la raie (Appourchaux 1988) ou le choix du préfiltre (Appourchaux 1989). Cette dernière étude permet de prédire et de vérifier les performances d'autres instruments héliosismiques tels que LOWL ou MDI/SOI[17].

2.3.2 Mesures en intensité

La mesure en intensité ne présente pas de difficulté d'optimisation particulière. Il y a en général suffisamment de photons principalement parce que le filtre utilisé est plus large

[17]Michelson Doppler Imager / Solar Oscillations Investigation

spectralement et mesure dans le continuum solaire. Le seul domaine restant à optimiser est la géométrie des pixels du détecteur nécessaire à la détection des modes. En général pour observer des modes de degrés élevés ($l > 20 - 30$) un détecteur avec des pixels carrés est amplement suffisant; la géométrie n'a pas besoin d'être plus évoluée. Ce n'est pas le cas lorsque l'on veut détecter des modes de bas degrés (inférieur à 7). C'est le cas du LOI pour lequel nous avons étudié une géométrie à 16 pixels, et tous les aspects de détectabilité des modes p et g, qui y sont liés (Appourchaux & Andersen 1990). Cette théorie a pu être vérifiée et validée en utilisant les données au sol et en vol de l'instrument (Appourchaux et al. 1995a, Appourchaux et al. 1997, Appourchaux 1998a).

2.3.3 Analyse de données

Maximum de vraisemblance

Une instrumentation stable et performante est nécessaire pour la détection des modes. Une fois que cette condition est obtenue, l'analyse des séries temporelles consiste généralement à calculer la transformée de Fourier pour en obtenir son spectre. Le spectre obtenu doit ensuite être analysé pour obtenir les caractéristiques des modes: fréquences, dédoublements fréquenciels (ou 'splittings'), largeurs et amplitudes. La méthode la plus souvent employée est d'ajuster le profil mesuré à un modèle paramétrique en utilisant la méthode du Maximum de Vraisemblance. La connaissance à priori de la statistique du profil mesuré est mise à profit pour estimer les paramètres du modèle en maximisant la vraisemblance de l'événement. La précision sur les estimateurs des paramètres du modèle peut être déduite simplement en calculant le Hessian. Cette matrice est l'inverse de la matrice de la courbure du Maximum de Vraisemblance (Toutain & Appourchaux 1994). Cette matrice est en général calculée pour une observation donnée (paires de l=0 et l=2 modes par exemple) et peut varier avec la 'réalisation'. Dans Toutain & Appourchaux (1994), nous donnons, pour une expérience en lumière intégrée, une expression analytique et asymptotique des précisions sur la fréquence, amplitude, largeur et bruit pour l=0; des précisions sur la fréquence et le splitting pour l=1. Ces expressions sont très utiles pour prédire l'effet de la qualité des inférences héliosismiques sur les inversions de la structure du Soleil et de sa rotation interne. Ces expressions permettent surtout de comprendre les sources d'erreurs statistiques. Ce travail a essentiellement généralisé pour tous les paramètres déduits des observations héliosismiques le travail commencé par Libbrecht (1992) pour la fréquence.

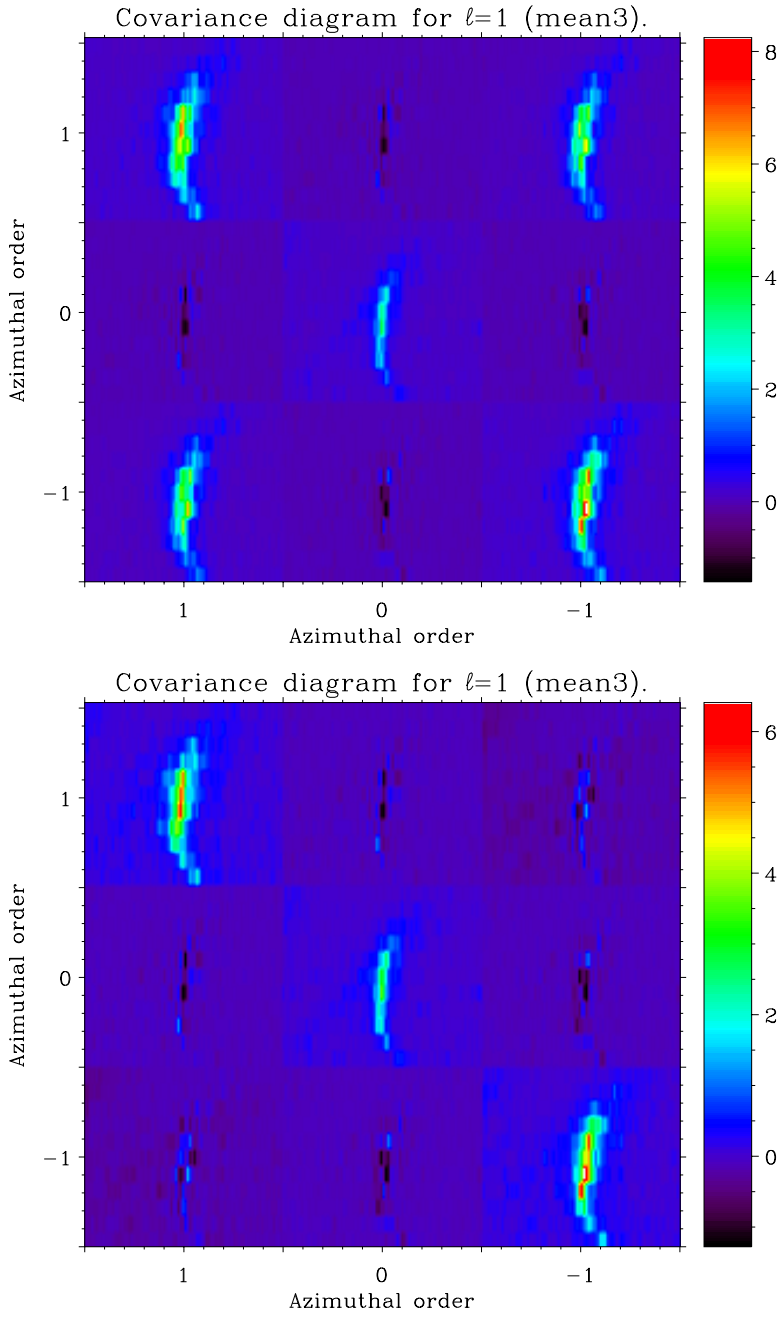

Figure 2.4: Diagramme de covariance pour le LOI: avant application de la matrice de fuite (haut), après application de la matrice de fuite (bas). Chaque diagramme de covariance est consistué de 9 diagrammes échelle de la partie réelles des spectres croisées entre m et m'; lorsque $m = m'$ on obtient le spectre de puissance. Dans le diagramme du haut, les fuite du spectre $m = 1$ dans le spectre $m = -1$ (et vice-versa) sont bien visible. Dans le digarmme du bas, ces fuites ont disparues: les spectres ont été nettoyés des fuites en m pour $l = 1$.

L'ajustement par Maximum de Vraisemblance est aussi utilisé pour les instruments faisant des images tels que le LOI ou le réseau GONG. Dans ce cas la technique d'ajustement est aussi basée sur la connaissance à priori de la distribution statistique des $2l+1$ signaux d'un mode de (n, l) donné, qui est dans ce cas une distribution multinormale. La matrice de covariance associée à cette distribution est fonction de la matrice de fuite des modes qui est en fait une représentation de notre incapacité à pouvoir isoler un mode (n, l, m) dû au fait que l'on observe que la moitié de l'astre solaire. Une description du modèle théorique de la matrice de covariance est donnée dans Appourchaux et al. (1998c). Ce travail est dérivé du travail commençé par Schou (1992) dont j'ai précisé le cadre mathématique. Notamment, il est assez important de s'assurer que la matrice de fuite que l'on utilise pour ajuster un mode (n, l) est inversible. A cet usage j'ai développé des outils de visualisation qui permettent de mieux comprendre ce que l'on ajuste réellement (Appourchaux et al. 1998d). J'ai démontré dans Appourchaux et al. (1998c) que l'ajustement des données revenait à appliquer l'inverse de la matrice de fuite sur les données. Si la matrice de fuite n'est pas celle des observations, la matrice de covariance résultante ne sera pas diagonale. Par exemple, la figure 2.4 montre deux matrices de covariance pour les modes $l = 1$ observés par le LOI: avant application de la matrice de fuite de $l = 1$ et après; on voit que la matrice de fuite est bien celle de l'observation. Il est à noter que cette méthode a été aussi appliquée pour des degrés différents pour nettoyer les spectres de la présence de degrés non désirés. Par exemple, j'ai démontré que les modes $l = 1$ observés par GONG pouvaient être nettoyés des degrés fantômes $l = 6, 9$ (Appourchaux et al. 1998d). Cette technique s'applique aussi au nettoyage des degrés $l = 4, 5$ perturbés par les modes fantômes $l = 7, 8$ (Rabello-Soares & Appourchaux 1999) et permet ainsi de réduire les sources de biais dans les mesures des fréquences et splittings.

Les modèles de matrice de fuite ainsi testés et validés sont utilisés pour effectivement ajuster les spectres du LOI, de GONG et de SOI/MDI (Appourchaux 1998a, Rabello-Soares & Appourchaux 1998, Rabello-Soares & Appourchaux 1999, Toutain et al. 1998).

Biais dans les mesures

J'ai aussi contribué aux études des sources de biais associées à la technique d'ajustement des modes ou au modèle paramétrique utilisé. Dans ma revue invitée et présentée durant la

dernière conférence SOHO6/GONG98, j'ai résumé mon travail sur les différentes sources de biais sur la mesure du 'splitting' (Appourchaux 1998b). Par exemple j'y ai mentionné que les estimateurs de maximum de vraisemblance n'étaient pas forcemment exempt de biais (voir aussi Appourchaux et al. 1998d; Appourchaux et al. 1996). Notamment j'ai montré que les mesures en disque intégré pouvaient surestimer la mesure du splitting surtout pour $l = 1$; ce biais peut être minimisé en choisissant le domaine où les modes ne sont pas larges devant le 'splitting' et en observant longtemps (Appourchaux et al. 2000a).

Les modèles d'ajustement peuvent aussi être en cause, ajustement de spectres de Fourier contre spectres de puissance. La présence de degrés fantômes (i.e. des modes de différents degrés à la même fréquence) est aussi source de biais aussi bien pour le 'splitting' (Appourchaux 1998b, Rabello-Soares & Appourchaux 1999) que pour les fréquences des modes (Appourchaux 1998a). La figure 2.5 rend bien compte du gain obtenu en nettoyant les spectres en utilisant les matrices de fuites (voir section précédente).

Finalement un biais sur les fréquences peut aussi être généré par un modèle incorrect du profil du mode. Le profil le plus utilisé est Lorentzien et donc symétrique. Pourtant de par la position de la source excitant les modes, le profil théorique est plutôt assymétrique. Ainsi, Toutain et al. (1997) ont montré, en utilisant les données de SOHO, que les modes avaient une fréquence différente suivant l'observable utilisée, intensité ou vitesse. Cette observation a été confirmée en utilisant les données sol de BiSON et du LOI (Appourchaux et al. 1998b). Cet effet systématique est attribué à l'existence d'une assymétrie différente suivant l'observable (intensité ou vitesses radiales). Un modèle assymétrique a été récemment mis en place qui supprime en majeure partie ce biais (Toutain et al. 1998).

2.4 Contributions à la connaissance du Soleil

Ma contribution à la connaissance de l'intérieur du Soleil par l'intermédiaire de l'héliosismologie a porté sur la structure et dynamique interne. D'autres contributions ont porté sur la tentative de détection des modes g, l'excitation des modes, sur l'effet de l'activité solaire, et sur la production de fréquences et splittings pour les inverseurs.

2.4.1 Structure interne

Les premières données en vol du LOI ont permis la mesure des fréquences des modes de pression de bas degrés pour $l < 9$ (Appourchaux et al. 1997, Fröhlich et al. 1997). Ces

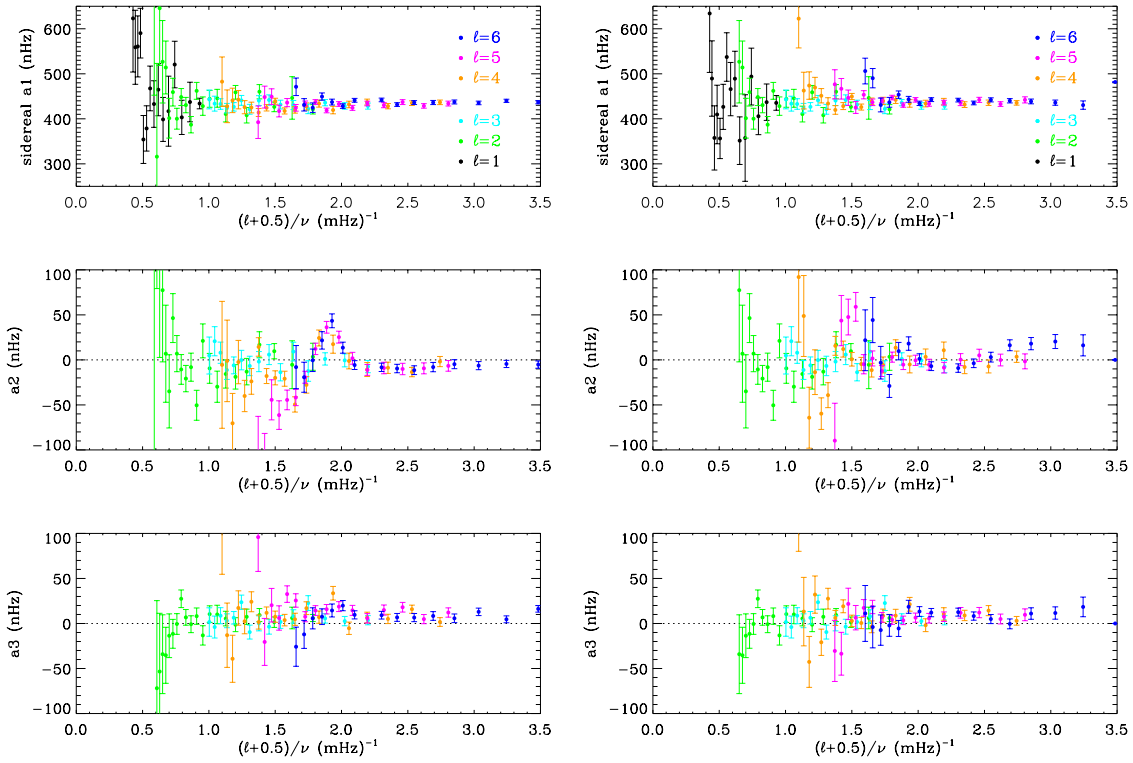

Figure 2.5: Biais dans les mesures de 'splitting' (a_i) causés par les degrés fantômes: *à droite* sans enlever les degrés fantômes; *à gauche* après suppression des degrés fantômes. On voit notamment que le 'splitting' a_1 pour $l = 1$ est plus bas et ne présente plus le saut observé à 0.5 mHz^{-1}. Ce saut était du à la presence de $l = 6, 9$ à haute fréquence. On constate aussi que la structure observée à 2 mHz^{-1} dans a_2 disparait. Cette structure est due aux $l = 7$ présents dans les $l = 4$

fréquences ont permis de connaître, par inversion, la structure interne près du coeur solaire. Ces inférences ont été comparées avec celles obtenues par des instruments plus précis tels que SOI/MDI ou LOWL. Bien que la précision de ces inférences soit moins bonne que celles de SOI/MDI, il n'en est pas moins vrai que les inversions de structure effectuées avec le LOI soient les seules effectuées en intensité. Ce sont ces inférences qui ont permis de mettre à jour un écart systématique entre les inversions d'observables de vitesses et celles d'intensité (Fröhlich et al. 1997). Cet écart était produit par la différence systématique de fréquences observée entre mesures en vitesse et mesures en intensité (Toutain et al. 1997; Appourchaux et al. 1998b). On a compris depuis que ces écarts de fréquences étaient produits par une certaine cohérence entre le processus d'excitation et les modes. La cohérence est différente

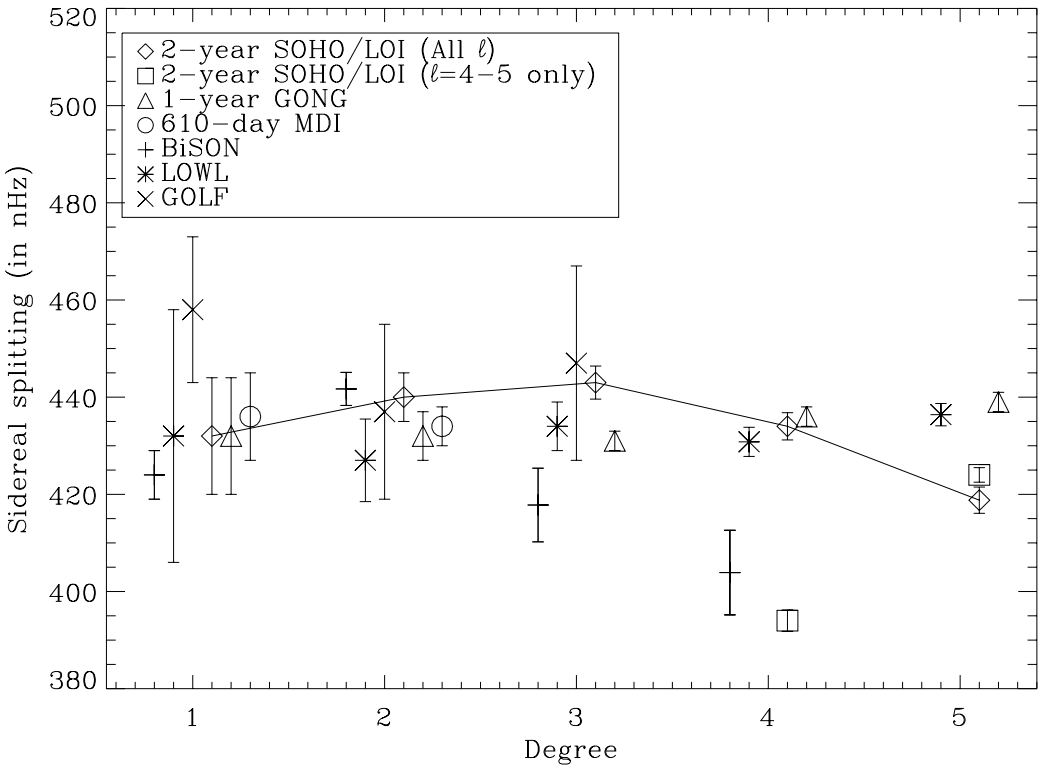

Figure 2.6: Comparaison de 'splitting' mesurés par différents instruments.

suivant l'observable, ce qui produit des profils de modes avec des assymétries de sens opposé. Ce problème fut résolu en utilisant un modèle du profil du mode qui tienne compte de cette cohérence (Toutain et al. 1998). L'influence des profils assymétriques sur les inversions de structure a un effet négligeable pourvu que le set de données utilisé ait été ajusté de manière consistente; c'est à dire sans mélanger des sets de données obtenus en ajustant des profils différents (Rabello-Soares et al. 1999). Cette consistence n'avait pas été respectée par Fröhlich et al. (1997) puisque qu'ils avaient utilisé des données en vitesse de LOWL combinées avec des données en intensité de VIRGO.

2.4.2 Dynamique interne

La mesure du 'splitting' des modes permet une mesure de la dynamique solaire interne. Par exemple, la rotation solaire permet de lever la dégénérescence du mode. Par analogie à l'effet Zeeman, un mode de degré donné l et d'ordre azimuthal m verra sa

fréquence modifiée comme m Ω, ou Ω est la rotation moyennée par le noyau du mode en question. En observant, des modes de différents l, m et n, on peut ainsi connaître le profil de rotation à l'intérieur du Soleil. Mon travail principal dans ce domaine fut de m'attacher à mesurer le 'splitting' pour les modes de degré bas ($0 < l < 4$). J'ai ainsi pu mesurer pour la première fois du sol, le 'splitting' en intensité (Appourchaux et al. 1995b; Appourchaux et al. 1995a). Cette première ébauche me permit de me familiariser avec le traitement de données des imageurs. Il en résulta de nombreuses mesures de 'splitting' pour SOI/MDI et GONG (Toutain et al. 1998; Rabello-Soares & Appourchaux 1999) Rabello-Soares et Appourchaux, 1998), ainsi que pour le LOI à bord de SOHO (Appourchaux 1998a). Ces différentes mesures furent ensuite comparées entre elles pour confirmer que le coeur solaire tourne plus probablement de manière rigide comme le montre la figure 2.6 (Appourchaux 1998b, Rabello-Soares et al, 1998).

La technique d'analyse de données développée dans la section 2.3.3 permet aussi de mesurer l'inclinaison du coeur solaire (Gizon et al. 1998). Cette technique a été utilisée seulement sur les données LOI mais peut aussi être appliquée sur d'autres d'imageurs.

2.4.3 Détection de mode g

Un des buts principaux de l'héliosismologie depuis 20 ans est de détecter les modes g. Les modes p nous renseignent sur la structure interne du Soleil depuis la surface jusqu'à la zone radiative en excluant le coeur. Malheureusement, les modes p ne pénètrent pas complètement jusqu'au coeur, seuls les modes g le font. Ces modes sont donc d'une extrême importance pour la connaissance du coeur. Malheureusement, ces modes se propagent vers la surface du Soleil que par effet tunnel. Ils sont donc considérablement atténués et de ce fait très difficile à détecter. Avec le lancement de SOHO, trois instruments d'héliosismologie essaient de détecter ces modes. En Janvier 1997, j'ai formé un groupe de travail consistué de scientifiques de VIRGO, SOI/MDI et de BiSON, en espérant pouvoir détecter les modes g dans un effort de collaboration internationale où toutes les données existantes seraient librement accessibles au groupe; celui-ci est appelé le groupe *Phoebus*. Nous avons eu 3 ateliers de travails en Novembre 97, 98 et 99. Ceux-ci nous ont permis de comprendre que bien que ces modes soient très difficiles à détecter, il n'était pas impossible d'imaginer de pouvoir les détecter un jour (Appourchaux 1998b; Fröhlich et al. 1998). De nouvelles méthodes d'analyse ont été élaborées qui ont permis déjà de détecter des modes p à durée de vie

extrêmement longue, qui mime le comportement mathématique des modes g (Appourchaux 1998b; Appourchaux et al. 1998a).

Le résultat de ces 3 ans de travail est résumé dans un article récemment accepté par *The Astrophysical Journal* (Appourchaux et al. 2000b). Nous y mentionnons une valeur limite supérieure pour l'amplitude de la vitesse des modes g de quelques 10 mm/s (limite à 10 σ environ) à environ 200 μHz.

Devant la difficulté de la détection des modes g, d'autres techniques observationnelles seront nécessaires. Par exemple, nous fondons beaucoup d'espoir dans l'observation du bord solaire. En effet, Appourchaux et Toutain (1996) ont montré que les fluctuations d'intensité des modes p, observées sur le bord solaire avec le LOI, pouvaient être 5 fois plus grandes que celles observées en disque intégré. Ce fait a été confirmé par Toner et al. (1999) en utilisant les données de MDI. C'est cette propriété qui sera utilisée pour détecter les modes g avec des missions telles que PICARD ou SPHERIS.

2.4.4 Autres contributions

Les autres contributions relèvent de travaux nouveaux et en cours. Beaucoup de ceux-ci nécessitent des observations longues tel que l'étude de l'effet de l'activité solaire sur les fréquences et largeurs de raie (Appourchaux 1998a) ou sur la modulation de l'amplitude des modes (Andersen et al, 1998a); d'autres requièrent des études d'erreurs systématiques plus complètes et détaillées, mais fastidieuses (Appourchaux 1998a).

D'autres travaux rapportent de l'étude de la position de la source excitant les modes p, ainsi que de la corrélation du bruit de fond en intensité avec la perturbation en intensité (Chaplin & Appourchaux 1999); cette dernière étant à l'origine des écarts de fréquences entre les observables vitesse et intensité (Voir Section 2.3.3). Une autre étude porta sur les caractéristiques de la source ainsi que de ses éventuelles relations avec l'activité solaire (Chaplin et al. 2000).

D'autre part n'étant pas un inverseur, je m'attache à fournir des tables de fréquences, 'splittings' et largeurs de raies avec des erreurs systématiques les plus faibles possible (Appourchaux 1998b; Appourchaux 1998a, Rabello-Soares & Appourchaux 1999).

2.5 De l'héliosismologie à l'astérosismologie

Un prolongement naturel de la sismologie solaire est bien sûr son application aux étoiles. Ma fonction de scientifique à l'Agence Spatiale Européenne m'a permit de suivre le projet spatial PRISMA (Probing Rotation and the Interior of Stars: Microvariability and Activity) et d'être partiellement associé au projet spatial STARS (une version amélioré de PRISMA). La non sélection de ces missions poussa la communauté scientifique française à développer la mission COROT (une version améliorée du Large Photomètre de PRISMA). D'autres missions similaires sont en train de voir le jour et mon implication dans MONS apparait naturelle. La démonstration que la sismologie des étoiles de type solaire est possible est néanmoins souhaitable. Pour ce, j'ai contribué au travail de Martić et al. (1999) en fournissant le Fabry-Pérot nécessaire au contrôle des dérives instrumentales. Martić et al. (1999) confirma que l'excès de puissance dans les spectres de Procyon observés précédemment (Gelly et al. 1986, Brown et al. 1991, Brown et al. 1996, Horner et al. 1997, Mosser et al. 1998) était bien causé par la présence de modes de pression.

Références

Andersen B., Domingo V., Jones A., Jiménez A., Pallé P., Régulo C., Roca Cortés T. 1988, 'Luminosity Oscillations Imager (LOI)', in Seismology of the Sun and Sun-like Stars, V.Domingo and E.Rolfe (eds.), ESA SP-286, ESA Publications Division, Noordwijk, The Netherlands, p. 385

Anderson E. R., Duvall, T. L. J., Jefferies S. M. 1990, 'Modeling of solar oscillation power spectra', *ApJ*, **364**, 699

Appourchaux T. 1987, 'The Faraday effect in a magneto-optical filter', *Sol. Phys.*, **109**, 393

Appourchaux T. 1988, 'Solar oscillations instrumentation and measurement theory', in Seismology of the Sun and Sun-Like Stars, V.Domingo and E.Rolfe (eds.), European Space Agency Publications Division, ESA SP-286, Noordwijk, The Netherlands, p. 595

Appourchaux T. 1989, 'Optimization of parameters for helioseismology experiments measuring solar radial velocities', *A&A*, **222**, 361

Appourchaux T. 1998a, 'Results from the Luminosity Oscillations Imager on board SOHO: low-degree p-mode parameters for a 2-year data set', in Structure and Dynamics of the

Interior of the Sun and Sun-like Stars, S. Korzenik and A. Wilson (eds.), ESA SP-418, ESA Publications Division, Noordwijk, The Netherlands, p. E30

Appourchaux T. 1998b, 'The structure of the solar core: an observer's point of view', in Structure and Dynamics of the Interior of the Sun and Sun-like Stars, S. Korzenik and A. Wilson (eds.), ESA SP-418, ESA Publications Division, Noordwijk, The Netherlands, p. E18

Appourchaux T., Andersen B., Chaplin W., Elsworth Y., Finsterle W., Fröhlich C., Gough D., Hoeksema J. T., Isaak G., Kosovichev A., Provost J., Scherrer P., Sekii T., Toutain T. 1998a, 'Comparative studies of low-order and low-degree solar p-modes', in 'Structure and Dynamics of the Interior of the Sun and Sun-like Stars, S. Korzenik and A. Wilson (eds.), ESA SP-418, ESA Publications Division, Noordwijk, The Netherlands, 95

Appourchaux T., Andersen B., Fröhlich C., Jiménez A., Telljohann U., Wehrli C. 1997, 'In-flight performance of the VIRGO Luminosity Oscillations Imager aboard', *Sol. Phys.*, **170**, 27

Appourchaux T., Andersen B. N. 1990, 'Observations of low-degree solar oscillations with few detector elements', *Sol. Phys.*, **128**, 91

Appourchaux T., Chang H.-Y., Gough D., Sekii T. 2000a, 'On measuring low-degree p-mode frequency splitting with full-disc integrated data', *MNRAS*, *in press*

Appourchaux T., Chaplin W. J., Elsworth Y., Isaak G. R., MCLeod C. P., Miller B. A., New R. 1998b, 'A comparison of low-degree solar p-mode frequencies from BISON and LOI', in New eyes to see inside the sun and the stars, IAU 185, F.-L. Deubner, J.Christensen-Dalsgaard and D.Kurtz (eds.), Kluwer Academic Publishers, Dordrecht, The Netherlands, p. 45

Appourchaux T., Cislaghi M. 1992, 'Passive thermal control of a multilayer filter for space-based solar observations', Optical Engineering, **31**, 1715

Appourchaux T., Fröhlich C., Andersen B., Berthomieu G., Chaplin W., Elsworth Y., Finsterle W., Gough D., Hoeksema J. T., Isaak G., Kosovichev A., Provost J., Scherrer P., Sekii T., Toutain T. 2000b, 'Observational upper limits for low-degree solar g modes', *ApJ*, **538**, *in press*

Appourchaux T., Gizon L., Rabello-Soares M. C. 1998c, 'The art of fitting p-mode spectra. I. Maximum likelihood estimation', *A&AS*, **132**, 107

Appourchaux T., Gough D., Sekii T., Toutain T. 1996, 'An unbiased average rotational splitting from VIRGO/SPM?', in Sounding solar and stellar interiors, IAU 181, Poster

Volume, J.Provost and F.-X. Schmider (eds.), Université de Nice, France, 3

Appourchaux T., Rabello-Soares M.-C., Gizon L. 1998d, 'The art of fitting p-mode spectra. II. Leakage and noise covariance matrices', *A&AS*, **132**, 121

Appourchaux T., Toutain T., Jiménez A., Rabello-Soares M., Andersen B., Jones A. 1995a, 'Results from the Luminosity Oscillations Imager', in Helioseismology, 4th SOHO workshop, J. Hoeksema, V. Domingo, B. Fleck and B. Battrick (eds.), ESA SP-376, ESA Publications Division, Noordwijk, The Netherlands, 265

Appourchaux T., Toutain T., Telljohann U., Jiménez A., Rabello-Soares M. C., Andersen B. N., Jones A. R. 1995b, 'Frequencies and splittings of low-degree solar p modes: results of the Luminosity Oscillations Imager', *A&A*, **294**, L13

Appourchaux T. P. 1993, 'Effect of space radiations on optical filters', *Proc. SPIE*, **2018**, 80

Appourchaux T. P., Gourmelon G., Johlander B. 1994, 'Effect of gamma-ray irradiations on optical filter glass', Optical Engineering, **33**, 1659

Appourchaux T. P., Martin D. D., Telljohann U. 1992, 'Temperature dependence of silicon photodiode quantum efficiency: theoretical and experimental results', *Proc. SPIE*, **1679**, 200

Basu S., Christensen-Dalsgaard J., Perez Hernandez F., Thompson M. J. 1996, Filtering out near-surface uncertainties from helioseismic inversions, *MNRAS*, **280**, 651

Blamont J., Roddier F. 1961, *Phys. Rev. Lett.*, **7**, 437

Brookes J. R., Isaak G. R., van Der Raay H. B. 1976, Observation of free oscillations of the sun, *Nature*, **259**, 92

Brown T. M. 1979, 'Observed brightness oscillations at the solar limb', *ApJ*, **230**, 255

Brown T. M. 1985, 'Solar rotation as a function of depth and latitude', *Nature*, **317**, 591

Brown T. M., Christensen-Dalsgaard J., Dziembowski W. A., Goode P., Gough D. O., Morrow C. A. 1989, Inferring the sun's internal angular velocity from observed p-mode frequency splittings, *ApJ*, **343**, 526

Brown T. M., Gilliland R. L., Noyes R. W., Ramsey L. W. 1991, 'Detection of possible p-mode oscillations on Procyon', *ApJ*, **368**, 599

Brown T. M., Kennelly E. J., Noyes R. W., Korzennik S. G., Nisenson P., Horner S. D., Catala C. 1996, 'A Radial Velocity Search for p-modes in Procyon', in American Astronomical Society Meeting, Vol. **188**, p. 5902

Brown T. M., Stebbins R. T., Hill H. A. 1978, 'Long-period oscillations of the apparent solar diameter - Observations', *ApJ*, **223**, 324

Cacciani A., Croce V., Fortini T., Torelli M. 1981, 'Searching for $l = 1$ modes of solar oscillations', *Sol. Phys.*, **74**, 543

Cacciani A., Rosati P., Ricci D., Egidi A., Appourchaux T., Marquedant R., Smith E. 1991, 'Theoretical and experimental study of the magneto=optical filter', Technical report, Jet Propulsion Laboratory, Loas Angeles, CA

Chaplin W. J., Appourchaux T. 1999, Depth of excitation and reversal of asymmetry of low-l solar p modes: a complementary analysis of BiSON and VIRGO/SPM data, *MNRAS*, **309**, 761

Chaplin W. J., Appourchaux T., Elsworth Y., Isaak G., Miller B., New R. 2000, 'Source of excitation of low-l p modes: characteristics and solar-cycle variations', *MNRAS*, in press

Chou D. Y., Sun M. T., Huang T. Y., Jiménez A., Lai S. P., Chi P. J., Ou K. T., Wang C. C., Lu J. Y., Chu A. L., Niu C. S., Mu T. M., Chen K. R., Chou Y. P., Rabello-Soares M. C., Ai G. X., Wang G. P., Zirin H., Marquette W., Nenow J. 1995, Taiwan oscillation network, *Sol. Phys.*, **160**, 237

Christensen-Dalsgaard J. 1998, 'Lecture notes on helio- and asteroseismology', Århus Univeristet, Århus, Denmark

Christensen-Dalsgaard J., Gough D. O. 1982, 'On the interpretation of five-minute oscillations in solar spectrum line shifts', *MNRAS*, **198**, 141

Christensen-Dalsgaard J., Gough D. O., Perez Hernandes F. 1988, Stellar disharmony, *MNRAS*, 235, 875

Claverie A., Isaak G., McLeod C., van der Raay H., Roca Cortés T. 1979, 'Solar structure from global studies of the 5-minute oscillation', *Nature*, **282**, 591

Delache P., Scherrer P. H. 1983, 'Detection of solar gravity mode oscillations', *Nature*, **306**, 651

Deubner F. 1975, 'Observations of low wavenumber nonradial eigenmodes of the sun', *A&A*, **44**, 371

Dicke R. H. 1965, 'Icarus and relativity', *AJ*, **70**, 395

Dicke R. H., Goldenberg H. M. 1967, '', *Phys.Rev. Letters*, **18**, 313

Dittmer P. H., Scherrer P. H., Wilcox J. M. 1978, 'An observational search for large-scale organization of five-minute oscillations on the sun', *Sol. Phys.*, **57**

Duvall, T. L. J. 1982, 'A dispersion law for solar oscillations', *Nature*, **300**, 242

Duvall, T. L. J., Dziembowski W. A., Goode P. R., Gough D. O., Harvey J. W., Leibacher J. W. 1984, 'Internal rotation of the sun', *Nature*, **310**, 22

Duvall, T. L. J., Harvey J. W. 1983, 'Observations of solar oscillations of low and intermediate degree', *Nature*, **302**, 24

Duvall, T. L. J., Harvey J. W. 1984, 'Rotational frequency splitting of solar oscillations', *Nature*, **310**, 19

Duvall, T. L. J., Harvey J. W. 1986, 'Solar Doppler shifts - Sources of continuous spectra', in Seismology of the Sun and the Distant Stars, p. 105

Duvall, T. L. J., Harvey J. W., Pomerantz M. A. 1986, 'Latitude and depth variation of solar rotation', *Nature*, **321**, 500

Dziembowski W. 1977, 'Light and radial velocity variations in a nonradially oscillating star', *Acta Astronomica*, **27**, 203

Dziembowski W. A., Pamyatnykh A. A., Sienkiewicz R. 1990, Solar model from helioseismology and the neutrino flux problem, *MNRAS*, **244**, 542

Egamberdiev S., Fossat E. 1991, 'IRIS (International Research on the Interior of the Sun) Workshop, 2nd, Tashkent, Uzbek SSR, Sept. 1989, Proceedings', *Sol. Phys.*, **133**

Einstein A. 1916, 'Die Grundlage der allgemeinen Relativitättheorie', *Annalen der Physik*, **49**, 769

Elsworth Y., Howe R., Isaak G. R., McLeod C. P., New R. 1991, 'Low-l p-mode solar eigenfrequency measurements from the Birmingham Network', *MNRAS*, **251**, 7P

Elsworth Y. P., Jefferies S. M., McLeod C. P., New R., Palle P. L., van Der Raay H. B., Regulo C., Cortes T. R. 1989, 'The 160 minute solar oscillation - an artifact?', *ApJ*, **338**, 557

Fossat E., Kholikov S., Gelly B., Schmider F. X., Fierry-Fraillon D., Grec G., Palle P., Cacciani A., Ehgamberdiev S., Hoeksema J. T., Lazrek M. 1999, 'Full disk helioseismology: repetitive music and the question of gap filling', *A&A*, **343**, 608

Fröhlich C., Andersen B. N., Appourchaux T., Berthomieu G., Crommelynck D. A., Domingo V., Fichot A., Finsterle W., Gomez M. F., Gough D., Jiménez A., Leifsen T., Lombaerts M., Pap J. M., Provost J., Cortés T. R., Romero J., Roth H., Sekii T., Telljohann U., Toutain T., Wehrli C. 1997, 'First results from VIRGO, the experiment for helioseismology and solar irradiance monitoring on SOHO', *Sol. Phys.*, **170**, 1

Fröhlich C., Finsterle W., Andersen B., Appourchaux T., Chaplin W., Elsworth Y., Gough D., Hoeksema J. T., Isaak G., Kosovichev A., Provost J., Scherrer P., Sekii T., Toutain

T. 1998, 'Observational upper limits for low-degree solar g modes', in Structure and Dynamics of the Interior of the Sun and Sun-like Stars, S. Korzenik and A. Wilson (eds.), ESA SP-418, ESA Publications Division, Noordwijk, The Netherlands, 67

Fröhlich C., Romero J., Roth H., Wehrli C., Andersen B. N., Appourchaux T., Domingo V., Telljohann U., Berthomieu G., Delache P., Provost J., Toutain T., Crommelynck D. A., Chevalier A., Fichot A., Däppen W., Gough D., Hoeksema T., Jiménez A., Gómez M. F., Herreros J. M., Cortés T. R., Jones A. R., Pap J. M., Willson R. C. 1995, 'VIRGO: Experiment for Helioseismology and Solar Irradiance Monitoring', *Sol. Phys.*, **162**, 101

Fröhlich C., Van der Raay H. B. 1984, 'Global solar oscillations in irradiance and velocity: a comparison', in The Hydromagnetics of the Sun, T.D.Guyenne and J.J.Hunt (eds.), ESA SP-220, ESA Publications Division, Noordwijk , The Netherlands, p. 17

Gabriel A. H., Grec G., Charra J., Robillot J. ., Cortés T. R., Turck-Chièze S., Bocchia R., Boumier P., Cantin M., Cespedes E., Cougrand B., Cretolle J., Dame L., Decaudin M., Delache P., Denis N., Duc R., Dzitko H., Fossat E., Fourmond J., Garcia R. A., Gough D., Grivel C., Herreros J. M., Lagardère H., Moalic J., Pallé P. L., Petrou N., Sanchez M., Ulrich R., van der Raay H. B. 1995, 'Global Oscillations at Low Frequency from the SOHO Mission (GOLF)', *Sol. Phys.*, **162**, 61

Gabriel M. 1992, 'On the solar p-mode spectrum excited by convection', *A&A*, **265**, 771

Gabriel M. 1994, 'The probability-density function of a Fourier line', *A&A*, **287**, 685

Gelly B., Gree G., Fossat E. 1986, 'Evidence for global pressure oscillations in Procyon and Alpha Centauri', *A&A*, **164**, 383

Gizon L., Appourchaux T., Gough D. O. 1998, 'LOI/SOHO constraints on oblique rotation of the solar core, IAU Symposia, **185**, 37

Goldreich P., Keeley D. A. 1977, 'Solar seismology. II - The stochastic excitation of the solar p-modes by turbulent convection', *ApJ*, **212**, 243

Gough D. 1986, 'EBK quantization of stellar waves', in Proceedings of the Workshop in honor of Professor Wasaburo Unno's 60th birthday on Hydrodynamics and Magnetohydrodynamics Problems in the Sun and Stars, Y.Osaki (ed.), Department of Astronomy, Tokyo, Japan, p. 117

Gough D. O. 1984, 'On the rotation of the sun', Royal Society of London Philosophical Transactions Series, **313**, 27

Grec G. 1981, *Ph.D. thesis*, Univeristé de Nice

Grec G., Fossat E., Pomerantz M. 1980, 'Solar oscillations - Full disk observations from the geographic South Pole', *Nature*, **288**, 541

Harvey J., the GONG instrument development team 1988, 'The GONG instrument', in Seismology of the Sun and Sun-like Stars, V.Domingo and E.Rolfe (eds.), ESA SP-286, ESA Publications Division, Noordwijk, The Netherlands, p. 203

Hill F., Rust D. M., Appourchaux T. 1988, 'Rotation in the solar convection sone inferred from Fabry-Pérot observations of the 5-min oscillations', IAU Symposia, **123**, 49

Hill H. A. 1985, 'Detection and classication of resolved multiplet members of the solar 5-minute oscillations through solar diameter-type observations', *ApJ*, **290**, 765

Hill H. A. 1992, 'Tests of the detection and mode classifications of low-degree solar gravity modes with 1978 solar diameter observations', *ApJS*, **78**, 283

Hill H. A., Caudell T. P. 1985, 'Confirmation of the detection and classification of low-order, low-degree solar acoustic modes with the 1978 solar diameter observations', *ApJ*, **299**, 517

Hill H. A., Stebbins R. T. 1975, The intrinsic visual oblateness of the sun, *ApJ*, 200, 471

Horner S. D., Brown T. M., Kennelly E. J., Korzennik S., Nisenson P., Noyes R. W. 1997, 'Asteroseismology of Procyon with the AFOE', in American Astronomical Society Meeting, Vol. **191**, p. 4310

Houdek G. 1996, *Ph.D. thesis*, Univeristät Wien

Jiménez A., Pallé P. L., Roca Cortés T., Domingo V., Korzennik S. 1987, 'Ground-based measurements of solar intensity oscillations', *A&A*, **172**, 323

Korzennik S. 1990, *Ph.D. thesis*, University of California, Los Angeles, CA

Kuhn J. R., Dicke R. H., Libbrecht K. G. 1986, 'Solar ellipticity fluctuations yield no evidence of g modes', *Nature*, **319**, 128

Kuhn J. R., Libbrecht K. G., Dicke R. H. 1985, 'Observations of a solar latitude-dependent limb brightness variation', *ApJ*, **290**, 758

Kumar P., Franklin J., Goldreich P. 1988, 'Distribution functions for the time-averaged energies of stochastically excited solar p modes', *ApJ*, **328**, 879

Leighton R. B., Noyes R. W., Simon G. W. 1962, 'Velocity Fields in the Solar Atmosphere. I. Preliminary Report.', *ApJ*, **135**, 474

Libbrecht K. G. 1992, 'On the ultimate accuracy of solar oscillation frequency measurements', *ApJ*, **387**, 712

Libbrecht K. G., Kuhn J. R. 1984, 'A new measurement of the facular contrast near the solar limb', *ApJ*, **277**, 889

Libbrecht K. G., Zirin H. 1986, 'Properties of intermediate-degree solar oscillation modes', *ApJ*, **308**, 413

Martić M., Schmitt J., Lebrun J. C., Barban C., Connes P., Bouchy F., Michel E., Baglin A., Appourchaux T., Bertaux J. L. 1999, 'Evidence for global pressure oscillations on Procyon', *A&A*, **351**, 993

Mosser B., Maillard J. P., Mekarnia D., Gay J. 1998, 'New limit on the p-mode oscillations of Procyon obtained by Fourier transform seismometry', *A&A*, **340**, 457

Nishikawa J., Hamana S., Mizugaki K., Hirayama T. 1986, 'Detection of solar five-minute oscillations through white-light intensity', *PASJ*, **38**, 277

Rabello-Soares M. C., Appourchaux T. 1998, 'GONG low-degree p-mode parameters, in 'Structure and Dynamics of the Interior of the Sun and Sun-like Stars', p. E75

Rabello-Soares M. C., Appourchaux T. 1999, 'Solar low-degree p-mode parameters from the GONG network', *A&A*, **345**, 1027

Rabello-Soares M. C., Christensen-Dalsgaard J., Rosenthal C. S., Thompson M. J. 1999, 'Effects of line asymmetries on the determination of solar internal structure', *A&A*, **350**, 672

Rhodes, E. J. J., Cacciani A., Blamont J., Tomczyk S., Ulrich R. K., Howard R. F. 1984, 'Evaluation of a magneto-optical filter and a Fabry-Perot interferometer for the measurement of solar velocity fields from space', in *Solar Seismology from Space*, JPL 84–84, p. 125

Rhodes, E. J. J., Cacciani A., Korzennik S., Tomczyk S., Ulrich R. K., Woodard M. F. 1990, 'Depth and latitude dependence of the solar internal angular velocity', *ApJ*, **351**, 687

Roddier F. 1967, 'Observation of the Solar Line Oscillations with an Atomic-Beam Spectro-Photometer', *ApJ*, **147**, 1113

Rust D., Appourchaux T. 1988, 'Stable Solar Analyzer', in Seismology of the Sun and Sun-Like Stars, V.Domingo and E.Rolfe (eds.), European Space Agency Publications Division, ESA SP-286, Noordwijk, The Netherlands, 227

Rust D., Burton C., Thomas J., Stenflo J., Gold R., Brown J., Ulrich R., Cram L., Hathaway D., Duvall T., Gurman J., Hill F., Appourchaux T. 1987, 'Stable Solar Analyzer: a proposal to the ESA and to the NASA for SOHO', Applied Physics Laboratory, MD

Rust D. M., Appourchaux T., Hill F. 1988, 'Performance of a stabilized Fabry-Pérot solar analyzer', IAU Symposia, **123**, 475

Scherrer P. H., Bogart R. S., Bush R. I., Hoeksema J. T., Kosovichev A. G., Schou J., Rosenberg W., Springer L., Tarbell T. D., Title A., Wolfson C. J., Zayer I. 1995, 'The Solar Oscillations Investigation – Michelson Doppler Imager', *Sol. Phys.*, **162**, 129

Scherrer P. H., Wilcox J. M., Christensen-Dalsgaard J., Gough D. 1982, 'Observation of additional low-degree 5-min modes of solar oscillation', *Nature*, **297**, 312

Scherrer P. H., Wilcox J. M., Christensen-Dalsgaard J., Gough D. O. 1983, 'Detection of Solar 5-Minute Oscillations of Low Degree', *Sol. Phys.*, **82**, 75

Schou J. 1992, *Ph.D. thesis*, Århus Universitet, Denmark

Schou J., Brown T. M. 1994, 'Generation of artificial helioseismic time-series', *A&AS*, **107**, 541

Schou J., Christensen-Dalsgaard J., Thompson M. J. 1994, 'On comparing helioseismic two-dimensional inversion methods', *ApJ*, bf 433, 389

Severnyi A. B., Kotov V. A., Tsap T. T. 1976, 'Observations of solar pulsations', *Nature*, **59**, 87

Tassoul M. 1980, Asymptotic approximations for stellar nonradial pulsations, *ApJS*, **43**, 469

Tomczyk S. 1988, *Ph.D. thesis*, University of California, Los Angeles, CA

Tomczyk S., Schou J., Thompson M. J. 1995a, 'Measurement of the Rotation Rate in the Deep Solar Interior', *ApJ*, **448**, L57

Tomczyk S., Streander K., Card G., Elmore D., Hull H., Cacciani A. 1995b, 'An Instrument to Observe Low-Degree Solar Oscillations', *Sol. Phys.*, **159**, 1

Toner C. G., Jefferies S. M., Toutain T. 1999, 'Increasing the Visibility of Solar Oscillations', *ApJ*, **518**, L127

Toutain T., Appourchaux T. 1994, Maximum likelihood estimators: AM application to the estimation of the precision of helioseismic measurements, *A&A*, **289**, 649

Toutain T., Appourchaux T., Baudin F., Fröhlich C., Gabriel A., Scherrer P., Andersen B. N., Bogart R., Bush R., Finsterle W., Garcia R. A., Grec G., Henney C. J., Hoeksema J. T., Jiménez A., Kosovichev A., Cortès T. R., Turck-Chièze S., Ulrich R., Wehrli C. 1997, 'Tri-Phonic Helioseismology: Comparison of Solar p Modes Observed by the Helioseismology Instruments Aboard SOHO', *Sol. Phys.*, **175**, 311

Toutain T., Appourchaux T., Fröhlich C., Kosovichev A. G., Nigam R., Scherrer P. H. 1998, 'Asymmetry and Frequencies of Low-Degree p-Modes and the Structure of the Sun's Core', *ApJ*, **506**, L147

Toutain T., Fröhlich C. 1992, 'Characteristics of solar p-modes - Results from the IPHIR experiment', *A&A*, **257**, 287

Ulrich R. K. 1970, 'The Five-Minute Oscillations on the Solar Surface', *ApJ*, **162**, 993

Unno W., Osaki Y., Ando H. 1989, 'Nonradial oscillations of stars', Tokyo: University of Tokyo Press, 1989, 2nd ed.

Willson R. C. 1979, 'Active cavity radiometer type IV', *Appl. Opt.*, **18**, 179

Woodard M. 1984, *Ph.D. thesis*, University of California, San Diego

Woodard M., Hudson H. 1983, 'Solar oscillations observed in the total irradiance', *Sol. Phys.*, **82**, 67

Partie II

Articles majeurs

Chapitre 3

Résultats du LOI basé au sol

A&A, 1995, 294, L13

A&A manuscript no.
(will be inserted by hand later)

Your thesaurus codes are:
06.15.1; 03.13.5; 03.09.4

ASTRONOMY
AND
ASTROPHYSICS
22.1.2000

Frequencies and splittings of low-degree solar p modes: Results of the Luminosity Oscillations Imager

T.Appourchaux[1], T. Toutain[1,2], U.Telljohann[1], A.Jiménez[3], M.C.Rabello-Soares[3], B.N.Andersen[4] and A.R.Jones[5]

[1] Space Science Department of ESA, ESTEC, NL-2200 AG Noordwijk
[2] Observatoire de la Côte d'Azur, F-06003 Nice Cedex
[3] Instituto de Astrofisica de Canarias, Universidad de La Laguna, E-38071 La Laguna, Tenerife
[4] Norwegian Space Centre, N-0309 Oslo 3
[5] Bartol Research Institute, 950 N. Cherry Avenue, P. O. Box 26732, Tucson, Arizona 85719

Received 3 November, 1994; accepted 8 December 1994. Letter to A&A, 294, L13

Abstract. The Luminosity Oscillations Imager is a part of the VIRGO instrument to be flown aboard the Solar and Heliospheric Observatory in mid 1995. Using a ground-based version of the instrument, we have detected low-l modes with a time series spanning 163 days. The low resolution capability of the instrument allows the identification of individual tesseral orders for $l = 2$ to 5. The data reduction method prevents from observing the $l = 0$ modes, and reduces the amplitude of the $l = 1$ modes with $m = \pm 1$. The frequencies and, for the first time, the linear component of the mode splitting (a_1) are given for l=2 to 5 for each order n. The frequencies and the a_1 are obtained by fitting simultaneously the $2l + 1$ spectra using maximum likelihood estimators. The splittings are compared with other published values.

Key words: solar oscillations - p modes - internal rotation

1. Introduction

Helioseismology is a powerful tool to infer the internal structure of the Sun. Over the past two decades, various apparatus reported on the detection of global solar p modes. High resolution imaging instruments can detect degree down to $l = 3$ (Harvey, 1988) while separating the individual tesseral orders m, allowing to measure the splitting of the modes. Unfortunately the instability of these instruments prevents to detect modes with $l < 3$. Integrated sunlight instruments do not have any resolution, but they can detect degree from $l = 0$ to $l = 3$ (Harvey, 1988). The various m components are not all detected and are mixed in the power spectra, making difficult the determination of mode splitting at low l. Various attempts to measure those splittings are starting to give consistent results (Jiménez et al, 1994; Loudagh et al, 1993; Toutain and Kosovichev, 1994). Nevertheless, the rotational splitting given by these authors is an average over various n and l.

It is hoped that with the Solar and Heliospheric Observatory (SOHO), long observations combined with the absence of atmospheric noise will lead to significant improvements in the knowledge of the internal solar rotation (Domingo and Poland, 1989). From the ground, it has been proposed by Tomczyk et al (1994b) to observe the splitting of low-l modes using an imaging instrument with a very stable zero point. Their seminal work gave us the momentum for trying to detect from the ground the mode splitting with the Luminosity Oscillations Imager (LOI). The LOI was built by the Space Science Department of the European Space Agency as a contribution to the VIRGO instrument (Variability of Solar Irradiance and Gravity Oscillations), one of the helioseismology instruments of SOHO. After the completion of the flight programme, we installed in May 1994 the Qualification Model of the LOI at the Observatorio del Teide (Izaña, Tenerife) for detecting in intensity low-l p modes. Due to the atmospheric noise, the detection of p modes in intensity is difficult (Jiménez et al, 1987; Andersen and Domingo, 1988). Nevertheless, the successful observation of low-l p modes by the LOI leads to improvement in the determination of the rotational splitting of low-l modes. Here we present new measurements using a technique to fit the spectra that was developed independently of Tomczyk et al (1994a). The frequencies and, for the first time, the a_1 component of the splitting are given for each n and l.

In this letter, we describe firstly the LOI instrument and secondly how the data were obtained and reduced. In

Send offprint requests to: T. Appourchaux

2

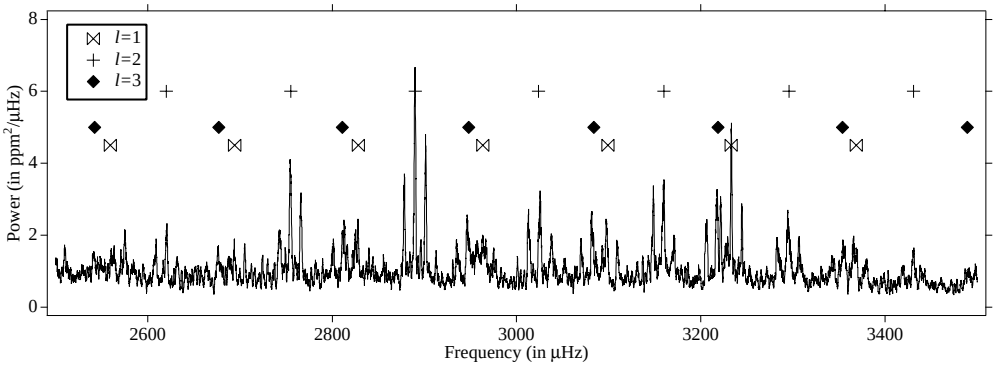

Fig. 1. Power spectrum for the $l = 1, m = 0$ optimal filter, smoothed to 21 points to enhance the modes. The frequency resolution is 0.071 μHz. Each mode and its two aliases can be identified. In addition, the spatial sidelobes are clearly visible; they are the $l = 2, m = \pm 1$, and the $l = 3, m = 0$ modes

the third section, we expose how the spectra were analysed. In the last section, we compare our results with other available values and then conclude.

2. Description of the LOI instrument

The design of the LOI instrument was an original idea of Andersen et al (1988). It consists of a Ritchey-Chrétien telescope (f=1300 mm) imaging the Sun through an 5-nm passband interference filter at 500 nm. The image is projected on a photodiode array detector built to our specifications (Appourchaux et al, 1992). The detector is made out of 12 scientific pixels and of 4 guiding pixels. The shape of the scientific pixels are trimmed to detect low degree modes for $l < 7$ (Appourchaux and Andersen, 1990). The guiding pixels are 4 quadrants of an annulus with an inner and outer radius of 0.95 and 1.05 solar radius, respectively. The error signals for the guiding servo are the differences between two opposite pixels. The error signals are fed back to two piezoelectric actuators that move the secondary mirror around its vertex. The actuators provide both the coarse and fine pointing; the total range of the Qualification Model is $\pm 5'$ with a 0.2" precision; the 3db bandwidth of the servo control is 10 Hz. The current of each scientific pixel is amplified and digitised using Voltage-to-Frequency Converters (VFCs). The current of each guiding pixel is amplified and digitised using A/D converters. The 12 scientific pixels are read simultaneously while the 4 guiding pixels are read sequentially. The sampling time of the instrument is 53.687523 s. The integration time of the scientific pixels is the same as the sampling time. The integration time of the guiding pixels is about 2 s. The instrument is controlled with a PC and all scientific and housekeeping data are stored on a hard disk.

3. Observation and data reduction

The LOI instrument was installed on an equatorial mount on May 2, 1994 in Tenerife. The time series analysed here starts from May 2 and ends on October 11. The duty cycle is about 33 %. Most observations were performed when the Sahara desert blows sand in the sky of Tenerife, and therefore lowers the transparency and increases the scattered light. The clock of the PC was drifting from day to day. This drift was daily measured and if necessary the PC clock was readjusted. The observed stability of the guiding was about 0.2-0.4". This is an upper limit since the atmospheric transparency changes as the guiding pixels are read. The LOI was not aligned with the solar rotation axis and the Sun was rotating from day to day with respect to the detector.

The data reduction was done in three steps. Firstly, we correct the pixels for the fluctuations in the atmospheric transparency; this is done by dividing, at a given time, each pixel by an average over the 12 pixels. Thanks to the coherence of the atmosphere over the solar disk, this reduces by a factor 20 the main atmospheric effect. Secondly, we correct the pixels for their different sensitivity and of the differential extinction; this is done by dividing each pixel by a running mean of the pixel. The running mean is a gaussian filter; the frequency cut-on of this filter is 0.5 mHz. For each pixel, the lowest σ of the series is used to remove spikes greater than 5 σ; the spikes are replaced by zeros. Thirdly, the time series for each pixel are resynchronised every day using a linear interpolation. No other instrumental correction are performed. These data

are used for computing the time series for a given l, m mode.

4. Frequencies and splittings

The optimal linear combination of the pixels to obtain a given l, m mode was reported by Appourchaux and Andersen (1990). Here we used their optimal filters computed for a perfect LOI detector having neither tracks nor guiding pixels. This approximation has proven to be sufficient for our purpose and correct optimal filters are being computed for the SOHO instrument. Since the Sun rotates with respect to the detector (the P and B angles are not negligible) the optimal filters are updated every week and a linear interpolation provide the daily optimal filter. If one were to neglect this image rotation, one would see the effect by an increased cross talk between the modes. For the l, m mode to be analysed, a single time series is obtained by computing the weighted average of the 12 pixels using the optimal filter of the l, m mode. The optimal filters are complex and allow to separate the prograde and retrograde modes in the Fourier space. To minimise the atmospheric noise, the time series for the given l, m mode are weighted by the daily variance; this provides a significant improvement in the power spectra. The time series are normalised to take into account the weighted window function. The frequency resolution of the power spectra is 0.071 μHz.

Figure 1 shows the power spectrum for the $l = 1, m = 0$ optimal filter; modes with $l = 1, 2$ and 3 are clearly detected with amplitudes of about a few part-per-million (ppm). The noise level is about 0.8 ppm$^2/\mu$Hz which is about a factor 4 higher than the noise obtained from space by IPHIR. The signal-to-noise ratio in the power spectra ranges from 1 to 4. It must be pointed out that contrary to what has been reported by Pallé et al (1993), the $l = 1, m = 0$ modes are detected by Tomczyk (1994) and by us. Figure 2 shows a $m - \nu$ diagram for an $l = 2$ mode; the rotational splitting is also clearly visible. The data reduction procedure prevents from detecting the $l = 0$ mode because this mode is filtered out when correcting for the fluctuations of the atmospheric transparency. For the same reason the $l = 1, m = \pm 1$ modes are attenuated by a factor of 4 in the power spectrum. In addition these modes are mixed in the power spectra because their relative phases are lost in the process.

In order to extract in the best way the information contained in the spectra, we chose to fit simultaneously the $2l + 1$ spectra of a given n, l mode using maximum likelihood estimators (MLE); this technique is also used by Tomczyk et al (1994a). The window for the MLE was 14.2 μHz centred on the frequency of the $m = 0$ mode. We assumed that the linewidth is the same for the $2l + 1$ components of an n, l mode; and that the frequency of an m component is $\nu_m = \nu_0 + m a_1$, where a_1 is the linear component of the splitting. The maximum likelihood

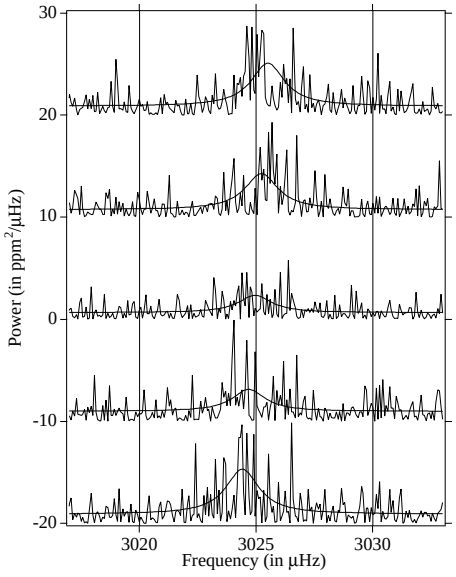

Fig. 2. $m - \nu$ diagram for the $l = 2, n = 20$ mode. The spectra are not smoothed. The fit for this mode are superimposed in bold

technique is well known and its error propagation properties are well understood (Toutain and Appourchaux, 1994). The use of MLE leads to two major approximations. Firstly, it is assumed that in a power spectrum the frequency bins are independent of each other. This is not true as we have gaps in the data (Gabriel, 1994). Nevertheless, the method we used is much simpler than the method suggested by Gabriel (1994), and will not bias the estimate on frequency (Lazrek and Hill, 1992) and splittings. Secondly, we assumed that for a given l, the $2l + 1$ spectra are independent of each other. This is a very good approximation even if there is a crosstalk (due to the imperfect isolation of a given l, m mode) between the $2l + 1$ spectra. The effect of the crosstalk is to couple for a given n, l mode the m components with each other; this was taken into account in the analysis. Due to the small correlation between the $2l+1$ spectra, the error bars on the frequency and splitting will be slightly underestimated. The same underestimation happens if one uses the temporal sidelobes at 11.57 μHz: the error bars would be underestimated by about a factor $\sqrt{3}$. The correct treatment of the power spectra taking into account the statistical dependencies (frequency bins, temporal and spatial sidelobes) remain to be done using the method described by Gabriel (1994). However we believe that only the estimate of the

error bars on the frequency and splitting are biased, and not the values themselves. To minimise this bias, the error bars have been corrected at least from the crosstalk between the various m components. Table 1 and Table 2 summarise, respectively the frequencies and the splittings of the detected modes. In addition, an optimal weighted average (<>) of a_1 is given in Table 2.

5. Discussion and conclusion

For $l = 2$, we are in agreement with Elsworth et al (1994), and Toutain and Kosovichev (1994) (average over $l = 1, 2$: 440 ± 10 nHz, 452 ± 20 nHz respectively), and in disagreement with Fossat et al (1994) (low order modes: 499 ± 15 nHz); these 3 values represent an average of the splitting of sectoral modes, and should therefore be slightly higher than our a_1 by a few nHz (D.O.Gough, 1994, private communication). For $l = 3$, we are in disagreement with Fossat et al (1994) (low order modes: 463 ± 15 nHz). On the other hand, we are in good agreement with the values of a_1 found by Rhodes et al (1990) for $l = 3, 4$ and 5 (426 $\pm$ 28 nHz, 412 $\pm$ 10 nHz, 406 $\pm$ 8 nHz, respectively). It must be pointed out that the agreement with Rhodes et al (1990) may be even better as the autocorrelation method, that they used, systematically overestimates the splittings below $l = 10$ (Brown and Morrow, 1987).

The splitting we found for $l = 2$ confirm the findings of Elsworth et al (1994), Fossat et al (1994), Jiménez et al (1994), and of Toutain and Kosovichev (1994) about a core not rotating much faster than the solar surface.

The measurements made by the LOI are an improvement for low-l p-mode analysis, because the various m components of the modes can be individually detected.

Table 1. LOI frequencies and 1-σ error in (μHz) of low-l p modes (d: modes detected but no frequency estimate available)

n	l=1	l=2	l=3
15	-	-	2407.68 ± 0.15
16	-	2486.06 ± 0.13	2542.00 ± 0.15
17	-	2619.69 ± 0.16	2676.35 ± 0.20
18	d	2754.38 ± 0.10	2811.50 ± 0.18
19	d	2889.74 ± 0.10	2946.80 ± 0.16
20	-	3024.96 ± 0.11	3082.16 ± 0.11
21	3097.71 ± 0.31	3159.67 ± 0.17	3217.84 ± 0.11
22	3233.08 ± 0.15	3295.41 ± 0.18	3353.83 ± 0.45
23	-	3430.89 ± 0.18	3490.05 ± 0.30
n	l=4	l=5	l=6
15	2458.70 ± 0.23	2506.02 ± 0.18	-
16	2592.87 ± 0.17	2641.30 ± 0.21	d
17	2728.80 ± 0.21	2777.20 ± 0.14	d
18	2864.09 ± 0.08	2913.56 ± 0.15	d
19	3000.21 ± 0.14	3049.78 ± 0.12	d
20	3135.89 ± 0.13	3186.23 ± 0.15	d
21	3271.61 ± 0.16	3322.96 ± 0.31	-
22	3407.98 ± 0.24	3460.42 ± 0.32	-
23	3544.12 ± 0.29	-	-

Table 2. LOI sidereal a_1 component of the splitting (in nHz) for low-l p modes. The errors are 1-σ values

n	l=2	l=3	l=4	l=5
15	-	445 ± 46	455 ± 92	438 ± 39
16	457 ± 110	319 ± 59	243 ± 79	405 ± 51
17	525 ± 101	450 ± 74	322 ± 80	409 ± 39
18	362 ± 65	281 ± 73	408 ± 23	418 ± 40
19	258 ± 74	476 ± 59	319 ± 39	430 ± 32
20	301 ± 65	317 ± 52	331 ± 33	408 ± 34
21	497 ± 109	387 ± 50	480 ± 53	405 ± 103
22	807 ± 116	613 ± 215	425 ± 81	132 ± 102
23	484 ± 127	527 ± 140	198 ± 97	-
<>	402 ± 31	392 ± 21	373 ± 14	413 ± 15

References

Andersen, B.N. and Domingo, V., IAU Symposium 123, J.Christensen-Dalsgaard and S.Frandsen eds, Reidel, p. 67

Andersen, B.N, Domingo, V., Jones, A.R. et al, 1988, ESA SP-286, Eds V.Domingo and E.J.Rolfe, p. 385

Appourchaux, T., Martin, D. and Telljohann, U., 1992, SPIE 1679, 200

Appourchaux, T. and Andersen, B.N., 1990, Sol.Phys. 128, 91

Brown, T.M. and Morrow, C.A., 1987, 'The internal Solar Angular Velocity', B.R.Durney and S.Sofia eds, Reidel, p. 7

Domingo, V. and Poland, A., 1989, 'The SOHO mission', ESA SP-1104, p. 7

Elsworth, Y., Howe, R., Isaak, G.R. et al, 1994, To appear in the proceedings of the GONG-94 conference

Fossat, E., Loudagh, S., Gelly, B. et al, 1994, To appear in the proceedings of the GONG-94 conference

Gabriel, M., 1994, A&A 287, 685

Harvey, J., 1988, ESA SP-286, Eds V.Domingo and E.J.Rolfe, p. 55

Jiménez, A., Pallé, P.L., Roca Cortés, T. et al, 1987, A&A 172, 323

Jiménez, A., Perez Hernandez, F., Claret, A. et al, 1994, ApJ 435, 874

Lazrek, M. and Hill, F., 1992, A&A 280, 704

Loudagh, S., Provost, J., Berthomieu, G. et al, 1993, A&A 275, L25

Pallé, P.L., Perez Hernández, F., Régulo, C. and Roca Cortés, T., 1993, ASP Conference Series 42, p. 189

Rhodes, E.J., Jr, Cacciani, A., Korzennik, S. et al, 1990, ApJ 351, 687

Tomczyk, S., 1994, To appear in the proceedings of the GONG-94 conference

Tomczyk, S., Schou, J. and Thompson, M.J., 1994a, submitted to ApJ Letter

Tomczyk, S., Streander, K., Card, G. et al, 1994b, submitted to Sol. Phys.

Toutain, T. and Appourchaux, T., 1994, A&A 289, 649

Toutain, T. and Kosovichev, A., 1994, A&A 284, 265

This article was processed by the author using Springer-Verlag LaTeX A&A style file *L-AA* version 3.

Chapitre 4

Performances du LOI spatialisé

Solar Physics, **1997, 170, 27**

IN-FLIGHT PERFORMANCE OF THE VIRGO LUMINOSITY OSCILLATIONS IMAGER ABOARD SOHO

THIERRY APPOURCHAUX[1], BO N. ANDERSEN[2], CLAUS FRÖHLICH[3], ANTONIO JIMÉNEZ[4], UDO TELLJOHANN[1] and CHRISTOPH WEHRLI[3]

[1]) *Space Science Department, European Space Research and Technology Center, 2200 AG Noordwijk, The Netherlands*

[2]) *Norwegian Space Centre, 0309 Oslo 3, Norway*

[3]) *Physikalisch-Meteorologisches Observatorium Davos World Radiation Center, 7260 Davos Dorf, Switzerland*

[4]) *Instituto de Astrofísica de Canarias, Universidad de La Laguna, 38071 La Laguna, Tenerife, Spain*

received 15 October 1996; revised 26 November 1996

Abstract. The Luminosity Oscillations Imager (LOI) is a part of the VIRGO instrument aboard the Solar and Heliospheric Observatory (SOHO). The scientific objective of the LOI experiment is to identify and characterize pressure and internal gravity oscillations of the sun by observing the radiance variations. The LOI is a low-resolution imager with 12 pixels, for the measurement of the radiance distribution over the solar disk at 500 nm. The low resolution capability of the instrument allows the identification of individual azimuthal orders for l=0 to 7, without suffering the mixing that affects integrated solar disk instruments. The performance, calibrations and instrumental effects of the LOI are described together with the procedures for extracting the solar p modes.

Key words: Helioseismology – SOHO Mission

1. Introduction

The European Space Agency (ESA) embarked in 1985 on a collaborative mission with the National Aeronautics and Space Administration, the so-called Solar and Heliospheric Observatory (SOHO). On board this spacecraft are 3 helioseismology instruments: Michelson Doppler Imager/Solar Oscillation Instrument, Global Oscillations at Low Frequency, both in velocity, and VIRGO (Variability of solar Irradiance and Gravity Oscillations). They respectively observe the Sun, in velocity and in intensity on a detector with 1000 × 1000 pixels, in velocity as a star, and in intensity at three different wavelengths.

VIRGO aims specifically at detecting the gravity modes of the Sun. These modes are extremely important, as they propagate mainly in the core and the radiative zone. They would considerably improve our knowledge of the deep interior of the Sun, which is presently known only by inverting the frequencies of the pressure modes, which have a smaller resolving power than the gravity modes in the core. The VIRGO experiment (Fröhlich *et al.*, 1996) consists of several instruments. One of these, the Luminosity Oscillations

Imager (LOI) was designed and built by the Space Science Department of ESA. Its scientific objective is to detect the p and g modes of the Sun and to study the radiance variability due to solar active regions and other phenomena.

Here we discuss the performance and operation of the LOI and present some first results as an illustration. First we describe how the instrument cover was opened; it is a story of perseverance that has to be told once and for all. Next we briefly describe the instrument and show how it performs and how the data are analyzed for extracting reliable p-mode parameters.

2. The opening of the cover

On December 2, 1995, the SOHO satellite was launched by an Atlas-Centaur rocket from Cape Canaveral. A few days later, VIRGO was powered on, and the LOI remained in calibration mode until December 24, 1995 when its cover was opened for 5 minutes for a 'first light' experiment. Then the cover was closed to continue the outgassing of the instrument. On January 17, 1996, we tried to open the cover in order to start the regular operation of the LOI. Unfortunately, the cover remained closed, even after several attempts. During this operation the LOI could see the Sun for about 1-2 sec which was sufficient to lock the guider onto the Sun. The cover is operated by a 90-degree motor which is switched to the open position by a nominal current pulse length of 710 msec. The only explanation we had was that the cover was bouncing back to the closed position and/or that the length of the impulse sent to the motor was too short to keep it in the open position.

At this stage, the inability to open the cover concerned the whole SOHO community and a team was set up to resolve the problem. A model of the cover was developed in collaboration with the Mechanics Section of the Mechanical Systems Department of the European Space Research and Technology Centre. The first idea to open the cover by reducing even more the length of the pulse sent to the motor was confirmed. The pulse length to be used was determined empirically from the extensive modeling of the cover movement together with actual measurements on the spare in Davos. The major question was how to perform the same operation on an experiment without computer and thus without the necessary flexibility. The only way was to send a command for opening the cover, and then to switch-off VIRGO with a delay according to the pulse length wanted. To achieve this, MATRA/MARCONI (main contractor of SOHO), SAAB (on board computer) and the SOHO project devised a patch that would allow the accurate timing of the switch-off of VIRGO. One week before the real execution with the spacecraft, a rehearsal was performed at the SAAB premises using the VIRGO flight spare and a prototype of the SOHO onboard computer. The timing of the switch-off worked very well and allowed a variation in the pulse

length from 70–700 ms with a precision of a few ms.

On March 27, 1996, the two most likely pulse lengths were sent to the spacecraft and the second one with 480 msec length worked. Clearly, this was a relief to all of us that had been working for more than 10 years on this project. The opening of the LOI cover was a concerted effort by many people as listed in the acknowledgments. The success was mainly due to the highly motivated co-operation between the different parties in order to allow LOI to play its important role for the unambiguous identification of low degree solar oscillations.

3. Description of the LOI

The design of the LOI instrument is extensively described in Appourchaux *et al.*, 1995a. Briefly, it consists of a Ritchey-Chrétien telescope (f=1300 mm) imaging the Sun through a 5 nm bandpass interference filter at 500 nm. The image is projected on a photodiode array detector built to our specifications (Appourchaux *et al.*, 1992). The detector has 12 scientific pixels and 4 guiding pixels (Fig.1). The shape of the scientific pixels are trimmed to detect low degree modes for $l < 7$ (Appourchaux & Andersen, 1990). The guiding pixels are 4 quadrants of an annulus with an equivalent inner and outer radius of 0.95 and 1.05 solar radius, respectively. The error signals for the guiding servo are the differences between two opposite pixels. The error signals are fed back to two piezoelectric actuators that move the secondary mirror around its vertex. The actuators provide both the coarse and fine pointing; the total range is $\pm 7.5'$ with a 0.2" resolution; the 3db bandwidth of the servo control loop is at 10 Hz. The current of each scientific pixel is amplified and digitised using Voltage-to-Frequency Converters (VFCs). The current of each guiding pixel is amplified and digitised by the common data acquisition system of VIRGO. The 12 scientific pixels are read simultaneously while the 4 guiding pixels are read sequentially. The sampling time of the instrument is 60 s. The integration time of the scientific pixels is the same as the sampling time. The integration time of the guiding pixels is about 3 s distributed over the 1 minute period.

The LOI data products are of two kinds: the level 1 and the level 2 data. The level-1 data are those that have been converted from raw counts (level 0 data) to physical units; they include the calibrations and contain all the corrections known *a priori* for instrument-related effects, such as the influence of temperature variations. The signals are also reduced to 1 AU distance and to zero radial velocity. The level-2 data are the level-1 data corrected for degradation. The data products at either level are the following:

- 12 radiances of the LOI scientific pixels every minute
- 4 radiances of the LOI guiding pixels every minute
- 2 diameters (N/S and E/W) every minute

Fig. 1. Configuration of the in-flight detector of the LOI with the correct orientation.

– 4 VIRGO sunphotometers (SPM) flux corrections every day.

The first year's level-2 data will be made available to the scientific community one year after completion; for more detail on the data dissemination, see Fröhlich *et al.*, 1996. From the level-2 data products the following data are derived for the scientific evaluation:

– Time series of an l, m mode for p-mode analysis ($l < 9$)

– p-mode characteristics such as frequencies, splittings, amplitudes and linewidths

– Same as the above but for the g modes if they are found.

The level 0 and level 1 data will be made available to the scientific community only on request by a specific proposal to the VIRGO Principal Investigator. The proposal will be discussed and eventually approved by the VIRGO team.

4. Instrument performances

4.1 Operations

The LOI was switched on December 6, 1995 and began, on this date, calibration measurements with the cover closed. These measurements entailed applying reference voltages to the amplifiers of the 16 pixels. The calibration measurements continued until the opening of the cover on March 27, 1996. A few minutes after the opening of the cover, the guiding servo loop was activated and the LOI was in its nominal observational mode where all 16 pixels are acquired every minute. On April 17, 1996, the calibration voltages were switched off, allowing a better determination of the offset voltages.

In addition to the normal operations of the LOI, the instrument took part in various useful joint payload operations: J3 (for guiding calibrations) and the roll operations. J3 occurred from April 3 to 5, 1996. During J3, the spacecraft scanned the solar rotation axis by ± 5 arcmin (North-South) and the solar equator (East-West) by ± 20 arcmin. During the North South scan the LOI active guiding was activated in the range -10 to 0 arcmin, and switched off outside this range. Similarly during the East-West scan the guiding was activated in the range ± 5 arcmin. The roll maneuver was performed on May 20, 1996. During the roll operations the spacecraft was rotated by 90° around the line of sight for about 20 hours.

Other regular spacecraft operations, such as the momentum management perturb the normal operations of the LOI; but due to the large guiding range, they can be handled without any additional specific operation of the LOI. Nevertheless, the data quality during such short periods is somewhat degraded.

4.2 In-flight performance

4.2.1 Dark current noise

During the 4 months that the cover was closed, we had ample time to characterize the noise of the electrical chain. This was derived using the so-called calibration mode described above. Fig.2 shows the power spectrum of an equivalent $l = 0$ mode together with a typical real solar spectrum. A similar spectrum was measured from the ground (Fröhlich *et al.*, 1996) for a single pixel, confirming an adequate performance of the instrument in space. The noise in the p mode range, mainly due to solar granulation, is about 0.1 $\mathrm{ppm}^2/\mu\mathrm{Hz}$ at 3000 μHz which is about a factor 4 lower than what was observed from the ground by Appourchaux *et al.*, 1995b. This higher noise is obviously due to the Earth's atmosphere.

4.2.2 Guiding calibrations and performance

The J3 operations permitted calibration of the guiding when the servo loop was activated. This was useful to make sure that the piezoelectric actuators

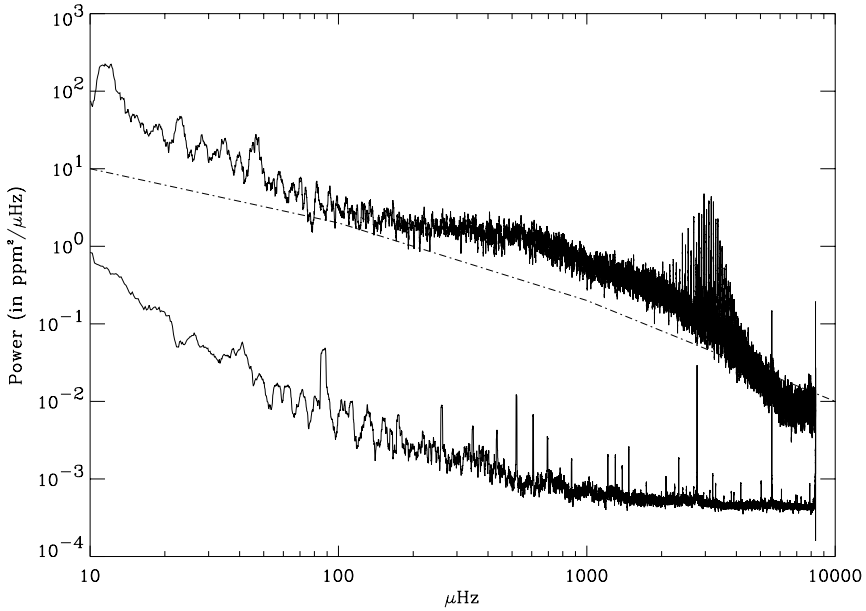

Fig. 2. (Top) LOI full power spectrum for an l=0, showing the 5-min oscillation modes. The spectrum becomes flatter around 1 mHz and then rises again; this is mostly due to the granulation noises and a Sun at its minimum of activity. (Dashed) This is the noise as simulated by Andersen *et al.*, 1994. (Bottom) This is the equivalent l=0 noise obtained during the calibration mode of the LOI (with the cover closed). The spectrum shows the noise due only to the electronic chain. The noise level in the p-mode range is about two order of magnitude less than the one of the granulation noise. Several spikes are present which are due to changing calibration modes (at regular intervals) of another VIRGO instrument. A large spike at 3 minutes is also present (at 5555 μHz and its 'harmonics' at 2778 μHz). This is due to the basic acquisition block rate of VIRGO, which is 3 minutes.

were performing as expected. It helped also to measure an offset towards the South pole already observed by all the SOHO instruments. This offset was due to the spacecraft and amounted to 3 arcmin for the LOI. A repointing occurred on April 17, 1996 that put the solar image close to the LOI optical axis. Fig. 3 shows the calibration of the guiding, i.e. the high voltage applied to the actuators as a function of the offset angle. The sensitivity is about 1.6 arcsec/volt. The performance is the same as measured on ground. Fig. 4 shows the guiding stability of the instrument which is better than 0.01 arcsec at 1 σ. It is interesting to note that higher noise in the E-W direction remained when the spacecraft was rotated by 90° which indicates that the

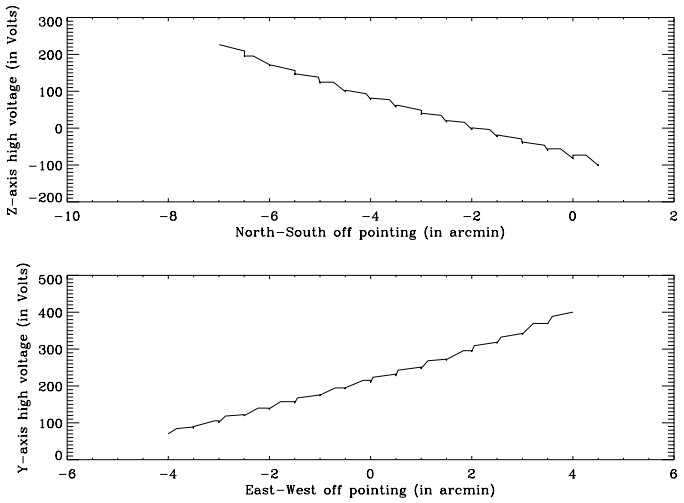

Fig. 3. High voltage as a function of the offset in arcmin for the East-West axis (bottom), and the North-South axis (top). The variations observed in voltage for a given offset angle are due to the creep in the piezoelectric material of the actuators.

noise is from the pointing system of the spacecraft and not a solar feature.

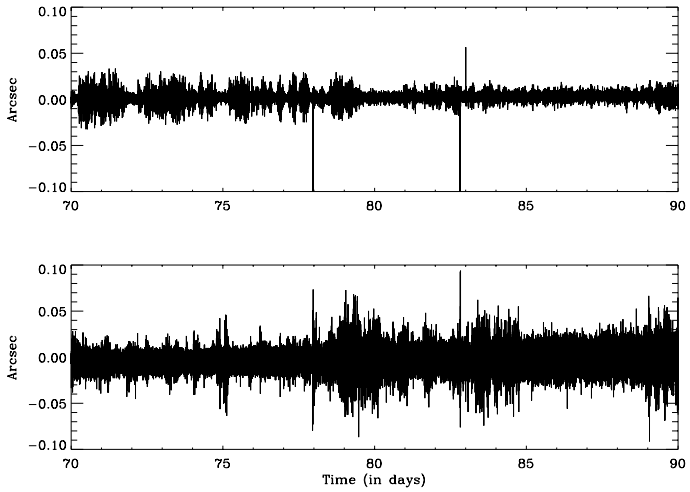

Fig. 4. Guiding stability for the East-West and North-South direction as a function of time. The East-West guiding pixels are noisier than those of North-South; this could be due to a combination of instrumental and spacecraft pointing noise. It is probably not of solar origin.

4.2.3 Pixel sensitivity calibrations

The J3 operations were also used to perform a flat field calibration. The idea is derived from Kuhn *et al.*, 1991: a flat field of a multi-element detector (such as a charge coupled device or a photodiode array) can be derived by moving an image with a known intensity distribution on the detector. We tried to use a very similar technique for flat fielding the LOI pixels.

As an example, Fig. 5 shows how the intensity varied on the pixels as a function of the offset angle. The measured profile is then compared with a theoretical profile, taking into account the limb darkening at 500 nm (Neckel & Labs, 1994) and the LOI pixel shapes. Since the active guiding was off (a fixed voltage was applied to the actuators) the position of the Sun was derived by maximizing the correlation between the measured and theoretical profiles (Fig. 6).

Unfortunately, the precision on the sensitivity obtained using this technique was not better than 1 %. It did not work because the departure from the theoretical profiles was about a few %, mainly due to the effect of the point spread function (PSF) of the telescope that needs to be taken into account. The PSF of the instrument varies a lot, especially when the image is not centered on axis; the variation of the PSF in the field can lead to variations in the intensity falling on the pixels of a few %. The effect of a varying PSF was also measured when the active guiding was on. For example on Fig.7, the pixel intensity varies with the offset angle. These variations are calibrated for each pixel and used for producing the level-1 data.

4.2.4 Solar diameters

The guiding pixels of the LOI are also used to derive an equivalent solar diameter. We used the limb darkening function at 500 nm to derive the ratio of the guiding pixels to the central pixels. This ratio is almost a linear function of the size of the solar image, but it is insensitive to the decrease in flux which is due to the degradation. The diameters derived, for the North-South and East West directions, are then converted to 1 AU using the orbit data of SOHO. Fig. 8 shows the solar diameters for June 1996. At that time, the Sun's apparent diameter was still decreasing. The opposite trend is still visible in Fig. 8 showing that the calibration has a systematic error of about 5%. The seasonal variation of the Sun apparent diameter will be used to correct for this systematic error. The noise in a 0.3–Hz bandwidth on the diameters is in a 0.3–Hz bandwidth about 0.1 arcsec and 0.2 arcsec peak-to-peak for the North-South and East-West directions, respectively.

4.2.5 Solar image distortion

Although most of the performance characteristics are excellent, the LOI is still very sensitive to slight distortion in the shape of the solar image. The distortion affects both the size of the image and its circular shape. In addi-

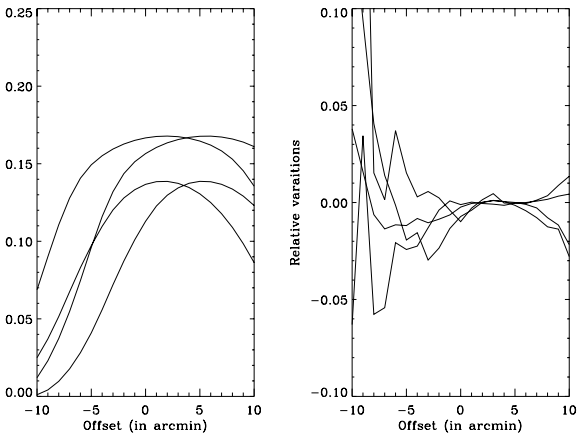

Fig. 5. (Left) Theoretical East-West pixel intensity as a function of the offset angle during the North-South scan. The lack of symmetry between the 4 profiles is due to the offset of the Sun during the J3 operations; the active guiding was off and a fixed voltage was applied to each actuator. (Right) Relative difference between the measured profile and the theoretical ones for these pixels.

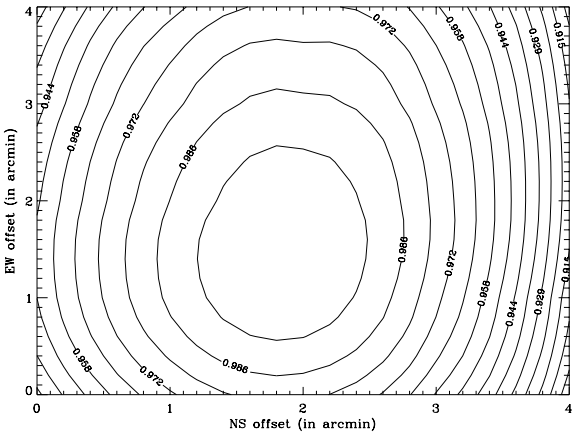

Fig. 6. Correlation map between the measured profiles and theoretical profiles for the East-West pixels as a function of the North-South and East-West offset angles. The scan was North-South which explains why the minimum is better defined in this direction. The maximum is very close to 1. Its location gives the offset of the solar image with respect to the center of detector during the J3. Similar correlation maps have been obtained for the other pixels and the other East-West scan.

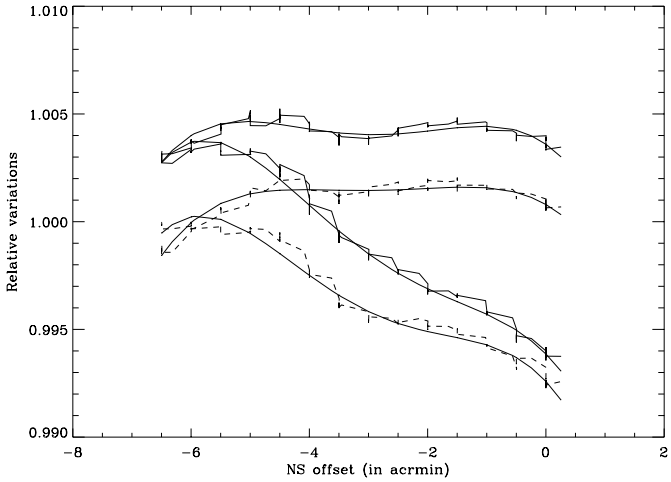

Fig. 7. Variation of the intensity of the 4 East-West pixels as a function of the offset angle when the guiding is active and during the North-South scan; (solid line) for the pixels 6 and 7, (dashed line) for the pixels 5 and 8. The smooth lines are fifth order polynomial fits.

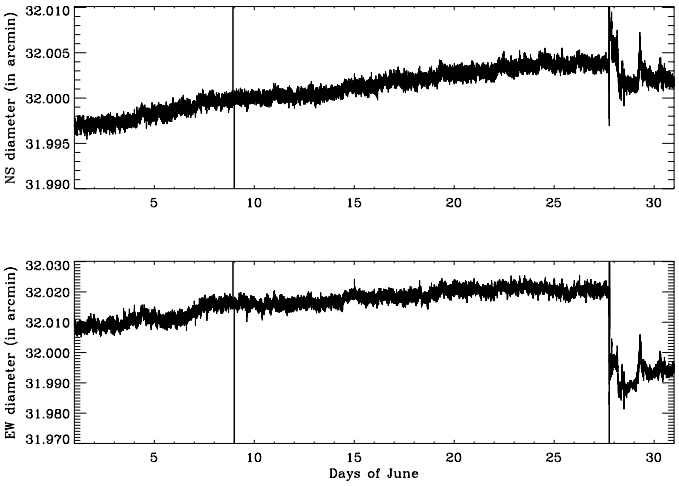

Fig. 8. The 1 AU diameters for the North-South (top) and East-West (bottom) as a function of time for the month of June. The slight trend remaining is due the imperfect correction for a decreasing apparent solar diameter; the SOHO spacecraft was moving away from the sun. The typical precision over one day is less than 1 marsec.

tion, this distortion has a 1-day periodicity creating, mainly in the $m = \pm l$ spectra, harmonics below 200 μHz, making the detection of the g modes more difficult. It has been empirically found that the temperature of the DC-DC converter of the high voltage can be used for compensating the distortion. Using the guiding pixels, we can derive that the magnitude of the distortion of the solar image is about 0.4 arcsec and 1.3 arcsec for a temperature change of 1 °C on the DC-DC for the North-South and East-West diameters, respectively. The magnitude of the correction is about 900 ppm/°C, 1550 ppm/°C and <400 ppm/°C, for the pixels 1–4, 5–8 and 9–12 respectively. The most affected pixels are, of course, the ones closest to the limb. The linear correction given above can reduce the amplitude of these harmonics by about a factor 3. This attenuation is not sufficient to facilitate the detection of the g modes in this range. A non-linear correction has yet to be derived that would provide better attenuation of the harmonics and would cope with larger temperature variations occurring after the spacecraft's momentum management. An example of undercorrection can be seen in Fig.8 after the momentum management of 27 June 1996.

At the time of writing, the reason for the distortion is not yet understood. However since it has been observed that the distortion redistributes the flux among the pixels (i.e. the distortion disappears when summing up all the 16 pixels), there is great confidence that the effect will be explained. We used the linear corrections mentioned above for producing the level-1 data.

5. Scientific data analysis

5.1 Level 0 to level 1 processing

After unpacketizing the data, the level-0 data are built from the 3 delayed transmissions of the VIRGO data; this is done at the VIRGO data center (VDC). The data are then converted from counts to engineering values using the calibration performed on ground. The offset calibrations were refined in flight after the calibration mode switch off. The 16 pixels are then converted to flux measured at 1 AU using the SOHO-Sun distance derived from the orbital data. The correction takes into account the real shape of the pixels, the limb darkening at 500 nm, and the in-flight size of the solar image at 1 AU. The precision of the correction better than 0.1 % is for all the scientific pixels. The pixels are also converted to zero velocity using the orbital data. These level-1 conversions are done at the VDC.

In addition, for comparing the LOI integrated flux with the SPM, 4 conversion factors are derived. These factors take into account the pixel shapes, the limb darkening and the non sensitive tracks on the detector. Since the variations are slow, these factors are generated once for a whole day. This is also done at the VDC.

The 16 pixels are corrected for the variations in intensity using the atti-

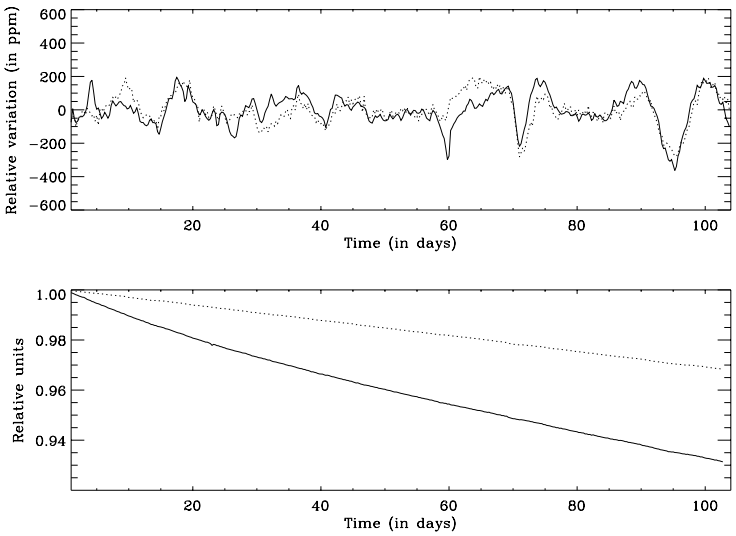

Fig. 9. Comparison of the LOI (solid) and SPM (dotted) green channel, both viewing the sun as a star. The time series starts on May 1, 1996. (Top) Relative variations. The agreement is quite good but there are still unexplained differences which need more detailed analysis. Both signals show very nicely the emergence and passage of an active region on day 70 and 90 respectively. (Bottom) Absolute variations normalized to the first datum.

tude data of the spacecraft. Finally, the distortion effect is corrected, using the temperature of the DC-DC, by applying the same coefficient for all pixels having the same shape. These latter corrections are yet to be implemented at the VDC.

5.2 Comparison with the green channel of the SPM

Using the 4 SPM conversion factors, we compared the LOI integrated flux with the SPM. Fig. 9 shows the result of the comparison. The LOI flux decreases much faster than that of the SPM. The degradation affects all the pixels in the same manner. The stronger degradation is probably due either to the fact that the LOI entrance filter has a much larger viewing angle for the solar wind than the SPM, or to the higher temperature of the LOI filter (about 50°C), and possibly also to the fact that the filters were produced by different manufacturers. After correction for degradation, the LOI integrated flux compared quite well with the SPM. Especially the decrease in flux due to the emergence and the passage of a sunspot is very well correlated.

5.3 P-MODE ANALYSIS

After the production of the level-1 data, the 12 scientific pixels are ready to be used for extracting the p modes. Each pixel is detrended using a triangular smoothing with a full width of 1 day, and then the residuals are converted to relative values. For extracting a given degree, the 12 pixels are combined using so-called optimal filters. The optimal filters were derived by Appourchaux & Andersen, 1990. Since these filters are complex they allow each m to be separated in a l, n multiplet. These filters were successfully used by Appourchaux *et al.*, 1995b,c and Rabello-Soares *et al.*, 1996. The optimal filters were computed weekly using the real size of the solar image (calibrated in flight) and the orientation of the Sun (only the B angle as P is maintained to zero by the spacecraft attitude control).

The spectra obtained have been used to derive the p-mode parameters. A given (m, ν) diagram is fitted using the maximum-likelihood method as described by Appourchaux *et al.*, 1995b. As outlined in that paper, the different $2l+1$ components spectrum of a given l, n multiplet are correlated with each other because of the imperfect isolation of the modes (see also Rabello-Soares, 1996). In principle, the full covariance matrix should be used to fit not the power spectra, but the amplitude or Fourier spectra (Schou, 1992). An additional complication is taken into account in the fitting of the spectra, higher-degree modes leaking into the lower-degree modes, and *vice versa*. For example, in the $l = 1$ signal we can detect $l = 6$ and *vice versa*; the $l = 4$ signal is contaminated by $l = 7$ (Fig. 10) and *vice versa*, the $l = 5$ by $l = 8$ and *vice versa*. The full leakage between the $2l + 1$ modes of a multiplet and between mode of the higher (or lower) degree has been computed using the computed optimal filters in a manner similar to that of Rabello-Soares, 1996. This is an improvement of the procedure adopted by Appourchaux *et al.*, 1995b, who regarded the mode leakage matrix not to be known a priori and fitted it to the data. The amplitudes of all the modes in the spectrum, together with the frequencies of the target and leaked modes, were fitted simultaneously. The frequencies of the unwanted leaked modes were sometimes fixed using the frequencies obtained from BBSO (Libbrecht *et al.*, 1990). This simplification did not influence the frequencies of the target modes substantially, yet it increased the rate of convergence of the iterations in the fitting. In this way the bias on the frequency estimates due to spatial mode leakage was reduced.

As far as the rotational splitting is concerned, we believe that the estimates are biased for ($l \leq 3$) because we do not fit the amplitude. In addition, the inaccuracy in the knowledge of the leakage matrix will lead to a bias on the splitting, the sign of which depends on the under– or over–estimation of the leakage. This effect is more important for low degree modes ($l \leq 3$). Fortunately, fitting the amplitude spectra is easier to implement for

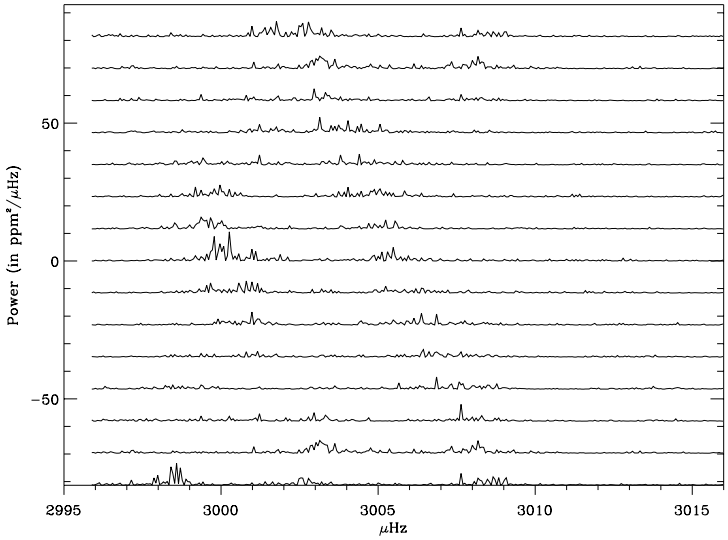

Fig. 10. The m, ν diagram for the $l = 7$, $n = 18$ multiplet; $m = -7$ is at the top. The resolution is about 84 nHz. It shows an example of the effect of the leakage of the l=4, n=19 into the l=7. We see clearly the splitting of the l=7 mode and also the effect of the leakage of unwanted modes with different values of m. The splitting of the $l = 4$ is not visible because the leakage is more complex: the $l = 4, m = +4$ mode is partially transmitted by the filter for $l = 7, m = -7$, and the $l = 4, m = -4$ is transmitted by the $l = 7, m = +7$.

these degrees because the higher degree aliases are either very weak or non-existent. In any case, the sources of systematic errors in the estimate of the low degree splitting have to be carefully assessed before drawing any conclusion on e.g. the internal rotation of the Sun. From this point of view, longer time series will improve the situation.

6. Conclusion

In retrospect, only a few changes would have improved the instrument's performance. For example, we could have had more pixels; it would have reduced the leakage from the higher (or lower) degree. We could have read the guiding pixels using also individual VFCs, it would have reduced the high frequency noise by a factor of about 4–5.

Up to now the LOI has been performing extremely well. There are also great expectations from the measurement of the diameters. Nevertheless, a lot of work remains to be done to understand the cause of the distortion of the solar image, especially if we want to detect the g modes. The data allow

to measure the p modes for $l \leq 7$ with a very high precision as shown in the first scientific result paper by Fröhlich *et al.*, 1997.

Acknowledgements

The responsible for the LOI (ThA) is eternally thankful to Trevor Sanderson of the Solar and Heliospheric Science Division Of ESA. He was the one who proposed to replace the 'non-intelligence' of VIRGO by a well timed 'pulling of its plug'. We are also grateful to our colleagues of the Mechanics Section of ESTEC without whom the model of the cover could have not been validated: P.Coste, M.Eiden, M.York and M.Verin. The latter performed several tests on the motor in the Mechanical and Thermal Laboratory of ESTEC. Sincere thanks also to F.Dufrechou and P.Temporelli of MATRA-MARCONI-SPACE for the general management of the problem, to A.Lago and P.Roos of SAAB for the implementation of the software patch and to P.Strada of the SOHO project for coordinating the software patch efforts. Last but not least, we are thankful to H.J. Roth for his faithful dedication to the VIRGO instrument and all tests performed on the spare.

The building of the LOI would have not been possible without the contribution of the following ESTEC personnel: J.Fleur, R.Scheper, A.Smit for the mechanical designs; J.Blommers, J.Postema, M.J.Kikkert, K.F.Frumau, for the machining and the assembling; K.Bouman, A.Fransen, J.Heida, L.Smit for the electronics; T.Beaufort and D.Martin for the electronic design; S.Lévêque for the optical and detector tests; additional contributions were given by G.Gourmelon for the spectrophotometry, by B.Johlander for various irradiations tests, by J.M.Guyt for checking the contamination, by A.Zwaal for the cleanliness levels and by P.Brault for the bakings; we also thank R.Czichy for loaning us the Zygo interferometer and D.Doyle for the technical assistance on this interferometer. The various parts of the LOI instrument could not have been built without the help of the following individuals in industry: T.E.Hansen at Ame for the detector, C.Shannon and T.Hicks at Queensgate for the piezoelectric actuators, and P.Robert at SESO for the telescope.

Last but not least the LOI would never have had a place in space without the efforts of the whole VIRGO team which are gratefully acknowledged.

One of the author (ThA) is very grateful to Richard Marsden for checking the English.

References

Andersen, B.N., Leifsen, T. and Toutain, T.: 1994, *Solar Phys.* **152**, 247.
Appourchaux, T. and Andersen, B.N.: 1990, *Solar Phys.* **128**, 91.
Appourchaux, T., Martin, D. and Telljohann: 1992, *SPIE* **1679**, 200.
Appourchaux, T., Telljohann, U., Martin, D., Lévêque, S. and Fleur, J.: 1995a, 'The Luminosity Oscillations Imager' in V.Domingo and T.Hoeksema, ed(s)., *Fourth SOHO*

workshop on helioseismology, ESA SP-376, 359

Appourchaux, T., Toutain, T., Telljohann, U., Jiménez, A., Rabello-Soares, M.C., Andersen, B.N. and Jones, A.R.: 1995b, *Astr. Astrophys.* **294**, L13.

Appourchaux, T., Toutain, T., Telljohann, U., Jiménez, A., Rabello-Soares, M.C., Andersen, B.N. and Jones, A.R.: 1995c, 'Results from the Luminosity Oscillations Imager' in V.Domingo and T.Hoeksema, ed(s)., *Fourth SOHO workshop on helioseismology*, ESA SP-376, 265

Fröhlich, C., Romero, J., Roth, H., Wehrli, C., Andersen, B.N., Appourchaux, T., Domingo, V., Telljohann, U., Berthomieu, B., Delache, P., Provost, J., Toutain, T., Crommelynck, D., Chevalier, A., Fichot, A., Däppen, W., Gough, D.O., Hoeksema, T., Jiménez, Gómez, M., Herreros, J., Roca-Cortés, T., Jones, A.R., Pap, J. and Willson, R.C.: 1996, *Solar Phys.* **162**, 101

Fröhlich, C., Roth, H., Wehrli, C., Andersen, B.N., Appourchaux, T., Domingo, V., Berthomieu, B., Provost, J., Toutain, T., Crommelynck, D., Chevalier, A., Gough, D.O., Jiménez, Gómez, M., Herreros, J., Roca-Cortés, T. and Pap, J.: 1997, *Solar Phys.* **This volume**, ?

Kuhn, J.R., Lin, H. and Loranz, D.: 1991, *PASP* **103**, 1097

Neckel, H. and Labs, D.: 1994, *Solar Phys.* **153**, 91

Libbrecht, K.G., Woodard, M.F. and Kaufman, J.M.: 1990, *ApJ Supp.* **74**, 1129

Rabello-Soares, M.C.: 1996, *Helioseismological study of the solar interior*, PhD thesis, Universidad de La Laguna: La Laguna, Tenerife, Spain

Rabello-Soares, M.C., Roca-Cortes, T., Jiménez, A., Appourchaux, T. and A.Eff-Darwich.: 1996, *Submitted to ApJ* ,

Schou, J.: 1992, *On the analysis of helioseismic data*, PhD Thesis, Aarhus University: Aarhus, Denmark

Chapitre 5

L'art de l'ajustement
Part I & II

A&A Sup. Series, **1998, 132, 107–132**

ASTRONOMY & ASTROPHYSICS
SUPPLEMENT SERIES

OCTOBER I 1998, PAGE 107

Astron. Astrophys. Suppl. Ser. **132**, 107–119 (1998)

The art of fitting p-mode spectra

I. Maximum likelihood estimation

T. Appourchaux[1], **L. Gizon**[1,2], **and M.-C. Rabello-Soares**[1,3]

[1] Space Science Department of ESA, ESTEC, NL-2200 AG Noordwijk, The Netherlands
[2] W.W. Hansen Experimental Physics Laboratory, Center for Space Science and Astrophysics, Stanford University, Stanford, CA 94305-4085, U.S.A.
[3] Teoretisk Astrofysik Center, Århus Universitet, DK-8000 Århus C, Denmark

Received October 17, 1997; accepted March 24, 1998

Abstract. In this article we present our state of the art of fitting helioseismic p-mode spectra. We give a step by step recipe for fitting the spectra: statistics of the spectra both for spatially unresolved and resolved data, the use of Maximum Likelihood estimates, the statistics of the p-mode parameters, the use of Monte-Carlo simulation and the significance of fitted parameters. The recipe is applied to synthetic low-resolution data, similar to those of the LOI, using Monte-Carlo simulations. For such spatially resolved data, the statistics of the Fourier spectrum is assumed to be a multi-normal distribution; the statistics of the power spectrum is *not* a χ^2 with 2 degrees of freedom. Results for $l = 1$ shows that all parameters describing the p modes can be obtained with negligible bias and with minimum variance provided that the leakage matrix is known. Systematic errors due to an imperfect knowledge of the leakage matrix are derived for all the p-mode parameters.

Key words: methods: analytical; data analysis; statistical — Sun: oscillations

1. Introduction

In the past decade, helioseismology has been able to provide the internal structure of the Sun and its dynamics. These inferences have been made possible by inverting the frequencies and rotational splitting of the pressure modes. The most commonly used technique for obtaining the p-mode parameters is to fit the p-mode spectra using Maximum Likelihood Estimators (MLE) assuming that the statistical distribution of the p modes in the power spectra is a χ^2 with 2 degrees of freedom (Woodard 1984). The MLE with this statistics were first applied on helioseismology data by Duvall & Harvey (1986) and Anderson et al. (1990). This technique is used for fitting spectra obtained with integrated sunlight instruments. For low- or high-resolution instruments, the (m, ν) power spectra are commonly fitted assuming that each m spectrum has the same statistics as the for the integrated sunlight instruments (LOI instrument: Appourchaux et al. 1995; Rabello-Soares et al. 1997; GONG instrument: Hill et al. 1996). Unfortunately, none of these implementations are correct since the assumed statistics is wrong. Only Schou (1992) described a more correct way of fitting (m, ν) diagrammes using *not* the power spectra but the complex Fourier spectra.

The pioneering work of Schou (1992) has inspired this series of 3 articles for addressing our state of the art of fitting (m, ν) diagrams. In this paper (Part I), we describe the statistics of the p modes, and how the MLE can be used in helioseismology. In Appourchaux et al. (1997) (hereafter Part II), we show how one can measure the mode leakage matrix and the noise correlation from the data which knowledge is required for using the Part I. In Appourchaux & Gizon (1998) (hereafter Part III), we will apply these techniques to the LOI instrument of VIRGO on board SOHO (For a description of the performance of the instrument see Appourchaux et al. 1997).

In this paper, we explain how the MLE can be used in helioseismology. In the first section, we recall the properties of MLE. In the second section, we describe the statistics of the p-mode Fourier spectra. In this section, we have generalized the approach of Schou (1992), to any complex leakage matrices. We have also used complex matrices to generate the covariance matrices of the p modes and of the noise. In the third section we show how to use Monte-Carlo simulations for testing both the use of MLE and the model of the p-mode spectra, and then conclude.

Send offprint requests to: thierrya@so.estec.esa.nl

2. Maximum likelihood estimators

Some of the properties of MLE were given by Toutain & Appourchaux (1994). We repeat them here for completeness. We also address 2 issues that were not covered in their paper: are MLE biased?, and how significant are the estimated parameters.

2.1. Fundamental properties

The aim of this section is to introduce some definitions and properties of MLE. A comprehensive study of this area of statistics can be found, e.g. in Kendall & Stuart (1967). Given a random variable x with a probability distribution $f(x, \boldsymbol{\lambda})$, where $\boldsymbol{\lambda}$ is a vector of p parameters. We define the logarithmic likelihood function ℓ of N independent measurements x_k of x as

$$\ln L = \ell = -\sum_{k=1}^{N} \ln f(x_k, \boldsymbol{\lambda}). \quad (1)$$

where L is the likelihood. The main property of ℓ is that the position of its minimum in the $\boldsymbol{\lambda}$-space gives an estimate of the most likely value of $\boldsymbol{\lambda}$, denoted hereafter as $\tilde{\boldsymbol{\lambda}}$. Hence $\tilde{\boldsymbol{\lambda}}$ is the solution of the set of p simultaneous equations:

$$\frac{\partial \ell}{\partial \lambda_i} = 0 \text{ with } i = 1, 2, ..., p. \quad (2)$$

Moreover, in the limit of very large sample ($N \to \infty$) this estimator $\tilde{\boldsymbol{\lambda}}$ tends to have a multi-normal probability distribution. In this case, this estimator is asymptotically unbiased with minimum variance; which implies its expectation and variance are respectively:

$$\lim_{N\to\infty} E(\tilde{\boldsymbol{\lambda}}) = \boldsymbol{\lambda}. \quad (3)$$

$$\lim_{N\to\infty} \sigma^2(\tilde{\boldsymbol{\lambda}}) = c_{ii} \quad (4)$$

where c_{ii} are the diagonal elements of the inverse of the Hessian matrix h, with elements:

$$h_{ij} = E(\frac{\partial^2 \ell}{\partial \lambda_i \partial \lambda_j}). \quad (5)$$

The covariances between any 2 components of $\tilde{\boldsymbol{\lambda}}$ are given by the corresponding off-diagonal elements of the inverse matrix. Equation (5) is used when computing the so-called formal error bars on $\tilde{\boldsymbol{\lambda}}$; as a matter of fact according to the Cramer-Rao theorem, Eq. (5) gives only a lower bound to the error bars (Kendall & Stuart 1967, reference therein). Toutain & Appourchaux (1994) showed that Eq. (5) is valid for most purpose in helioseismology.

2.2. Biased or unbiased?

The fact that MLE are asymptotically unbiased does not necessarily mean that this property is kept for a finite amount of data. As an example, it is well known that an estimator of the standard deviation (σ) of N measurement of a normally distributed random variable x is given by:

$$\sigma^2 = \frac{1}{N-1} \sum_{i=1}^{N} (x_i - \tilde{m})^2 \quad (6)$$

where x_i is the i-th measurement of the random variable x and $\tilde{m}$ is an estimate of the mean. It is well known that the σ of Eq. (6) is unbiased. In this case, MLE would give the following estimator:

$$\sigma^2_{\rm MLE} = \frac{N-1}{N} \sigma^2 \quad (7)$$

Clearly the MLE expression give a bias that vanish asymptotically for an infinite number of points. It is often difficult to derive explicit relation, similar to Eq. (7) between the estimator and the finite number of data points. When analytical expression can not be found, we advice to use Monte-Carlo simulations to verify the unbiasness; an example for $l = 1$ splittings is given in Chang (1996) and Appourchaux et al. (1997).

In any case MLE are intrinsically biased estimators because they are also minimum variance estimators (Kendall & Stuart 1967). It may be useful to find other estimators that do not bias the estimates (Quenouille 1956); they might not necessarily have minimum variance. These estimators are yet to be found.

2.3. Significance of fitted parameters

When one uses Least Square for fitting data, one can test the significance of its fitted parameters using the so-called R test (Frieden 1983). For MLE, a useful test can be used: the likelihood ratio test. It was first used by Appourchaux et al. (1994). This method requires to maximize the likelihood $e^{-\ell(\omega_p)}$ of a given event where p parameters are used to described the line profile. If one wants to describe the same event with n additional parameters, the likelihood $e^{-\ell(\Omega_{p+n})}$ will have to be maximized. The likelihood ratio test consists in making the ratio of the two likelihood (Brownlee 1965). Using the logarithmic likelihood, we can define the ratio Λ as:

$$\ln(\Lambda) = \ell(\Omega_{p+n}) - \ell(\omega_p). \quad (8)$$

If Λ is close to 1, it means that there is no improvement in the maximized likelihood and that the additional parameters are not significant. On the other hand, if $\Lambda \ll 1$, it means that $\ell(\Omega_{p+n}) \ll \ell(\omega_p)$ and that the additional parameters are very significant. In order to define a significance for the n additional parameters, we need to know the statistics of $\ln(\Lambda)$ under the null hypothesis, i.e. when the n additional parameters are not significant. For this null hypothesis, Wilks (1938) showed that for large sample size the distribution of $-2\ln\Lambda$ tends to the $\chi^2(n)$ distribution.

3. The statistics of p-mode spectra

3.1. Single mode

It is well known that p modes are stochastically excited oscillators (Kumar et al. 1988). The source of excitation lies in the many granules covering the Sun. The modes are assumed to be independently excited provided that their spatial scale is larger than the granule size (Chang 1996). From the equation of an oscillator, the statistics of the p-mode profile can be derived as:

$$\frac{\mathrm{d}^2x}{\mathrm{d}t^2} + 2\pi\gamma\frac{\mathrm{d}x}{\mathrm{d}t} + (2\pi)^2\nu_0^2 x = F(t) \tag{9}$$

where t is the time, x is the displacement, γ is the damping term or the linewidth, ν_0 is the frequency of the mode and $F(t)$ is the forcing function. From this equation the Fourier transform of x can be written as:

$$\tilde{x}(\nu) = \frac{\tilde{F}(\nu)}{(2\pi)^2(\nu_0^2 - \nu^2 + i\gamma\nu)} \tag{10}$$

where $\tilde{x}(\nu)$ and $\tilde{F}(\nu)$ are the Fourier transform of $x(t)$ and $F(t)$. From the large number of granules, it can be derived that the forcing function is normally distributed. Therefore the 2 components (the real and imaginary parts) of the Fourier transform of the forcing function are also normally distributed. For the p modes, each component of the Fourier transform is normally distributed with a mean of zero, and a variance given by:

$$\sigma^2(\nu) = \frac{1}{2}\frac{\sigma_{\tilde{F}}^2(\nu)}{(2\pi)^4[(\nu_0^2 - \nu^2)^2 + \nu^2\gamma^2]}. \tag{11}$$

The square of the modulus of $\tilde{x}(\nu)$, or power spectrum, has a χ^2 with 2 degree of freedom statistics and its mean is twice that of Eq. (11). This is the p-mode profile that is usually approximated by a Lorentzian profile. Similarly other effects such as asymmetry can be introduced in the profile of Eq. (11).

3.2. Unresolved observations

Instruments integrating over the solar surface the velocity or the intensity signal observe a superposition of various modes of different degrees. They are mainly sensitive to the low-degree modes ($l \leq 4$). For a given l, they detect a mixing of azimuthal order m for which a visibility is prescribed (Toutain & Gouttebroze 1994; Christensen-Dalsgaard & Gough 1982). Most often they can only detect modes for which $l+m$ is even. Since the Fourier components of the observed time series have a normal distribution, and since the different m are uncorrelated, the statistics of the power spectra of unresolved observation is a χ^2 with 2 degrees of freedom. Toutain & Appourchaux (1994) gave an analysis of the problem associated with these observations; we will not repeat it here.

3.3. Resolved observations

When the solar image is resolved many more degrees can be detected making the data analysis somewhat more complicated. In order to extract a single l, m mode from resolved observations, one has to apply a specific spatial filter or weight to the velocity or intensity images. Most often these weights are such that imperfect isolation of the l, m mode is achieved; especially because the most commonly used filters (spherical harmonics) are *not* orthogonal over half a sphere. This leads to the existence of other modes in the Fourier spectrum generated for a given l, m filter. Therefore, the observed Fourier spectrum is a linear combination of the modes to be detected. This linear combination of the modes can be understood as modes leaking into each other spectrum: this is represented by the so-called *leakage* matrix. These leakages will produce correlations between the different Fourier spectra. These correlations will modify the statistics of the Fourier spectra, such that their power spectra cannot be described as a χ^2 with 2 degrees of freedom. Therefore the statistics of the $2l+1$ power spectra of a given l cannot be derived from the product of $2l+1$ χ^2 with 2 degrees of freedom as in Appourchaux et al. (1995). Nevertheless, the real and imaginary parts of the Fourier spectra will still be normally distributed; in other words, the Fourier spectra have a *multi-normal distribution* defined by a covariance matrix. This fact will be used to derive the statistics of the observation. The covariance matrix is the sum of the noise and mode covariance matrices, which are not necessarily the same. Last but not least, the theoretical probability distribution has to be generated using the previous covariance matrix.

In summary, to understand the statistics of resolved observation, one has to follow four steps:

- Compute leakage matrices,
- Compute mode covariance matrices (related to the leakage),
- Compute noise covariance matrices,
- Generate the likelihood from the theoretical probability distribution.

Each step is described in detail hereafter.

3.3.1. Leakage matrices

Due to the spherical symmetry of the Sun, the most likely weights to be used to isolate the modes are the spherical harmonics $Y_{l,m}$. Here we generalize the approach to any weight $W_{l,m}$. The result is the observation of Fourier spectra $y_m^l(\nu)$ that are related to what we want to detect, i.e. the Fourier spectra of the individual Fourier spectrum $x_{m'}^{l'}(\nu)$, by the so-called leakage matrix (Schou 1992; Schou & Brown 1994). The following expression can be derived for as many different degrees as needed; for simplicity we wrote it for 2 different degrees l, l' as:

$$\boldsymbol{y} = \mathcal{C}^{(l,l')}\boldsymbol{x} \tag{12}$$

where $\boldsymbol{x}(\nu)$ and $\boldsymbol{y}(\nu)$ are 2 complex vectors made each of $2l+2l'+2$ component: $2l+1$ components for l, $2l'+1$ components for l' and $\mathcal{C}^{(l,l')}$ is the leakage matrix of both l and l'. The dimension of $\mathcal{C}^{(l,l')}$ is $(2l+2l'+2)\times(2l+2l'+2)$. The coefficient of the leakage matrix can be computed as:

$$\mathcal{C}^{(l,l')}_{m,m'} = \frac{b^{(l,l')}_{m,m'}}{b^{(l',l')}_{m',m'}} \tag{13}$$

with:

$$b^{(l,l')}_{m,m'} = \int_{\mathcal{D}} \frac{W^*_{l,m}(\theta,\phi)}{n_{l,m}} \tilde{Y}_{l',m'}(\theta,\phi) A(\theta,\phi) \sin\theta \mathrm{d}\theta\mathrm{d}\phi \tag{14}$$

where $m=-l,\ldots,l$, $m'=-l',\ldots,l'$, $*$ denotes the complex conjugate, θ, ϕ are the angles in a spherical coordinate system, $\mathcal{D}$ is the integration domain, $\tilde{Y}_{l',m'}$ is the generalized velocity or intensity perturbation of the mode (l',m'). The $\tilde{Y}_{l',m'}$ are not necessarily the usual spherical harmonics $Y_{l',m'}$. For instance, the horizontal component of the velocity perturbation, and the intensity perturbation due the distortion of the the surface by the modes are both expressed as derivative of spherical harmonics. $A(\theta,\phi)$ is an apodization function, $n_{l,m}$ is a sensitivity correction factor associated with $W_{l,m}$. The ratio ensures that $\mathcal{C}^{(l,l)}_{m,m}=1$. The apodization function A is the product of 3 different function as:

$$A(\theta,\phi) = A_{\mathrm{n}}(\theta,\phi) A_{\mathrm{d}}(\theta,\phi) A_{\mathrm{a}}(\theta,\phi) \tag{15}$$

A_{n} is the natural apodization function due to the way the images are obtained: for intensity this is the limb darkening ($I(\mu)$), and for velocity the projection factor ($\mu=\sin\theta\cos\phi$). A_{d} is the data analysis apodization: for data re-mapped on the Sun's surface it is unity; for no re-mapping, it is the projection factor ($\mu=\sin\theta\cos\phi$). A_{a} is the artificial apodization that can take into account the non-linear velocity (or intensity) response of the instrument over the solar disk, or can help to reduce limb effects. Here we must point out that the leakage matrix has a useful property such as:

$$\mathcal{C}^{(l,l')}_{m,m'} = \mathcal{C}^{(l',l)*}_{m',m} \frac{b^{(l,l)*}_{m,m}}{b^{(l',l')}_{m',m'}} \frac{b^{(l,l')}_{m,m'}}{b^{(l',l)*}_{m',m}}. \tag{16}$$

It shows that $\mathcal{C}^{(l,l')}$ is in general *not* hermitian nor symmetrical. Nevertheless, when $W_{l,m}=\tilde{Y}_{l,m}$, it is possible with a proper sensitivity factor correction of $W_{l,m}$ to have such a property. In this case the sensitivity correction is given by:

$$n_{l,m} = \sqrt{\int_{\mathcal{D}} \tilde{Y}^*_{l,m}(\theta,\phi) \tilde{Y}_{l,m}(\theta,\phi) A(\theta,\phi) \sin\theta \mathrm{d}\theta\mathrm{d}\phi} \tag{17}$$

which is the "natural" normalization factor of the perturbation $\tilde{Y}_{l,m}$. Of course in this latter case, we have:

$$\mathcal{C}^{(l,l')}_{m,m'} = \mathcal{C}^{(l',l)*}_{m',m}. \tag{18}$$

Unfortunately, the leakage matrix does not always have such a nice property, especially because $W_{l,m}\neq\tilde{Y}_{l,m}$. This was the case for the ground-based Luminosity Oscillations Imager (LOI) (Appourchaux et al. 1994) and for the GONG instrument (Hill 1997, private communication). In both cases, this is *not* produced by the observation techniques but by the data analysis techniques.

If the weight functions $W_{l,m}$ and the observed perturbations $\tilde{Y}_{l,m}$ have the same symmetry properties as the spherical harmonics $Y_{l,m}$ (or if $W_{l,m}=\tilde{Y}_{l,m}=Y_{l,m}$), the leakage matrix is real as shown by Schou (1992). In addition the leakage elements of $\mathcal{C}^{(l,l')}_{m,m'}$ are zero if $l+m+l'+m'$ is odd; this is the case when the Sun is *not* tilted with respect to the observer's axis of reference ($P=0$, $B=0$). If the axes of reference of $W_{l,m}$ differ from that of the $Y_{l,m}$ these 2 properties can be lost. For instance, an incorrect orientation of the Sun axis with respect to the detector axis could lead to a complex leakage matrix; or a Sun seen at an angle $B\neq 0$ give a real leakage matrix with non-zero elements with $l+m+l'+m'$ odd. This latter property has been used by Gizon et al. (1997) to infer the inclination of the Sun's core.

Equation (13) is valid when the size of the pixel is small compared with the spatial scale of the degree. When the pixels are larger, one should write the following:

$$\mathcal{C}^{(l,l')}_{m,m'} = \frac{n_{l',m'}}{n_{l,m}} \frac{\sum_i w_i^{(l,m)*} \tilde{y}_i^{(l',m')}}{\sum_i w_i^{(l',m')*} \tilde{y}_i^{(l',m')}} \tag{19}$$

where the $\tilde{y}_i$ are given by:

$$\tilde{y}_i^{(l',m')} = \int_{\mathcal{D}_i} \tilde{Y}^{m'}_{l'}(\theta,\phi) A(\theta,\phi) \sin\theta \mathrm{d}\theta\mathrm{d}\phi \tag{20}$$

where $\mathcal{D}_i$ is the area defined by the i-th pixel and $w_i^{(l,m)}$ is the weight applied to the i-th pixel to extract the l,m mode. Equation (19) is the more general form used for the LOI (Appourchaux & Andersen 1990). As a starting point, the $w_i^{(l,m)}$ can also be taken as the $\tilde{y}_i^{(l,m)}$.

3.3.2. p-mode covariance matrix

To compute the covariance of the complex vector $\boldsymbol{y}(\nu)$ as a real number we form the vector $\boldsymbol{z}_{\boldsymbol{y}}(\nu)$ defined as:

$$\boldsymbol{z}^{\mathrm{T}}_{\boldsymbol{y}}(\nu) = (\mathrm{Re}(\boldsymbol{y}^{\mathrm{T}}), \mathrm{Im}(\boldsymbol{y}^{\mathrm{T}})).$$

In absence of noise, the covariance matrix $\mathsf{M}(\nu)$ of the vector $\boldsymbol{z}_{\boldsymbol{y}}(\nu)$ can be generated using a complex notation:

$$\mathsf{M}^{(l,l')}(\nu) = \begin{pmatrix} \mathcal{M}_r(\nu) & \mathcal{M}_i(\nu) \\ -\mathcal{M}_i(\nu) & \mathcal{M}_r(\nu) \end{pmatrix}. \tag{21}$$

$\mathsf{M}^{(l,l')}$ is a super matrix where $\mathcal{M}_r(\nu)$ and $\mathcal{M}_i(\nu)$ are the real and imaginary parts of a complex matrix $\mathcal{M}^{(l,l')}$ which elements are given by:

$$\mathcal{M}^{(l,l')}_{m,m'}(\nu) = \sum_{l''=l,l'} \sum_{m''=-l''}^{l''} \mathcal{C}^{(l'',l')}_{m'',m'} \mathcal{C}^{(l'',l)*}_{m'',m} f^{l''}_{m''}(\nu) \tag{22}$$

where $f^{l''}_{m''}(\nu)$ is the variance of the l'',m'' mode which profile is given by Eq. (11), in which ν_0 is a function of m.

The real and imaginary parts of Eq. (22) will give respectively the covariance of the real (or imaginary) part of $\boldsymbol{y}$, and the covariance between the real and imaginary part of $\boldsymbol{y}$. It is obvious from Eq. (22) that $\mathcal{M}^{(l,l')}$ is hermitian.

Schou (1992) gave an equation similar to Eq. (22) for a real leakage matrix and for a single degree. Here we add a subtlety to the formulation of Schou (1992), the matrix $\mathsf{M}^{(l,l')}(\nu)$ can be decomposed as follows:

$$\mathsf{M}^{(l,l')}(\nu) = \begin{pmatrix} \mathsf{v}(\nu) & \mathsf{w}(\nu) \\ -\mathsf{w}(\nu) & \mathsf{v}(\nu) \end{pmatrix} \begin{pmatrix} \mathsf{v}^{\mathrm{T}}(\nu) & -\mathsf{w}^{\mathrm{T}}(\nu) \\ \mathsf{w}^{\mathrm{T}}(\nu) & \mathsf{v}^{\mathrm{T}}(\nu) \end{pmatrix} \tag{23}$$

where T is the transpose of a matrix. The elements of v and w are given by:

$$\mathsf{v}^{(l,l')}_{m,m'}(\nu) = \sqrt{f^l_m(\nu)}\mathrm{Re}(\mathcal{C}^{(l,l')}_{m,m'}) \tag{24}$$

$$\mathsf{w}^{(l,l')}_{m,m'}(\nu) = \sqrt{f^l_m(\nu)}\mathrm{Im}(\mathcal{C}^{(l,l')}_{m,m'}). \tag{25}$$

We will see later on that this decomposition is of prime importance for understanding the statistics of the observation.

3.3.3. Noise covariance matrix

Unfortunately, the observed vector $\boldsymbol{y}(\nu)$ include a noise contribution. Due to the way the data are combined, the noises between the different $2l+2l'+2$ components of this vector are also correlated. Schou (1992) gave the correlation matrix when the filter used are spherical harmonics $Y_{l,m}$. A more general formulation can be written as:

$$\mathsf{B}^{(l,l')}(\nu) = \begin{pmatrix} \mathcal{B}_r(\nu) & \mathcal{B}_i(\nu) \\ -\mathcal{B}_i(\nu) & \mathcal{B}_r(\nu) \end{pmatrix} \tag{26}$$

$\mathsf{B}^{(l,l')}$ is a super matrix where $\mathcal{B}_r(\nu)$ and $\mathcal{B}_i(\nu)$ are the real and imaginary parts of the complex matrix $\mathcal{B}^{(l,l')}$. The dimension of $\mathcal{B}^{(l,l')}$ is $(2l+2l'+2)\times(2l+2l'+2)$. Its elements are given by:

$$\mathcal{B}^{(l,l')}_{m,m'} = \int_{\mathcal{D}} \frac{W^*_{l,m}(\theta,\phi)}{n_{l,m}} \frac{W_{l',m'}(\theta,\phi)}{n_{l',m'}} a(\theta,\phi)\sin\theta \mathrm{d}\theta\mathrm{d}\phi \tag{27}$$

with

$$a(\theta,\phi,\nu) = A^2_{\mathrm{a}}(\theta,\phi)A^2_{\mathrm{d}}(\theta,\phi)\sigma^2_{\odot}(\theta,\phi,\nu) \tag{28}$$

where a is an apodization function which characterizes through $\sigma^2_{\odot}(\theta,\phi,\nu)$ how the noise varies over the solar image, assuming that the noise is uncorrelated between different points on the Sun; A_{a}, A_{d} are defined in Eq. (15). When the instrumental noise is low, a is derived from the characteristics of the solar noise. The evaluation of $\mathcal{B}^{(l,l')}$ is less straightforward than that of $\mathcal{C}^{(l,l')}$ because we need to know a model of the solar noise. An easier way to understand the noise correlation is to built the ratio covariance matrix or "pseudo" noise leakage matrix $\mathcal{R}$ as:

$$\mathcal{R}^{(l,l')}_{m,m'} = \frac{\mathcal{B}^{(l,l')}_{m,m'}}{\mathcal{B}^{(l',l')}_{m',m'}}. \tag{29}$$

Here we can see the similarity between $\mathcal{R}$ and $\mathcal{C}$. In velocity, the granulation noise is rather low at the center of the disk and then increases towards the limb; the meso- and super-granulation exhibits somewhat different or complementary center-to-limb variations. In intensity, the granulation noise is a function of the number of granules; the noise is larger at the center of the disk and decreases slowly towards the limb. In addition the solar noise in intensity has no contribution from mesogranulation (Fröhlich et al. 1997), making the spatial dependence of the noise almost independent of frequency across the p-mode range. This is not the case in velocity where mesogranulation still contributes to the noise in the p-mode range. Therefore in intensity the apodization a is closer to A than in velocity, making the ratio covariance matrix $\mathcal{R}^{(l,l')}$ very close to the leakage matrix $\mathcal{C}^{(l,l')}$. Although $\mathcal{R}^{(l,l')}$ is not mathematically useful, it is a matrix easy to visualize and understand (See Part II). The ratio matrix has some properties of the leakage matrix like being not necessarily hermitian. This is not the case of $\mathcal{B}^{(l,l')}$ which is hermitian by definition.

Again, when the size of the pixel is large compared with the spatial scale of the degree, Eq. (27) is rewritten as follows:

$$\mathcal{B}^{(l,l')}_{m,m'}(\nu) = \sum_i w^{*(l,m)}_i w^{(l',m')}_i b_i(\nu) \tag{30}$$

where b_i is the variance of the noise of pixel i. Equation (30) is the more general form used for the LOI.

3.3.4. Probability density of the observation and likelihood

The statistical distribution of the Fourier spectra or of the vector $\boldsymbol{z_y}$ is a multi-normal distribution. The probability density is given by:

$$p_{\boldsymbol{y}}(\nu) = \frac{\mathrm{e}^{-\frac{1}{2}\boldsymbol{z}^{\mathrm{T}}_{\boldsymbol{y}}(\nu)\mathsf{V}^{-1}(\nu)\boldsymbol{z}_{\boldsymbol{y}}(\nu)}}{(2\pi)^{d/2}\sqrt{|\mathsf{V}(\nu)|}} \tag{31}$$

where d is the number of elements of $\boldsymbol{z_y}$, V is a short notation for the following matrix: $\mathsf{V}^{(l,l')}(\nu) = \mathsf{M}^{(l,l')}(\nu) + \mathsf{B}^{(l,l')}(\nu)$; this is the matrix given by the sum of the p-mode and noise covariance matrix; the p modes and the noises are assumed to be independent of each other. The matrix $\mathsf{V}^{(l,l')}(\nu)$ can also be built from sub-matrices as: $\mathcal{V}^{(l,l')} = \mathcal{M}^{(l,l')} + \mathcal{B}^{(l,l')}$; as a result $\mathcal{V}^{(l,l')}$ is also hermitian. Equation (31) is the most general formulation for any multi-normal distribution with a given covariance matrix V (Kendall & Stuart 1967).

Using Eq. (31), we can write the likelihood L of an observation of $\boldsymbol{z_y}(\nu_i)$ at N different frequencies ν_i as given by:

$$L^{(l,l')}_{\boldsymbol{y}} = \prod_{i=1}^{N} \frac{\mathrm{e}^{-\frac{1}{2}\boldsymbol{z}^{\mathrm{T}}_{\boldsymbol{y}}(\nu_i)\mathsf{V}^{-1}(\nu_i)\boldsymbol{z}_{\boldsymbol{y}}(\nu_i)}}{(2\pi)^{d/2}\sqrt{|\mathsf{V}(\nu_i)|}}. \tag{32}$$

We assumed that the frequency bins are independent of each other. This is the case when the data have no gaps. For unresolved observation having gap, the expression of

the likelihood becomes extremely complicated as shown by Gabriel (1994). For resolved observation having gaps, as for the LOWL data of Tomczyk et al. (1995), it is impracticable to use the full formulation of the likelihood: Tomczyk et al. (1995) used Eq. (32) as an approximation for fitting the LOWL data.

In principle, given the observed vector $\boldsymbol{y}$, it is always possible in the absence of noise to recover the vector $\boldsymbol{x}$. Due to the presence of noise only a solution close to the ideal one can be found that will minimize the correlation between the components. Provided that the leakage matrix can be inverted, we have by analogy to Eq. (12):

$$\tilde{\boldsymbol{x}} = \mathcal{C}^{-1}\boldsymbol{y} \tag{33}$$

where $\mathcal{C} = \mathcal{C}^{(l,l')}$. Then we can write a similar equation for $\boldsymbol{z_y}$ and $\boldsymbol{z_{\tilde{x}}}$ as:

$$\boldsymbol{z_{\tilde{x}}} = \mathsf{C}^{-1}\boldsymbol{z_y} \tag{34}$$

where C is defined as:

$$\mathsf{C}^{(l,l')}(\nu) = \begin{pmatrix} \mathcal{C}_r(\nu) & \mathcal{C}_i(\nu) \\ -\mathcal{C}_i(\nu) & \mathcal{C}_r(\nu) \end{pmatrix} \tag{35}$$

$\mathsf{C}^{(l,l')}$ is a super matrix where $\mathcal{C}_r$ and $\mathcal{C}_i$ are the real and imaginary parts of the complex matrix $\mathcal{C}^{(l,l')}$. Using Eq. (34) to replace $\boldsymbol{z_y}$ by $\boldsymbol{z_{\tilde{x}}}$ in Eq. (32) we can rewrite this latter as:

$$L^{(l,l')}_{\boldsymbol{y}} = \prod_{i=1}^{N} \frac{\mathrm{e}^{-\frac{1}{2}\boldsymbol{z}^{\mathrm{T}}_{\tilde{\boldsymbol{x}}}(\nu_i)\mathsf{V}'^{-1}(\nu_i)\boldsymbol{z}_{\tilde{\boldsymbol{x}}}(\nu_i)}}{(2\pi)^{d/2}\sqrt{|\mathsf{V}'(\nu_i)|}} \frac{1}{|\mathsf{C}|} = \frac{1}{|\mathsf{C}|^N} L^{(l,l')}_{\tilde{\boldsymbol{x}}} \tag{36}$$

with V' given by:

$$\mathsf{V}' = \mathsf{C}^{-1}\mathsf{V}\mathsf{C}^{\mathrm{T}^{-1}} = \mathsf{C}^{-1}\mathsf{M}^{(l,l')}\mathsf{C}^{\mathrm{T}^{-1}} + \mathsf{C}^{-1}\mathsf{B}^{(l,l')}\mathsf{C}^{\mathrm{T}^{-1}}. \tag{37}$$

We recognize in Eq. (36) the probability density of the vector $\boldsymbol{z_{\tilde{x}}}(\nu)$ to a constant (i.e. $|\mathsf{C}|^{-N}$). As a matter of fact, it is well known that using a linear transformation similar to that of Eq. (34) will produce the new covariance matrix V' of $\boldsymbol{z_{\tilde{x}}}$ as written in Eq. (37) (Davenport & Root 1958). It can be easily shown using Eqs. (23) and (37) that the matrix $\mathsf{D}(\nu) = \mathsf{C}^{-1}\mathsf{M}^{(l,l')}\mathsf{C}^{\mathrm{T}^{-1}}$ is diagonal and its element are given by:

$$\mathsf{D}_{m'',m''}(\nu) = f^{l''}_{m''}(\nu) \tag{38}$$

where $l'' = l$ or l' and $m'' = -l'', \ldots, l''$. Therefore Eq. (37) is the sum of a diagonal matrix representing the correlation between the p modes; and of a new noise covariance matrix representing the correlation of the components of the vector $\tilde{\boldsymbol{x}}$ after the transformation of Eq. (33). It means that $\tilde{\boldsymbol{x}}$ has no correlation due to the p modes as we could expect from Eq. (33): the leakage matrix of $\tilde{\boldsymbol{x}}$ is the identity matrix. In summary, *there is no gain in fitting data for which the leakage matrix is the identity matrix: the 2 approaches are identical.* The main problem is really to know the leakage matrices, not only theoretically but also experimentally: this is the subject of the Part II.

It can be derived from Eq. (37) that it is also possible to remove correlation due to the noise by replacing C by a proper matrix associated with $\mathsf{B}^{(l,l')}$. The derivation of this matrix is given in Appendix A.

3.3.5. The use of the likelihood in practice

When a single degree is observed, it is quite simple to maximize the likelihood of Eq. (32) using $\boldsymbol{y}$, or using $\tilde{\boldsymbol{x}}$ as in Eq. (36). For low degree and low frequency modes, this is possible for $l = 0, 2, 3$. As soon as the mode linewidth increases, at high frequencies, the assumption of a single degree is not valid anymore. For example, $l = 0$ and $l = 1$ overlap with $l = 2$ and $l = 3$, respectively. At high frequencies, the effect of the aliasing degree should be taken into account.

For the other low degree modes, the likelihood becomes somewhat more complicated. It is well known, that in the (m, ν) diagramme of $l = 1$, there are leaks coming from other degrees. The $l = 6$ and $l = 9$ modes overlap with the $l = 1$, while the $l = 3$ modes overlap only at higher frequencies when the linewidth is larger than about 5 μHz. In the (m, ν) diagramme of $l = 4$, there are leaks of $l = 7$ and vice versa (Appourchaux et al. 1997). The leaks have severe effects on determination of the p-mode parameters of the $l = 1$. When many degrees are overlapping, one should use Eq. (32) using the covariance matrix for l and l'. Nevertheless, we do not advice to do so for fitting the p modes; it has some severe computer speed penalty. Instead we advice to clean the data by inverting the full leakage matrix taking into account the effects of the various degrees on each other, in a similar way to Eq. (33). For example for $l = 1$, one should compute the leakage matrix on a sub-space of degrees namely for $l = 1$, 6 and 9. These 3 degrees interact strongly in the Fourier spectra. For $l = 4$ and $l = 5$ one should compute the leakage matrix on sub-spaces for $l = 4$ and 7, and for $l = 5$ and 8. The advantage of this direct cleaning is to replace the original aliasing degrees by new aliasing degrees which are further away, in frequency, from the modes to be fitted. This technique has been applied to the LOI and GONG data, and is developed in Part II.

Last but not least, when the signal-to-noise ratio is high (i.e. we neglect $\mathsf{B}^{(l,l')}$ in Eq. (37)), the elements of the vector $\boldsymbol{z_{\tilde{x}}}(\nu)$ are all independent of each other, leading to a statistical distribution which is a product of χ^2 with 2 degree of freedom. This is an approximation which is useful and less incorrect that using this statistics for the GONG data for the vector $\boldsymbol{z_y}(\nu)$ as in Hill et al. (1996).

4. Monte-Carlo simulations

4.1. Why are they needed?

Before applying Eq. (32) to real data, it is always advisable to test the power of MLE on synthetic data, i.e. performing Monte-Carlo simulations. They are not merely for playing games; these simulations are real tools for understanding what we fit and how we fit it. Assuming that the statistics of the real solar spectra is known, performing Monte-Carlo is useful for the following reasons:

- Assessing the model of the mode and noise covariance
- Assessing the statistical distribution of the parameters
- Assessing the precision of parameters.

First, the model of the covariances can be imperfect. The effect of an imperfect knowledge of the covariance can help us understand how these will influence the determination of the parameters, i.e. deriving the sensitivity of the systematic errors to this imperfect knowledge. Second, the parameters derived by the MLE should have the desirable properties of having a normal distribution; if not we advise to apply a change of fitted parameters. For example, as we will see later on, we do not fit the linewidth itself but the log of the linewidth. A normal distribution is necessary to derive meaningful error bars, this is the assumption behind Eq. (5). Third, in order to be able to derive a good estimate of the error bars using one realization, the standard deviation of a large sample of fitted parameters should be equal to the mean of formal errors return by the fit (See Eq. (4)).

4.2. Generation of synthetic data for the LOI

The performance of this instrument has been described in Appourchaux et al. (1997). Briefly, it is a small instrument made of 12 pixels for detecting solar intensity fluctuations. The p-mode signals were generated in the Fourier spectra by using the following:

$$\boldsymbol{y}(\nu) = \mathcal{C}^{(l,l)}\boldsymbol{x}(\nu) + \sum_{i=1}^{N_{\rm pix}} \tilde{\boldsymbol{y}}_i^l p_i \tag{39}$$

where $\boldsymbol{y}$ is the observed vector of $2l+1$ Fourier spectra, $\mathcal{C}^{(l,l)}$ is the leakage matrix given by Eq. (19), $\boldsymbol{x}$ is a complex random vector with $2l+1$ components (each component represents the signal of an l,m mode, with uncorrelated real and imaginary part), $\tilde{\boldsymbol{y}}_i^l$ are computed as in Eq. (20) using spherical harmonics, and p_i is the noise for a given pixel i. The variance of the real or imaginary part of the m-th component of $\boldsymbol{x}$ is given by $f_m^l(\nu)$; the mean of $\boldsymbol{x}$ is 0. The function $f_m^l(\nu)$ describes the profile of each m which is displaced from m by an amount which is given by:

$$\nu_m = \nu_0 + l\sum_{i=1}^{5} a_i \mathcal{P}_i^{(l)}(m/l) \tag{40}$$

where the $\mathcal{P}_i^{(l)}$ are derived from the Clebsch-Gordan coefficients, the expression of which can be found in Ritzwoller & Lavelly (1991); they are normalized such that $\mathcal{P}_i^{(l)}(1) = 1$. Here we assumed a common linewidth for the l,n mode, and different amplitudes for the $2l+1$ components. The profile are symmetrical in the shape of a lorentzian.

The variance of the pixel noise is assumed to be the same for the pixels with the same shape. The mean of the pixel noise is 0. For the LOI with its 12 pixels, there are 3 different shapes giving 3 independent noises.

After generating the synthetic signals according to Eq. (39), the data are fitted by minimizing the likelihood of Eq. (32). Figure 1 shows an example of Fourier spectra generated synthetically. The typical signal-to-noise ratio in the power spectra is about 20-30. The frequency resolution is equivalent to 4 months of data. We performed 1000 simulations of the spectra.

4.3. Results

4.3.1. For the nominal leakage matrix

The data are fitted assuming a perfect knowledge of the leakage and noise covariance matrices, i.e. we know what we fit. Figure 2 shows the distribution of the fitted parameters: the central frequency, splitting, log(linewidth), $3\times$ log(amplitude), $3\times$ log(pixel noise). For the last 7 parameters, we fit the log of the parameter because this transformation give a statistical distribution closer to a normal distribution (or log-normal distribution). It can be observed that the parameters derived are in most cases unbiased. Figure 3 shows the distribution of the error bars returned by the fit. In most case the mean of the error bars (returned by the fit) is not very different from the 1-σ deviation of the parameter distribution. Similar simulations have been performed for various degree (up $l=3$). They show the same typical results as for Figs. 2 and 3, i.e. the fitted parameters are not, or weakly, biased, and the error bars returned by the fit give a good estimate of the real error bars.

4.3.2. Influence of a wrong leakage matrix

As was shown by Eq. (36), fitting p-mode spectra for which the leakage matrix is explicitly diagonal is equivalent to fitting p-mode spectra for which the matrix is *not* diagonal. Of course, it is always possible to construct data with a purely diagonal leakage matrix using Eq. (33), but we do so assuming that we know the leakage matrix $\mathcal{C}$. As a matter of fact, what matters is not to have the identity matrix as leakage matrix, but more the knowledge of the latter.

Hereafter, we have investigated the influence of a wrongly assumed leakage matrix on the fitted parameters of $l=1$. We made 100 realizations and change the leakage parameter between $m=-1$ and $m=+1$ by $\pm 50\%$ from a nominal value for the LOI of 0.45. Figure 4 shows the influence of varying the assumed leakage element on the fitted parameters. It is quite interesting to note that the inferred central frequency is insensitive to mistakes in the leakage matrix. The linewidth becomes underestimated when the error is larger than 20%, while the amplitudes become overestimated. The most important result is the fact that the systematic error made on the splitting is not linear but quadratic. This systematic error can become as large

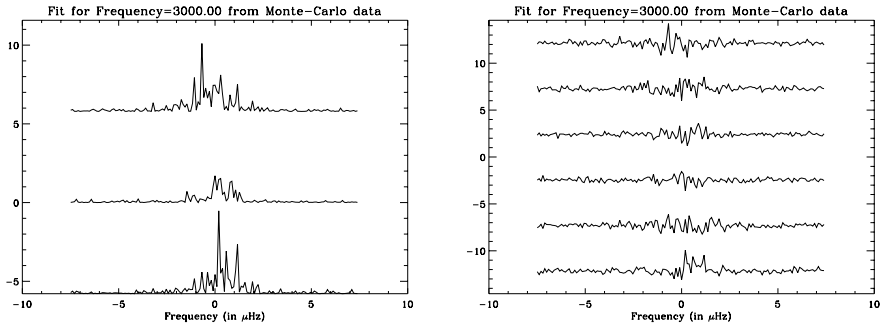

Fig. 1. (Left) Power spectra of a synthetic $l = 1$ as it would be observed by the LOI. The frequency resolution corresponds to 4 months of data. The signal-to-noise ratio is about 20-30. The traces from bottom to top corresponds to $m = -1$, 0, $+1$. (Right) Fourier spectra for $l = 1$ (same data). The first, third and fifth traces from the bottom represents the real part of the spectrum of $m = -1, 0$ and 1, respectively; the other traces are the imaginary parts. The leakage between $m = -1$ and $m = +1$ is 0.45 in the Fourier spectra

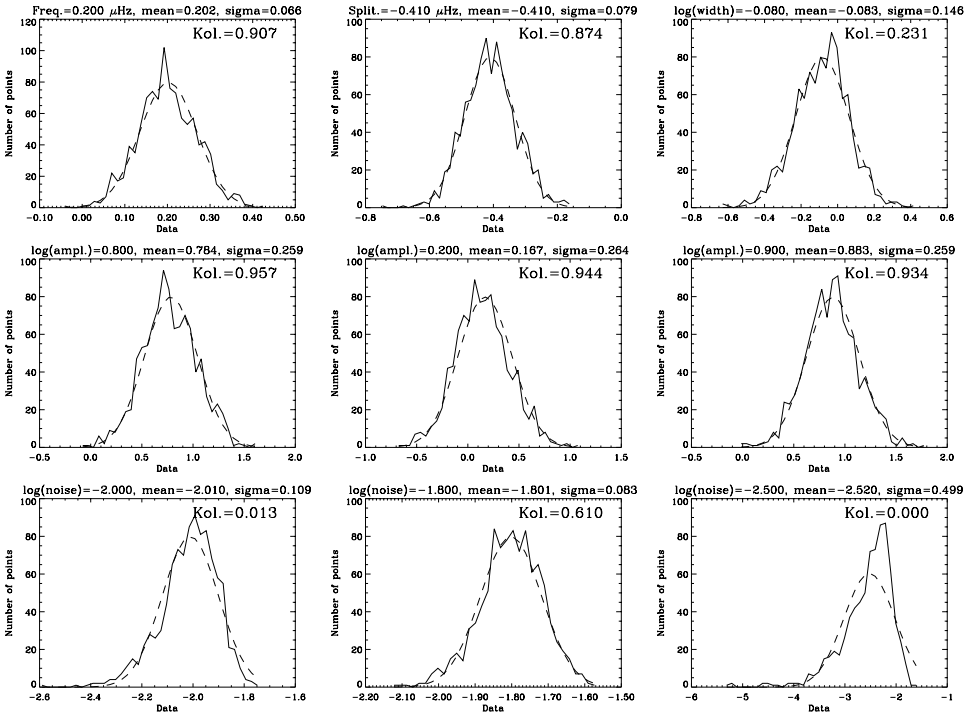

Fig. 2. Histograms for the fitted parameters: (Plain line) Data, (Dashed line) Normal distribution with the same mean and σ as the fitted parameters. (Top) Frequency (in μHz), splitting a_1 (in μHz), $\log(\gamma)$ (γ in μHz); (Middle) log(Amplitude) for $m = -1$, 0, 1; (Bottom) log(pixel noise). For each histogram, the target value, the mean fitted value and the 1-σ fitted valued are displayed. The Kolmogorov-Smirnov test (Kol.) is displayed for each histogram; a number close to 0 show that the distribution is not normal

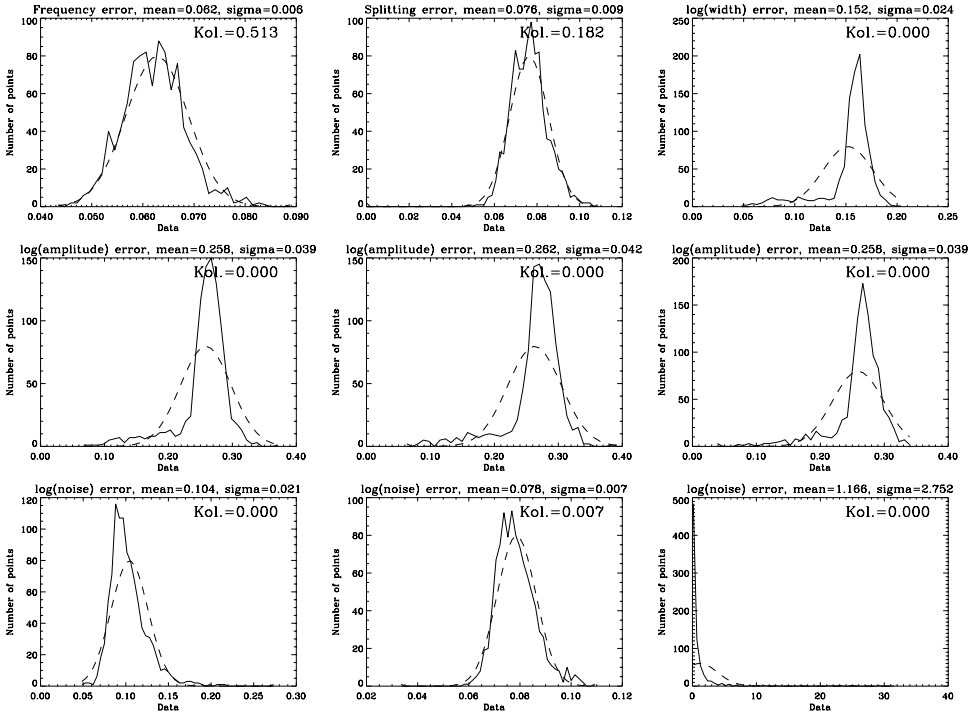

Fig. 3. Histograms for the error bars: (Plain line) Data, (Dashed line) Normal distribution with the same mean and σ. (Top) Frequency error (in μHz), splitting a_1 error (in μHz), $\log(\gamma)$ error (γ in μHz); (Middle) log(Amplitude) error for $m = -1$, 0, 1; (Bottom) log(pixel noise) error. For each histogram, the target value, the mean fitted value and the 1-σ fitted valued are displayed. The Kolmogorov-Smirnov test is displayed for each histogram; a number close to 0 show that the distribution is not normal

as the error bars. For example, with 1 year of LOI data and averaging over 10 modes, the error bars on the mean splitting is about 15 nHz; this should be compared to a systematic error of 10 nHz for an error of 10% of the $l = 1$ leakage elements.

Another test similar to that of the $l = 1$ was performed with the $l = 2$ mode. We have assumed that all the off-diagonal elements of the leakage matrix were wrong by the same fixed amount. Figure 5 shows the results only for the splitting coefficients (from a_1 to a_4). The other parameters linewidth, amplitudes and noises behave in the same manner as for $l = 1$. The systematic error on the splitting has also the same quadratic dependence as for $l = 1$. For $l = 2$ the splitting error bars are typically $\sqrt{5}$ smaller than for $l = 1$. In this case the systematic errors become larger than the error bars, and therefore start to influence the inverted solar rotation.

It means that it is quite easy to underestimate the splitting whenever we under- or overestimate the leakage element. As a matter of fact, this behaviour was also found in the GONG data for $l = 1$ and 2 (Rabello-Soares & Appourchaux 1998, in preparation). On the other hand, errors in the leakage matrix will not result in overestimating the splitting. If the splitting is overestimated, the most likely source should be the presence of other degrees not taken into account in the analysis.

We also checked the correlation of the splitting coefficients derived for $l = 2$. Figures 6 and 7 show respectively the variance and the covariance of the splitting coefficients as a function of the leakage elements error. It can be concluded that the splitting coefficients become correlated only when a large overestimation of about 50% is made for the off-diagonal leakage elements. This result is only valid when fitting Fourier spectra. For other methods, such as fitting power spectra, possible correlation amongst the splitting coefficients could have drastic consequences for the inverted solar rotation profiles.

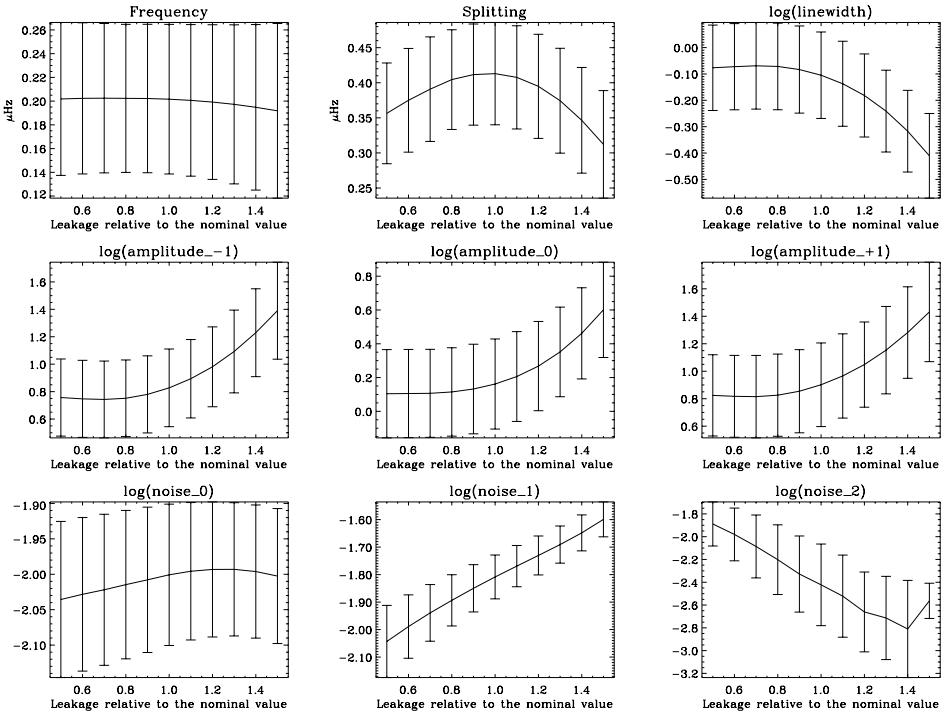

Fig. 4. Influence of the fitted parameters to relative changes of the assumed leakage element between $m = -1$ and $m = +1$ for $l = 1$. (Top) Frequency, splitting a_1, $\log(\gamma)$; (Middle) log(Amplitude) for $m = -1$, 0, 1; (Bottom) log(pixel noise). The target parameters are the same as for Fig. 2. Please note the parabolic shape for the splitting

4.3.3. Comparison with other methods

We have also performed Monte-Carlo simulations to compare the different fitting techniques commonly used. For each simulation of a mode, the data were fitted in 3 different ways:

- Assuming that the $2l + 1$ power spectra are independent of each other and are not influenced by m leaks, i.e. a single mode is present for a given m. This is the way the GONG data are commonly fitted.
- Assuming that the $2l + 1$ power spectra are independent of each other but are influenced by m leaks, i.e. we use only the diagonal of the mode covariance matrix. This is the way the LOI data were fitted by Appourchaux et al. (1995).
- Assuming that the $2l + 1$ Fourier spectra are dependent of each other and are influenced by m leaks. This is the way described in this paper after the work of Schou (1992).

Figure 8 shows the results of this comparison only for the splitting which is the parameter the most sensitive to the fitting way. The splittings derived by the GONG fitting way are obviously underestimated. This underestimation will eventually disappear with the degree but for $l = 1$ the bias is unacceptable. The splittings derived using the old LOI way are slightly overestimated with a bias of about 10 nHz for $l = 1$. Although this bias is not substantial for the LOI data, it can be of the same order of magnitude as the error bars for instrument with better signal-to-noise ratio than used in the simulations, such as GONG, and for observation time longer than these simulations. Last but not least, the Fourier spectra fitted according to the guidelines given in this paper provides a splitting without substantial bias and also with smaller error bars. This latter way of fitting will considerably improve the consistency of the splittings measured.

5. Conclusion

We have given a step by step recipe for fitting (m, ν) Fourier spectra. If one wants to implement similar fitting technique, one should compute, first the

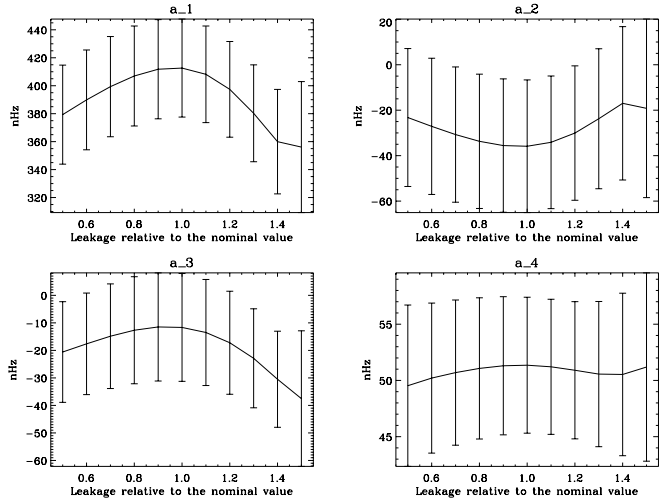

Fig. 5. Influence of the fitted splitting parameters to relative changes of the assumed of the assumed off-diagonal leakage element for $l = 2$. (Top, left) a_1, target value: 410 nHz; (Top, right) a_2, target value: -30 nHz; (Bottom, left) a_3, target value: -10 nHz; (Bottom, right) a_4, target value: $+50$ nHz

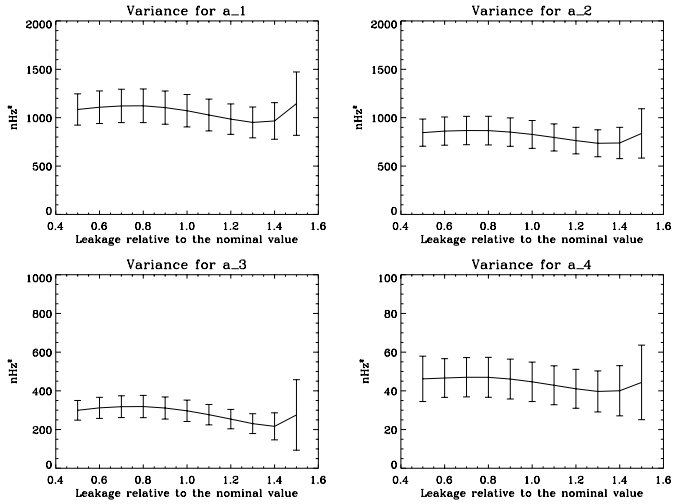

Fig. 6. Diagonal elements of the covariance matrix of the splitting coefficient, for $l = 2$. They are given as a function of the relative change of the assumed off-diagonal leakage element. (Top, left) For a_1; (Top, right) For a_2; (Bottom, left) For a_3; (Bottom, right) For a_4

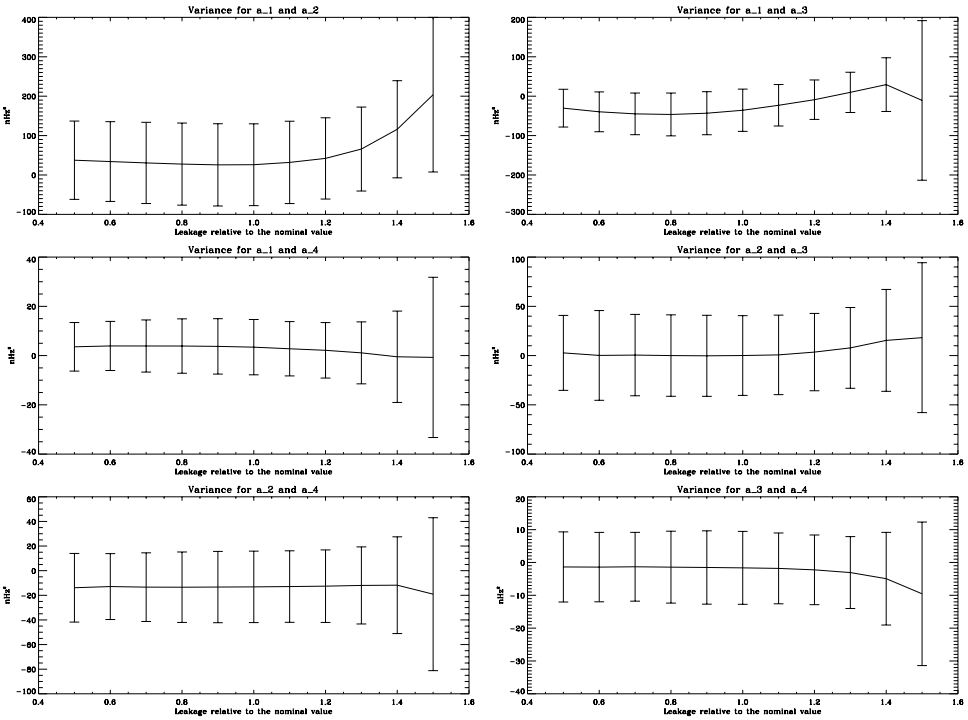

Fig. 7. Off-diagonal elements of the covariance matrix of the splitting coefficient, for $l = 2$. They are given as a function of the relative change of the assumed off-diagonal leakage element. (Top, left) For a_1 and a_2; (Top, right) For a_1 and a_3; (Middle, left) For a_1 and a_4; (Middle, right) For a_2 and a_3; (Bottom, left) For a_2 and a_4; (Bottom, right) For a_3 and a_4

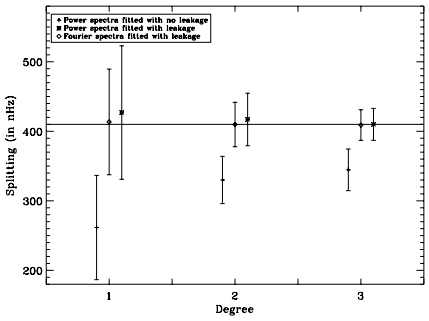

Fig. 8. Comparison of low-degree splittings measured using 1000 Monte-Carlo simulations by 3 different fitting techniques. The nominal splitting is 410 nHz. The + is the technique commonly used by GONG, the asterisk is the technique used by Appourchaux et al. (1995), the diamond is the technique described in this paper and also used for the SOI/MDI data. The error bars are the formal error bars for a single realization

leakage matrices according to Eqs. (13) and (14), second the mode covariance matrices with Eq. (22) (or using Eq. (23)), third the noise covariance matrices with Eq. (27) using a model of solar noise, fourth compute the likelihood function using Eq. (32). The use of Monte-Carlo simulations will ensure the success of the implementation. Routines for fitting p-mode Fourier spectra are available as freeware on the VIRGO home page: virgo.so.estec.esa.nl; they are written in the IDL macro language.

Last but not least, Eq. (36) showed us the equivalence between fitting data for which the leakage matrix is not the identity, and fitting data for which it explicitly is. This last statement is true provided that we know perfectly well the leakage matrix. In this case the p-mode parameters fitted using MLE are not, or very weakly, biased, and have minimum variance. For instance, we showed for the splitting that other commonly fitting methods result either in a bias and/or larger formal errors. We have also studied the effect of an imperfect knowledge of the leakage matrix on the fitted parameters, in order to derive the effect of systematic errors on the most interesting parameters:

the splitting and mode frequency. We found that the central frequency is insensitive to systematic errors in the leakage matrix, while the splitting coefficients (a_i) have a quadratic dependence upon those errors. These systematic errors will have influence on the inverted solar rotation profiles.

Finally, we would like to stress again that the correct statistical treatment of the p-mode data is of vital importance for deducing unbiased p-mode parameters.

Acknowledgements. Many thanks to Takashi Sekii for constructive comments on the manuscript, and for extensive cyberspace chatting :-). We are grateful to the referees for their constructive comments.

Appendix A:

The purpose of this appendix is to show that using a proper matrix $\mathsf{C_B}$, the noise covariance matrix of Eq. (37) given by:

$$\mathsf{B}'^{(l,l')} = \mathsf{C_B}^{-1}\mathsf{B}^{(l,l')}\mathsf{C_B}^{\mathrm{T}\,-1} \tag{A1}$$

can have a diagonal form. The matrix $\mathsf{B}^{(l,l')}$ can be diagonalized and we can write.

$$\mathsf{B}^{(l,l')} = \mathsf{P}^{-1}\mathsf{b}^{(l,l')}\mathsf{P}^{\mathrm{T}\,-1} \tag{A2}$$

where $\mathsf{b}^{(l,l')}$ is diagonal and P is an orthogonal matrix ($\mathsf{P}^{-1} = \mathsf{P}^{\mathrm{T}}$). Replacing Eq. (A2) into Eq. (A1), we have:

$$\mathsf{B}'^{(l,l')} = \mathsf{C_B}^{-1}\mathsf{P}^{-1}\mathsf{b}^{(l,l')}\mathsf{P}^{\mathrm{T}\,-1}\mathsf{C_B}^{\mathrm{T}\,-1}. \tag{A3}$$

Since $\mathsf{B}^{(l,l')}$ is positive definite all its eigenvalues are positive, therefore the square root of $\mathsf{b}^{(l,l')}$ is defined. Therefore if we apply the following transformation to the data:

$$\mathsf{C_B} = \mathsf{P}^{-1}\sqrt{\mathsf{b}^{(l,l')}} \tag{A4}$$

we can rewrite Eq. (A3) as:

$$\mathsf{B}'^{(l,l')} = \mathsf{I} \tag{A5}$$

where I is the identity matrix. So replacing C in Eq. (33) by $\mathsf{C_B}$ will have the effect of removing the artificial correlation due to the noise, and also of performing a normalization. We should point out that the transformation matrix $\mathsf{C_B}$ that can achieve this is not unique, and any multiplication by an orthogonal matrix will achieve this. Nevertheless, we give a solution to the problem which can be solved as an eigenvalue and eigenvector problem. The transformation given above does not remove the artificial correlation due the p modes but more or less preserve it. This can have some useful application when one wants to produce spectra with uncorrelated noise but with correlated p-mode signals.

References

Anderson E.R., Duvall Jr. T.L., Jefferies S.M., 1990, ApJ 364, 699
Appourchaux T., Andersen B.N., 1990, Sol. Phys. 128, 91
Appourchaux T., Andersen B.N., Fröhlich, Jiménez A., Telljohann U., Wehrli C., 1997, Sol. Phys. 170, 27
Appourchaux T., Gough D.O., Sekii T., Toutain T., 1997, IAU 181, Nice, Provost J. and Schmider F.-X. (eds.)
Appourchaux T., Gizon, 1998 (in preparation)
Appourchaux T., Toutain T., Telljohan U., Jiménez A., Andersen B.N., 1995, A&A 294, L13
Appourchaux T., Rabello-Soares M.C., Gizon L., 1998 (submitted to A&A)
Brownlee K.A., 1965, Statistical Theory and Methodology in Science and Engineering, 2nd edition. John Wiley and Sons, New York
Chang, 1996, PhD Thesis. University of Cambridge
Christensen-Dalsgaard J., Gough D.O., 1982, MNRAS 198, 141
Davenport W.B. Jr., Root W.L., 1958, An Introduction to the Theory of Random Signals and Noise. McGraw-Hill Eds., New York
Duvall T.L. Jr., Harvey J.W., 1986, Seismology of the Sun and the Distant Stars. Dordrecht, D. Reidel, p. 105
Frieden B.R., 1983, Probability, Statistical Optics, and Data Testing: A Problem Solving Approach. Springer-Verlag, Berlin
Fröhlich C., Andersen B.N., Appourchaux T., et al., 1997, Sol. Phys. 170, 1
Gabriel M., 1994, A&A 287, 685
Gizon L., Appourchaux T., Gough D.O., 1997, Proceedings of the Kyoto General Assembly
Hill F., Stark R.T., Stebbins R.T., et al., 1996, Sci 272, 1292
Kendall M.G., Stuart A., 1967, The advanced theory of Astrophysics: Inference and relationship, Vol. II, 2nd edition. Butler and Tanner Ltd. Eds., London
Kumar P., Franklin J., Goldreich P., 1988, ApJ 328, 879
Quenouille M.H., 1956, Biometrika 43, 353
Rabello-Soares M.C., Appourchaux T., 1998 (in preparation)
Rabello-Soares M.C., Roca Cortés T., Jiménez A., Appourchaux T., Eff-Darwich A., 1997, ApJ 480, 840
Ritzwoller M.H., Lavely E.M., 1991, ApJ 369, 557
Schou J., 1992, PhD thesis, On the analysis of helioseismic data, Aarhus University, Aarhus
Schou J., Brown T.M., 1994, A&AS 107, 541
Tomczyk S., Schou J., Thompson M.J., 1995, ApJ 488, L57
Toutain T., Appourchaux T., 1994, A&A 289, 649
Toutain T., Gouttebroze P., 1994, A&A 268, 309
Wilks S.S, 1938, Ann. Math. Stat. 9, 60
Woodard M., 1984, PhD Thesis, University of California, San Diego

ASTRONOMY & ASTROPHYSICS
SUPPLEMENT SERIES

OCTOBER I 1998, PAGE 121

Astron. Astrophys. Suppl. Ser. **132**, 121–132 (1998)

The art of fitting p-mode spectra

II. Leakage and noise covariance matrices

T. Appourchaux[1], **M.-C. Rabello-Soares**[1,2], **and L. Gizon**[1,3]

[1] Space Science Department of ESA, ESTEC, NL-2200 AG Noordwijk, The Netherlands
[2] Teoretisk Astrofysik Center, Århus Universitet, DK-8000 Århus C, Denmark
[3] W.W. Hansen Experimental Physics Laboratory, Center for Space Science and Astrophysics, Stanford University, Stanford, CA 94305-4085, U.S.A.

Received October 15, 1997; accepted March 24, 1998

Abstract. In Part I we have developed a theory for fitting p-mode Fourier spectra assuming that these spectra have a multi-normal distribution. We showed, using Monte-Carlo simulations, how one can obtain p-mode parameters using "Maximum Likelihood Estimators". In this article, hereafter Part II, we show how to use the theory developed in Part I for fitting real data. We introduce 4 new diagnostics in helioseismology: the (m, ν) echelle diagram, the cross echelle diagram, the inter echelle diagram, and the cross spectrum ratio. These diagnostics are extremely powerful to visualize and understand the covariance matrices of the Fourier spectra, and also to find bugs in the data analysis code. The diagrams are used to verify the computation of the leakage matrices, and also to measure quantitatively these matrices. Cross spectrum ratios are used to obtain quantitative information on the noise covariance matrices. Numerous examples using the LOI/SOHO and GONG data are given.

Key words: methods: data analysis — statistical — observational — Sun: oscillations

1. Introduction

The physics of the solar interior is known from inversion of solar p-mode frequencies and splittings. These measurements are derived from fitting p-mode Fourier spectra. Schou (1992) was the first one to assume a multi-normal distribution for p-mode Fourier spectra and using a real leakage matrix. Following this pioneering work, Appourchaux et al. (1997) (hereafter Part I), generalized the theoretical background for fitting p-mode Fourier spectra to complex leakage matrix, and included explicitly the correlation of the noise between the Fourier spectra. Using Monte-Carlo simulations, we showed that our fitted parameters were unbiased. We also studied systematic errors due to an imperfect knowledge of the leakage covariance matrix. Unfortunately, a theoretical knowledge of fitting data is not enough as only real data will teach us if our approach is correct. Contrary to fitting p-mode power spectra, the process of fitting the Fourier spectra as described in Part I is rather difficult to understand and visualize. Schou (1992) gave a few diagnostics for understanding how the Fourier spectra are fitted but without showing an easy way to visualize the covariance matrices.

In this paper, we show how one can easily visualize the mode and noise correlation matrices, and then derive the mode leakage matrix. In the first section, we describe 4 new diagrams that have various diagnostics power. In the second section, we describe how we use those diagrams for inferring the leakage and noise covariance matrices for the data of the Luminosity Oscillations Imager (LOI) on board the Solar and Heliospheric Observatory (SOHO) data (Appourchaux et al. 1997), and for the data of the Global Oscillations Network Group (GONG) (Hill et al. 1996). The LOI time series starts on 27 March 1996 and ends on 27 March 1997 with a duty cycle greater than 99%. The GONG time series starts on 27 August 1995 and ends on 22 August 1996 with a 75% duty cycle. In the last section we conclude by emphasizing the usefulness of these diagrams.

2. Diagnostics for helioseismic data analysis

The echelle diagram was first introduced by Grec (1981). It is based on the fact that the low-degree modes are essentially equidistant in frequency for a given l; the typical spacing for $l = 0$ is 135 μHz. The spectrum is cut into

Send offprint requests to: thierrya@so.estec.esa.nl

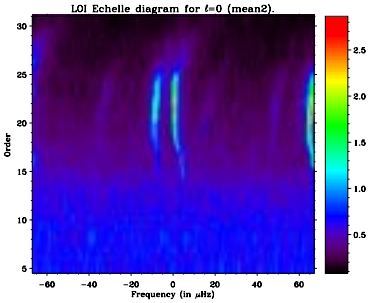

Fig. 1. Amplitude spectra echelle diagram for 1 year of LOI data seeing the Sun as a star. The scale is in part-per-million $\mu\mathrm{Hz}^{-1/2}$ (ppm $\mu\mathrm{Hz}^{-1/2}$). The spacing is tuned for $l = 0$ ($\Delta\nu = 134.8$ μHz). The $l = 0$ modes are at the center, the $l = 2$ modes are about 10 μHz on the left hand side, the $l = 1$ modes are about +65 μHz on the right hand side, the $l = 3$ can be faintly seen at about 12 μHz from the left hand side of the $l = 1$. Other modes such as $l = 4$ and $l = 5$ can also be seen faintly seen at -35 μHz and +15 μHz, respectively. The distortion of the ridges are due to sound speed gradients in the solar core

pieces of 135 μHz which are stacked on top of each other. Since the modes are not truly equidistant in frequency, the echelle diagram shows up power as distorted ridges; an example is given in Fig. 1 for the LOI/SOHO instrument seeing the Sun as a star.

Another useful diagram was introduced by Brown (1985), the so-called (m, ν) diagram which shows how the frequency of an l, m mode depends upon m. Most often this diagram is only shown for a single n and for intermediate degrees $l \geq 10$.

The purpose of these diagrams is always to show an estimate of the variance of the spectra. In our case we also want to visualize not only the variance but also the covariance of the Fourier spectra. Here we briefly recall from Part I that the observed Fourier spectra ($\boldsymbol{y}$) can be related to the individual Fourier spectra of the normal modes ($\boldsymbol{x}$) by the leakage matrix $\mathcal{C}^{(l,l')}$ by:

$$\boldsymbol{y} = \mathcal{C}^{(l,l')}\boldsymbol{x} \tag{1}$$

where $\boldsymbol{x}(\nu)$ and $\boldsymbol{y}(\nu)$ are 2 complex vectors made each of $2l + 2l' + 2$ components: $2l+1$ components for l, $2l'+1$ components for l'. Here only two l values have been used for simplicity, there is no difficulty to extend the expression of the leakage matrix for a number of degrees greater than 2. The covariance matrix $\mathsf{V}^{(l,l')}_{m,m'}$ of $\boldsymbol{z_y}$ ($\boldsymbol{z}^{\mathrm{T}}_{\boldsymbol{y}} = (\mathrm{Re}(\boldsymbol{y}^{\mathrm{T}}), \mathrm{Im}(\boldsymbol{y}^{\mathrm{T}}))$), can be derived from the submatrix $\mathcal{V}^{(l,l')}$ whose elements can be expressed as:

$$2\mathcal{V}^{(l,l')}_{m,m'} = E[y_{l,m}(\nu)y^*_{l',m'}(\nu)] =$$
$$2\sum_{l''=l,l'}\sum_{m''=-l''}^{m''=l''}\mathcal{C}^{(l',l'')}_{m',m''}\mathcal{C}^{(l,l'')*}_{m,m''}f^{l''}_{m''}(\nu) + 2\mathcal{B}^{(l,l')}_{m,m'} \tag{2}$$

where E is the expectation, $f^{l''}_{m''}(\nu)$ is the model of the line shape of the power spectrum of the (l'', m'') mode, $\mathcal{B}^{(l,l')}$ is the covariance matrix of the noise, and with the $y_{l,m}(\nu)$ having a mean of zero. The factor 2 comes from the fact that the real part of $\mathcal{V}^{(l,l')}$ represents both the covariance of the real or imaginary parts of the Fourier spectra (See Part I, Sect. 3.3.2); the same property applied to the imaginary part of $\mathcal{V}^{(l,l')}$ which represents the covariance between the real part and the imaginary part of the Fourier spectra. Equation (2) contains all the information that we need for visualizing an estimate of the real and imaginary parts of $\mathcal{V}^{(l,l')}$. Drawing from the usefulness of the diagrams of Grec and Brown, we created four new diagrams for visualizing an estimate of $\mathcal{V}^{(l,l')}$, all having various diagnostics power:

1. (m, ν) echelle diagram: estimate of the diagonal elements of $\mathcal{V}^{(l,l)}$ $(l = l')$
2. cross echelle diagram: estimate of the off-diagonal elements of $\mathcal{V}^{(l,l)}$ $(l = l')$
3. inter echelle diagram: estimate of the off-diagonal elements of $\mathcal{V}^{(l,l')}$ $(l \neq l')$
4. cross spectrum ratio: estimate of the ratio of the elements of $\mathcal{B}^{(l,l')}$.

Each diagnostic is described hereafter in more detail.

2.1. (m, ν) echelle diagram

The (m, ν) *echelle diagram* is made of $2l + 1$ echelle diagrams of each l, m power spectra or $|y_{l,m}(\nu)|^2$. The $2l + 1$ echelle diagrams are stacked on top of each other to show the dependence of the mode frequency upon m. These diagrams give an estimate of the diagonal of the covariance matrix of the observations as:

$$2\widetilde{\mathcal{V}}^{(l,l)}_{m,m}(\nu) = |y_{l,m}(\nu)|^2 \tag{3}$$

where $\widetilde{\mathcal{V}}^{(l,l)}$ symbolizes the estimate of $\mathcal{V}^{(l,l)}$. It is important when one makes these diagrams to tune the spacing for the degree to study. The spacing for a given l can be computed from available p-mode frequencies. Since the spacing varies with the degree, other modes with a significant different spacing can be seen more like diagonal ridges crossing the (m, ν) diagrams; this is a powerful tool to identify other degrees.

Nevertheless, the diagnostics power of the m, ν echelle diagram is rather limited for deriving the leakage matrix: it can be shown using Eq. (2) that the diagonal elements of $\mathcal{V}^{(l,l)}$ can be expressed as:

$$\mathcal{V}^{(l,l)}_{m,m} = \sum_{m''=-l}^{m''=l}|\mathcal{C}^{(l,l)}_{m,m''}|^2 f^l_{m''}(\nu) + \mathcal{B}^{(l,l)}_{m,m}. \tag{4}$$

As we can see with Eq. (4), the sign information of the elements of $\mathcal{C}^{(l,l)}$ is lost; second, their magnitude being typically less than 0.5, the leakage elements cannot be easily seen in the power spectra. Another kind of diagram that preserves the sign of the leakage elements had to be devised.

2.2. Cross echelle diagram

The *cross echelle diagram* of an l, m mode is made of $2l+1$ echelle diagrams of the cross spectrum of m and m' or $y_{l,m}(\nu)y^*_{l,m'}(\nu)$. The $2l+1$ real (or imaginary) parts of the cross spectra are stacked on top of each other to show the dependence upon m of the mode frequency. These diagrams give an estimate of the rows (or columns) of the covariance matrix of the observations as:

$$2\widetilde{\mathcal{V}}^{(l,l)}_{m,m'}(\nu) = y_{l,m}(\nu)y^*_{l,m'}(\nu). \quad (5)$$

Of course when $m = m'$ we get the echelle diagrams of the previous section. Only $l+1$ cross echelle diagrams are shown as the matrix $\mathcal{V}^{(l,l')}$ is hermitian by definition.

The imaginary part of the cross spectra has some diagnostic power: it represents the correlation between the real and imaginary parts of the Fourier spectra. When the leakage matrix is real, which is generally the case, there is no correlation between the real and imaginary parts. Nevertheless the imaginary part could be helpful to find errors in the filters applied to the images (See Part I, Sect. 3.3.1).

It can be shown that the elements of $\mathcal{V}^{(l,l)}$ can be expressed as:

$$\mathcal{V}^{(l,l)}_{m,m'} = \mathcal{C}^{(l,l)}_{m,m'} f^l_{m'}(\nu) + \mathcal{C}^{(l,l)*}_{m',m} f^l_m(\nu) + \sum_{m''\neq m',m} \mathcal{C}^{(l,l)}_{m',m''}\mathcal{C}^{(l,l)*}_{m,m''} f^{l''}_{m''}(\nu) + \mathcal{B}^{(l,l)}_{m,m'}. \quad (6)$$

As we can see with Eq. (6), these diagrams preserve the sign of the leakage matrix elements. In general, the cross spectra for m, m', representing $\mathcal{V}^{(l,l)}_{m,m'}$ carries information over the sign of the leakage elements $\mathcal{C}^{(l,l)}_{m,m'}$ and $\mathcal{C}^{(l,l)*}_{m',m}$. The other additional terms expressed as product of leakage elements are sometimes more difficult to interpret.

But the power of these diagrams is not only restricted to checking the sign of the elements of the leakage matrix. They are also real tools to get a first order estimate of the leakage matrix. We have shown in Part I, that there is no difference between fitting data for which the leakage matrix *is* the identity, and data for which the leakage matrix is *not*. We showed in Part I, that the covariance matrix of $\tilde{\boldsymbol{x}}$ ($\tilde{\boldsymbol{x}} = \mathcal{C}^{-1}\boldsymbol{y}$) can be written, similarly to that of Eq. (2)), by the sum of 2 matrices: the first one represents the mode covariance matrix and is diagonal, and the second term represents the covariance matrix of the noise. Therefore, applying the inverse of the leakage matrix to the data should, in principle, remove all artificial mode correlations between the Fourier spectra of $\tilde{\boldsymbol{x}}$: this can be verified using the cross echelle diagrams. This is the most powerful test for deriving the leakage matrices.

The cross echelle diagrams are useful to verify the correlation within a given degree, but other degrees are known to leak into the target degree, such as $l = 6$, 7 and 8 into $l = 1$, 4 and 8, respectively. The purpose of the next diagram is to assess the magnitude of these leakages.

2.3. Inter echelle diagram

The *inter echelle diagram* of an l, m mode for the degree l' is made of $2l'+1$ echelle diagrams of the cross spectrum of l, m and l', m' or $y_{l,m}(\nu)y^*_{l',m'}(\nu)$. The $2l'+1$ real part of the cross spectra are stacked on top of each other to show the dependence upon m'. These diagrams give an estimate of the rows (or columns) of the covariance matrix of the observations as:

$$2\widetilde{\mathcal{V}}^{(l,l')}_{m,m'}(\nu) = y_{l,m}(\nu)y^*_{l',m'}(\nu). \quad (7)$$

Similarly as for the cross echelle diagram, it will help to visualize the covariance matrix between different degrees, and to derive leakage elements of the full leakage matrix $\mathcal{C}^{(l,l')}$. One can derive an equation similar to Eq. (6) for different degrees showing that the inter echelle diagram carries information over the sign of the leakage elements $\mathcal{C}^{(l,l')}_{m,m'}$ and $\mathcal{C}^{(l',l)*}_{m',m}$.
As mentioned above applying the inverse of the leakage matrix will help to verify to the first order that there is no artificial correlation due to the p modes. When different degrees are involved the full leakage matrix $\mathcal{C}^{(l,l')}$ has to be used, producing diagrams that should have no artificial correlation due to the p modes.

2.4. Cross spectrum ratio

All the previous diagrams are helpful to understand and visualize the mode covariance matrices. Unfortunately, due to the high signal-to-noise ratio, these diagrams cannot be used to evaluate the correlation of the noise in the Fourier spectra. In between the p modes, these correlations can be more easily visualized as we have:

$$\mathcal{V}^{(l,l)}_{m,m'} \approx \mathcal{B}^{(l,l)}_{m,m'}. \quad (8)$$

But instead of visualizing $\mathcal{B}^{(l,l')}$, we prefer to look directly at the correlation by computing the ratio of the cross spectra as:

$$\frac{\widetilde{\mathcal{B}^{(l,l')}_{m,m'}}}{\mathcal{B}^{(l,l)}_{m,m}} = \frac{(y_{l,m}(\nu)y^*_{l,m'}(\nu)}{|y_{l,m}(\nu)|^2}. \quad (9)$$

This ratio is called the *cross spectrum ratio*. The cross spectrum ratio gives an estimate of the ratio matrix $\mathcal{R}^{(l,l')}$ (See Part I) which gives a better understanding of how much the noise background is correlated between the Fourier spectra. Nevertheless, in the p-mode frequency range, the cross spectrum ratio is more difficult to interpret as the noise correlation is affected by the presence of the modes. By looking away from the modes (at high or low frequency) or by looking between the modes, one could obtain a reasonable good estimate of the noise correlation.

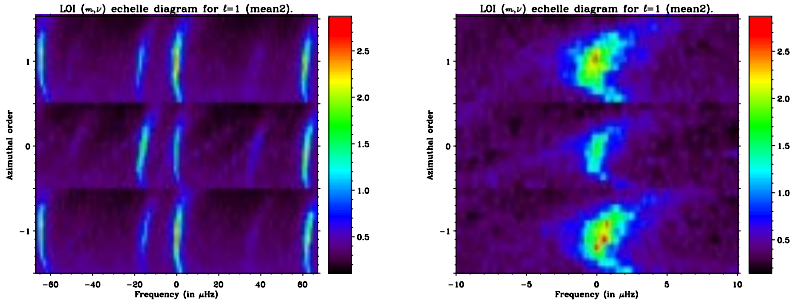

Fig. 2. (m,ν) echelle diagram for 1 year of LOI data for $l=1$. The scale is in ppm μHz$^{-1/2}$. The spacing is tuned for $l=1$ ($\Delta\nu=134.8$ μHz). (Left) The full diagram centered on $l=1$. The $l=3$ modes are located about 15 μHz at the left hand side of the $l=1$. The $l=2$ modes are on the right edge, while the $l=0$ are on the opposite side. The $l=4$ modes can be seen around $+40$ μHz. (Right) The same diagram but enlarged around $l=1$. The frequency shift or splitting of the modes due to the solar rotation can be seen: the 2 patches of power for $m=-1$ and $m=+1$ are slightly displaced from each other. The artificial correlation between $m=-1$ and $m=+1$ is not as clear

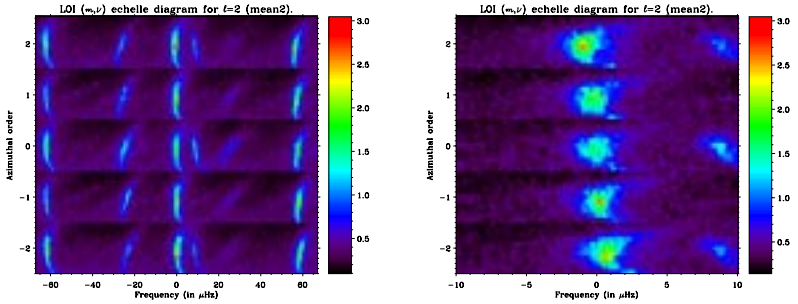

Fig. 3. (m,ν) echelle diagram for 1 year of LOI data for $l=2$. The scale is in ppm μHz$^{-1/2}$. The spacing is tuned for $l=2$ ($\Delta\nu=135.1$ μHz). (Left) The full diagram centered on $l=2$ with a spacing of 135. μHz. The $l=0$ modes are located about 10 μHz at the right hand side of the $l=2$ modes. The $l=3$ modes are on the right edge, while the $l=1$ modes are on the opposite side. The $l=4$ modes are easily seen at about -25 μHz; the $l=5$ starts to appear at $+25$ μHz. (Right) The same diagram but enlarged around $l=2$ with the $l=0$ modes at the right hand side. The splitting of the modes is clear. Note the absence of the $l=0$ modes for $m=\pm1$

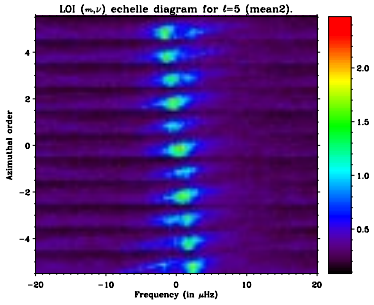

Fig. 4. (m,ν) echelle diagram for 1 year of LOI data for $l=5$. The scale is in ppm μHz$^{-1/2}$. The spacing is tuned for $l=5$ ($\Delta\nu=136.2$ μHz). Here we can clearly see the splitting of the $l=5$ modes. Unfortunately, the $l=5$ data of the LOI are heavily polluted by the presence of the $l=8$ modes. But since the spacing for the $l=8$ modes is different compared with that of the $l=5$ modes, the $l=8$ modes are seen as ridges going from lower left to upper right in each m panel; while the $l=5$ modes are seen more like straight ridges in each m panel. It can also be seen that the $|m|=5$ Fourier spectra contain information both about $m=\pm5$. This is the result of the large LOI pixel size creating oversampling. The $l=8$ modes are also distinguished because the "splitting" of this alias is in the opposite direction compared with that of the $l=5$ modes

3. Application to data

3.1. (m,ν) echelle diagram for the LOI/SOHO data

Example of these diagrams can be seen in Figs. 2, 3 and 4 for 1 year of LOI data for $l = 1, 2$ and 5, respectively. It is important when one makes such diagrams to tune the spacing for the degree to study. For example, one can see in Fig. 2 that the ridges of power of $l = 0, 1, 2$ and 3 have different shapes than in Fig. 3. Other modes with a significant different spacing can be seen more like diagonal ridges crossing the (m,ν) diagrams; this is a powerful tool to identify other degrees. In Fig. 4, the $l = 5$ (m,ν) echelle diagram is clearly contaminated by an other degree, i.e. $l = 8$, which appears at different frequencies depending on m. For $l = 5, m = -5$, the $l = 8, m = +8$ is quite strong; while for $l = 5, m = +5$, this is $l = 8, m = -8$ which shows up. This kind of 'anti'-splitting behaviour is typical of any aliasing degrees. It is more prominent in the LOI data because of the undersampling effect due to the large size of the LOI pixels.

3.2. A useful detail

Before using the other diagrams on real data, we need to point out a very important property coming from the way the m signals are built. If the weights $W_{l,m}$ applied to the images, to extract an l, m mode, have the same properties as of the spherical harmonics then we have:

$$W_{l,m} = W^*_{l,-m} \tag{10}$$

which means that both the Fourier spectra of $+m$ and $-m$ can be obtained from using a single filter $W_{l,+m}$. The Fourier spectrum of $+m$ will be in the positive part of the frequency range, while that of $-m$ will be in the negative part. This approach was first used by Rhodes et al. (1979) for measuring solar rotation, and mentioned theoretically by Appourchaux & Andersen (1990) for the case of the LOI. Due to the property of the Fourier transform, we recover, in the negative part of the frequency range, *not* the Fourier spectrum of $-m$ but its *conjugate*. This fact is very important, if one does not take care of the sign of the imaginary part of $-m$, it will lead to very serious problem. Needless to say that fitting data without taking into account this detail will have devastating effects. Obviously this important detail cannot be detected in the power spectra.

3.3. Leakage matrix measurement for a single degree

3.3.1. LOI/SOHO data

According to theoretical computation of the p-mode sensitivities of the LOI pixels (Appourchaux & Andersen 1990) and using the real shape of the LOI pixels (Appourchaux & Telljohann 1996), the leakage matrices of $l = 1$ and 2 are given by:

$$\mathcal{C}^{(1,1)} = \begin{pmatrix} 1 & 0 & \alpha \\ 0 & 1 & 0 \\ \alpha & 0 & 1 \end{pmatrix}$$

$$\mathcal{C}^{(2,2)} = \begin{pmatrix} 1 & 0 & \alpha_1 & 0 & \alpha_4 \\ 0 & 1 & 0 & \alpha_2 & 0 \\ \alpha_3 & 0 & 1 & 0 & \alpha_3 \\ 0 & \alpha_2 & 0 & 1 & 0 \\ \alpha_4 & 0 & \alpha_1 & 0 & 1 \end{pmatrix} \tag{11}$$

with: $\alpha = 0.474$, $\alpha_1 = \alpha_3 = -0.308$, $\alpha_2 = 0.576$, $\alpha_4 = -0.216$. These leakage matrices are mean value over one year. The leakages vary throughout the year because the distance between SOHO and the Sun varies. There is no B angle effect as the mean B is zero over 1 year. All the leakage elements are real as the LOI filters have the same symmetry as the spherical harmonics.

Figures 5 and 6 display the cross echelle diagram for $l = 1$ and 2, respectively. From Figs. 5 and 6, we can directly verify using Eq. (6) the sign, and sometimes even the magnitude of the leakage elements. The best cross check that our theoretical computations are correct is to apply the inverse of the leakage matrices to the original data (See Sect. 2.2). Figures 7 and 8 show how the artificial correlations (or m leaks) can be removed from the LOI data; for the latter we also cleaned the original data from the presence of the $l = 0$ modes. In this latter case, $\boldsymbol{y}$ and $\boldsymbol{x}$ (cf. Eq. (1)) are both 6-element vectors where the first element is the observed Fourier spectrum for $l = 0$, and the other 5 are the Fourier spectra for $l = 2$ and the associated m's. Both vectors are related to each other by the leakage matrix $\mathcal{C}^{(0,2)}$ of dimension 6×6. We shall see later on with the GONG data that cleaning, similar to that of the LOI, can be achieved not only for 2 degrees but also for 3 degrees ($l = 1, 6$ and 9).

Unfortunately, for the LOI data the leakage matrices of $l = 4, l' = 7$ and $l = 5, l' = 8$ cannot be inverted. It means that the $2l + 2l' + 2$ Fourier spectra of $l \geq 4$ are linearly dependent. This is the result of the pixel undersampling and has two dramatic consequences: the leakage matrix cannot be verified as for the other degrees, and fitting the data as described in Part I is not valid anymore as the leakage matrix needs to be invertible. This problem is specific to the LOI data. One way around the problem is to restrict the fitting to a subset of the spectra having no linear dependence.

3.3.2. GONG data

The leakage matrices of the GONG data have been computed by R. Howe (1996, private communication). We also computed similar leakage matrices using the equations developed in Part I. The integration was made in the θ, ϕ plane with $\theta_{\max} = 65.2°$, $\phi_{\max} = 53.5°$ without apodization. We also took into account the effect of subtracting

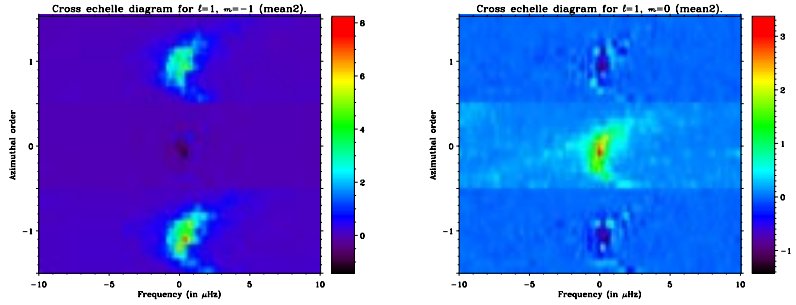

Fig. 5. Real part of the cross echelle diagrams for 1 year of LOI data for $l = 1$. The scale is in ppm^2 μHz^{-1}. The spacing is tuned for $l = 1$ ($\Delta\nu = 134.8$ μHz). (Left) For $l = 1, m = -1$. The lower panel represents the echelle diagram of $m = -1$. The 2 other panels are the cross spectra with $m = 0$ and $m = 1$. As predicted, there is no visible correlation between $m = -1$ and $m = 0$ while there is between $m = -1$ and $m = +1$. Here we visualize the first line of the real part of the matrix $\mathcal{V}^{(1,1)}$. (Right) For $l = 1, m = 0$. The bottom panel is the same as the middle panel of the left diagram but with a different color scale. The middle panel is the power spectra of $m = 0$ already shown in Fig. 2; the $l = 6$ modes are visible as a diagonal ridge crossing the ridge of the $l = 1$ modes

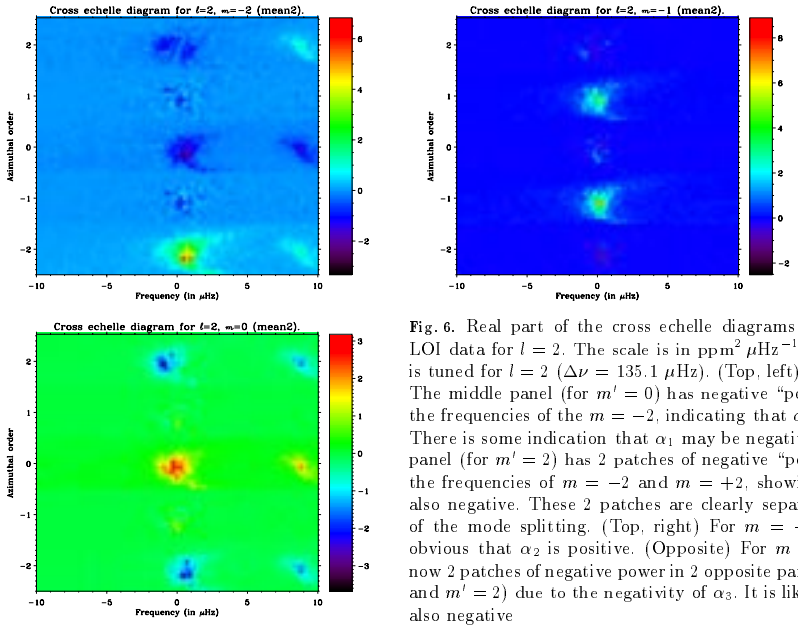

Fig. 6. Real part of the cross echelle diagrams for 1 year of LOI data for $l = 2$. The scale is in ppm^2 μHz^{-1}. The spacing is tuned for $l = 2$ ($\Delta\nu = 135.1$ μHz). (Top, left) For $m = -2$. The middle panel (for $m' = 0$) has negative "power" close to the frequencies of the $m = -2$, indicating that α_3 is negative. There is some indication that α_1 may be negative. The upper panel (for $m' = 2$) has 2 patches of negative "power" close to the frequencies of $m = -2$ and $m = +2$, showing that α_4 is also negative. These 2 patches are clearly separated because of the mode splitting. (Top, right) For $m = -1$. Here it is obvious that α_2 is positive. (Opposite) For $m = 0$. There is now 2 patches of negative power in 2 opposite panels ($m' = -2$ and $m' = 2$) due to the negativity of α_3. It is likely that α_1 is also negative

the velocity of the Sun seen as a star which affects GONG instrument's sensitivity to modes only detected by integrated sunlight instrument (mainly the modes for which $l + m$ is even). The theoretical leakage matrices of $l = 1$ and 2 for GONG are also given by Eq. (11) but with: $\alpha = -0.55$, $\alpha_1 = -0.268$, $\alpha_2 = 0.451$, $\alpha_3 = -0.122$, and $\alpha_4 = -0.290$. For $l = 1$, the leakage between $m = -1$ and $m = +1$ is negative due to the subtraction of the mean velocity which affects these modes. For $l = 2$, the leakage between $m = -1$ and $m = +1$ has about the same value as for the LOI; these modes are not affected by the subtraction.

The cross echelle diagrams of the $l = 2$ GONG data are very close to those of the LOI (See Fig. 6). Figure 9 shows an example of a GONG cross echelle diagram after having applied the inverse of the leakage matrix. It is clear that

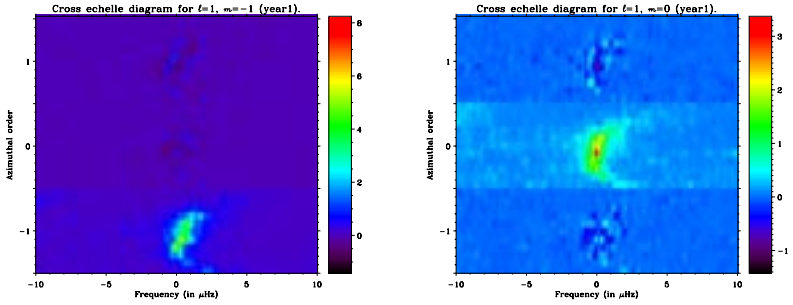

Fig. 7. Real part of the cross echelle diagrams of 1 year of LOI data for $l = 1$. The scale is in ppm$^2\,\mu$Hz^{-1}. The spacing is tuned for $l = 1$ ($\Delta\nu = 134.8$ μHz). The inverse of the theoretical leakage matrix has been applied to the original data with $\alpha = 0.474$. (Left) For $l = 1, m = -1$. The artificial correlation between $m = -1$ and $m = +1$ has been entirely removed (See Fig. 5 for comparison). (Right) For $l = 1, m = 0$. There is no improvement as there was no correlation before

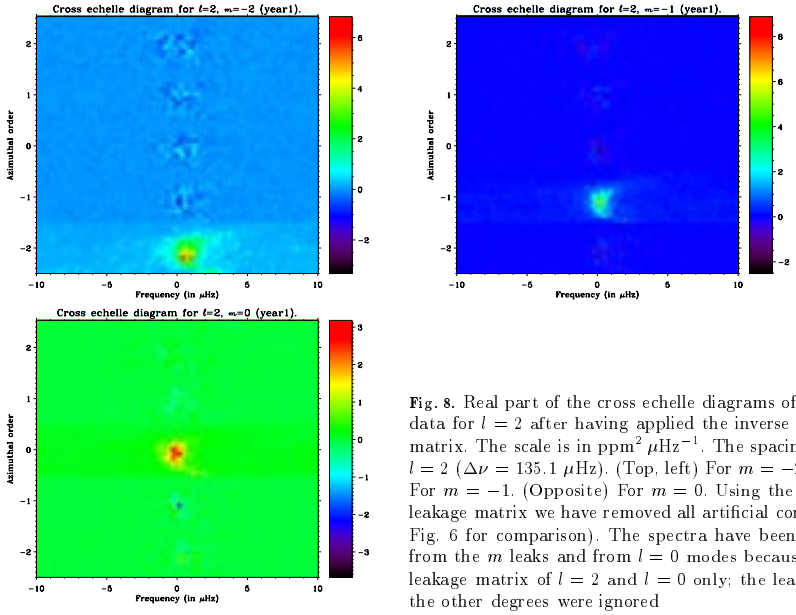

Fig. 8. Real part of the cross echelle diagrams of 1 year of LOI data for $l = 2$ after having applied the inverse of the leakage matrix. The scale is in ppm^2 μHz^{-1}. The spacing is tuned for $l = 2$ ($\Delta\nu = 135.1$ μHz). (Top, left) For $m = -2$. (Top, right) For $m = -1$. (Opposite) For $m = 0$. Using the inverse of the leakage matrix we have removed all artificial correlations (See Fig. 6 for comparison). The spectra have been cleaned both from the m leaks and from $l = 0$ modes because we used the leakage matrix of $l = 2$ and $l = 0$ only; the leakages from all the other degrees were ignored

the p-mode correlations are removed. For $l = 1$ we have used the cross echelle diagram of $m = -1$ and $m = 1$ for inferring quantitatively the off-diagonal leakage element α. We first applied the inverse of a leakage matrix to the $l = 1$ data, and then constructed the cross echelle diagram of $m = -1$ and $m' = 1$ for these data. We then collapsed this diagram by adding up all the modes with $n = 10 - 26$, and finally we corrected the collapsed diagram from the solar noise background. The collapsed diagram is shown in Fig. 10 (Left) for no correction ($\alpha = 0$) and for an α of -0.53; the corrected surface of the collapsed diagram as a function of α is shown in Fig. 10 (Right). When the corrected surface is close to 0, there is no artificial correlation remaining.

Cleaning the data from artificial correlations has also been done in a different way by Toutain et al. (1998). Using Singular Value Decomposition, they recomputed pixel filters for the MDI/LOI proxy so as to remove the m leaks and the other aliasing degrees. Here we have shown, that data cleaning is also possible *without* having the pixel time series, but using the Fourier spectra.

This latter cleaning technique is more useful as one has to reduce a smaller amount of data.

3.4. Leakage matrix measurement for many degrees

3.4.1. LOI/SOHO data

Figure 11 shows the inter echelle diagram for $l = 1$, $l' = 6$. This diagram is more difficult to interpret, but using specific spacing for l or l', one can unambiguously identify which degree contributes to the correlation. For the LOI data, the $l = 5$ and $l = 8$ (similarly $l = 4$ and $l = 7$) are strongly contaminated by each other. This is again due to the spatial undersampling which prevents the LOI data to be cleaned from aliasing degrees making the leakage matrix not invertible. Fortunately, the $l = 1$ LOI data are far less affected by the presence of $l = 6$ compared with that of GONG (See in the next section); this is the result of an effective apodization function (limb darkening) which creates a narrower spatial response than that of GONG (line-of-sight projection).

Figure 8 has already shown that we could clean the $l = 2$ LOI data from the $l = 0$ mode. This was done by taking into account the leakage matrix $\mathcal{C}^{(0,2)}$. Unfortunately as mentioned above for the $l \geq 4$, the LOI data cannot be cleaned from aliasing degrees because the leakage matrice $\mathcal{C}^{(1,6)}$, $\mathcal{C}^{(4,7)}$ and $\mathcal{C}^{(5,8)}$ are singular.

3.4.2. GONG data

Figure 12 shows the inter echelle diagram for $l = 1, l' = 6$. The correlations are clearly visible. If they are not taken into account they are likely to bias the frequency and splittings of the $l = 1$ (See Rabello-Soares & Appourchaux 1998, in preparation). By using the inverse of the leakage matrix of $l = 1, 6$ and 9 (i.e. $\mathcal{C}^{(1,6,9)}$), one can clean the data from these spurious correlations arising both from the two aliasing degrees ($l = 6$ and 9) and from the m leaks. Figure 13 shows the "cleaned" inter echelle diagram which should be compared with Figs. 12. The correlations have been almost entirely removed. Some correlations between the $l = 1, m = -1$ modes and the $l = 6$ modes are still present. This is due to the fact that the computation of the leakage for $l = 1, m = \pm 1$ are very sensitive to the subtraction of the velocity of the Sun seen as a star. This is not the case for the $l = 1, m = 0$ modes as they are insensitive to this effect. Nevertheless, our imperfect knowledge of the leakage matrix can be adjusted in order to remove the residual correlations. It helped to reduce the systematic errors of the $l = 1$ splitting at high frequencies, mainly where the $l = 6$ and 9 modes start to cross over the $l = 1$ modes (Rabello-Soares & Appourchaux 1998, in preparation).

It is possible to apply this cleaning technique to higher degree modes ($l \approx 50 - 100$. In principle, this is feasible, although the plethora of data involved may be fairly substantial. For higher degrees, the ridges of the modes in the (m, ν) echelle diagrams are almost parallel to each other. The idea would be not to use the full Fourier spectra, as we did for the low degree GONG data, but to use only a small frequency range of about $\pm$ 30 μHz around the target degree. By doing so, we will not only clean the data from the aliasing degrees but also from the m leaks. In this case, the mode covariance matrix is diagonal. If we assume, wrongly, that the noise covariance matrix is diagonal, the statistics of each cleaned spectrum, for high degree modes, could be approximated by a χ^2 with 2 degree of freedom. Neglecting the off-diagonal elements of the noise covariance matrix will lead to larger mode linewidth, thereby producing underestimated splittings; this systematic bias will decrease as the degree. This approximation will produce much less systematic errors than the approximation used by Hill et al. (1996) for the original data. The use of the suggested approximation for the GONG data may help, at the same time, to reduce systematic errors, and to increase computing speed for higher degree modes. The degree where one needs to switch between this approximation and the correct analysis needs to be determined.

3.5. Noise covariance matrix measurement

3.5.1. LOI/SOHO data

The leakage and ratio matrices have similar properties (See Part I). For example, for a given l there is no correlation between the m for which $m + m'$ is odd for either matrix. As outlined in Part I, for a given degree, the ratio matrix is also close to the leakage matrix. For example, Fig. 14 shows that for the LOI data the measured ratio matrix element between $m = -1$ and $m = +1$ is about $+0.55$ which is rather close to the $\alpha = 0.474$ given in Eq. (11). The ratio matrix is also useful if one wants to reduce the number of noise parameters to be fitted. This is useful when the noise background, mainly of solar origin, varies slowly over the p-mode range. In this case the ratio can be assumed to be constant over the p-mode range. For example for $l = 1$ we can fit 2 noise parameters instead of 3. When the noise varies in the p-mode range, it is more advisable to fit as many noise parameters as required.

Figure 15 shows the cross spectrum ratios of $l = 2$ for the LOI data. As this is commonly the case for the LOI, the ratios are independent of frequency. In addition, as outlined in Part I, the ratio matrix is very close to the leakage matrix. Using the values of α given for the LOI in Eq. (11) and Fig. 15, one can see that this is the case for the LOI. The ratio matrix has even the same symmetry property as the leakage matrix (not shown here). In the case of the LOI, we sometimes use the independence of the ratio with frequency to reduce the number of free

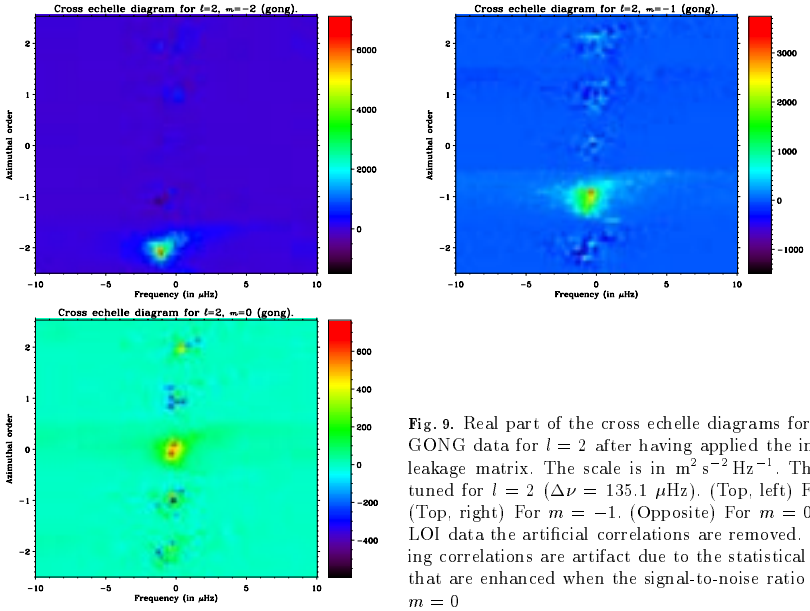

Fig. 9. Real part of the cross echelle diagrams for 360 days of GONG data for $l = 2$ after having applied the inverse of the leakage matrix. The scale is in $\mathrm{m^2\,s^{-2}\,Hz^{-1}}$. The spacing is tuned for $l = 2$ ($\Delta\nu = 135.1$ μHz). (Top, left) For $m = -2$. (Top, right) For $m = -1$. (Opposite) For $m = 0$. As for the LOI data the artificial correlations are removed. The remaining correlations are artifact due to the statistical fluctuations that are enhanced when the signal-to-noise ratio is low as for $m = 0$

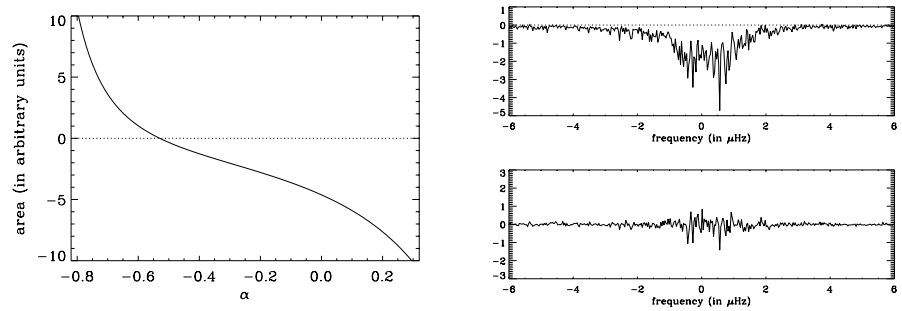

Fig. 10. (Left) Collapsed diagram of the real part of the cross spectrum of $m = -1$ and $m = +1$ for the GONG data after having applied the inverse of the leakage matrix, (top) no correction, (bottom) $\alpha = -0.53$. (Right) Surface of the collapsed diagram as a function of α, the surface is 0 for $\alpha = -0.53$

parameters. It is less straightforward to measure the noise correlation for the GONG data than for the LOI data. We recommend to measure it in between the p modes because that is what the fitting routines will determine.

3.5.2. GONG data

Figures 14 and 15 show the cross spectrum ratios of $l = 2$ for the GONG data. The ratio matrices (as the leakage matrices) are not symmetrical. Figure 14 shows also the effect of the subtraction of the full disk integrated velocity in the GONG data. In this case, the correlation is extremely high (about -0.8) and very different from the $\alpha = -0.55$ computed for GONG. Apart from the $l = 1$, these matrices tend to be very close to those of the leakage matrices (see previous section). It is also clear that the ratios depend upon frequency, probably due to the effect of mesogranulation affecting the spatial properties of the noise with frequency. In this case, the dependence of the noise correlation upon frequency has to be taken into account in the fit either by adding free parameters or by

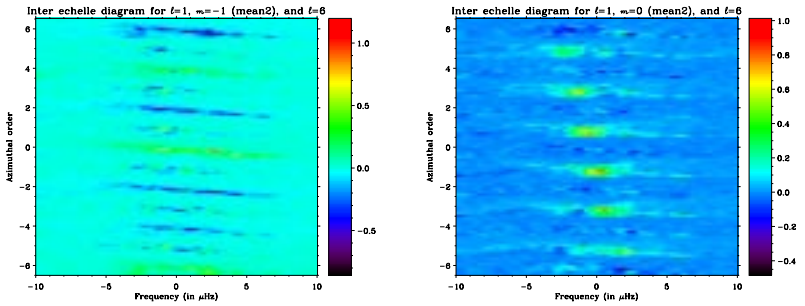

Fig. 11. Real part of the inter echelle diagrams for 1 year of LOI data for $l = 1$ and $l' = 6$. The scale is in $\mathrm{ppm}^2\,\mu\mathrm{Hz}^{-1}$. The spacing is tuned for $l' = 6$ ($\Delta\nu = 136.7$ μHz). (Left) For $l = 1, m = -1$. Given the structure of the ridges, it means that the $l = 1$ modes leak into the even m modes of $l' = 6$, while the $l' = 6$ modes do not leak into the $l = 1$. (Right) For $l = 1, m = 0$. Again using the structure of the ridges, the odd m' of $l' = 6$ leaks weakly into $l = 1, m = 0$

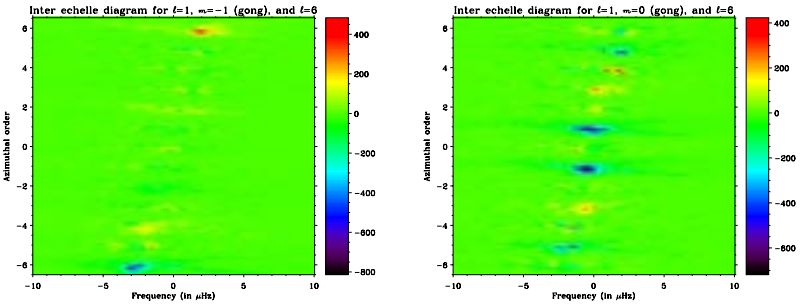

Fig. 12. Real part of the inter echelle diagrams of 1 year of GONG data for $l = 1$ and $l' = 6$. The scale is in $\mathrm{m}^2\,\mathrm{s}^{-2}\,\mathrm{Hz}^{-1}$. The spacing is tuned for $l' = 6$ ($\Delta\nu = 136.7$ μHz). (Left) For $l = 1, m = -1$. The strongest correlations are for $m' = \pm 6$ due to $l' = 6$. (Right) For $l = 1, m = 0$. The $l = 6$ modes are strong in all the panels. For $m' = \pm 1$ other modes can be seen as an "asterisk" ridge: the ridge going from bottom right to upper left represents the $l = 1$ modes; the ridge going from bottom left to upper right represents the $l = 9$ modes; the vertical ridge represents the $l = 6$ modes. At the far left, the ridge parallel to that of the $l = 1$ represents the $l = 3$ modes

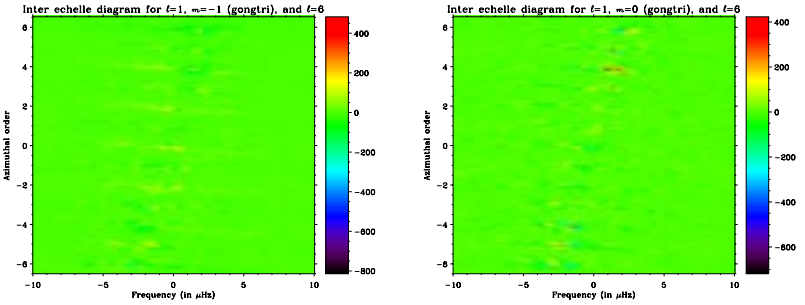

Fig. 13. Real part of the inter echelle diagrams of 1 year of GONG data for $l = 1$ and $l' = 6$ after having applied the inverse of the leakage matrix $\mathcal{C}^{(1,6,9)}$. The scale is in $\mathrm{m}^2\,\mathrm{s}^{-2}\,\mathrm{Hz}^{-1}$. The spacing is tuned for $l' = 6$ ($\Delta\nu = 136.7$ μHz). (Left) For $l = 1, m = -1$. The faint yellow oblique ridges are due to the $l = 1$ modes. (Right) For $l = 1, m = 0$. The correlations due to the $l = 1$ and 6 modes are almost entirely removed

measuring these correlations in the cross spectrum ratios (see Rabello-Soares & Appourchaux 1998, in preparation).

4. Summary and conclusion

For helping the understanding of fitting p-mode Fourier spectra, we have devised 4 new helioseismic diagnostics:

1. the (m, ν) echelle diagram helps visualizing:
   - which degree can be detected,
   - the mode splitting and
   - spurious degrees.
2. the cross echelle diagram helps verifying:
   - the sign of the imaginary parts of the Fourier spectra for $m < 0$,
   - the sign of the elements of the leakage matrix of the degree l,
   - to the first order the theoretical leakage matrix of the degree l by applying the inverse of this matrix to the data (i.e. cleaning the data from the m leaks),
   - the measurement of the real leakage matrix and
   - the cleaning of the data from m leaks.
3. the inter echelle diagram helps verifying:
   - the sign of the elements of the full leakage matrix for degrees l, l',
   - to the first order the theoretical leakage matrix of the degree l, l' by applying the inverse this matrix to the data,
   - the measurement of the real leakage matrix and
   - the cleaning of the data from aliasing degrees.
4. the cross spectrum ratio helps deriving:
   - the amplitude of the noise correlation between the Fourier spectra and
   - the frequency dependence of the correlations.

These steps will help to evaluate the matrices of the leakage, mode covariance, ratio and noise covariance directly from observations. The fitting of the p modes will be considerably eased by verifying that the theoretical knowledge of these matrices is correct.

These steps have been used both on data for which we design the spatial filtering (LOI instrument), and on data for which we did not design the filtering (GONG). As a matter of fact these diagnostics are so powerful that a theoretical knowledge of the various matrices is not always necessary to understand the data. Very often these diagnostics can also be used to find bugs in the data analysis routines. Nevertheless, it is advisable to know to the first order the leakage and ratio matrices for speeding up the analysis process.

Last but not least, the knowledge of the leakage matrices can be used for cleaning the data from m leaks and from undesired aliasing degrees. This cleaning can be performed either when the pixel time series are available (MDI data, Toutain et al. 1998) or more simply when only the Fourier spectra are available (LOI, GONG). The cleaning has very useful application for the GONG velocity data for removing aliasing degrees from $l = 1$, 6 and 9 for instance, and for inferring better $l = 1$ splittings (Rabello-Soares & Appourchaux 1998, in preparation). The cleaning is somewhat easier with Fourier spectra as one does not need to reduce large amount of image time series. It is advisable that, in the near future, this cleaning technique be used for higher degree modes. This will hopefully provide helioseismology with frequency and splitting data having much less systematic errors than before.

Acknowledgements. SOHO is a mission of international collaboration between ESA and NASA. This work utilizes data obtained by the Global Oscillation Network Group (GONG) project managed by the National Solar Observatory, a Division of the National Optical Astronomy Observatories, which is operated by AURA, Inc. under a cooperative agreement with the National Science Foundation. The GONG data were acquired by instruments operated by the Big Bear Solar Observatory, High Altitude Observatory, Learmonth Solar Observatory, Udaipur Solar Observatory, Instituto de Astrofísico de Canarias and Cerro Tololo Interamerican Observatory. Many thanks to Takashi Sekii for constructive comments on the manuscript, and for extensive cyberspace chatting. I am grateful Mihir Desai for proofreading the English. Last but not least, many thanks to my wife for her patience during the painful writing of these 2 articles.

References

Appourchaux T., Andersen B.N., 1990, Sol. Phys. 128, 91
Appourchaux T., Telljohann, 1996, LOI GSE and VDC specification Doc., Version 1.7, available on the VIRGO home page (http://virgo.so.estec.esa.nl)
Appourchaux T., Andersen B.N., Fröhlich, Jiménez A., Telljohann U., Wehrli C., 1997, Sol. Phys. 170, 27
Brown T., 1985, Nat 317, 591
Grec G., PhD thesis, Université de Nice, Nice
Hill F., Stark R.T., Stebbins R.T., et al., 1996, Sci 272, 1292
Rhodes E.J., Deubner F.-L., Ulrich R.K., 1979, ApJ 227, 629
Schou J., 1992, PhD thesis, On the analysis of helioseismic data, Århus Universitet, Århus
Toutain T., Kosovichev A., Appourchaux T., 1998, IAU General assembly, Kyoto

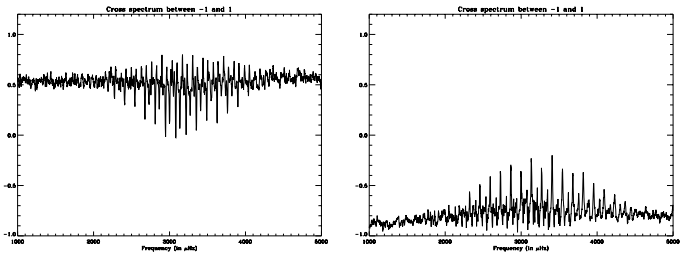

Fig. 14. Real part of the cross spectrum ratios for $l = 1$ smoothed to 10 μHz. (Left) LOI data: for $m = -1$ and $m' = 1$. The noise correlation is about 0.55. (Right) GONG data: for $m = -1$ and $m = 1$. The noise correlation is about -0.77. The large anti-correlation is due to the subtraction of the full-disk velocity which tends to reduce the amplitude of the $m = \pm 1$ modes

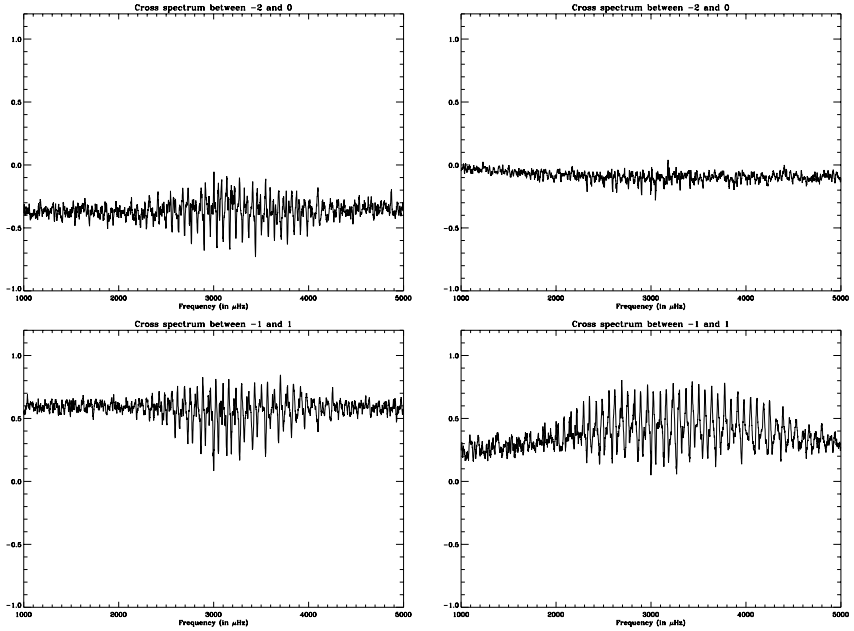

Fig. 15. Real part of the cross spectrum ratios of $l = 2$ smoothed to 10 μHz. (Left) For the LOI data: top, for $m = -2$ and $m' = 0$. The noise correlation is about -0.45; bottom, for $m = -1$ and $m = 1$. The noise correlation is about 0.60. (Right) For the GONG data: top, for $m = -2$ and $m' = 0$. The noise correlation is rather small and about -0.10; bottom, for $m = -1$ and $m' = 1$. The typical value is about 0.4

Chapitre 6

Observational upper limits for low-l solar g modes

ApJ, 2000, 538, in press

Preprint typeset using LaTeX style emulateapj v. 04/03/99

OBSERVATIONAL UPPER LIMITS FOR LOW-DEGREE SOLAR G MODES

T. APPOURCHAUX[1], C. FRÖHLICH[2], B. ANDERSEN[3], G.BERTHOMIEU[4], W. J. CHAPLIN[2,5], Y. ELSWORTH[5], W. FINSTERLE[1], D. O. GOUGH[6,7], J .T. HOEKSEMA[8], G. R. ISAAK[5], A. G. KOSOVICHEV[8], J. PROVOST[4], P. H. SCHERRER[8], T. SEKII[6], T. TOUTAIN[4]

ABSTRACT

Observations made by the Michelson Doppler Imager (MDI) and Variability of solar IRradiance and Gravity Oscillations (VIRGO) on the Solar and Heliospheric Observatory (SOHO) and by the ground-based Birmingham Solar Oscillations Network (BiSON) and Global Oscillations Network Group (GONG) have been used in a concerted effort to search for solar gravity oscillations. All spectra are dominated by solar noise in the frequency region from 100 to 1000 μHz where g modes are expected to be found. Several methods have been used in an effort to extract any g-mode signal present. These include: (i) the correlation of data – both full-disc and imaged (with different spatial-mask properties) – collected over different time intervals from the same instrument, (ii) the correlation of near-contemporaneous data from different instruments, and (iii) the extraction – through the application of complex filtering techniques – of the coherent part of data collected at different heights in the solar atmosphere.

The detection limit is set by the loss of coherence caused by the temporal evolution and the motion (e.g. rotation) of superficial structures. Although we cannot identify any g-mode signature, we have nevertheless set a firm upper limit to the amplitudes of the modes: at 200 μHz, they are below 10 mm s^{-1} in velocity, and below 0.5 parts per million in intensity. The velocity limit corresponds very approximately to a peak-to-peak vertical displacement of $\delta R/R_\odot = 2.3 \cdot 10^{-8}$ at the solar surface. These levels which are much lower than prior claims, are consistent with theoretical predictions.

Subject headings: Sun: general – Sun: interior – Sun: oscillations – methods: data analysis

1. INTRODUCTION

Helioseismology has, over the past twenty five years, added immensely to our knowledge of the solar interior through the study of resonant p-mode oscillations. (See Christensen-Dalsgaard 1998 for a recent review of the field.) The current seismic signal are the manifestation of sound waves trapped within the body of the Sun. Gravity g modes remain undetected.

Sound waves which traverse the solar interior spend little time in the core regions, owing to the very high temperature. In spite of this short dwell time, the p modes are nonetheless a sensitive probe of the deep radiative interior since their frequencies can be measured to such high accuracy (a few parts in 10^6 for the lowest-frequency low-degree p modes detected to date). However, the g modes we seek to detect would be confined wholly within a resonant cavity in the radiative interior. Their detection therefore promises to provide an even more precise diagnostic of the core properties of the Sun. Since they are evanescent in the convection zone, the amplitudes of these modes are expected to be very low in the photosphere where the responses of the most commonly used observational techniques are peaked. This makes the task of obtaining a firm detection particularly challenging. In addition, the predicted g-mode amplitudes before the launch of SOHO were about 1 mm s^{-1} (Gough 1985). In view of the predicted solar noise (Harvey 1985), this made the detection of g modes a challenging task.

The first claims of detection of solar normal modes at frequencies below 500 μHz were made by a number of groups using different techniques. Severny et al. (1976) measured the difference between the radial velocity of a central portion and a circular annulus of the solar disc, and found a signal with period 160 minutes and ampli-

[1]Space Science Department, P.O.Box 299, NL-2200AG Noordwijk, The Netherlands
[2]Physikalisch-Meteorologisches Observatorium Davos, World Radiation Center, CH-7260 Davos Dorf, Switzerland
[3]Norwegian Space Centre, N-0212 Oslo, Norway
[4]Département Cassini, UMR CNRS 6529, Observatoire de la Côte d'Azur, F-06304 Nice, France
[5]School of Physics and Astronomy, University of Birmingham, Edgbaston, Birmingham, B15 2TT, United Kingdom
[6]Institute of Astronomy, University of Cambridge, Cambridge CB3 OHA, United Kingdom
[7]Department of Applied Physics and Theoretical Physics, University of Cambridge, Cambridge CB3 9EW, United Kingdom
[8]W.W.Hansen Experimental Physics Laboratory, Stanford University, Stanford, CA 94305, USA

tude $2.2\,\mathrm{m\,s^{-1}}$. Brookes et al. (1976) searched for minute radial velocity variations analogous to those of Cepheids and other pulsating stars. From the analysis of two days of data, they uncovered the presence of a statistically highly significant periodic signal at 2.65 hours with an associated amplitude of $2.7\,\mathrm{m\,s^{-1}}$. Later comparison between the two sets of measurements established that the oscillation phases of the two agreed. Brown et al. (1978) measured the diameter of the Sun using sophisticated edge-definition observations. To date, it is not clear whether the claimed oscillations were due to atmospheric disturbances or instrumental artifacts, or to temporal variations of true solar origin which have since subsided.

These early observations were followed up by numerous other measurements giving ever decreasing amplitudes or amplitude limits (e.g. Scherrer et al. 1979, Delache & Scherrer 1983). Subsequent intensity and Doppler velocity observations have failed to confirm these results. (For a review see Fröhlich & Andersen 1995.) More recently, Thomson et al. (1995) claim to have detected g modes in solar wind data collected by *Ulysses* (Marsden et al. 1996). However, this has now been cast into some doubt as the result of further analyses (Riley & Sonett 1996, Hoogeveen & Riley 1998, Denison & Walden 1999).

The modern field of helioseismology supports a broad range of high-quality observational programs, both spaceborne (e.g. GOLF[1], VIRGO[2] and MDI[3] on board the SOHO[4] spacecraft) and ground-based (e.g. BiSON[5], GONG[6], IRIS[7] and LOWL/ECHO[8]). Here, we report on attempts to detect low-degree g modes through the coordinated use of near-contemporaneous data collected by the VIRGO, MDI, BiSON and GONG programs. We describe in detail the various analysis strategies we have adopted. Particular attention is paid to the non-trivial issue of the precise calibration and comparison of frequency spectra generated from data collected in intensity and velocity. While we have failed to detect g modes, we have nevertheless placed the lowest limits to date on their amplitudes. The failure to detect any g mode is a confirmation of theoretical predictions (Gough 1985, Harvey 1985)

2. OBSERVATIONS

2.1. *MDI data*

The MDI data (Scherrer et al. 1995) used here are the LOI-proxy velocities (Hoeksema et al. 1998). They consist of a set of calibrated velocities measured in the 180 bins of the LOI-proxy "instrument" over a period of 784 days (from 1996 May 1 to 1998 June 23). The trend due to the radial orbital velocity of the spacecraft has been removed from the data using information contained in the SOHO orbit data files, and the remaining exponential trend removed by subtracting a boxcar average of width 1 day applied to the time series. The data have a sampling cadence of 15 sec (Nyquist frequency at 33.3 mHz) and an integration time of 1 %. The complete time series has a duty cycle of better than 98%. Individual time series were built for each (l, m) mode with spherical-harmonic masks.

2.2. *VIRGO data*

A detailed description of the instruments which comprise VIRGO, their operation and data acquisition procedures is given by Fröhlich et al. (1995). The data from PMO6V, SPM and LOI used in the present analysis are described in the following sections.

2.2.1. *Total and spectral irradiance*

The PMO6V and DIARAD radiometers measure the total solar irradiance (TSI), while the sunphotometers (SPM) measure the spectral irradiance in three 5-nm-wide spectral bands in the red (862nm), green (500nm) and blue (402nm) parts of the spectrum. The sampling cadence of the SPM is 60 s (Nyquist frequency at 8.3 mHz) with an integration time of 94%. The sampling cadence of the radiometers is 180 s (Nyquist frequency at 2.78 mHz) and an integration time of 31.3%. The performance of these instruments is described by Anklin et al. (1998). For the present study, we use data from the PMO6V radiometer and the SPM.

The total length of the time series used is 853 days, starting 1996 February 22. The duty cycles are 94.1% for the PMO6V, and 92.7%, 95.2%, and 95.8% for the red, green, and blue SPM channels respectively. Because the sensitivity of the SPM – and to a much lesser extent that of the radiometer – have suffered degradation over the course of the mission, proper de-trending of the time series is essential. A triangular-shaped filter of FWHM 1 day has been used to de-trend the time series and to calculate the relative variations.

2.2.2. *Luminosity Oscillation Imager*

The performance of the Luminosity Oscillation Imager (LOI), and the associated data-reduction procedures, are

[1]Global Oscillations at Low Frequency

[2]Variability of solar IRradiance and Gravity Oscillations

[3]Michelson Doppler Imager

[4]Solar and Heliospheric Observatory, an ESA/NASA Mission

[5]Birmingham Solar-Oscillations Network

[6]Global Oscillation Network Group

[7]Investigation on the Rotation and Interior of the Sun

[8]The low-l instrument

described by Appourchaux et al. (1997). Each pixel is detrended with a triangular-shaped filter of FWHM 1 day. In order to extract a given angular degree, the 12 pixels are combined using spherical harmonic filters (Appourchaux & Andersen 1990, Appourchaux et al. 1998b). Since these filters are complex, they allow one to separate each m in a given (l,n) multiplet. The leakage properties of the filters are well known (Appourchaux et al. 1998b). The filters are computed on a weekly basis using the real size of the solar image – which is calibrated in flight – and the orientation (latitude) angle of the Sun. (The position angle of the solar rotation axis is maintained at zero degrees by the orientation of the spacecraft.) The weekly filters are then averaged over the duration of the observations in order to produce a single filter which can be applied to the pixel time series to produce the targeted (l,m) signal. The sampling cadence of the LOI is 60 s (Nyquist frequency at 8.3 mHz) and an integration time of 99%. The time series utilized here is of length 819 days (from 1997 March 27, 1996 through 1998 June 24), and has a 99% duty cycle.

2.3. *BiSON data*

BiSON is a network of 6 stations distributed around the globe (Elsworth et al. 1995). The instruments use a Potassium resonance cell to measure solar radial velocities (Brookes et al. (1978b)). The sampling cadence of BiSON is typically 40 s (Nyquist frequency at 12.5 mHz) with a typical integration time of 40%.

Unlike those derived from the SOHO instruments, a BiSON frequency spectrum is generated from an appropriate (coherent) combination of data collected by six network instruments. The comparative quality of the data will inevitably vary, with some stations better suited to the study of low-frequency phenomena than others. In order to maximize one's ability to detect long-period solar p and g modes, data selection criteria are required that take into account the quality of the observations made at each site over the frequency range of interest. The need to maximize the duty cycle of the network implies that data should be used, where available, from a single station. However, there is a trade-off between: (i) the introduction of these data to the final time series; and (ii) the possibility that—if they are of poor quality—their use may drive up the noise power level of the combined network set to such an extent that this negates the apparent advantage of using the data in the first place.

The above can be expressed quantitatively as follows. First, consider a time series comprised of data from a single site. Let d be the fractional duty cycle of the time series, and $P(\nu)$ be the mean spectral noise power over the targeted frequency range (say, $\nu \rightarrow \nu + \delta\nu$). A simple "Figure Of Merit" (F.O.M) that encapsulates the trade-off is then:

$$\mathrm{F.O.M} = d/P(\nu). \tag{1}$$

For $d = 1.0$, i.e., a 100% fill in the time domain, the F.O.M. in Eq. (1) then corresponds simply to the inverse of the mean power over the frequency band of interest. If data are to be combined from several stations, this expression must be generalized somewhat. If the characteristics of the constituent sites are each tagged by the index i, such that for N stations, $1 \leq i \leq N$, the expanded expression becomes:

$$\mathrm{F.O.M} = \frac{D^2}{\sum_{i=1}^{N} d_i \cdot P_i(\nu)}, \tag{2}$$

where

$$D = \sum_{i=1}^{N} d_i. \tag{3}$$

As a first cut at the problem, we have implemented a set of code that makes use of the above in the following manner. Let $p_i(\nu,t)$ be the mean power, calculated over the target frequency range, on a day-by-day basis. Next consider a daily power rejection threshold for each site $T_i(\nu,t)$, again appropriate to the targeted frequency range. If we choose to reject individual days for which the the power $p_i(\nu,t) > T_i(\nu,t)$, this will alter: (i) $P_i(\nu)$, i.e., the overall mean power contribution from site i; and (ii) f_i, the fractional fill contribution from the site. Clearly, we wish to find some combination of site thresholds, $T_i(\nu,t)$ that will give the optimal overall combination, i.e., that which maximizes the F.O.M.. This can be realized by, in essence, performing a multi-parameter minimization – here, one varies, and then seeks to find at convergence, optimal estimates of the power rejection thresholds for each site. Here we should point out that our optimization procedure does not filter out any low frequency component.

The resulting procedure has been applied in order to select data – collected over the period 1994 May 16 through 1997 Jan 10 (971 days) – in order to optimize the combined BiSON time series for the frequency range $200 \leq \nu \leq 1000\,\mu$Hz. The post-optimization duty cycle is about 61% (reduced from 75%). At frequencies below $\sim 200\,\mu$Hz, contamination by window-function-related artifacts becomes severe; however, this is not of serious concern since the strongest g modes (i.e., those most-likely to be detected first) are expected to be found at higher frequencies.

2.4. *GONG data*

GONG consists of 6 stations distributed around the globe (Harvey et al. 1996). Each instrument measures solar radial velocities in the NiI 676.8-nm line with a Michelson interferometer. The GONG data reduction procedures are described by Hill et al. (1996). In order to extract the mode signal, spherical-harmonic filters are applied to the pixel time series in a manner similar to the MDI and LOI data. In addition, the mean velocity is subtracted from each image. Unfortunately, this subtraction –

combined with a merging optimized for the p-mode range – enhances considerably the low frequency noise. Consequently we choose to use only the available full-disc integrated signal (which remains unaffected). The sampling cadence of GONG is 60 s (Nyquist frequency at 8.3 mHz) and an integration time of 33%. The time series used is of length 1260 days (spanning the period 1995 May 24 through to 1998 September 29), and has a duty cycle of 84%.

The standard GONG pipeline reduction procedures are tailored to the higher-frequency p-mode range, and as such, a difference filter is applied to the time series in order to suppress very low-frequency drifts in the data. Since these frequencies are of interest to us here, we have recovered this information by dividing the computed GONG power spectrum by the corresponding transfer function, e.g. $f(\nu) = 4\sin^2(\pi\nu\Delta t)$, where ν is the frequency and Δt=60 sec is the sampling time (Hill and Leibacher, 1999, private communication).

3. ANALYSIS TECHNIQUE

In order to compare the data from the different instruments, we need to take into account the fact that: (i) the temporal and spatial filtering appropriate to the different observations will differ; and (ii) the observational responses may be peaked at different heights in the solar atmosphere. Here, we address these issues in turn, before considering in detail the techniques of analysis that we have applied in an effort to uncover g modes in our data.

3.1. *Spatial and temporal filtering*

3.1.1. *Temporal filtering*

All power spectra computed for this paper have been divided by the associated fractional duty cycle, $\mathcal{F}$, such that for a time-series of length N samples a white-noise (Gaussian) source with a zero mean, characterized by a sample standard deviation of σ, will give a mean power level in the frequency domain of σ^2/N. This means that they satisfy Parseval's theorem.

In order to ascribe the height of a prominent, narrow peak in such a spectrum to an associated signal amplitude in the time domain, we must allow properly for the fill. Consider first a coherent, periodic signal (e.g., a sine wave) with associated amplitude A. A power spectrum of a gap-free signal will have a peak of height A^2. If the same signal is now forced through a window function with fractional duty cycle $\mathcal{F}$, the presence of gaps in the time domain will result in a redistribution of power from the main signal peak into, for example, prominent sidebands if the gap structure has a strong periodic component. The height of the main peak will be reduced to $\mathcal{F}A^2$. All spectra shown are scaled to amplitude on the ordinate. In order to recover correctly an estimate of the amplitude of a signal which gives a prominent peak in the power spectrum, its measured height must be divided by the square root of the fractional fill. This compensates for the power aliased out of the peak.

Apart from the obvious correction performed on the GONG data, no attempt was made to correct the spectra from the different detrending filters or integration windows. Nevertheless we can assess their influence on the spectra. The 1-day boxcar filter will produce a 11.57-μHz sinusoidal modulation of power present in the frequency domain, with an amplitude of $\approx$ 1% above 300 μHz; around 100 μHz the modulation increases to $\pm$ 4 %. The 1-day triangle filter will modulate power by less than 0.2% at 100 μHz. As mentioned in a previous section the GONG detrending filter produces much larger disturbances that needed correction; this is not required for the other filters. The additional filtering effect of the integration window is rather negligible for the low-frequency part of the spectrum; it does, however, have some effect over the p-mode range when the integration time is close to 100%. This window also introduces spurious power from the aliasing of high frequency power. The power aliasing at low frequencies depends on the quality of the integration time and on the solar spectrum. When the integration time is high ($\approx$ 100 %), the aliased solar spectrum at low frequencies is filtered out by the integration window; this is the case for VIRGO/SPM and VIRGO/LOI. For the other instruments, which have a lower integration time, the aliased power is fully transmitted. However owing to the $1/f$ characteristics of the solar spectrum, 1% at most of the power is aliased into the low-frequency band (the worst case figure is given for the VIRGO radiometers). The low-frequency spectra presented in this paper are therefore negligibly affected by the aliased power and the detrending filters.

3.1.2. *Spatial filtering*

We must also take into account the spatial filter functions S_{nlm} of each instrument. These are defined such that the observed RMS velocity, $v_{\rm obs}^{nlm}$, of a mode identified by (n,l,m) is calibrated so as to yield its RMS value over time and space as:

$$v_{\rm obs}^{nlm} = S_{nlm} v_{\rm rms}^{nlm} \tag{4}$$

The appendix gives a proper definition of the spatial filter function, which should not be confused with the visibility. Dziembowski (1977), Brookes et al. (1978a) and Christensen-Dalsgaard (1989) have, amongst others, discussed issues relating to the spatial filter functions appropriate to full-disc observations. Here, we have derived the spatial filter functions for both the full-disc and imaging observations (See Tables 1 and 2). Their derivations are given in the appendix. These have been checked for consistency by applying the corrections to the various calibrated spectra and comparing the resulting mode amplitudes at the center of the p-mode spectrum (i.e.,

TABLE 1
P-MODE SPATIAL FILTER FUNCTIONS OF THE FULL-DISC INTEGRATING INSTRUMENTS.

l	m	S_{lm}^{Blue}	S_{lm}^{Green}	S_{lm}^{Red}	$S_{lm}^{\mathrm{BiSON}\dagger}$
0	0	1.00	1.00	1.00	0.72
1	0	0.00	0.00	0.00	0.00
1	1	0.90	0.88	0.85	0.70
2	0	0.41	0.38	0.34	0.33
2	1	0.00	0.00	0.00	0.00
2	2	0.50	0.46	0.41	0.50

† The BiSON values have been corrected for Doppler imaging effects as computed by Christensen-Dalsgaard (1989).

TABLE 2
P-MODE SPATIAL FILTER FUNCTIONS OF THE IMAGING INSTRUMENTS

l	m	S_{lm}^{LOI}	S_{lm}^{MDI}	S_{lm}^{GONG}
0	0	1.16	1.00	0.70
1	0	0.87	1.00	⋯
1	1	1.24	1.00	⋯
2	0	0.86	1.00	⋯
2	1	1.01	1.00	⋯
2	2	1.21	1.00	⋯

at a frequency of $\sim 3\,\mathrm{mHz}$). When we do so, we find that the velocity spectra all give maximum amplitudes of $\sim 20\,\mathrm{cm\,s^{-1}}$.

The comparison of amplitudes observed in the full-disc LOI data and the green channel of the SPM (nearest wavelength, and hence closest response height, to the LOI value) also validates the spatial filter functions computed in intensity.

It is, in principle, possible to compute the corresponding spatial filter functions for the g modes. They are highly frequency and degree dependent. However, since any computation of the intensity filter functions rely heavily on uncertain theoretical considerations, we choose here not to compute the spatial filter functions for the g modes. Instead we use the spatial filter functions for the p-mode frequencies and apply them in the g-mode frequency regime.

3.2. *Observation heights in the atmosphere for acoustic waves*

The trapped p modes and core-penetrating g modes are evanescent in the photosphere, where the instruments detect either intensity changes or spectral line shift interpreted as Doppler velocity variations. While the energy density of the modes therefore decreases with height, the decreasing mass density of the atmosphere means that the amplitude of the observed waves actually increases with increasing altitude.

The LOI and SPM both possess an observational response that is peaked very close to 0 km, i.e., at the base of the photosphere[9], while the BiSON, GONG and MDI velocity data reflect perturbations roughly $250-300\,\mathrm{km}$ above this level. We stress here that these values are very approximate, and a precise derivation is far from trivial. In addition, due to dependence on averaging of surface fine structure, an average mean formation height may be physically irrelevant. As such, our intention here is merely to flag the issue of height dependence, i.e., we have not attempted to re-normalize any of the data to a notional reference height.

A proper derivation requires a thorough treatment of the radiation hydrodynamics of the Fraunhofer line used (KI for BiSON, NiI for GONG and MDI), which gives the observations a different weighting over the solar disc. In addition, for GONG and MDI the observation height differs from that of the line formation height (Jones 1989). Further, the observation height changes over the course of the observing season – again, to an extent which depends upon the observational technique – as the passbands of the instrument sweep over the wings of the line, reflecting the changing relative velocity between different part of the Sun and the instrument. Clearly, this effect will be more pronounced for the ground-based data, and raises subtle issues regarding the manner in which contemporaneous observations from different sites in a network, whose longitudes may differ by several tens of degrees, are combined to yield the final coherent time series.

3.3. *Statistical analysis*

The statistical distribution that describes power spectra made from either full-disc or resolved-image data can be approximated by χ^2 with n d.o.f, where $n = 2$ for full-disc integrating instruments, and $n > 2$ for resolved data. This information can be used to derive the power level at which a peak due to noise has a probability, p_{det}, of appearing over a given range in frequency, Δ_{det}. This threshold depends upon the observing time (T), since the number of frequency bins over the considered bandwidth will increase with the length of the time series. The probability that a random variable X takes a value higher than a given value x is given by:

$$p(x < X) = \frac{\Gamma(n/2, x/2)}{\Gamma(n/2)}, \tag{5}$$

where $\Gamma(a,x') = \int_{x'}^{+\infty} e^{-t} t^{a-1} dt$, and $\Gamma(a)$ is the Gamma function. Therefore the probability, p_{det}, that at least one out of N peaks be higher than a given value, x, is given by:

$$p_{\mathrm{det}} = 1 - (1 - p(x < X))^N. \tag{6}$$

If $p(x < X)$ is small, we then have:

$$p_{\mathrm{det}} \approx N\, p(x < X). \tag{7}$$

Since $N = T\,\Delta_{\mathrm{det}}$, combining the above gives:

$$p_{\mathrm{det}} \approx T\,\Delta_{\mathrm{det}} \left(\frac{\Gamma(n/2, x/2)}{\Gamma(n/2)} \right). \tag{8}$$

Equation (8) can be used to derive the relative level s_{det} (measured in units of the mean, $\tilde{s}$, over the chosen frequency range of the spectrum) which corresponds to a given probability p_{det} for a chosen window and observing time.

3.3.1. *Analysis of full-disc integrated data*

The statistical distribution of power spectra made from full-disc integrated observations is known to be χ^2 with 2 d.o.f.[10] In this case we can write:

$$\frac{\Gamma(1, x/2)}{\Gamma(1)} = e^{-\frac{x}{2}} \tag{9}$$

by replacing $x/2$ by $s_{\mathrm{det}}/\tilde{s}$ in Eq. (9), we can solve analytically Eq. (8) to yield:

$$\frac{s_{\mathrm{det}}}{\tilde{s}} \approx \ln(T) + \ln(\Delta_{\mathrm{det}}) - \ln(p_{\mathrm{det}}), \tag{10}$$

[9] Here, we define the base of the photosphere to be where optical depth reaches unity at a wavelength of 500 nm. Note that solar models are usually normalized to unity radius where $T = T_{\mathrm{eff}}$; this height lies some $\sim 50\,\mathrm{km}$ above our chosen radial datum.

[10] This is not strictly correct if there are gaps in the time domain, which remove the statistical independence of bins in the frequency domain.

where T is in units of 10^6 sec and $\Delta_{\rm det}$ is given in μHz. So, for a $\approx$70-μHz bandwidth, a 1-year observing time and a probability level of 10%, the absolute detection level corresponds to 10 $\tilde{s}$. (Note that the 70-μHz band is approximately the separation of adjacent low-degree p-mode pairs; the band was adjusted slightly to yield the 10-$\tilde{s}$ level.) We computed thresholds for detectable modes at the low-frequency end of the p-mode spectrum in order to establish that the 10-$\tilde{s}$ level constitutes a meaningful detection criterion.

All levels hereafter are computed according to the 10-$\tilde{s}$ baseline – taking into account the observing time – such that $s_{\rm det}$ can be re-expressed according to:

$$\frac{s_{\rm det}}{\tilde{s}} \approx 10 + \ln(T_y), \tag{11}$$

where T_y is now given in years.

If we were to use only prejudice to guide our efforts to detect g modes, we might choose to home in on rather narrower bandwidths (i.e., in the vicinity of the model frequencies) of order 1 μHz or less. The corresponding 10% threshold would then be reduced to $s_{\rm det}/\tilde{s}$ = 5.75. However, because of the bandwidth reduction, one is likely to find rogue candidate peaks close to the theoretical frequencies if one maintains the 10% detection criterion. For example, the probability of having at most one peak higher than $s_{\rm det}/\tilde{s}$ = 5.75 out of 20 1-μHz windows is about 39 %. Therefore, the probability of having at least 2 peaks appearing in 20 similar windows is 61 %, i.e., the likelihood of finding prominent peaks which are simply part of the background noise distribution is then quite high. The utilization of a large window (e.g. 70 μHz) will be less subject to spurious detection.

Figure 1 shows the amplitude spectra of the three SPM channels and the full-disc LOI data. The upper detection limit for the red SPM is about 0.5 ppm at 200 μHz, and 0.3 ppm at 1000 μHz. The levels for the other colors scale approximately with the temperature perturbation induced on the blackbody spectrum, with a slightly lower signal-to-noise ratio in the blue channel. The noise in the LOI amplitude spectrum is about 10% higher than the green SPM above 200 μHz, and 30% higher below. The additional noise comes from several sources. The most important are probably small variations in the image size over the detector and the effect of structures rotating into and out of the non-sensitive inter-pixel areas of the detector.

Figure 2 displays the amplitude spectra for the velocity instruments that observe the Sun as a star. The MDI data contain harmonics of 52.125 μHz, which arise from beats between the spacecraft timing system and the instrument sampling rate. We have removed these from the spectrum displayed in the figure. The presence of gaps in the GONG and BiSON data gives rise to daily harmonics at very low frequencies that have not been removed.

The solid line in each panel indicates the 10% threshold level as a function of frequency. We stress again that the ordinate of each spectrum is scaled such that a commensurate sine wave with amplitude A will give a peak of amplitude $\sqrt{\mathcal{F}}A$ in the frequency domain. The upper detection limit is: for MDI, 15 mm s^{-1} at 200 μHz, and 6 mm s^{-1} at 1000 μHz; for BiSON, 12 mm s^{-1} at 200 μHz, and 4 mm s^{-1} at 1000 μHz; and for GONG, 20 mm s^{-1} at 200 μHz, and 5 mm s^{-1} at 1000 μHz. Taking into account the spatial filter functions, the MDI levels are typically 20-50% lower than those of GONG; in comparison, the BiSON instrument performs almost as well as MDI above 400 μHz.

3.3.2. *Analysis of resolved LOI, MDI and GONG data*

Various pattern-recognition techniques have been used in an effort to reveal the presence of g modes. All assume that the modes are split by rotation and (or) that their frequencies can be derived from an asymptotic formula (Fröhlich & Andersen 1995, Fröhlich & Delache 1984). For the resolved-Sun data, we have devised a new pattern technique for detecting the modes.

A *collapsogramme* is constructed from the m spectra available at a chosen (n,l). Each m spectrum is shifted from the m = 0 spectrum by $\delta_{nlm} = m\Omega_{nlm}$ (where Ω_{nlm} represents the splitting of the mode), and is then normalized by an estimate of the variance of the spectrum in the narrow frequency range of interest. The application of the variance renormalization procedure means that the collapsogramme differs from the well-known m-averaged spectrum, where the constituent sets are combined with equal weight. The resulting $2l$+1 shifted and renormalized spectra are then each divided by the appropriate (l,m) spatial filter functions, and co-added to yield the collapsogramme (which is itself renormalized for comparison with individual or full-disc spectra). The equation for the collapsed spectrum is therefore:

$$s_l(\nu) = \sum_{m=-l}^{m=l} w_m F_m^l(\nu - m\Omega_{nlm}), \tag{12}$$

where $F_m^l(\nu)$ is the spectrum corrected for the spatial filter functions for a given (l,m), and the weights w_m are given by:

$$w_m = \left(\frac{1}{\sum_{m=-l}^{m=l} \frac{1}{\tilde{f}_m}} \right) \frac{1}{\tilde{f}_m}. \tag{13}$$

In the above, $\tilde{f}_m$ is an estimate of the mean of the power spectrum in a narrow frequency band (700 to 800 μHz).

The use of this simple procedure is appealing since it effectively dilutes instrumental harmonics (which are invariant), and produces a spectrum with well defined statistics (very nearly χ^2 with $4l+2$ d.o.f.). However, since the rotational splitting of the g modes is expected to vary rather more with frequency than for p modes, the technique must be applied either: (i) over a band in frequency

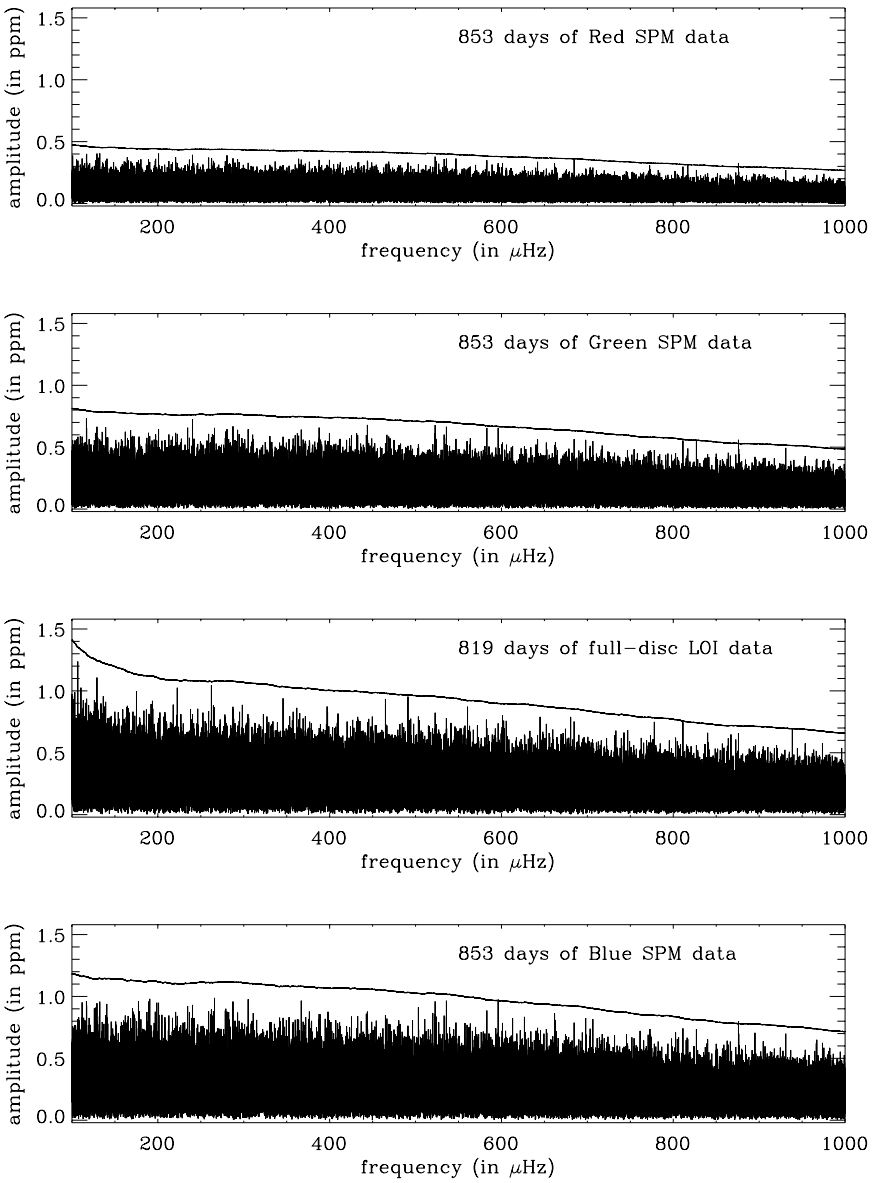

FIG. 1.— Full-disc intensity amplitude spectra for the three channels of the SPM and the full-disc LOI data. The continuous line gives the 0.1 probability limit that a peak be due to noise in a 70-μHz bandwidth. In the power spectrum, this level is about 10.8 $\tilde{s}$, i.e., about $\sqrt{10.8\tilde{s}}$ in the amplitude spectrum. Of course, $\tilde{s}$ differs for each of the spectra shown here.

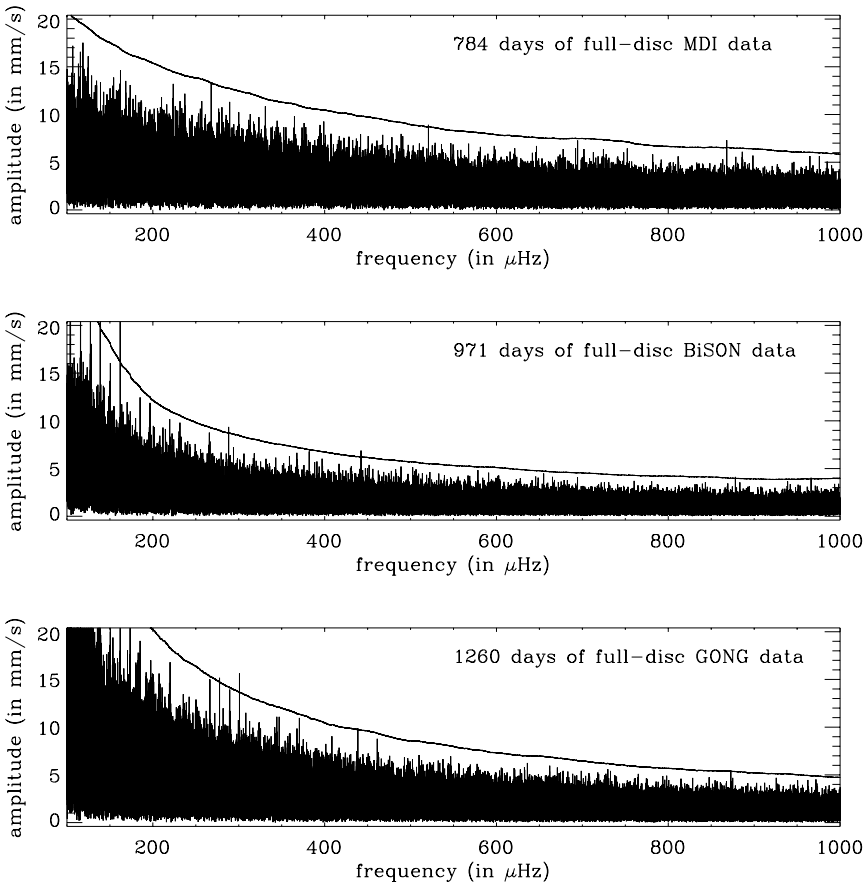

FIG. 2.— Full-disc velocity amplitude spectra for MDI (top), BiSON (middle) and GONG (bottom). The spectra are not corrected for the spatial filter functions. The continuous line gives the 0.1 probability limit that a peak be due to noise in a 70-μHz bandwidth. The limits in the amplitude spectra are $\sqrt{10.8\tilde{s}}$, $\sqrt{11.0\tilde{s}}$, $\sqrt{11.2\tilde{s}}$ for MDI, BiSON and GONG respectively. The MDI data contain harmonics of $52.125\,\mu$Hz, which arise from beats between the spacecraft timing system and the instrument sampling rate. We have removed these from the spectrum displayed in the figure. Daily harmonics, which arise from data gaps in the time domain, are visible in the BiSON and GONG spectra at very low frequencies. Of course, $\tilde{s}$ differs for each of the spectra shown here.

where the splitting varies slowly; or (ii) over a whole range of possible splitting values. We have successfully applied this technique to detect low-frequency p modes in the GONG dataset (Appourchaux et al. 1998a; Rabello-Soares & Appourchaux 1999). Figure 3 illustrates how the $l = 2$, $n = 7$ mode is uncovered with the MDI data by the use of the collapsogramme. The shift of 399 nHz was optimally chosen as to reveal low-degree p modes.

As for standard power spectra, we can define a detection probability ($p_{\rm det}$) which can be translated into a detection level $s_{\rm det}$ for the collapsogramme. The detection probability $p_{\rm det}$ is then related to $s_{\rm det}$ through the use of Eq. (8), where $x/2$ is now replaced by $(2l+1)s_{\rm det}/\tilde{s}$. This yields:

$$p_{\rm det} \approx T\Delta_{\rm det}\left(\frac{\Gamma(2l+1,(2l+1)s_{\rm det}/\tilde{s})}{\Gamma(2l+1)}\right) \qquad (14)$$

When $l = 0$, we recover an equation which can be solved analytically to yield Eq. (10). Note that we again chose $p_{\rm det} = 0.1$ to maintain consistency with the previous section.

We have applied the collapsogramme technique to the LOI and MDI resolved data. We tried a range of splitting values from 200 to 1000 nHz, but were unable to find any peaks that were significantly above the background noise. Please note that when one looks at N collapsogrammes, the right-hand side of Eq. (14) should be multiplied by N. Therefore to keep the same probability level p_{det} when looking at N collapsogrammes, the detection level will increase accordingly.

Figs. 4 and 5 show typical collapsogrammes for $l = 1$ and 2. The 52.125-μHz beat has again been removed from the MDI spectra. As expected, the detection limits scale approximately as $1/\sqrt{2l+1}$.

In velocity, the best detection limit is obtained with MDI; at $l = 1$, it is about $11\,{\rm mm\,s^{-1}}$ at 200 μHz and $3.5\,{\rm mm\,s^{-1}}$ at 1000 μHz; for $l = 2$, it is about $9\,{\rm mm\,s^{-1}}$ at 200 μHz and $2.5\,{\rm mm\,s^{-1}}$ at 1000 μHz.

3.4. *Analysis of combined data sets*

Multivariate Spectral Regression Analysis (MSRA) can be used to determine the extent to which the variance in one time series is explainable in terms of the variance of other simultaneous series (Koopmans 1974). This is analogous to coincidence methods used in cosmic ray, nuclear and particle physics. A *multivariate process* produces vector-valued events, whose components may be dependent on each other up to a certain degree. Here, we consider the full-disc time series of solar irradiance in red, green, blue and total to be the 4 components of such a multivariate process. To enhance the signal of a resonant mode we look for similarities in the variance of these 4 components. If we assume that any mode present affects all the components in a similar manner, then one would expect its signature to appear rather-more prominently in the coherent part of the four channels.

For the simpler case of two channels, the coherent part would simply correspond to the channels multiplied by their cross coherence. However, where more than two channels are available we must use MSRA to determine the coherent part (Koopmans 1974). Unlike the two-channel case, MSRA is not symmetric in the sense that the coherence is calculated with respect to only one of the channels (termed the *independent* channel).

3.4.1. *Multivariate Spectral Regression Analysis*

MSRA explains the *dependent* component $Y(t)$ of a multivariate process by linearly filtering its *n independent* components $X(t)$, as

$$Y(t) = L(X(t)) + \eta(t), \qquad (15)$$

where $Y(t)$ is the 1-dimensional process of the dependent component and $X(t)$ are the n processes of the independent components. L is a multivariate linear filter with unknown n-dimensional transfer functions $B(\lambda)$ which transform the coherent part of the independent time series $X(t)$ into the coherent part of the dependent series $Y(t)$. $\eta(t)$ is the unobservable 1-dimensional residual (error) process that is not correlated with $X(t)$.

The extent to which $Y(t)$ deviates from a linear function of $X(t)$ is measured by the unknown *spectral density function* $f^{\eta}(\lambda) = \frac{dF^{\eta}(\lambda)}{d\lambda}$, where $F^{\eta}(\lambda)$ is the spectral distribution of $\eta(t)$. $f^{\eta}(\lambda)$ and the *transfer function* are the principal parameters of interest. $B(\lambda)$ indicates how the various inputs are parceled to the output series. They are determined by minimizing the expectation value $E[\eta^2(t)]$. The transfer function of B and the spectral density function of $\eta(t)$ can be calculated according to

$$B(\lambda) = f^{Y,X}(\lambda) f^{X}(\lambda)^{-1}, \qquad (16)$$

and

$$f^{\eta}(\lambda) = f^{Y}(\lambda) - f^{Y,X}(\lambda) f^{X}(\lambda)^{-1} f^{X,Y}(\lambda), \qquad (17)$$

where $f^{X}(\lambda)$, $f^{Y,X}(\lambda)$ and $f^{X,Y}$ are the power and cross spectral density functions of $X(t)$ and $Y(t)$; they are matrices of dimension $(n \times 1)$, $(n \times n)$, $(1 \times n)$, respectively (Koopmans 1974).

Moreover, one also recovers the *total coherence*, $\rho(\lambda)$, which is analogous to the correlation coefficient in linear regression analysis. The coherence squared corresponds to the fraction of $Y(t)$ explained by $L(X(t))$; so it is a direct measure of the signal-to-noise ratio. The total coherence is derived from

$$\rho^2(\lambda) = \frac{f^{Y,X}(\lambda) f^{X}(\lambda)^{-1} f^{X,Y}(\lambda)}{f^{Y}(\lambda)}, \qquad (18)$$

and the contribution of each process to the explained part is given by the complex n-dimensional partial coherence

$$\gamma(\lambda) = \frac{f^{X}(\lambda)^{-\frac{1}{2}} f^{Y,X}(\lambda)}{f^{Y}(\lambda)^{\frac{1}{2}}}. \qquad (19)$$

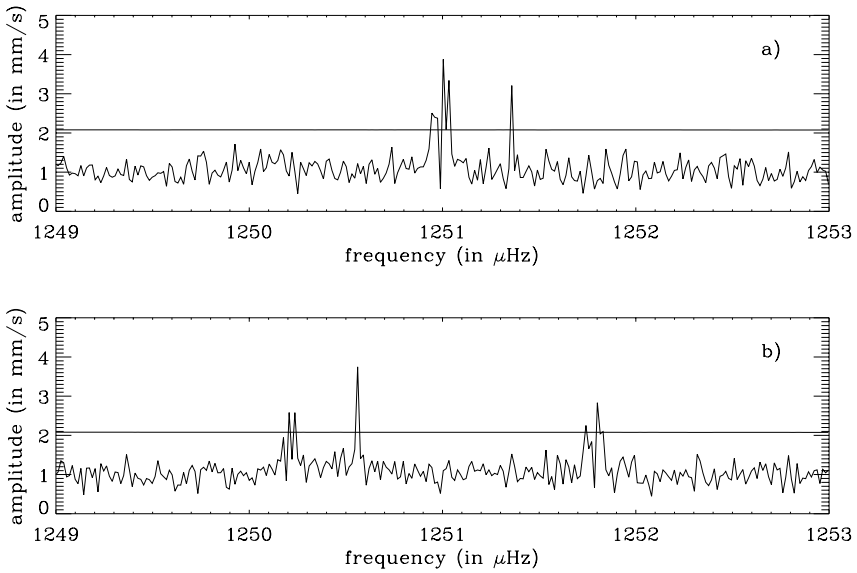

FIG. 3.— MDI collapsogramme for $l = 2$: unshifted (a), and shifted by Ω=399 nHz (b). The continuous line gives the 0.1 probability limit that a peak be due to noise in a 70 μHz bandwidth. In the amplitude spectrum, this level is about $\sqrt{4.0\bar{s}}$. This is to be compared with the value of $\sqrt{11.2\bar{s}}$ that would have been obtained from the full-disc amplitude spectrum. For the unshifted collapsogramme, the 0.1 probability limit was calculated assuming that the $2l+1$ spectra are indeed uncorrelated. Since in reality this is not the case, the limit shown underestimates the true level. The dilution of the 52.125-μHz harmonics (at 1251 μHz in the upper panel) is quite effective; peaks at 1250.2 μHz and at 1251.8 μHz are the shifted harmonics for m=2 and m=-2, respectively. The $l = 2, n = 7$ stands out well at 1250.57 μHz in the lower panel. The main contribution comes from the $l = 2, m = +2$, already detected at 1251.4 μHz in the upper panel. Some contributions from the other m help improve the signal-to-noise ratio in the lower panel.

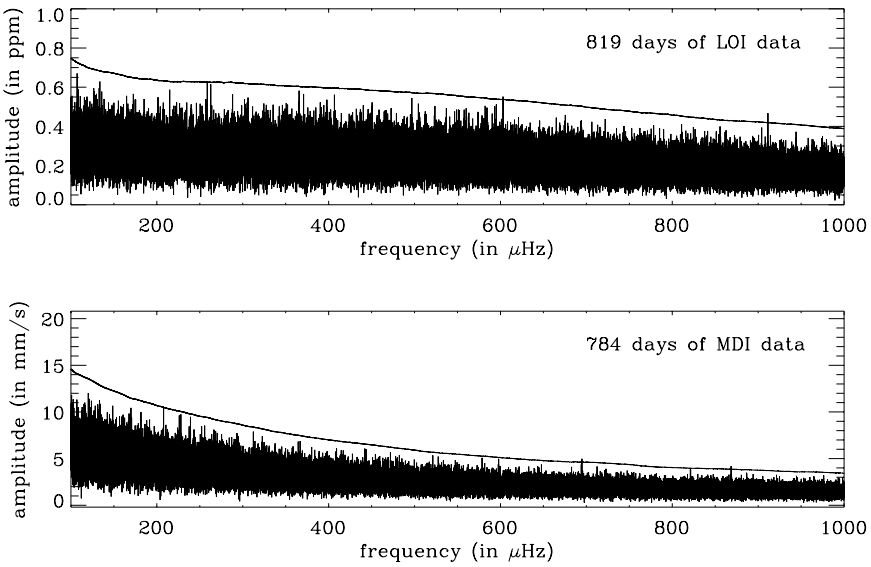

FIG. 4.— $l = 1$ collapsogramme for the LOI (top), MDI (bottom) resolved data, corrected for the spatial filter functions. The continuous line gives the 0.1 probability limit that a peak be due to noise in a 70 μHz bandwidth. The shift differs slightly between spectra since each was chosen to be an integer number of frequency bins (the observation times being different for each instrument). Note that while the magnitude of the shift is known to be valid for p modes, it is not expected to be so for g modes. The detection limit (in amplitude) is $\sqrt{5.3\bar{s}}$ both for LOI and MDI. This is to be compared with the $\sqrt{10.8\bar{s}}$ levels returned for the full-disc spectra.

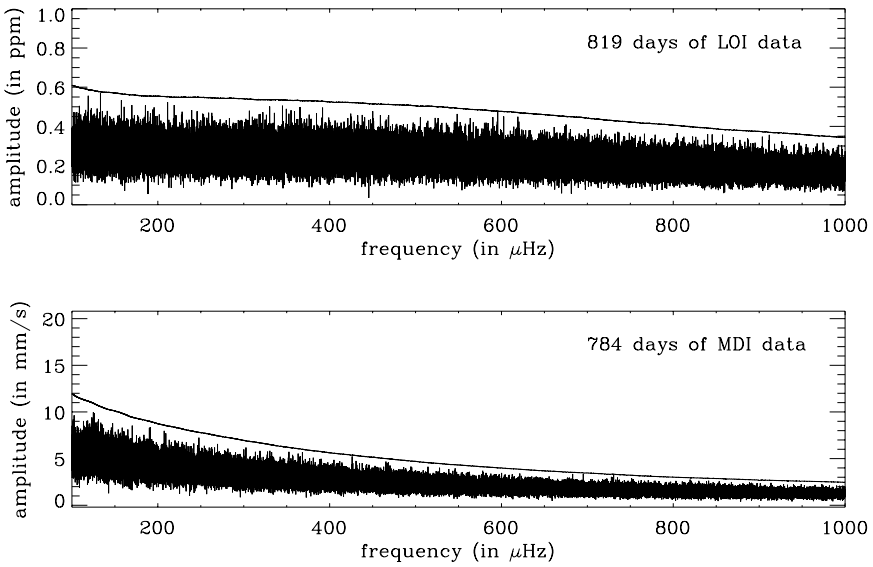

FIG. 5.— $l = 2$ collapsogramme for the LOI (top), MDI (bottom) resolved data, corrected for the spatial filter functions. The continuous line gives the 0.1 probability limit that a peak be due to noise in a 70 μHz bandwidth. The shift differs slightly between spectra, since each was chosen to be an integer number of frequency bins (the observation times being different for each instrument). Note that while the magnitude of the shift is known to be valid for p modes, it is not expected to be so for g modes. The detection limits (in amplitude) is $\sqrt{3.9\bar{5}}$ both for LOI and MDI. This is to be compared with the $\sqrt{10.8\bar{8}}$ for the full-disc spectra.

$A^{-\frac{1}{2}}$ denotes the square root of the inverse of the matrix A and the sum of $|\gamma_i(\lambda)|^2$ equals $\rho^2(\lambda)$.

3.4.2. *Application to VIRGO full-disc data*

We applied MSRA to the TSI time series measured by the PMO6 radiometer and the three spectral channels of the SPM, i.e., we selected TSI to be the independent channel and then calculated simultaneously the coherent part of all three colored channels with respect to the TSI. We set $Y(t)$ to the TSI time series and $X(t)$ to the three spectral time series and calculated the corresponding spectral density functions $f^{\rm PMO6}(\lambda)$ and $f^j(\lambda)$ (j = red, green, blue). From the *smoothed* density functions we calculated the transfer functions $B_j(\lambda)$, according to Eq. (16). Smoothing is necessary since the individual frequency bins of the density functions would otherwise be independent of each other, with the result that the coherence would then always be unity. The range of smoothing must be sufficiently large to achieve a certain confidence level, but also small enough to allow the power of a possible g mode to be of a similar level as the remaining noise power. We applied a boxcar running mean of 35 bins $\simeq 0.46$ μHz width. The total coherence squared in the g-mode range is about 0.8. This means that 80% of the variance of TSI (power in the spectrum) can be explained by the time series of the red, green and blue channels. Since the four instruments are on the same platform, the coherence is due not only to common solar noise, but also to common instrumental noise. Nevertheless, we believe that the main contribution is the Sun itself.

From the $f^j(\lambda)$ original, unsmoothed, Fourier spectra of the red, green, and blue channels of the SPM, we can calculate the coherent part of the 3 spectra with respect to the TSI spectrum according to:

$$f^{\rm coh}(\lambda) = \sum_{j=r,g,b} B_j(\lambda) f^j(\lambda). \qquad (20)$$

Here $f^{\rm coh}(\lambda)$ is the sum of all coherent features in the SPM spectra with respect to the PMO6 spectrum. If the signature of some resonant mode appears in any of the SPM spectra, it will also appear in the TSI spectrum, since these measurements also contain the response at the three colored wavelengths (but not *vice versa*). Therefore, provided the signature is present in at least one of the SPM spectra, we can be sure that it will also appear in the coherent part. This argument does not hold if the signature of some resonant mode appeared only in the TSI. This could be the case if, for example, the mode signature were much stronger at infrared wavelengths (i.e., $> 1\mu$m), that are not sampled by the SPM. In this case the infrared signal would be seen in the *incoherent residual* of the MSRA.

$$f^{\rm incoh}(\lambda) = f^{\rm PMO6}(\lambda) - f^{\rm coh}(\lambda) = f^{\rm PMO6}(\lambda) - \sum_{j=r,g,b} B_j(\lambda) f^j(\lambda), \qquad (21)$$

with $f^{\rm PMO6}(\lambda)$ the original, unsmoothed, Fourier spectrum of the TSI.

The method of analyzing the coherent part (Eq. 20) has been tested by introducing artificial modes into the VIRGO data. We added 100 sine waves of constant amplitude to the time series of all three SPM channels, and that of the TSI. In the coherent part $f^{\rm coh}(\lambda)$ of the spectra, the amplitude ratio of these sine waves was amplified by up to a factor of 2 with respect to the ambient noise level. While this certainly constitutes an improvement, it is nevertheless insufficient to reveal any g modes.

Figure 6 shows the results of the MSRA analysis for the SPM and PMO6 data. The residual spectrum does not show any evidence for g modes or very low-frequency p modes. The peaks that are visible arise from beats between the VIRGO and spacecraft timing. As noted earlier, a similar phenomenon is present in the MDI data.

3.4.3. *Application to velocity-intensity data*

A similar MSRA analysis was performed between the PMO6 intensity and MDI velocity data (Fig. 7). Here the coherence between the instruments is rather low, which implies that the solar noise in both intensity and velocity is largely uncorrelated. This fact is yet to be fully utilized in attempts to extract undetected low-frequency p modes.

4. DISCUSSION

The theoretical predictions of the expected amplitudes of solar internal g modes are at best very uncertain. Uncertainty arises from our inability to describe adequately the nature of the interaction of the modes with the convection zone and the solar atmosphere. The possibility that low-order g modes are overstable is probably no longer of relevance: amplitude limitation by three-mode resonant coupling to a stable pair of g modes of higher degrees seems likely to prevent overstable modes from achieving observable amplitudes (Dziembowski 1983, Jordinson & Gough 2000)

Andersen (1996) and Kumar et al. (1996) have recently reconsidered the problem of the excitation of g modes by turbulence in the convection zone, in somewhat different manners. Both derive similar estimates of upper limits. The larger spread in possible mode amplitudes presented by Andersen (1996) may be due to an inadequate treatment of mode damping. The upper limits for low-order g modes derived in these studies are in the range 0.01 to $1\,{\rm mm\,s^{-1}}$.

The transformation of a theoretical g-mode $\delta R/R_\odot$ perturbation to an observable Doppler shift or intensity variation is a non-trivial problem. Several papers have addressed the issues involved (Dziembowski 1977, Berthomieu & Provost 1990 and Toutain & Gouttebroze 1993, Toutain et al. 1999). Further, the determination of the theoretical conversion factor between velocity and intensity perturbations is fraught with difficulties. The simplistic approach of Isaak (1980) is to adopt

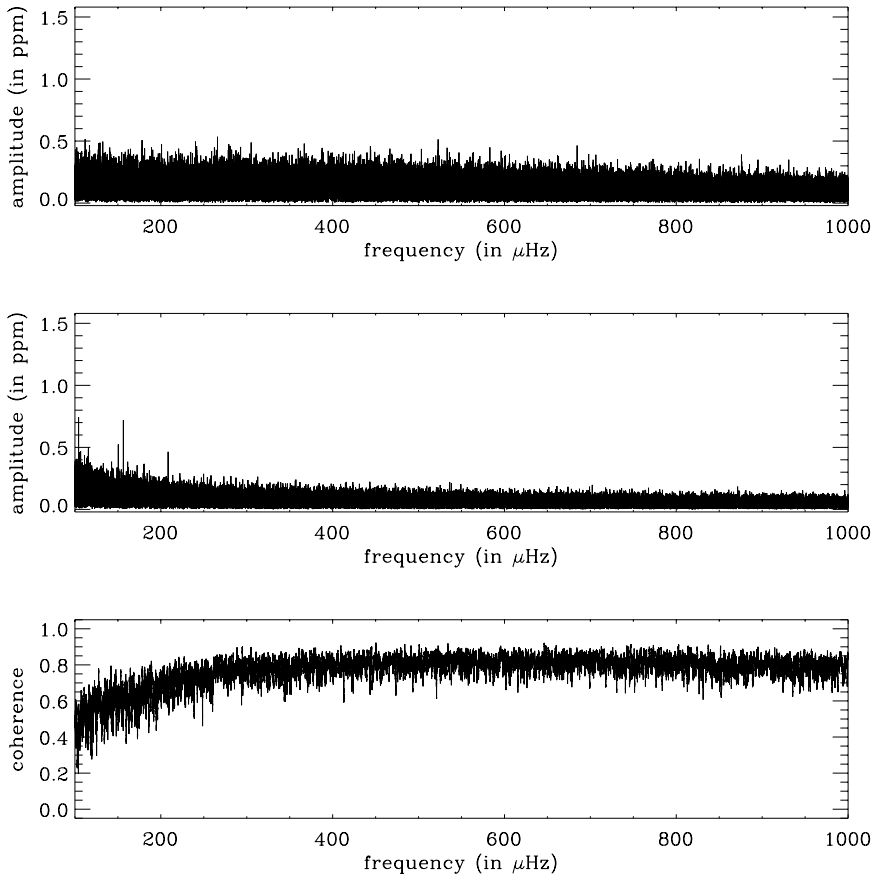

FIG. 6.— MSRA analysis of the SPM and PMO6 data: coherent part (top), incoherent part (middle), and coherence (bottom). Three out of four of the most prominent peaks are harmonics of 52.125 μHz that arise from beats between the VIRGO instrument and spacecraft timing. This phenomenon is also observed in the MDI data.

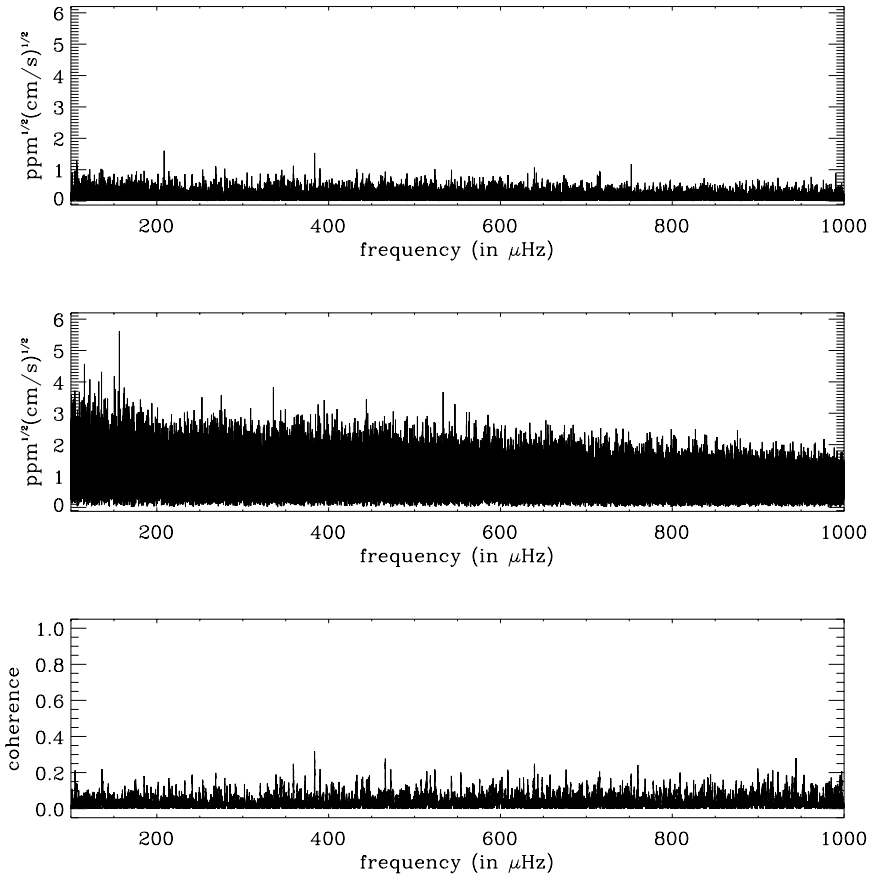

FIG. 7.— MSRA analysis of 784 days of coeval MDI velocity and PMO6 intensity data: coherent part (top), incoherent part (middle), and coherence (bottom).

the value appropriate to Cepheid variable, namely about 4 $\mathrm{cm\,s^{-1}\,ppm^{-1}}$. Theoretical calculations (Toutain et al. 1996, Houdek 1996) indicate that the ratio is strongly dependent on the frequency of oscillation, and give values for $l = 1$ of 50 to $80\,\mathrm{cm\,s^{-1}\,ppm^{-1}}$ for oscillations with frequency near 200 μHz. For higher value of l the results give numbers in the range 1 to 10 $\mathrm{cms^{-1}ppm^{-1}}$. However, both of these calculations are deficient in potentially serious respects: Houdek's calculations (which have been extended to $\nu = 200\mu$Hz , yielding the ratio $80\,\mathrm{cm\,s^{-1}\,ppm^{-1}}$) are strictly applicable to radial modes, and therefore account for neither the non-radial geometrical complexities of the radiative transfer in the atmosphere nor the effect of shear on the convective heat and momentum fluxes, whereas in the non-radial calculations of Toutain et al. convective flux perturbations are ignored altogether. If we adopt cautiously the above values, they indicate that for velocity amplitudes of a few millimeters per second we might expect intensity perturbations for low-degree g modes of below 0.01 ppm. These theoretical upper-limit estimates are well below the observational limits set by the work presented here. Here we must also point that by comparing the MDI and GOLF data (Henney et al. 1999), we can derive, as defined above in this paper, a 10% detection limit for GOLF of about $10\,\mathrm{mm\,s^{-1}}$. This is similar to the limit given in this paper. The limits set by our data suggest that the g-mode candidates of Gabriel et al. (1998) are more likely to be due to the solar noise because we are unable to detect and identify any significant peaks with an amplitude of $8\,\mathrm{mm\,s^{-1}}$ in the range 200 to 300 μHz, even if the modes are present.

In addition, we should make the reader aware that such lack of detection is consistent with the prediction by Gough (1985) and Harvey (1985). Gough predicted g-mode amplitudes no greater than $1\,\mathrm{mm\,s^{-1}}$ using turbulent stochastic excitation, while Harvey predicted a $1-\sigma$ solar noise of about 8 $\mathrm{mms^{-1}}$ for a 2-year time series. Clearly solar noise at such a level would have prevented us from detecting the g modes, even if this noise was found to be lower by about a factor 2 (Elsworth et al. 1994, Henney et al. 1999).

Given our current prejudices regarding the expected characteristics of core-penetrating g modes, it therefore seems unlikely that a firm, unambiguous detection will be made in the near future by one instrument or network alone using straightforward Fourier techniques. For example, an improvement in the signal-to-noise ratio in amplitude from single-instrument data by a factor ten – assuming a stable noise power spectral density, and a coherent mode signature over the duration of the observations – requires a factor hundred-fold increase in observing time. A coordinated, coherent approach that involves the utilization of contemporaneous data from the various active observational programs would seem to offer the best prospect of future progress. Further improvements may also come from concentrating our attentions at the solar limb. There is observational evidence to suggest that the p-mode intensity signal is amplified at the limb with respect to the disc-center values (Appourchaux & Toutain 1998, Toner et al. 1999), an effect that the PICARD instrument will attempt to take advantage of (Damé et al. 1998) in its efforts to detect g modes.

5. CONCLUSION

Nearly contemporaneous, high-quality data from both space (MDI, VIRGO on board SOHO) and ground-based (BiSON, GONG) observations have been used in an attempt to detect solar g modes. We have applied statistical analyses, a Multivariate Spectral Analysis (MSRA), and pattern-recognition techniques to these data. Although we have been unable to uncover the presence of a g-mode signature, we have nevertheless established firm upper-limit estimates to their amplitudes. These are defined as the level at which a peak has only a 10-% probability of appearing by chance over a 70-μHz bandwidth. At a frequency of $\sim 200\,\mu$Hz the statistical approach yields an upper limit of about 10 $\mathrm{mms^{-1}}$ in velocity, and 0.5 ppm in intensity. The MSRA gives a slightly lower limit. The results confirmed theoretical prediction regarding the non-detectability of the solar g modes.

The authors of this paper form the *Phoebus* collaboration. The *Phoebus* team members gratefully acknowledges the support of ESA in organizing and financing this collaboration. SOHO is a mission of international collaboration between ESA and NASA. BiSON is funded by the UK Particle Physics and Astronomy Research Council (PPARC). We would like to thank the members of the VIRGO and MDI teams for providing such excellent instrumentation. We thank all members of the BiSON team in Birmingham, and our hosts at each of the BiSON sites. WJC acknowledges the support of an ESA Internal Fellowship. TS acknowledges the support of PPARC. This work utilizes data obtained by the Global Oscillation Network Group (GONG) project managed by the National Solar Observatory, a Division of the National Optical Astronomy Observatories, which is operated by AURA, Inc. under a cooperative agreement with the National Science Foundation. The GONG data were acquired by instruments operated by the Big Bear Solar Observatory, High Altitude Observatory, Learmonth Solar Observatory, Udaipur Solar Observatory, Instituto de Astrofísico de Canarias and Cerro Tololo Interamerican Observatory. One of the authors (TA) would like to dedicate this paper to the memory of *Ah Kin* (He of the Sun in the Maya language), a caring cat, always purring to console the family.

APPENDIX

SPATIAL FILTER FUNCTION CALCULATION

Definition of the spatial filter function

Let us suppose that $q(\theta,\phi,t)$ is some physical quantity (say, velocity) on the Sun expressed as:

$$q(\theta,\phi,t) = \sum_{l,m} q_{l,m}(t) Z_l^m(\theta,\phi) \tag{A1}$$

where t is the time, (θ,ϕ) are the spherical coordinates, $q_{l,m}(t)$ represents the time dependence of the oscillation generated by stochastic oscillations and $Z_l^m(\theta,\phi)$ describes the horizontal variation of the radial velocity (or intensity) whose normalization is defined as:

$$\frac{1}{4\pi}\int_\Omega |Z_l^m(\theta,\phi)|^2 d\Omega' = 1 \tag{A2}$$

where Ω represents the solar sphere. Observation and data analysis procedures produce the observed component $Q(t)$. The observable $Q(t)$ is derived from the local perturbation. For instance, the line-of-sight velocity is derived from the horizontal and vertical displacements, while the intensity is derived from opacity and temperature perturbations. The observable $Q_{l',m'}(t)$ is assumed to have the form:

$$Q_{l',m'}(t) = \int_{\mathcal{D}_\odot} q(\theta,\phi,t) D_{l'}^{m'}(\theta,\phi) d\Omega \tag{A3}$$

where $\mathcal{D}_\odot$ is the visible solar disc and $D_m^l(\theta,\phi)$ is a weight applied to the solar disc for extracting the (l,m) mode signal. $D_m^l(\theta,\phi)$ depends on the way the observation has been made and also on the data analysis procedure; it includes the projection effect, limb darkening (if applicable), and the (l,m) mask and any other factor that might arise from the procedure. Putting Eq. A1 into Eq. A3, we get:

$$Q_{l',m'}(t) = \sum_{l,m} q_{l,m}(t) \int_{\mathcal{D}_\odot} Z_l^m(\theta,\phi) D_{l'}^{m'}(\theta,\phi) d\Omega \tag{A4}$$

$$= \sum_{l,m} q_{l,m}(t) s_{l,m}^{l',m'} \tag{A5}$$

where

$$s_{l,m}^{l',m'} = \int_{\mathcal{D}_\odot} Z_l^m(\theta,\phi) D_{l'}^{m'}(\theta,\phi) d\Omega \tag{A6}$$

When there is only one component 'present', i.e. $l = l'$ and $m = m'$, then $Q(t) = S_{l,m} q_{l,m}(t)$, and the RMS amplitude of the observed signal is related to the RMS amplitude of the perturbation via:

$$< Q(t) > = |S_{l,m}| < q_{l,m}(t) > \tag{A7}$$

where $S_{l,m}$ is defined as:

$$S_{l,m} = \int_{\mathcal{D}_\odot} Z_l^m(\theta,\phi) D_l^m(\theta,\phi) d\Omega \tag{A8}$$

Spatial filter function for velocity

Perturbation

The velocity is the derivative of the displacement. We have assumed that the main contribution to the velocity is a vertical displacement whose spatial distribution is proportional to the spherical harmonics. Therefore, we have for the vertical velocity:

$$Z_l^m(\theta,\phi) = \sqrt{4\pi} Y_l^m(\theta,\phi) \tag{A9}$$

where $Y_l^m(\theta,\phi)$ are the spherical harmonics.

Full-disc calculation

For full-disc velocity observation, the weight function is given by:

$$D_l^m(\theta,\phi) = \frac{I(\sin\theta\cos\phi)\sin^2\theta\cos^2\phi}{\int_{\mathcal{D}_\odot} I(\sin\theta\cos\phi)\sin^2\theta\cos\phi d\theta d\phi}, \tag{A10}$$

where I is the intensity on the solar disk. Thus the spatial filter function can be written as:

$$S_{l,m}^{\rm BiSON} = \frac{\sqrt{4\pi}\int_{\mathcal{D}_\odot} Y_l^m(\theta,\phi) I(\sin\theta\cos\phi)\sin^3\theta\cos^2\phi d\theta d\phi}{\int_{\mathcal{D}_\odot} I(\sin\theta\cos\phi)\sin^2\theta\cos\phi d\theta d\phi}. \tag{A11}$$

Imaging instrument calculation

For resolved velocity observations, the weight function is given by:

$$D_l^m(\theta,\phi) = \frac{1}{n_{l,m}} Y_l^{m*}(\theta,\phi)\sin^2\theta\cos^2\phi \tag{A12}$$

where the symbol * denotes the complex conjugate and $n_{l,m}$ is a normalization factor. Depending on how the data reduction is performed, the normalization may vary. In the case of MDI, $n_{l,m}$ is chosen such that:

$$S_{l,m}^{\rm MDI} = 1 \tag{A13}$$

Spatial filter function for intensity

Perturbation

For intensity, the main contribution was assumed to come from the perturbation of the temperature. This is an approximation because opacity perturbations and surface distortions should also be included. In this case we also have:

$$Z_l^m(\theta,\phi) = \sqrt{4\pi} Y_l^m(\theta,\phi) \tag{A14}$$

Full-disc calculation

For full-disc intensity observations, the weight function is given by:

$$D_l^m(\theta,\phi) = \frac{I(\sin\theta\cos\phi)\sin\theta\cos\phi}{\int_{\mathcal{D}_\odot} I(\sin\theta\cos\phi)\sin^2\theta\cos\phi d\theta d\phi} \tag{A15}$$

and the spatial filter function can be written as:

$$S_{l,m}^{\rm SPM} = \frac{\sqrt{4\pi}\int_{\mathcal{D}_\odot} Y_l^m(\theta,\phi) I(\sin\theta\cos\phi)\sin^2\theta\cos\phi d\theta d\phi}{\int_{\mathcal{D}_\odot} I(\sin\theta\cos\phi)\sin^2\theta\cos\phi d\theta d\phi} \tag{A16}$$

Imaging instrument calculation

The LOI is an imaging intensity instrument with pixels that are rather large compared to the degrees to be observed. A continuous calculation is not proper. The spatial filter function is then derived from the way the pixel data is combined:

$$S_{l,m} = \frac{1}{3}\sum_i w_i^{(l,m)*}\tilde{y}_i^{(l,m)} \tag{A17}$$

where $\tilde{y}_i^{(l,m)}$ is the spatial filter function of pixel i given by:

$$\tilde{y}_i^{(l,m)} = \frac{\sqrt{4\pi}\int_{\mathcal{D}_i} Y_l^m(\theta,\phi) I(\sin\theta\cos\phi)\sin^2\theta\cos\phi d\theta d\phi}{\int_{\mathcal{D}_i} I(\sin\theta\cos\phi)\sin^2\theta\cos\phi d\theta d\phi} \tag{A18}$$

where $\mathcal{D}_i$ is the integration domain of the i-th LOI pixel. The weights applied are then:

$$w_i^{(l,m)} = \frac{\tilde{y}_i^{(l,m)}}{\sqrt{\sum_i \tilde{y}_i^{(l,m)*}\,\tilde{y}_i^{(l,m)}}} \tag{A19}$$

and the spatial filter function is written as:

$$S_{l,m}^{\mathrm{LOI}} = \sqrt{\frac{1}{9}\sum_i \tilde{y}_i^{(l,m)*}\,\tilde{y}_i^{(l,m)}} \tag{A20}$$

REFERENCES

Andersen B. N. 1996, A&A, 312, 610
Anklin M., Fröhlich C., Finsterle W., Crommelynck D. A., Dewitte S. 1998, Metrologia, 35, 686
Appourchaux T., Andersen B., Chaplin W., Elsworth Y., Finsterle W., Fröhlich C., Gough D., Hoeksema J. T., Isaak G., Kosovichev A., Provost J., Scherrer P., Sekii T., Toutain T. 1998a, in S. Korzenik, A. Wilson (eds.), Structure and Dynamics of the Interior of the Sun and Sun-like Stars, ESA SP-418, ESA Publications Division, Noordwijk, The Netherlands, p. 95
Appourchaux T., Andersen B., Fröhlich C., Jimenez A., Telljohann U., Wehrli C. 1997, Sol. Phys., 170, 27
Appourchaux T., Andersen B. N. 1990, Sol. Phys., 128, 91
Appourchaux T., Gizon L., Rabello-Soares M. C. 1998b, A&AS, 132, 107
Appourchaux T., Toutain T. 1998, in J. Provost, F.-X. Schmider (eds.), Sounding solar and stellar interiors – IAU 181 – Poster volume, 5
Berthomieu G., Provost J. 1990, A&A, 227, 563
Brookes J. R., Isaak G. R., van der Raay H. B. 1976, Nature, 259, 92
Brookes J. R., Isaak G. R., van der Raay H. B. 1978a, MNRAS, 185, 19
Brookes J. R., Isaak G. R., van Der Raay H. B. 1978b, MNRAS, 185, 1
Brown T. M., Stebbins R. T., Hill H. A. 1978, ApJ, 223, 324
Christensen-Dalsgaard J. 1989, MNRAS, 239, 977
Christensen-Dalsgaard J. 1998, in S. Korzenik, A. Wilson (eds.), Structure and Dynamics of the Interior of the Sun and Sun-like Stars, ESA SP-418, ESA Publications Division, Noordwijk, The Netherlands, 17
Damé L., Hersé M., Thuillier G., Appourchaux T., Crommelynck D., Dewitte S., Joukoff, A. Fröhlich C., Laclare F., Delmas C., Boumier P. 1998, Adv. Space Research, 24 (2), 295
Delache P., Scherrer P. H. 1983, Nature, 306, 651
Denison D. G. T., Walden A. T. 1999, ApJ, 514, 972
Dziembowski W. 1977, Acta Astronomica, 27, 203
Dziembowski W. A. 1983, Sol. Phys., 82, 259
Elsworth Y., Howe R., Isaak G. R., McLeod C. P., Miller B. A., New R., Speake C. C., Wheeler S. J. 1994, MNRAS, 269, 529
Elsworth Y., Howe R., Isaak G. R., McLeod C. P., Miller B. A., van Der Raay H. B., Wheeler S. J., New R. 1995, in ASP Conf. Ser. 42: GONG 1992. Seismic Investigation of the Sun and Stars, p. 392
Fröhlich C., Andersen B. N. 1995, in J. T. Hoeksema, V. Domingo, B. Fleck, B. Patrick (eds.), Forth SOHO Workshop: Helioseismology (Invited Reviews), ESA-SP-376, Noordwijk NL, p. 137
Fröhlich C., Delache P. 1984, in R. K. Ulrich, J. Harvey, E. J. Rhodes, J. Toomre (eds.), Solar Seismology from Space, JPL Publ.84-84, Pasadena, p. 183
Fröhlich C., Romero J., Roth H., Wehrli C., Andersen B. N., Appourchaux T., Domingo V., Telljohann U., Berthomieu G., Delache P., Provost J., Toutain T., Crommelynck D. A., Chevalier A., Fichot A., Dappen W., Gough D., Hoeksema T., Jimenez A., Gomez M. F., Herreros J. M., Cortès T. R., Jones A. R., Pap J. M., Willson R. C. 1995, Sol. Phys., 162, 101
Gabriel A., Turck-Chièze S., García R., Pallé P., Boumier P., Thiery S., Grec G., Ulrich R., Bertello L., Roca Cortés, Robillot J.-M. 1998, in S. Korzenik, A. Wilson (eds.), Structure and Dynamics of the Interior of the Sun and Sun-like Stars, ESA SP-418, ESA Publications Division, Noordwijk, The Netherlands, 61
Gough D. O. 1985, in E. Rolfe, B.Battrick (eds.), Future Missions in Solar, Heliospheric and Space Plasma Physics, ESA SP-235, ESA Publications Division, Noordwijk, The Netherlands, p. 183
Harvey J. 1985, in E. Rolfe, B.Battrick (eds.), Future Missions in Solar, Heliospheric and Space Plasma Physics, ESA SP-235, ESA Publications Division, Noordwijk, The Netherlands, p. 199
Harvey J., Hill F., Hubbard J., Kennedy J., Leibacher J., Pintar J., Gilman P., Noyes R., Title A., Toomre J., Ulrich R., Bhatnagar A., Kennewell J., Marquette W., Patrón J., Saá O., Yasukawa E. 1996, Science, 272, 1284
Henney C. J., Ulrich R. K., Bertello L., Bogart R. S., Bush R. I., Scherrer P. H., Cort/'es T. R., Turck-Chièze S. 1999, A&A, 348, 627
Hill F., Stark P., Stebbins R., Anderson E., Antia H., Brown T., Duvall, Jr. T., Haber D., Harvey J., Hathaway D., Howe R., Hubbard R., Jones H., Kennedy J., Korzennik S., Kosovichev A., Leibacher J., Libbrecht K., Pintar J., Rhodes, Jr. E., Schou, J. Thompson M., Tomczyk S., Toner C., Toussaint R., Williams W. 1996, Science, 272, 1292
Hoeksema J., Bush R., Mathur D., Morrison M., Scherrer P. 1998, IAU Symposia, 181, 31
Hoogeveen G. W., Riley P. 1998, Sol. Phys., 179, 167
Houdek G. 1996, *Ph.D. thesis*, Universität Wien
Isaak G. R. 1980, Nature, 283, 644
Jones H. P. 1989, Sol. Phys., 120, 211
Jordinson C., Gough D. 2000, in L.Szabados, D.W.Kurtz (eds.), The impact of large-scale surveys on pulsating-star research, in press
Koopmans L. 1974, The Spectral Analysis of Time Series, Academic Press, Inc., London, GB
Kumar P., Quataert E. J., Bahcall J. N. 1996, ApJ, 458, L83
Marsden R. G., Smith E. J., Cooper J. F., Tranquille C. 1996, A&A, 316, 279
Rabello-Soares M. C., Appourchaux T. 1999, A&A, 345, 1027
Riley P., Sonett C. P. 1996, Geophys. Res. Lett., 23, 1541
Scherrer P. H., Bogart R. S., Bush R. I., Hoeksema J. T., Kosovichev A. G., Schou J., Rosenberg W., Springer L., Tarbell T. D., Title A., Wolfson C. J., Zayer I., Mdi Engineering Team 1995, Sol. Phys., 162, 129
Scherrer P. H., Wilcox J. M., Kotov V. A., Severny A. B., Tsap T. T. 1979, Nature, 277, 635
Severny A. B., Kotov V. A., Tsap T. T. 1976, Nature, 259, 87
Thomson D. J., Maclennan C. G., Lanzerotti L. J. 1995, Nature, 376, 139
Toner C. G., Jefferies S. M., Toutain T. 1999, ApJ, 518, L127
Toutain T., Berthomieu G., Provost J. 1999, A&A, 344, 188
Toutain T., Berthomieu G., Provost J., Gouttebroze P. 1996, in J. Hoeksema, V. Domingo, B. Fleck, B. Battrick (eds.), 4th SOHO workshop – Helioseismology – Vol 2, ESA SP-376, ESA Publications Division, Noordwijk, The Netherlands, p. 419
Toutain T., Gouttebroze P. 1993, A&A, 268, 309

Partie III

Transfert de connaissances

Chapitre 7

Gestion d'équipes de travail

7.1 Equipe LOI

Le succès de la construction d'un instrument spatial tel que le Luminosity Oscillations Imager a été rendu possible par une équipe de travvail que j'ai dirigée de 1989 à 1996. Cette équipe était composée de:

- Udo Telljohann: ingénieur électronicien principal, chargé du système d'acquisition des données du LOI et de ses interfaces électriques avec VIRGO,
- Didier Martin: ingénieur électronicien assitant, chargé de la conception de l'alimentation haute-tension pour le guidage et de la modélisation du comportement du detecteur optique,
- Thierry Beaufort: technicien chargé du contrôle et des tests des cartes électroniques,
- Samuel Lévêque: ingénieur chargé de la propreté du LOI et des tests thermo-optiques du détecteur,
- Jos Fleur: dessinateur chargé de la mécanique du LOI et de ses interfaces mécaniques avec VIRGO

En plus de cette gestion humaine, il faut ajouter une gestion de contrats nécessaires pour la fabrication des actuateurs piézo-électriques (Queensgate, Royaume-Uni), du détecteur (AME, Norvège), du filtre (Andover, Etats-Unis) et du télescope (SESO, France). Bien sûr le succès du LOI n'aurait pas été non plus possible sans une communication scientifique

et technique avec l'équipe de PMOD/WRC qui était en charge de construire l'instrument VIRGO.

7.2 Equipe Phoebus

En 1997, j'ai initié la création d'un groupe de travail dont le but principal est de détecter les modes g. Cette équipe est composée de membres des équipes de BiSON, MDI et VIRGO nomémment:

- Georges Isaak, William Chaplin, Yvonne Elsworth, Université de Birmingham (BiSON)
- Phil Scherrer, Alexander Kosovichev, Todd Hoeksema, Université de Stanford (MDI)
- Bo Andersen, Norwegian Space Center (VIRGO)
- Claus Fröhlich, Wolfgang Finsterle, World Radiation Center (VIRGO)
- Thierry Toutain, Gabrielle Berthomieu, Janine Provost, Observatoire de Nice (VIRGO)
- Douglas Gough, Takashi Sekii[9], Université de Cambridge (MDI et VIRGO)

Le groupe s'est réuni 3 fois lors de séances de travail que j'ai organisées au centre de l'ESA situé à Noordwijk. Ces séances de travail étaient préparées par des téléconférences bimensuelles. Les résultats de ces travaux sont accessibles sur la page Internet de VIRGO. Ils incluent un article accepté par *The Atrophysical Journal* relatant la valeur limite supérieure de l'amplitude des modes g.

[9]Maintenant à l'Observatoire Astronomique National de Tokyo

Chapitre 8

Encadrement d'étudiants et de post-docs

J'ai encadré les étudiants ou post-doc suivants:

- Thierry Toutain (post-doc) de 1992 à 1994 avec lequel j'ai co-signé un article dans A&A. Le travail porta sur la détermination des barres d'erreurs dans la détermination des paramètres héliosismiques. Il a maintenant un poste permanent de Chargé de Recherches à l'Observatoire de Nice.

- Laurent Gizon (stagiaire) de Novembre 1996 à Mai 1997 avec lequel j'ai co-signé 2 articles dans A&A Sup. Series et 2 articles dans des conférences. Le travail porta sur de nouvelles techniques d'ajustement des mesures héliosismiques, permettant notamment de déterminer l'inclinaison de l'axe de rotation du coeur solaire. Il prépare une thèse à l'Université de Stanford, Californie.

- Maria-Cristina Rabello-Soares (post-doc) d'Avril 1997 à Octobre 1997 avec laquelle j'ai co-signé 2 articles dans A&A Sup. Series, un article dans A&A et 4 articles dans des conférences. Le travail porta sur de nouvelles techniques d'ajustement des mesures héliosismiques appliquée aux données GONG. Après avoir eu une position de post-doc à l'université d'Århhus, elle a maintenant un autre post-doc à l'Université de Stanford.

- Mohamed Lazrek (post-doc) de Juin 1998 à Novembre 1998 avec lequel j'ai co-signé un article dans un atelier de travail. Le travail porta sur la détermination des biais dans

les mesures héliosismiques effectuées par des instrument regardant le Soleil comme une étoile.

- William Chaplin (post-doc) d'Octobre 1998 á Août 1999 avec lequel j'ai co-signé 2 articles acceptés par MNRAS. Le travail porta sur la détermination des caractéristiques de la source excitant les modes p solaires. Il a maintenant un poste de chercheur-enseignant à l'Université de Birmingham.

- David Fierry-Fraillon (post-doc) depuis Février 2000. Son travail porte sur l'effet de l'activité solaire sur le 'splitting' rotationnel, et de l'étude de la qualité de l'image solaire observée par le LOI.

Chapitre 9

Page Internet de Virgo

Tout travail scientifique ne saurait se faire sans avoir recourt aux moyens modernes de communications. L'introduction d'Internet il y quelques 30 ans a initié une révolution qui commença à se faire sentir dans le milieu des années 1990. Il devenait assez populaire de créer une 'home page': une fenêtre sur une activite particulière. En Février 1995, je me lançait aussi dans la creation d'une 'home page' pour l'instrument VIRGO. Apres quelques évolutions, la page VIRGO a maintenant un aspect bien connu. Sur cette page on peut trouver differentes informations utiles telles que:

- Description de l'instrument VIRGO et de ses sous-ensembles
- La science faite avec VIRGO: héliosismologie et radiométrie
- Les activités de mise à jour de la page
- Les membres de l'équipe VIRGO
- La liste des papiers des co-investigateurs de VIRGO rangée par thèmes
- En accès libre, des procédures IDL pour ajuster les données héliosismiques
- Le statut de l'instrument

Il est aussi possible de pointer vers d'autres pages utiles tel que celle du satellite SOHO, ou celle d'autres instruments héliosismiques. Un pointeur dirige aussi directement vers la 'home page' du groupe Phoebus (groupe de recherche de modes g).

Chapitre 10

Interventions dans les écoles

Je me aussi suis impliqué dans l'école française de La Haye aux Pays-Bas. J'estime qu'il est important de transmettre sa passion à des jeunes enfants en démythifiant l'aura que peut avoir un chercheur astrophysicien de surcroit. Il est aussi important de leur faire prendre conscience de notre place dans l'Univers. Cette prise de conscience doit se faire jeune, plus tard beaucoup trop de conceptions erronnées peuvent être un frein quant à la compréhension de la place de l'Humanité dans l'Univers.

J'ai réalisé les exposés suivants:

- Terminale: l'exploration scientifique du Soleil (1996)
- CE1, CE2: Le Soleil et le satellite SOHO (1996, 2000)
- Lycée de La Haye: une soirée au télescope avec la comète Hale-Bopp (1997)
- Grande section de Maternelle: Les premiers hommes sur la Lune (1997)
- CE1, CE2: Le système solaire (1999, 1997)
- CM2: Héliosismologie (1998)
- CM1: Exploration spatiale du système solaire (1998)

Partie IV

Liste de publications

Journaux à comité de lecture

Appourchaux T. 1987, 'The Faraday effect in a magneto-optical filter', *Sol. Phys.*, **109**, 393

Appourchaux T. 1989, 'Optimization of parameters for helioseismology experiments measuring solar radial velocities', *A&A*, **222**, 361

Appourchaux T., Andersen B., Fröhlich C., Jiménez A., Telljohann U., Wehrli C. 1997, 'In-Flight Performance of the Virgo Luminosity Oscillations Imager Aboard SOHO', *Sol. Phys.*, 170, 27

Appourchaux T., Andersen B. N. 1990, 'Observations of low-degree solar oscillations with few detector elements', *Sol. Phys.*, **128**, 91

Appourchaux T., Cislaghi M. 1992, Passive thermal control of a multilayer filter for space-based solar observations, *Optical Engineering*, **31**, 1715

Appourchaux T., Fröhlich C., Andersen B., Berthomieu G., Chaplin W., Elsworth Y., Finsterle W., Gough D., Hoeksema J. T., Isaak G., Kosovichev A., Provost J., Scherrer P., Sekii T., Toutain T. 2000, 'Observational upper limits for low-degree solar g modes', *ApJ*, **538**, *in press*

Appourchaux T., Gizon L., Rabello-Soares M. C. 1998a, 'The art of fitting p-mode spectra. I. Maximum likelihood estimation', *A&AS*, **132**, 107

Appourchaux T., Rabello-Soares M. C., Gizon L. 1998b, 'The art of fitting p-mode spectra. II. Leakage and noise covariance matrices', *A&AS*, 132, 121

Appourchaux T., Toutain T., Telljohann U., Jiménez A., Rabello-Soares M. C., Andersen B. N., Jones A. R. 1995, 'Frequencies and splittings of low-degree solar p modes: results of the Luminosity Oscillations Imager', *A&A*, **294**, L13

Appourchaux T. P., Gourmelon G., Johlander B. 1994, Effect of gamma-ray irradiations on optical filter glass, *Optical Engineering*, **33**, 1659

Chaplin W. J., Appourchaux T. 1999, 'Depth of excitation and reversal of asymmetry of low-l solar p modes: a complementary analysis of BiSON and VIRGO/SPM data, *MNRAS*, **309**, 761

Chaplin W. J., Appourchaux T., Elsworth Y., Isaak G., Miller B., New R. 2000, 'Source of excitation of low-l p modes: characteristics and solar-cycle variations', *MNRAS*, in press

Fröhlich C., Andersen B., Appourchaux T., Berthomieu G., Crommelynck D. A., Domingo V., Fichot A., Finsterle W., Gomez M. F., Gough D., Jiménez A., Leifsen T., Lombaerts M., Pap J. M., Provost J., Cortés T. R., Romero J., Roth H., Sekii T., Telljohann U.,

Toutain T., Wehrli C. 1997, 'First results from VIRGO, the experiment for helioseismology and solar irradiance monitoring on SOHO', *Sol. Phys.*, **170**, 1

Fröhlich C., Romero J., Roth H., Wehrli C., Andersen B. N., Appourchaux T., Domingo V., Telljohann U., Berthomieu G., Delache P., Provost J., Toutain T., Crommelynck D. A., Chevalier A., Fichot A., Däppen W., Gough D., Hoeksema T., Jiménez A., Gomez M. F., Herreros J. M., Cortés T. R., Jones A. R., Pap J. M., Willson R. C. 1995, 'VIRGO: Experiment for Helioseismology and Solar Irradiance Monitoring', *Sol. Phys.*, **162**, 101

Martić M., Schmitt J., Lebrun J. C., Barban C., Connes P., Bouchy F., Michel E., Baglin A., Appourchaux T., Bertaux J. L. 1999, 'Evidence for global pressure oscillations on Procyon', *A&A*, **351**, 993

Oliviero M., Severino G., Straus T., Jefferies S. M., Appourchaux T. 1999, 'Space and Time Analysis of the Solar Photospheric Dynamics at Moderate-l Values', *ApJ*, **516**, L45

Rabello-Soares M. C., Appourchaux T. 1999, 'Solar low-degree p-mode parameters from the GONG network', *A&A*, 345, 1027

Rabello-Soares M. C., Roca Cortés T., Jiménez A., Andersen B. N., Appourchaux T. 1997, 'An estimate of the solar background irradiance power spectrum', *A&A*, **318**, 970

Rabello Soares M. C., Roca Cortés T., Jiménez A., Appourchaux T., Eff-Darwich A. 1997, 'Contribution of Low-l p Modes to the Solar Equatorial Rotation Profile', *ApJ*, **480**, 840

Toutain T., Appourchaux T. 1994, 'Maximum likelihood estimators: an application to the estimation of the precision of helioseismic measurements', *A&A*, **289**, 649

Toutain T., Appourchaux T., Baudin F., Fröhlich C., Gabriel A., Scherrer P., Andersen B. N., Bogart R., Bush R., Finsterle W., Garcia R. A., Grec G., Henney C. J., Hoeksema J. T., Jiménez A., Kosovichev A., Cortés T. R., Turck-Chièze S., Ulrich R., Wehrli C. 1997, 'Tri-Phonic Helioseismology: Comparison of Solar P Modes Observed by the Helioseismology Instruments Aboard SOHO', *Sol. Phys.*, **175**, 311

Toutain T., Appourchaux T., Fröhlich C., Kosovichev A. G., Nigam R., Scherrer P. H. 1998, 'Asymmetry and Frequencies of Low-Degree p Modes and the Structure of the Sun's Core', *ApJ*, **506**, L147

Publications dans des conférences

Andersen B., Aarset M., Leifsen T., Appourchaux T., Fröhlich C., Hoeksema J. T., Jiménez A., Toutain T., Wehrli C. 1998a, 'Statistical properties of the amplitude modulation of solar p modes', in Structure and Dynamics of the Interior of the Sun and Sun-like Stars, S. Korzenik and A. Wilson (eds.), ESA SP-418, ESA Publications Division, Noordwijk, The Netherlands, p. 897

Andersen B., Appourchaux T., Crommelynck D., Fröhlich C., Jiménez A., Rabello-Soares M., Wehrli C. 1998b, 'Properties of the solar background signal from VIRGO', in Sounding Solar and Stellar Interiors, IAU 181, Poster volume, J. Provost and F.-X. Schmider (eds.), Kluwer Academic Publishers, Dordrecht, p. 3

Andersen B., Leifsen T., Appourchaux T., Fröhlich C., Hoeksema J. T., Toutain T., Wehrli C. 1998c, 'The effect of amplitude modulation on asymmetries of solar p modes', in Structure and Dynamics of the Interior of the Sun and Sun-like Stars, S. Korzenik and A. Wilson (eds.), ESA SP-418, ESA Publications Division, Noordwijk, The Netherlands, p. 893

Appourchaux T. 1984, 'Correction of Atmospheric Transparency Gradient Effect on Solar Radial Velocities', in Space Research in Stellar Activity and Variability, A.Mageney and F.Praderie (eds.), Observatoire de Meudon, p. 117

Appourchaux T. 1988, 'Solar oscillations instrumentation and measurement theory', in Seismology of the Sun and Sun-Like Stars, V.Domingo and E.J.Rolfe (eds.), ESA SP-286, ESA Publications Division, Noordwijk, The Netherlands, p. 595

Appourchaux T. 1993, 'Effect of space radiations on optical filters', in SPIE, Vol. **2018**, p. 80

Appourchaux T. 1998, 'The Structure of the Solar Core: an Observer's Point of View', **Revue invitée**, in Structure and Dynamics of the Interior of the Sun and Sun-like Stars, S. Korzenik and A. Wilson (eds.), ESA SP-418, ESA Publications Division, Noordwijk, The Netherlands, p. 37

Appourchaux T., Andersen B., Chaplin W., Elsworth Y., Finsterle W., Frohlich C., Gough D., Hoeksema J. T., Isaak G., Kosovichev A., Provost J., Scherrer P., Sekii T., Toutain T. 1998a, 'Comparative Studies of Low-Order and Low-Degree Solar p Modes', in Structure and Dynamics of the Interior of the Sun and Sun-like Stars, S. Korzenik and A. Wilson (eds.), ESA SP-418, ESA Publications Division, Noordwijk, The Netherlands, p. 95

Appourchaux T., Chaplin W. J., Elsworth Y., Isaak G. R., MCLeod C. P., Miller B. A., New R. 1998b, 'A comparison of low-degree solar p-mode frequencies from BISON and LOI', in New eyes to see inside the sun and the stars, IAU 185, F.-L. Deubner, J.Christensen-Dalsgaard and D.Kurtz (eds.), Kluwer Academic Publishers, Dordrecht, The Netherlands, p. 45

Appourchaux T., Domingo V., Fröhlich C., Romero J., Wehrli C., Andersen B. N., Berthomieu G., Delache P., Crommelynck D., Jiménez A., Roca Cortés T., Jones A. R. 1995a, 'VIRGO - the Solar Monitor Experiment on SOHO', in ASP Conf. Ser. 76: GONG 1995. Helio- and Astero-Seismology, p. 408

Appourchaux T., et al. 1995a, 'Results from the Luminosity Oscillations Imager', in Helioseismology, 4th SOHO workshop, Poster session, J. Hoeksema, V. Domingo, B. Fleck and B. Battrick (eds.), ESA SP-376, ESA Publications Division, Noordwijk, The Netherlands, p. 265P

Appourchaux T., et al. 1995b, 'The Luminosity Oscillations Imager on Board Virgo: Design and Performances', in Helioseismology, 4th SOHO workshop, Poster session, J. Hoeksema, V. Domingo, B. Fleck and B. Battrick (eds.), ESA SP-376, ESA Publications Division, Noordwijk, The Netherlands, p. 359P

Appourchaux T., Gizon L. 1998, 'The art of fitting p-mode spectra', in New eyes to see inside the sun and the stars, IAU 185, F.-L. Deubner, J.Christensen-Dalsgaard and D.Kurtz (eds.), Kluwer Academic Publishers, Dordrecht, The Netherlands, p. 43

Appourchaux T., Gough D., Sekii T., Toutain T. 1998c, 'An unbiased average rotational splitting from VIRGO/SPM?', in Sounding Solar and Stellar Interiors, IAU 181, Poster volume, J. Provost and F.-X. Schmider (eds.), Kluwer Academic Publishers, Dordrecht, p. 3

Appourchaux T., Martin D., Telljohann U. 1992, 'Temperature dependence of silison photodiode quantum efficiency: theoretical and experimental results', in SPIE, Vol. **1679**, p. 200

Appourchaux T., Sekii T., Gough D., Lee U., Wehrli C., the VIRGO team 1998d, 'Structure inversions with the VIRGO data', in Sounding Solar and Stellar Interiors, IAU 181, J. Provost and F.-X. Schmider (eds.), Kluwer Academic Publishers, Dordrecht, p. 159

Appourchaux T., The Virgo Team 1998, 'Results from the Luminosity Oscillations Imager on board SOHO: Low-degree p-mode Parameters for a 2-year Data Set', in Structure

and Dynamics of the Interior of the Sun and Sun-like Stars, S. Korzenik and A. Wilson (eds.), ESA SP-418, ESA Publications Division, Noordwijk, The Netherlands, p. 99

Appourchaux T., Toutain T. 1998, 'Detection of solar p modes in the guiding signals of the luminosity oscillations imager', in Sounding Solar and Stellar Interiors, IAU 181, Poster volume, J. Provost and F.-X. Schmider (eds.), Kluwer Academic Publishers, Dordrecht, p. 5

Appourchaux T., Toutain T., Gough D. O., Kosovichev A. 1995b, 'Testing the Statistical Significance of the Asymmetries of p-Mode Line Profiles: Application to the IPHIR Data', in ASP Conf. Ser. 76: GONG 1994. Helio- and Astero-Seismology, p. 314

Cacciani A., Rosati P., Ricci D., Egidi A., Appourchaux T., Marquedant R., Smith E. 1991, 'Theoretical and experimental study of the magneto-optical filter', Technical report, Jet Propulsion Laboratory

Domingo V., Sanchez L., Appourchaux T., Andersen B. 1998, 'Observations of the latitudinal variation of the solar radiance of non-active regions of the sun', in New eyes to see inside the sun and the stars, IAU 185, F.-L. Deubner, J.Christensen-Dalsgaard and D.Kurtz (eds.), Kluwer Academic Publishers, Dordrecht, The Netherlands, p. 111

Eff-Darwich A., Korzennik S., Rabello-Soares M., Appourchaux T., Tomczyk S., schou J. 1998, 'Yet another inversion of the solar core rotation rate', in Sounding Solar and Stellar Interiors, IAU 181, Poster volume, J. Provost and F.-X. Schmider (eds.), Kluwer Academic Publishers, Dordrecht, p. 85

Fröhlich C., Finsterle W., Andersen B., Appourchaux T., Chaplin W., Elsworth Y., Gough D., Hoeksema J. T., Isaak G., Kosovichev A., Provost J., Scherrer P., Sekii T., Toutain T. 1998, 'Observational upper limits for low-degree solar g modes', in Structure and Dynamics of the Interior of the Sun and Sun-like Stars, S. Korzenik and A. Wilson (eds.), ESA SP-418, ESA Publications Division, Noordwijk, The Netherlands, p. 67

Gelly B., Fossat E., Pallé P., Appourchaux T., S. E., Fierry-Fraillon D., Grec G., Hoeksema T., Khalikov S., Lazrek M., Loudagh S., Pantel A., Régulo C., Sanchez L., Schmider F.-X. 1995, 'Solar p-mode frequencies from the IRIS network', in Helioseismology, 4th SOHO workshop, Poster session, J. Hoeksema, V. Domingo, B. Fleck and B. Battrick (eds.), ESA SP-376, ESA Publications Division, Noordwijk, The Netherlands, p. 373

Gizon L., Appourchaux T., Gough D. O. 1998, 'LOI/SOHO constraints on oblique rotation of the solar core', in New eyes to see inside the sun and the stars, IAU 185, F.-L. Deubner,

J.Christensen-Dalsgaard and D.Kurtz (eds.), Kluwer Academic Publishers, Dordrecht, The Netherlands, p. 37

Hill F., Rust D. M., Appourchaux T. 1988, 'Rotation in the Solar Convection Zone Inferred from Fabry-Perot Observations of the 5-min Oscillations', in IAU Symp. 123: Advances in Helio- and Asteroseismology, J.Christensen-Dalsgaard and S.Frandsen (eds.), D.Reidel Publishing Company, Dordrecht, p. 49

Leifsen T., Andersen B., Appourchaux T., Fröhlich C., Hoeksema T., Jiménez A., Toutain T., Wehrli C. 1998a, 'Sources of amplitude modulation of low degree solar p modes', in Structure and Dynamics of the Interior of the Sun and Sun-like Stars, S. Korzenik and A. Wilson (eds.), ESA SP-418, ESA Publications Division, Noordwijk, The Netherlands, p. 939

Leifsen T., Andersen B., Appourchaux T., Fröhlich C., Jiménez A., Toutain T., Wehrli C. 1998b, 'Temporal behaviour of p modes from VIRGO', in Sounding Solar and Stellar Interiors, IAU 181, Poster volume, J. Provost and F.-X. Schmider (eds.), Kluwer Academic Publishers, Dordrecht, p. 47

Leifsen T., Andersen B. N., Appourchaux T., Fröhlich C., Jiménez A., Toutain T., Wehrli C. 1998c, 'Amplitude modulation of radial p modes from Virgo', in New eyes to see inside the sun and the stars, IAU 185, F.-L. Deubner, J.Christensen-Dalsgaard and D.Kurtz (eds.), Kluwer Academic Publishers, Dordrecht, The Netherlands, p. 113

Provost J., Berthomieu G., Toutain T., Appourchaux T., the VIRGO team 1998, 'Low-degree oscillations modes and VIRGO results', in Sounding Solar and Stellar Interiors, IAU 181, Poster volume, J. Provost and F.-X. Schmider (eds.), Kluwer Academic Publishers, Dordrecht, p. 113

Rabello-Soares M., Appourchaux T., Jiménez A., Roca-Cortés T. 1995a, 'Preliminary results of the diameter signal on LOI', in Helioseismology, 4th SOHO workshop, Poster session, J. Hoeksema, V. Domingo, B. Fleck and B. Battrick (eds.), ESA SP-376, ESA Publications Division, Noordwijk, The Netherlands, p. 397

Rabello-Soares M., Jiménez A., Roca-Cortés T., Appourchaux T. 1995b, 'An attempt to estimate the intensity background spectra', in Helioseismology, 4th SOHO workshop, Poster session, J. Hoeksema, V. Domingo, B. Fleck and B. Battrick (eds.), ESA SP-376, ESA Publications Division, Noordwijk, The Netherlands, p. 365

Rabello-Soares M., Roca Cortés T., Jiménez A., Appourchaux T. 1998a, 'The solar equatorial rotation profile measured by LOI-T', in Sounding Solar and Stellar Interiors, IAU

181, Poster volume, J. Provost and F.-X. Schmider (eds.), Kluwer Academic Publishers, Dordrecht, p. 115

Rabello-Soares M. C., Appourchaux T. 1998, 'Measurement of GONG Low-Degree p-Mode Parameters', in Structure and Dynamics of the Interior of the Sun and Sun-like Stars, S. Korzenik and A. Wilson (eds.), ESA SP-418, ESA Publications Division, Noordwijk, The Netherlands, p. 299

Rabello-Soares M. C., Appourchaux T., Christensen-Dalsgaard J. 1998b, 'Rotation of the Solar Core Inferred from GONG Data', in Structure and Dynamics of the Interior of the Sun and Sun-like Stars, S. Korzenik and A. Wilson (eds.), ESA SP-418, ESA Publications Division, Noordwijk, The Netherlands, p. 837

Rust D., Appourchaux T. 1988, 'The Stable Solar Analyzer', in Seismology of the Sun and Sun-Like Stars, V.Domingo and E.J.Rolfe (eds.), ESA SP-286, ESA Publications Division, Noordwijk, The Netherlands, p. 227

Rust D. M., Appourchaux T., Hill F. 1988, Performance of a Stabilized Fabry-Perot Solar Analyzer, in IAU Symp. 123: Advances in Helio- and Asteroseismology, J.Christensen-Dalsgaard and S.Frandsen (eds.), D.Reidel Publishing Company, Dordrecht, p. 475

Toutain T., Appourchaux T., Fröhlich C., Kosovichev A., Nigam R., Scherrer P. 1998a, 'Line asymmetry of VIRGO and MDI low-degree p modes', in Structure and Dynamics of the Interior of the Sun and Sun-like Stars, S. Korzenik and A. Wilson (eds.), ESA SP-418, ESA Publications Division, Noordwijk, The Netherlands, p. 973

Toutain T., Appourchaux T., Kosovichev A. 1998b, 'Observation of low-degree modes from SOHO/MDI using optimal masks', in New eyes to see inside the sun and the stars, IAU 185, F.-L. Deubner, J.Christensen-Dalsgaard and D.Kurtz (eds.), Kluwer Academic Publishers, Dordrecht, The Netherlands, p. 179